University of Southampton Research Repository

UNIVERSITY OF SOUTHAMPTON

FACULTY OF ENGINEERING AND THE ENVIRONMENT

INSTITUTE OF SOUND AND VIBRATION RESEARCH

THE MECHANISM OF RAILWAY CURVE SQUEAL

By

Bo Ding

Thesis for the degree of Doctor of Philosophy

September 2018

UNIVERSITY OF SOUTHAMPTON

<u>ABSTRACT</u>

FACULTY OF ENGINEERING AND THE ENVIRONMENT

INSTITUTE OF SOUND AND VIBRATION RESEARCH

Thesis for the degree of Doctor of Philosophy

THE MECHANISM OF RAILWAY CURVE SQUEAL

Bo Ding

Railway is an energy-efficient means of transport and it is also an important solution to traffic congestion. However, the noise and vibration problems caused by railways attract more and more attention now. One particularly severe problem is curve squeal noise, which is an intense tonal noise that arises in tight curves under certain running and environmental conditions. The mechanism behind this squeal noise is still the subject of controversy. Two causes have been proposed over the last several decades: falling friction and mode coupling. The first one supposes that a decrease of the friction coefficient with increasing lateral sliding velocity occurs and this is equivalent to introducing negative damping into the system, which then feeds energy into the system. In the mode coupling phenomenon, coupling occurs between the vibration in two different directions and energy can be transferred between them.

In this thesis, firstly, these two mechanisms are explored by using an existing curve squeal model to predict the curve squeal in both the frequency domain and the time domain. This model is improved by including a track model based on mass-spring systems, which is more physical and easier to use in the time domain. The results show that both falling friction and mode coupling can lead to instability. Also, the inclusion of the rail dynamics is found to play an important role in the generation of curve squeal. Moreover, it is found that the inclusion of wheel rotation in the model affects the results for different wheels to different extents. To illustrate the findings in terms of wheel mode coupling and wheel-rail coupling instability from this model, several further studies are then performed.

A two-mode model is developed to assess the respective roles of the mode-coupling and falling-friction instability mechanisms in the generation of curve squeal. Different pairs of

modes from different wheels are considered. A parametric study is performed including investigation of the effect of the adhesion coefficient, contact angle, lateral offset of the contact point, wheel damping and friction curve slope. Two basic features are found to be characteristic of the wheel vibration in the presence of mode coupling. The first is a frequency shift meaning that the squealing frequency can be different from the natural frequency of the corresponding wheel mode. The second is a phase difference between the vibration in vertical and lateral directions. Previous wheel vibration measurements are used to give a qualitative comparison with the model to identify these features.

To study the effect of rail dynamics on curve squeal, the rail is firstly modelled as an infinite beam over a continuous elastic foundation. In contrast with the wheel, it is not characterised by vibration modes. Results show that the presence of the rail plays a role in the instability. Various effects are then considered that may change the resonant behaviour contained in the rail dynamics. These include the effect of varying the rail pad stiffness, the influence of the periodic support of the rail, reflections between multiple wheels on the rail, rail cross-section deformation and the inclusion of rail cross mobility. Finally, a reduced model is developed to identify the essential elements of the dynamic behaviour of the rail that can cause instability. In this model, a single wheel mode is included and the rail is represented as a mass, a spring or a damper. It is found that it is not necessarily the introduction of 'modes' in the rail that causes the wheel modes to couple with the rail; instead the equivalent mass and/or damper behaviour of an infinite rail is the origin of a wheel-rail coupling phenomenon.

Finally, a laboratory measurement is performed by modifying an available machine originally designed to perform pin-on-disc friction measurements. By using a 1:5 scale model of a railway wheel, squeal noise is observed at two different frequencies. During the measurements the wheel is stationary and is set in the vertical plane while the rotating disc lies in the horizontal one. The axis of the wheel is tangent to the rotating disc. Lateral force and wheel vibration in radial and axial direction are recorded. From the vibration data it is found that the response of the wheel in the vertical and lateral directions are almost in phase and that the squealing frequencies is always almost coincident with a natural frequency of the wheel. For the friction, a mild falling trend can be observed when the sliding velocity increases. For sliding velocities below 0.15 m/s the peak axial vibration velocity is found to be equivalent to the velocity of the rotating disc at the contact point. These observations suggest that stick-slip and/or falling friction can be responsible for the squealing in this test-rig while there is no evidence of mode coupling in this specific situation.

Table of contents

List of figures

xii

List of tables

Declaration of Authorship

I, Bo Ding, declare that this thesis entitled THE MECHANISM OF RAILWAY CURVE SQUEAL and the work presented in it are my own and have been generated by me as the result of my own original research.

I confirm that:

1. This work was done wholly or mainly while in candidature for a research degree at this University;

2. No part of this thesis has previously been submitted for a degree or any other qualification at this University or any other institution;

3. Where I have consulted the published work of others, this is always clearly attributed;

4. Where I have quoted from the work of others, the source is always given. With the exception of such quotations, this thesis is entirely my own work;

5. I have acknowledged all main sources of help;

6. Where the thesis is based on work done by myself jointly with others, I have made clear exactly what was done by others and what I have contributed myself;

7. Parts of this work have been published. A full list of these publications is given in Appendix A.

Signed: ....

Date: ....

Acknowledgements

It is a long journey for me to finish this thesis but I have really enjoyed it. During the last four years study in ISVR, there are many people who have been very helpful and I would like to express my gratitude to them.

First of all, many thanks to my first supervisor, Prof. David Thompson. I knew he is a nice person even before I came to ISVR. I still remember how patient he was in the emails between us in which he tried to tell me how to apply the scholarship and reviewed my research proposals carefully at that time. During the last four years, I learned many things from him, not only the academic knowledge but also life experiences. After writing several reports and journal papers, I learned the rigorous research attitude and English writing skills from him. Moreover, his hard working and his enthusiasm for this research area inspires me when I had a hard time. The meeting we had together every week (sometime every other week) will be a precious memory to me. It is really a great honour for me to become one of his students.

I would like to thank my second supervisor, Dr. Giacomo Squicciarini, for his help and supervision in these years. Especially when I have problems with programming, he is always there to help and explain everything in detail with lots of patience. He also taught me how to analyse results and how to write journal papers. When conducting the measurements, I also learned many skills from setting up to carrying out measurement. The most important and useful thing I learned from him is his enthusiasm for the research. He is always full of energy and hardworking. This gives me more inspiration and motivation to continue doing the research when I face some difficulties.

Many thanks to the colleagues in Dynamics Group. This is an amazing group like a family together. Xianying Zhang, Hongseok Jeong, Boniface Hima, Jin Zhang, Qiyun Jin, Zoe Shih, Johannes Schmid, and Xiaowan Liu, etc, I am very grateful for them to help me in many things. The lunch or dinner we had together, the football matches we watched together, the office room where we study together, the same PhD journey we had together, are all valuable memories to me. Also, I would like to thank Dr. John Walker for his help in the measurement.

I deeply appreciate for the support from my family. The endless love from them is crucial power for me to finish this journey.

Finally, thanks for the financial support from China Scholarship Council.

xx

List of symbols

a	Longitudinal semi-axis of contact ellipse
$\mathbf{A}^w\ \mathbf{A}^r$	System matrix of wheel and rail dynamics
$\mathbf{B}^w\ \mathbf{B}^r$	Input matrix of wheel and rail dynamics
$\mathbf{C}^w\mathbf{C}^r$	Output matrix of wheel and rail dynamics
c_1	Damper in mass-belt system
c_e	Equivalent damping due to the friction force
$\mathbf{C_q}$	Modal damping diagonal matrix in the two degree of freedom mass-belt system
d_3^c	Dynamic approach of wheel and rail
F_i	Amplitude of the contact forces
$\mathbf{F^f}$	Vector of friction forces
f_x	Force in horizontal direction (x) in the two degree of freedom mass-belt system
f_y	Dynamic part of the friction force in the one degree of freedom mass-belt system (Section 3.2, Section 3.3).
	Force in vertical direction (y) in the two degree of freedom mass-belt system (Section 3.4);
f_t	Force in tangential direction (t) in the two degree of freedom mass-belt system
f_n	Force in normal direction (n) in the two degree of freedom mass-belt system

f_{ytot}	Sliding friction force in the one degree of freedom mass-belt system
f_{y0}	Equilibrium part of the friction force in the one degree of freedom mass-belt system
f_y	Dynamic part of the friction force in the one degree of freedom mass-belt system
f_i	Dynamic forces (and moments) in the wheel/rail contact system
f_{itot}	Total forces (and moments) in the wheel/rail contact system
f_{i0}	Steady forces (and moments) in the wheel/rail contact system
$\{f^w\}$	Wheel force vector
G	Shear modulus
$\mathbf{G}$	Mobility matrix
$\mathbf{H_1}$	Matrix of the derivatives of non-dimensional friction forces in the self-excited loop
$\mathbf{H_2}$	Matrix of the fluctuation of normal force in the self-excited loop
$\mathbf{I}$	Identity matrix in the two degree of freedom system
$\mathbf{K_q}$	Modal stiffness diagonal matrix in the two degree of freedom system
k_i	Stiffness of the spring in mass-belt system
k_H	Hertz contact stiffness in wheel/rail contact
m_1	Mass in mass-belt system
$M_w; K_w; C_w$	Equivalent mass, stiffness and damping for a single wheel mode
$M_R; K_R; C_R$	Equivalent mass, stiffness and damping for rail

N_0	Normal force in mass-belt system
N_w	Number of multiple wheels
Q	Open loop transfer function
$\mathbf{R}; \dot{\mathbf{R}}$	Vector of rail state-space variables and its first derivative with respect to time
$\mathbf{T}_{rot}; \mathbf{T}_{off}$	The rotation matrix and the translation matrices
V	Belt velocity to represent the sliding velocity of the wheel
V_0	Rolling velocity
V_b	Belt velocity in the one degree of freedom mass-belt system
$\mathbf{V^w}$	Output wheel dynamic velocities
$\mathbf{V^s}$	Vector of sliding velocities
$V_i^w \, V_i^r \, V_i^s$	Amplitude of the wheel velocities, rail velocities and sliding velocities
v_{ytot}^s	Sliding velocity of the mass in the one degree of freedom mass-belt system
v_{y0}^s	Equilibrium part of the sliding velocity of the mass in the one degree of freedom mass-belt system
v_t	Dynamic part of the sliding velocity (tangential direction) in the two degree of freedom mass-belt system
$v_i^w \, v_i^r \, v_i^c$	Dynamic velocities of the wheel, rail, contact spring,
v_{itot}^s	Total sliding velocity between the rail and wheel
v_i^s	Dynamic sliding velocities between the rail and wheel
$\mathbf{W}; \dot{\mathbf{W}}$	Vector of wheel state-space variables and its first derivative to time

y_{tot}	Total displacement in the one degree of freedom mass-belt system
y_0	Equilibrium part of the displacement of the mass in the one degree of freedom mass-belt system
y	Dynamic part of the displacement in the one degree of freedom mass-belt system
$Y^{\mathrm{w}}; Y^{\mathrm{r}}; Y^{c}$	Mobility of wheel, rail and contact dynamics
γ	Creepage
γ_0	Steady-state creepage
ζ	Damping ratio
κ	Saturation coefficient in the heuristic falling function
λ	Falling ratio in the heuristic falling function
μ_d	Dynamic friction coefficient
μ_s	Static friction coefficient
ϕ_{ij}	Modeshape of mode j in i direction
Ψ	Mass-normalised mode shape of the additional mode in the equivalent rail model
$\mathbf{\Phi}$	Modeshape matrix
Γ_i	Normalised creep in Vermeulen and Johnson's friction model
ω	The natural frequency
Ω	Natural frequency of additional mode in the equivalent rail model

1 Introduction

1.1   Background

Railways are generally acknowledged to be an environmentally-friendly means of transport with the potential to operate with considerably less pollution, energy use and CO_2 emissions per passenger-km than road or air [1]. Moreover, due to their high capacity and efficiency, railways are a very important solution to traffic congestion. However, the expansion of railways can cause noise and vibration problems, which can become an important issue as it can cause annoyance and discomfort to the residents.

Railway noise can be generated by two main mechanisms [1]: 1) structural vibration, in particular due to the wheel/rail contact; 2) aerodynamic fluctuations due to the air turbulence when wind flows over solid objects. Aerodynamic noise is only a dominant source of noise from high-speed trains moving at speeds of 300 km/h and above. For most trains running below this speed, the wheel/ rail rolling contact is the main noise source [2]. In [3], Thompson and Jones divided wheel/rail contact noise into three main categories: 1) Rolling noise, the main source of noise from railway operations, generated by unevenness of the wheel/rail running surfaces. 2) Impact noise, generated by the wheel running over discontinuities at rail joints, dipped welds, points and crossings, or wheel flats. 3) Curve squeal noise: a high amplitude tonal noise, which often occurs when a train or tram negotiates a tight curve. This curve squeal noise is the topic of this thesis. It is probably the most annoying type of noise produced by the railway system due to its tonal nature and its high noise levels. In a recent review paper [4], it has been described as 'unpredictable' and more 'chaotic' rather than 'deterministic'.

When a rail vehicle negotiates a sharp curve the leading wheelset of a bogie or vehicle exhibits a considerable yaw angle relative to the running direction, leading to a lateral sliding velocity at the wheel-rail contact [5]. The sliding velocity normalised by the running velocity is termed the creepage and has components in all three directions (two translations and one rotation), with each component giving rise to a friction force (creep force) [6]. This force is considered to be the main cause of curve squeal noise [4].

Through decades of study, two mechanisms for curve squeal have been proposed associated with the lateral creep force. Originally, curve squeal was associated with the 'falling friction' mechanism. In this mechanism, the friction force is considered to be dependent on the sliding

velocity of the wheel-rail contact (see Figure 1-1(a)). If the magnitude of friction force reduces as the sliding velocity increases, it is equivalent to introducing negative damping into the system. This then can feed energy into the wheel-rail system and make it unstable. More recently, a number of authors have proposed an alternative mechanism based on 'mode coupling' which can also generate squeal in the presence of constant coefficient of friction. This can be explained using a model shown in Figure 1-1(b). The mass is held by two linear springs k_1 and k_2; k_H represents the vertical contact stiffness. In this case, from the equations of motion, it can be found that vertical force fluctuations influence the lateral force, but not vice versa, leading to an asymmetric stiffness matrix, which can give instabilities [4]. More detailed explanations of this model can be found in Chapter 3. Both mechanisms have been studied by many researchers both theoretically and experimentally. These previous studies are reviewed in the next section.

(a)   (b)
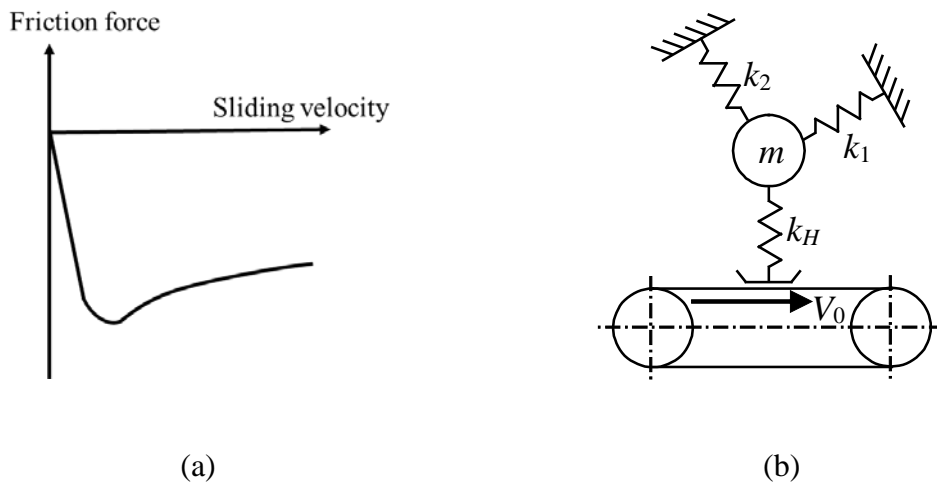
Figure 1-1. Falling friction and mode coupling.

1.2   Literature review

1.2.1 Theoretical studies

To understand the mechanisms behind curve squeal, many theoretical models have been proposed in the last few decades and the solution methods can be divided into frequency domain and time domain approaches. For frequency domain approaches, two methods have been utilized in the stability analysis of the curve squeal models. They are eigenvalues analysis and the Nyquist criterion [7]. In time domain models, the nonlinearities of the system can be taken into account. Details of these studies and their contributions are given in the following.

1.2.1.1 Falling friction mechanism

Von Stappenbeck [8] was the first to propose that the main mechanism for the generation of curve squeal was lateral sliding of the wheel across the rail, which occurs when a bogie with two or more rigid axles runs in a curve (see Figure 1-2). The wheels on the front axle tend to run out of the curve, but those on the trailing axle try to run into the curve. This curving behaviour will also be introduced in more detail in Chapter 2. Von Stappenbeck [8] observed, by measurements, that the high sound pressure levels of squealing noise can be associated with the natural frequencies of the wheel and squeal was found to occur at the front inner wheel of a bogie.
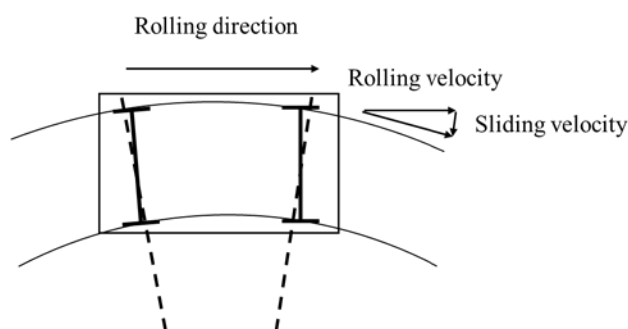
Figure 1-2. A railway bogie in a curve.

Rudd [9] described three possible mechanisms for squeal noise, which are: 1) the differential longitudinal slip between the inner and outer wheels; 2) wheel flange rubbing; 3) wheel/rail lateral 'crabbing', i.e. lateral creepage. However Rudd discounted the first two of these three possibilities, and believed that the lateral creepage at the wheel/rail contact is the main reason to induce squeal noise. At large creepage, the magnitude of the friction force decreases with increasing sliding velocity (see Figure 1-1(a)). Rudd showed that this results in a negative damping effect which then feeds energy into the system. Based on an assumed relationship between the friction force and the sliding velocity, Rudd developed a simple squeal model to study the stability of the wheel vibration and to predict the squeal noise level. According to this model, the falling friction mechanism causes unstable vibration of a single wheel mode. Oscillations grow up to a limit cycle defined by the non-linearities in the creep forces. Rudd's model was also adopted by van Ruiten [10] to investigate the squeal noise of trams.

Yokoi and Nakai [11-13] studied the generation mechanism of frictional noise in dry friction experimentally and theoretically. In their experiments, a steel disc representing the wheel was fixed in the centre of an axis and it was resting on a steel rod with a square section. This rod represented the rail and when the rod was moving in the lateral direction of the disc/rod contact, squeal noise was generated. Although different sizes of rod and different contact

loads were applied, the results showed that the dominating frequencies of squeal were usually at the frequency of axial modes of the disc with three, four and five nodal diameters. These modes were found to have low damping. In their theoretical study, by developing the governing equations of the frictional vibration of the disc and performing an eigenvalue analysis, the stability of the disc was discussed under different conditions. It was also found both experimentally and theoretically that squeal only occurred for a specific range of contact positions and the occurrences of squeal increased with increasing contact load.

In a review paper, Remington [14] described the state of knowledge of railway curve squeal up to 1985. Based on Rudd's model [9], he concluded that lateral creepage of the wheel was the most important cause for curve squeal noise and stated that flange contact was not believed to be a source of squeal noise. He suggested that a comprehensive analytical model of squeal was required to get a full understanding of the curve squeal problem. This should include the wheel dynamics, bogie dynamics in the curve and a detailed friction model. Since then, a number of increasingly complex models for curve squeal, consisting of various sub-models, have been published.

Schneider et al. [15] modelled the wheel as a disc with the finite element (FE) method and obtained the self-sustained vibration of the wheel disc using a modal expansion technique. They used Kraft's falling friction model [16] and solved the non-linear equations of motion in the time domain. From the frequency spectrum of the vibration velocity at the contact point, they showed that more than one frequency could be dominant in the limit cycle. It was also found that different wheel geometries could lead to different dominant frequencies. The sound pressure level and sound power were also obtained using a Rayleigh integral. Different wheel designs were considered and the acoustically optimal design of the wheel discs were then discussed. It was found that a type of wheel with a thicker wheel hub and web radiated a higher sound power level.

Fingberg [17] extended the model of Schneider et al. [15] to use a detailed finite element model of the wheel, an equivalent modal model of the track and a boundary element model for the sound radiation from the wheel. The model was again solved in the time domain [16]. Simulation results showed that a limit cycle response was obtained and the dominant frequencies varied for different running velocities (see Table 1-1). This work was extended further by Périard [18] who also included the vehicle curving behaviour in the same time-stepping calculation procedure as the squeal model. In his model, a finite element approach was used to model the rail dynamics and different empirical models of sliding friction were used to describe the decrease in creep force with increasing creepage. Périard compared the

4

results obtained using a rigid track to those with a flexible track; it was found that the track dynamics mainly affected the squealing noise at the entry and exit of the curve.

Table 1-1. Predicted squeal frequency against running velocity obtained by Fingberg (reproduced from [17]).

Velocity (m/s)	Squeal frequency (Hz)
2	260
3-4	870
5	1570
6	1580
7	1930
8-11	260
12	280
13-14	840
15-18	1400
19-20	840

Heckl et al. [19, 20] considered a model rig to simulate wheel lateral sliding and investigated models in both the frequency domain and time domain. In her model, the wheel was represented by a circular disc, which rolls on a turntable. The friction force was assumed to act at a single contact point. In the time domain, results showed two different responses: (1) simulations with a linear friction curve containing only a slip part led to unstable oscillations the amplitudes of which kept growing; (2) with a non-linear friction characteristic containing both a stick and a slip part, a limit cycle response was obtained and its amplitude determined the intensity of the squeal. The frequency of the limit cycle is determined by one unstable mode of the wheel or its harmonics. In a frequency domain approach, the friction force was considered as a piecewise function with a falling part and by assembling the governing equation of the friction-driven wheel, the growth rate, frequency and amplitude of the wheel vibration were obtained for different damping loss factors.

De Beer et al. [21-24] developed a frequency domain squeal model, which combines models of wheel dynamics, rail dynamics and contact dynamics. For the wheel and rail dynamics, mobilities obtained from the TWINS software [25] were used. For the contact dynamics in the vertical direction, a contact spring mobility was adopted, while in the lateral direction, Fingberg's [17] friction force model, which includes a falling regime, was employed. To allow the frequency domain analysis, this needs to be linearized about a nominal working position. The Nyquist criterion was used to assess the stability of the system in the frequency domain. The wheel lateral contact position was found to be important in the generation of curve squeal; squeal was only found to occur when the contact position shifted to the field side of the wheel tread. This model appears to be the first in which the variation of the normal contact force as well as the lateral force was included in a curve squeal model. As discussed

above, this can potentially introduce mode-coupling phenomena. However, the authors did not discuss mode coupling in this paper. Monk-Steel and Thompson [26] extended de Beer's model to include longitudinal and spin creepage as well as lateral creepage and normal load variations.

Huang [27, 28] extended de Beer's model to include all possible degrees of freedom at the wheel/rail contact. A self-excited feedback loop model was built to describe the relations between wheel-rail motions and contact forces. A finite element model of the wheel, an analytical rail model and a contact model based on Hertz contact were included in his model. The steady-state curving parameters were obtained from a preliminary vehicle dynamics model. He also implemented the wheel sound radiation model developed by Thompson and Jones [29]. For the friction model, the linear part of the creep force model was determined using Kalker's FASTSIM algorithm [30], which is a simplified theory for rolling contact problems. The falling function of the friction curve was based on Kraft's formula [16]. Both frequency domain and time domain analyses were performed. A parametric study was carried out, which included varying values of steady-state creepage, contact position and contact angle. As in other models described so far only a single contact point between wheel and rail was considered. Based on Huang's frequency domain model, Squicciarini et al. [31] studied the effect of a second contact point. Although in [14, 32] it was indicated that flange contact could suppress squeal, it was found that a second contact point on the wheel flange (or on the back of it) can play a role but it does not necessarily suppress the occurence of curve squeal. Two-point contact was also investigated in a time domain model in [33] and the results suggested that squeal in that two-point-contact case was because of wheel mode coupling. De Beer's model was also adopted by Xie et al. [34]. They introduced a modified version of the Kalker's FASTSIM algorithm [30] developed by Giménez et al. [35] into a vehicle dynamics calculation package to obtain the wheel/rail contact properties.

Liu and Meehan [36] developed a simple single-degree-of-freedom model for curve squeal. In this simple model, the vertical dynamics was not included. This means that mode coupling was not present and the only possibility of generating squeal noise would be the negative slope of the friction force relation. This model was used to explain the increase in sound level with increasing rolling speed and with increasing angle of attack found in a test rig. They also explained the generation mechanism of wheel squeal from the point of view of energy input per cycle of vibration. The same model was used again by Meehan and Liu in [37] to investigate the sensitivity of squeal noise to various means to reduce it. The results showed that the most important parameter is the lateral sliding velocity: only a 34%

reduction in lateral sliding velocity (or angle of attack) is required to achieve a 50% reduction of squeal vibration amplitude, corresponding to a 6 dB reduction in squeal noise. While the other parameters, including the modal damping, rolling velocity, creep curve parameters and contact parameters, all have an influence, larger percentage changes were required to obtain the same reduction in squeal vibration amplitude.

1.2.1.2 Mode coupling mechanism

More recently a number of authors have focussed on the mode coupling mechanism for curve squeal. This mechanism is another type of friction-induced vibration. It is sometimes also addressed as flutter and results in two modes of a system merging, under the action of an external non-conservative force, into a single unstable mode. In [38, 39], Hoffmann et al. developed a two-degree-of-freedom mass-belt model to explain this phenomenon. Two basic feature of mode coupling are presented in [38]. One is: a shift of frequency between the unstable frequency and the natural frequency of the two modes. The other one is: a phase lag between the vertical and lateral vibrations.

Mode coupling is more widely adopted in brake squeal analysis [40]. In [41], North first attributed disc brake squeal to flutter instability. By using the complex eigenvalue approach, he found that two modes can couple under the influence of friction and the system becomes unstable. Flutter can also occur for wing profiles or suspension bridges, where the external force in this case is of aerodynamic nature [40]. More recently, mode coupling was also applied to curve squeal and a number of studies have been carried out to investigate it.

Brunel et al. [42] performed a transient analysis of a wheel using an axi-harmonic finite element model. Two friction laws were considered based on measurements from Kooijman et al. [24], one with a falling characteristic and one with an increasing friction force. It was found that even the positive friction law could lead to a limit cycle solution, which the authors identified with the coupling of the normal and lateral dynamics of the wheel (which following the terminology used in brake-squeal they referred to as sprag-slip [43]). However, it was found that the falling friction characteristic led to much higher levels of squeal than the one with increasing friction force.

In [32, 44], Chiello et al. developed a squeal model that considered tangential and normal contact forces, as well as axial and radial wheel dynamics. The friction law considered had a linearly decreasing regime at large creepages. Two possibilities for instability can exist according to the authors: one is the negative damping effect from the falling friction, the other is the asymmetry of the stiffness matrix. Both frequency and time domain analyses

were performed for a monobloc metro wheel. It was found that mode coupling was important at large lateral offsets of the contact point (but not at most values of offset) when the vertical dynamics was included. Time domain results showed that two modes can coexist in the limit cycle response if they are harmonically related (i.e. the natural frequency of the higher frequency mode is close to a higher harmonic of the lower frequency mode). Collette [45] investigated the influence of vertical dynamics and showed that, even with a constant friction coefficient, this could lead to unstable vibration.

Glocker et al. [46] developed a squeal model with a flexible wheel and a rigid rail. The wheel dynamic properties were obtained from a finite element computation; a commercial multi-body software was used to obtain values of contact position, nominal contact forces, direction and magnitude of nominal creep. A constant friction coefficient was considered as the authors stated that the squeal is expected to be insensitive to the slope of friction curve. The frequency domain results showed that the leading inner wheel was prone to squeal and reprofiling of the leading inner wheel was suggested as a means to eliminate squeal. However, this was not further explored by the authors. Time domain analysis was also carried out and a limit cycle response was obtained, the frequency of which was around 4 kHz.

In [47] Pieringer also found that squeal noise can occur with a constant friction coefficient. She built a detailed time-domain model for the dynamic wheel/rail interaction. In this model, vehicle and track were represented by impulse response functions derived from detailed FE models which only considered vertical and lateral dynamics. For the contact model, Kalker's exact theory [48] was implemented to obtain a transient, three-dimensional and nonlinear contact model. She used the rms (root mean square) value of the lateral contact force to characterise the relative instability. The influence of lateral creepage, friction coefficient and lateral contact position were studied. Results showed that these three could be key parameters for the occurrence of curve squeal. Squeal could be observed for a constant friction coefficient. The effect of wheel rotation was investigated by Pieringer et al. in [49] but the results shows the effect was insignificant. Based on Pieringer's high-frequency wheel/rail interaction model [47], Zenzerovic [50, 51] developed an engineering time-domain model and investigated the effect of lateral creepage, spin creepage, friction and wheel/rail contact position.

Chen et al. [52] used commercial software to perform finite element complex eigenvalue analysis of a wheel in contact with a rail. However, in this model, the rail was only 5 m long and damping was assumed as zero, which was not a good representation of the infinite track.

The imaginary parts of the eigenvalues showed the merging of adjacent frequencies, which is a typical phenomenon seen in mode coupling. It was also found that the rail support stiffness had a significant effect on squeal in their case. The coefficient of friction needed to prevent curve squeal increased from 0.1 to 0.4 when the rail support stiffness was increased by 50%.

Similarly, by making use of commercial finite element analysis software, Fourie et al. [53] developed a FE model for the wheel and rail and then performed complex eigenvalue analysis of the system. In their model, they considered a saturated longitudinal creepage in the absence of lateral creepage. The curve radius they considered is 1000m, which is consistent with the site at which they performed measurement. In contrast to [47] they explained that the wheel rotation, which can spilt the wheel natural frequencies into pairs, has an important effect on curve squeal. They showed that the doublet modes of the wheel circumferential mode with two nodal diameters can be coupled with each other. This wheel mode was also found to be predominantly unstable during the field measurement in [54].

1.2.1.3 Summary

An overview of the previous theoretical studies of curve squeal is given in Table 1-2. They are classified according to whether rail dynamics and normal contact dynamics are included in the modelling, and whether frequency domain and/or time domain analysis is used in the approach.

Table 1-2. Summary of previous theoretical studies on curve squeal

	Reference	Inclusion of rail dynamics	Inclusion of normal contact dynamics	Frequency domain	Time domain
Falling friction	Rudd [9] Van Ruiten [10] Schneider et al. [15] Liu et al. [36, 37]	✗	✗	✗	✓
	Nakai et al. [11-13]	✗	✗	✓	✓
	Fingberg [17]	✓	✗	✗	✓
	Périard [18]	✓	✓	✗	✓
	Heckl et al. [19, 20]	✗	✗	✓	✓
	de Beer et al. [21-24] Monk-steel and Thompson [26] Xie et al. [34] Squicciarini et al. [31]	✓	✓	✓	✗
	Huang [27, 28]	✓	✓	✓	✓
Mode coupling	Brunel et al. [42]	✗	✓	✗	✓
	Koch et al.[32, 44] Collette [45] Glocker et al. [46]	✗	✓	✓	✓
	Pieringer et al. [47, 50]	✓	✓	✗	✓
	Chen et al. [52] Fourie et al. [53]	✓	✓	✓	✗

In these studies, it was also found that the curve squeal noise is usually associated with wheel axial modes. These are summarized in Table 1-3. The wheel modes responsible for instability are identified by their approximate natural frequencies and by the number of nodal diameters n and nodal circles m: (n, m). Radial and circumferential modes are identified as (n, r) and (n, c) modes [1]. This identification of wheel modes will be used throughout this thesis.

Table 1-3. Summary of responsible wheel modes for curve squeal from previous theoretical studies

Reference	Wheel modes (n, m)	Frequency
Schneider et al. [15]	(3, 0)	1.1 kHz
	(5, 0)	2.8 kHz
	(6, 0)	4 kHz
Heckl et al. [19, 20]	(2, 1)	2.7 kHz
	(3, 1)	6.5 kHz
de Beer et al. [21-24]	(2, 0) to (6, 0)	Not given
Huang [27, 28]	(3 ,0)	1.1 kHz
Brunel et al. [42]	(2, 0)	1 kHz
	(3 ,0)	2 kHz
	(4, 0)	3 kHz
Koch et al.[32, 44]	(3, 0)	1.1 kHz
Glocker et al. [46]	Coupling between (6, 0), (4, r) and (2, r)	close in frequency, all around 4 kHz
Pieringer et al. [47]	(2, 0)	430 Hz
	(3, 0)	1.1 kHz
	Coupling between (7, 0) and (2, c)	Both are around 5.2 kHz
Fourie et al. [53]	Doublet mode (2, c) due to wheel rotation	4.2 kHz

1.2.2 Measurements

Many measurements of squeal noise have also been presented in literature. These can be divided into laboratory measurements and field measurements. In laboratory measurements, usually reduced scale test rigs are used and the vibration response of the discs can be measured. The contact forces can also be measured although they are usually averaged values over time and not the instantaneous ones. This is because the force measurement systems are influenced by the dynamics of the systems. In field measurements, usually sound or vibration data are obtained, but it is generally not possible to obtain information about the contact forces.

1.2.2.1 Laboratory measurements

De Beer et al. [22, 24, 55] developed a 1/3 scale twin disc test rig to measure the friction coefficient and to assess the presence of squeal. The rig consisted of a pair of discs, the 'wheel disc' running on the 'rail disc'. In these measurements, the 'rail disc' has a finite radius of curvature in the tangential direction, whereas for a real rail this radius is infinite.

The authors compensated for this effect by adjusting the lateral radius of curvature of the 'rail disc'. Also, thin steel plates were bolted onto the 'rail disc' to increase its damping. Sound pressure levels were measured. The measurement results showed that the occurrence of squeal noise was related to the falling of the friction coefficient. It was found that squeal occurred when the rolling contact angle was above 0.4˚ which is also the region where falling friction was found (see Figure 1-3), which corresponds to 0.7% lateral creepage. A frequency shift was also found in [55] but no explanation was given.
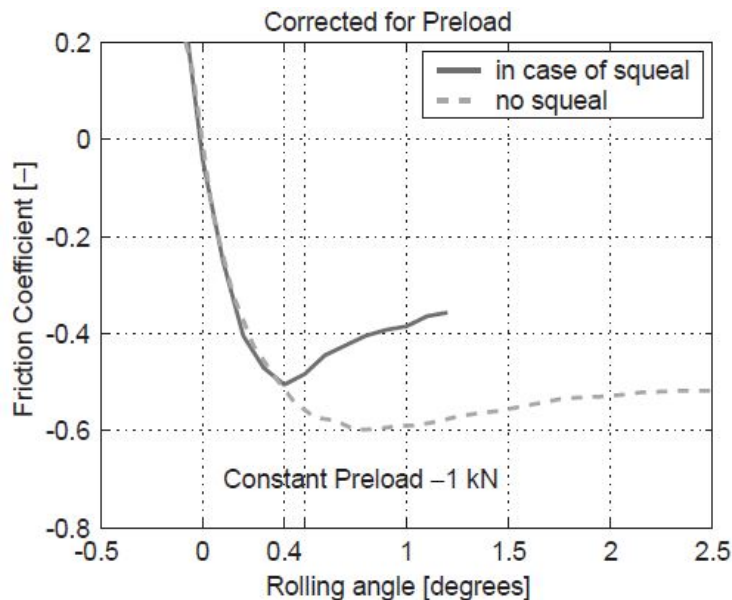
Figure 1-3. Measured friction coefficient for stable and unstable creepage (from de Beer et al. [22]).

Monk-Steel et al. [56] developed and modified de Beer et al.'s test rig to introduce a longitudinal creepage. For a longitudinal creepage of 2% the level of lateral creep force was reduced and the shape of the lateral friction curve was modified so that the falling regime only developed at higher values of yaw angle (in this case above 1° or a creepage of 1.7%). The sound pressure level was also measured. It was found that in the presence of longitudinal creepage, the onset of squeal noise occurred at a yaw angle of 1.4°, whereas this critical yaw angle was only 0.4° without longitudinal creepage (see Figure 1-4).
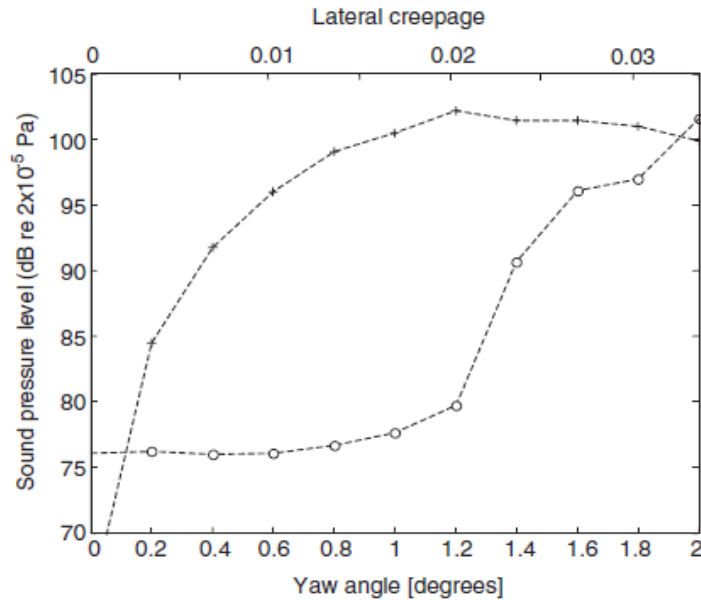
Figure 1-4. Measured sound pressure level in the 1250 Hz one-third octave band at 0.5 m from the web of the wheel; - - + - - lateral creepage only; - - ○ - - with a longitudinal creepage of 0.02 (from Monk-Steel et al. [56]).

Another 1/3 scale twin disc rig model was built by Hsu et al. [28]. In their measurement, the lateral creepage was adjusted by changing the yaw angle of one of the roller disc. The lateral force was measured using strain gauge bridges. The sound pressure level (SPL) results showed that when the rail roller had no additional damping, squeal noise occurred at a yaw angle of 1° (creepage of 1.74%), while this value becomes 0.45° (creepage of 0.79%) when damping was added to the rail roller. This finding was not explained but it could be related to mode coupling; the effect of damping on mode coupling will be discussed in Chapter 6.

Huang [27] made use of the twin disc rig model from [28] to obtain new data. Three different surface conditions were considered: dry, watered and lubricated. It was found from the SPL measurements that the watered case did not significantly reduce squeal noise whereas in the lubricated case the squeal noise was eliminated. The friction coefficient data showed that a falling region was observed with both dry and watered cases; however, with the lubricated surface condition, no falling region was present.

Koch et al. [32] developed a 1/4 scale test rig. This contained a single 1/4 scale wheelset on a very large roller on which the rail was mounted. The effect of rolling speed, wheel/rail lateral position, angle of attack and vertical load were investigated. It was shown that squeal noise occurred when the angle of attack was larger than 8 mrad (creepage of 0.8%). The sound pressure level was found to increase by 4-8 dB for a doubling of the rolling speed. The effect of vertical load was found to be negligible and the contact position was also

13

unimportant except for flange contact; no squeal was observed for flange contact. The effect of damping was investigated by adding 1/4 scale ring dampers to the test axle. A minimum damping loss factor for the wheel was found to prevent squeal noise, which was 3%. Importantly, from the measurement of lateral friction force, no falling regime was detected for either dry or watered cases. The authors assumed that this was due to the fact that the average friction was measured instead of the transient one.

Another wheelset test rig was developed more recently by Jie et al. [57]. A negative slope of friction force characteristic was observed and squeal noise was detected when the yaw angle was larger than 0.7° (creepage of 1.2%). Four dominant frequencies were found in the sound pressure level spectra. These were compared with the measured driving point mobilities of the wheel and rail discs. Results showed that two of the four dominant frequencies matched the resonance frequencies of the wheel and rail discs while the other two were not found in the mobilities. This might be related with the frequency shift due to mode coupling or some of them are the higher harmonics. However, they only showed the axial mobility of the wheel and rail discs in the paper.

1.2.2.2 Field measurements

Van Ruiten [10] reported squeal measurements on trams at different sites with different wheel types in the Netherlands. The squeal frequency was found to occur in the 500 Hz, 1250 Hz and 2500 Hz one-third octave bands. These corresponded to wheel axial modes with 2, 3 and 4 nodal diameters. In most cases, the squeal was attributed to the inside of the curve. It was also observed, for only one tram type, that differences in the track structure affected the squeal measurement results. This could either be due to the change in track dynamics or the change of curving conditions. However no further discussion of this effect from the track structure was given.

Merideno [58] reported a squeal problem in a 25 m radius tramway line in Spain. The squealing frequency was found to be in the frequency range 780-800 Hz and was associated with the wheel axial mode with 2 nodal diameters.

A study at a new line in London, UK, was described in [4]. Measurements were performed in two curves with the same trains. At the first curve, the squeal was found at 800 Hz (corresponding to a circumferential mode) and at 1.2 kHz, 2.3 kHz and 4 kHz (axial modes with 3, 4 and 6 nodal diameters). On the second curve, the squeal was found at 7.25 kHz and 9.4 kHz. The corresponding wheel modes were either radial modes with 8 and 10 nodal diameters or axial modes with 9 and 11 nodal diameters, as in each case the natural

frequencies are close to the squeal frequencies found in the measurement. The close proximity of pairs of modes could also suggest mode coupling is likely.

Glocker et al. [46] measured squeal noise at both sides of a tight curve with 200 m radius. In their measurements, 83 regular train passages of a total of 3085 train passages were identified as squealing. To identify the wheels responsible for squeal, the noise intensity and rail acceleration levels taken at the inside and outside of the curve were compared. As a result, they found that in 62 of these 83 passages, the squeal noise occurred at the inside of the curve; in 32 of these 62 squeal events, the squealing wheel was the leading inner wheel of the leading bogie of the driving trailer. Squeal noise was also observed at the outside of the curve although it was less frequent. The frequency of the squeal noise was 4 kHz; higher harmonics at 8 and 12 kHz were also observed. Some frequency shift was observed but it was attributed to Doppler effect and not to mode coupling.

Vincent et al. [59] carried out field measurements at two different sites. One was performed with a metro bogie running on a curve with 75 m radius. The wheels were monobloc with low damping. For different running speeds (10, 20, 30 and 40 km/h), it was shown that the highest noise level was always associated with the front inner wheel. The squealing frequencies were identified with three wheel modes: axial modes with 2, 3, and 4 nodal diameters. The other field measurement was conducted on a 60 m radius tramway with trams with resilient wheels. The rails of this tramway were grooved rails and equipped with anti-squeal welded strips. The results showed that, for both the motor bogie and the trailing bogie, squeal occurred at the front inner wheel for a lower running speed, but the rear outer wheel of the trailing bogie squealed at higher speeds. It was also found from this tramway measurement that all wheel axial modes between $n = 3$ and 9 nodal diameters were excited when the tram passed the test curve, although only one mode was predominant at any one time.

Corradi et al. [60] performed a curve squeal measurement on a tramway curve with 17.5 m radius. The track was fitted with grooved rails and the wheels were resilient wheels which have relatively high damping. The results showed that both inner and outer wheels were able to squeal. Interestingly, one of the dominant squeal frequencies was at 1.5 kHz which did not correspond to any of the wheel modes. This squealing frequency was about 80 Hz higher than the closest wheel mode. This frequency shift can be an evidence of mode coupling. The measurements reported in [62] have been made available for this thesis and will be analysed further in Chapter 1.

Fourie et al. [54] measured squeal noise on a curve with 1000 m radius with a freight train service. They found that the squealing noise comes from the trailing inner wheel of some bogies under empty wagons, where the lateral creepage was very small but the longitudinal creepage exceeded the creep saturation. They associated the squeal frequencies with the doublet modes due to wheel rotation. The modes responsible were: a radial mode with 6 nodal diameters, a circumferential mode with 2 nodal diameters and a radial mode with 7 nodal diameters.

Anderson et al. [61, 62] summarised field measurements carried out in Australia for both passenger and freight traffic. They proposed that curve squeal noise can be divided into three categories. 1) "Friction controlled": this type of squeal noise was relatively moderate and was generated by approximately 10% of passing stock. Top-of-rail friction modifiers can efficiently reduce this squeal noise. Additionally, it was also affected by the environmental conditions, which makes this squeal noise vary randomly. 2) "Steering controlled": this type of squeal noise was severe and associated with about 2% of passing stock. Poor steering was usually observed. Top-of-rail friction modifiers had little effect on this squeal noise. 3) "Systemic": this type of squeal noise involved a large proportion of passing stock. The underlying effects could involve one or both of the friction controlled and steering controlled types. However, this classification scheme was based more on mitigation measures than on the mechanisms of squeal.

Curley et al. [63] carried out a seven month measurement campaign on a curve with 290 m radius. They applied friction modifiers and lubrication at this test site to determine their effect. Friction modifiers are usually used to reduce or eliminate the falling friction characteristic without reducing the level of friction too much. Lubrication is used to reduce the friction levels and hence it is usually applied to the rail gauge corner or wheel flange to ensure the safe running of the train [1]. The results showed that lubrication had a better effect on reducing squeal noise than top-of-rail friction modifiers. It was also found that using the friction modifier or the lubrication at only the inner rail gave no benefit. This indicated that at this test site, curve squeal noise was caused at the outer rail.

Jiang et al. [64] reported squeal noise measurements at a curve with 284 m radius used for freight traffic. At this test site, it was found that the lateral vibration level of the outer rail was about 20 dB higher than that of inner rail, which indicated that the squeal noise was mostly associated with the outer rail. The angle of attack was also measured in this study and it was found that the magnitude and likelihood of squeal appeared to increase with increasing angle of attack. In [65], Jiang et al. showed more measurement data and proposed

that mode coupling could be responsible for the squeal noise measured at this site. This was due to the observation of a phase difference between vertical and lateral rail vibration, which is a typical feature of mode coupling. More recently, data collected in a three-year period using a wayside condition monitoring system at a curve with 300 m radius was presented by Jiang et al. [66]. This system recorded the noise level, angle of attack, lateral position and running speed of the trains. It was found that freight trains generated more severe squeal than passenger trains and the likelihood of squeal increased with increasing angle of attack but it was also found that, even at large angles, not every wheel squealed.

1.2.2.3 Summary

Both test rigs and field measurements have their own difficulties and limitations. Test rigs are usually produced at reduced scale and hence the dynamic behaviour is different from the one in traffic. The contact patch is also smaller and the normal load may not be representative. Sound or vibration data can be obtained in field measurements but friction measurements directly associated with squeal are not present in the literature. Adhesion curves measured in the field are usually determined for traction and not for lateral creepage [4]. Moreover, in both test rigs and field measurements it would not be easily possible to distinguish in the measured data between mode coupling and falling friction mechanisms unless some characteristic features of these mechanisms can be found in the measured results.

The laboratory measurements and field tests are summarized in Table 1-4 and Table 1-5 (Table 1-5 is reproduced from [4]). The critical yaw angle or lateral creepage is the value at which the friction starts to decrease. It can be seen from Table 1-4 that only in [32] was the falling regime of friction not detected. In this case, the critical yaw angle or lateral creepage listed is the corresponding value at which the squeal noise occurs. From Table 1-5, it can be seen that curve squeal can occur for different types of train and both inner and outer wheel can squeal. Also, it can be found from both laboratory and field tests that the squealing frequency is usually over 1 kHz, and mainly corresponds to wheel axial modes.

Both laboratory measurements and field measurements were also reviewed in [4]. It was concluded that although many measurements of adhesion coefficient for both longitudinal and lateral creepage have shown the existence of a falling region, mode coupling cannot be excluded and the two mechanisms may coexist during curve squeal. Moreover, it is unclear whether the friction laws that are measured quasi-statically apply for high frequency small amplitude motions.

Table 1-4. Summary of laboratory measurements of curve squeal

Reference	Testing setup and scale	Friction	Critical yaw angle /lateral creepage	Frequency	Wheel modes
[21-24]	1:3 scale twin disc	Falling	0.3° / 0.5%	1150 Hz 1200 Hz	n/a
[56]	1:3 scale twin disc	Falling	1° / 1.7%	n/a	n/a
[27, 28]	1:3 scale twin disc	Falling	0.2° / 0.35%	1094 Hz	(2, 0)
[32]	1:4 scale twin disc	no falling regime	0.46° / 0.8%	1730 Hz	(2 0)
[36, 67-69]	Reduced scale twin disc rig	Falling	0.3° / 0.5%	1100 Hz	(3, 0)
[57]	Reduced scale twin disc	falling	0.7° / 1.2%	1990 Hz, 3980 Hz	n/a

Table 1-5. Summary of field measurements of curve squeal [4].

Train type	reference	Curve radius	Frequency	Wheel modes	Wheel
Tram	[10]	n/a	500 Hz, 1250 Hz, 1600 Hz	$(2,0)$, $(3,0)$, $(4,0)$	Inner
	[59]	60 m	1200-8100 Hz	$(3,0)-(9,0)$	Leading inner
	[60]	17.5 m	1500 Hz	$(3,0)+(3,r)$ (frequency shift observed)	Inner and outer
	[58]	25 m	800 Hz	$(2,0)$	n/a
Suburban	[59]	75 m	450 Hz, 1100 Hz, 2000 Hz	$(2,0)$, $(3,0)$, $(4,0)$	Leading inner
	[4]	180 m	800 Hz, 1200 Hz, 2300 Hz, 4000 Hz	$(0,c)$, $(3,0)$, $(4,0)$, $(6,0)$	n/a
	[46]	200 m	4000 Hz	$(6,0)$ with $(4,r)+(2,2)$ (frequency shift observed)	Leading inner
Freight train	[54]	1000 m	4000-5000 Hz	$(2,c)$, $(6,r)$, $(7,r)$ (frequency shift observed)	Trailing inner
	[64]	284 m	1000-3000 Hz	n/a	Outer

1.2.3 Mitigation measures

A number of mitigation measures for squeal noise have been proposed and tested in the literature. These are summarised in this section. They include wheel damping treatments, lubrication, friction modifiers, rail damping treatments, modified curving behaviour and modified rail profiles.

1.2.3.1 Wheel damping treatments

There are several types of wheel damper that are commercially available, including tuned absorbers, constrained layer treatments, ring dampers and resilient wheels [4]. Figure 1-5 shows examples of these wheel damping treatments [4].
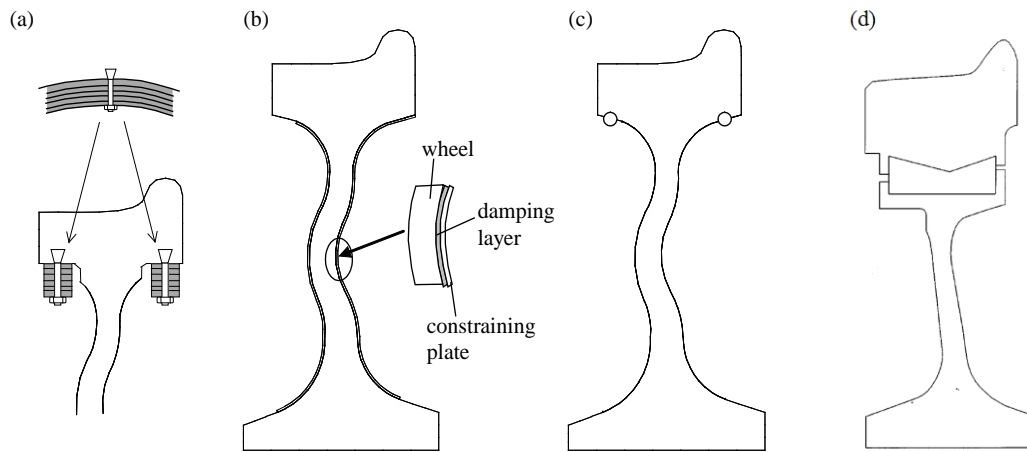
Figure 1-5. Examples of wheel damping treatments [4]: (a) tuned absorbers; (b) constrained layer damping; (c) ring dampers; (d) resilient wheel. [4]

In [70], Brunel el al. explained the mechanism of the attenuation of squeal noise by using ring dampers. These are a simple way to increase the wheel damping by inserting a metallic ring into a groove under the wheel rim. The finite element method was adopted and results showed that the frictional contact of the ring in the groove dissipated energy. According to the authors, the measured noise attenuation can be from 5 dB to 10 dB in some transit applications after using this ring damper. However, in some cases, this solution was less efficient. The efficiency varies even for similar wheels at different sites.

Bühler and Thallemer [71] reported some results of applying wheel tuned absorbers. In one case, it was found that the application of the absorber eliminated the squeal noise with dominant frequencies between 2 and 8 kHz, while for another case with dominant frequency at 700 Hz, the absorber did not work. This was not explained by the authors, but it could be that the damping limit was not achieved in terms of either mode coupling or falling friction mechanism. This will be explored in Chapter 6 of this thesis.

Marjani and Younesian [72] studied theoretically the effect of shunted piezoelectric patches on the suppression of squeal noise as a means of introducing damping. The frequency of the shunt circuit was tuned to be the same as the dominant squeal frequency. Results showed that a resonant shunt circuit was more effective when adding the damping at a specific frequency, but a resistance shunt circuit had better performance, in terms of the increase in damping, in a broadband frequency range. However, the effect of these patches on curve squeal was not directly presented.

Merideno et al. [58] also developed a damper system which was applied to eliminate squeal. This was described as a tuned constrained layer damper (CLD) treatment but in fact

resembles typical tuned absorber systems. A significant reduction of the sound pressure level was achieved when a proper design of damper was used to damp the wheel modes responsible for squeal.

1.2.3.2 Lubrication and friction modifiers

Eadie et al. [73-75] reported some applications of top-of-rail friction modifiers applied by a trackside applicator. This friction modifier can provide material with positive friction characteristics between the wheel and the rail. At the same time the friction level decreased and is maintained in the range of 0.35 ± 0.05. The positive friction slope can in theory suppress the squeal noise induced by the negative damping effect. Field tests at different sites showed that this friction modifier is an effective way to reduce curve squeal noise and it can also provide a good reduction of corrugation growth rates in curves.

Curley et al. [63] carried out some field tests of various top-of-rail friction modifiers and gauge face lubrication, which were applied in a curve with 290 m radius where freight trains always squealed. After several months of monitoring, it was found that only gauge face lubrication of the outer rail could eliminate the squeal noise, whereas squeal noise was not affected when top-of-rail friction modifiers were applied to the inner rail.

Corradi et al. [60] investigated the squeal noise in a sharp tramway curve in Milan. They found that water lubrication of the contact could completely prevent the squeal noise from occurring. However, although not reported in the paper, it was found that the squeal noise appeared again when the rail started to dry [4]. In addition, tram drivers also communicated that, according to their experience, the most severe and frequent squealing events usually happened just after the track had been washed by the rain and was drying[1].

Liu and Meehan [36, 67-69] used a twin-disc test rig to carry out a series of experimental studies of curve squeal. The measured sound pressure level was found to increase with increasing rolling speed and angle of attack. It was also found that a higher relative humidity can make the squeal more likely. The negative slope of the friction force characteristic was no longer observed after the application of an oil-based friction modifier and instead a positive slope was measured. This friction modifier was beneficial for reducing the sound pressure level, but it did not completely eliminate the squeal noise. Two possible explanations were given. First, the friction force measured by the authors was the averaged

---

[1] Personal communication from the authors.

value of force over time whereas if it was measured instantaneously the negative slope may still exist. Second, another possibility mentioned by the authors was mode coupling.

1.2.3.3 Rail damping and track dynamics

Rail dampers, consisting of a tuned mass-spring absorber system installed on each side of the rail, are an efficient way to reduce rolling noise by increasing the track decay rate [76]. However, this treatment only modifies the point mobilities of the track to a minimal extent and it is therefore not expected to modify the occurrence of curve squeal. It may slightly affect the overall noise level as it reduces the average rail vibration. If found to be effective for squeal it could be a more attractive solution than measures that must be applied to whole vehicle fleets.

In [4], Thompson et al. reported that rail dampers were installed at a site in London. Some reduction of the squeal noise level and occurence was found. However, because friction modifiers were also applied in this curve prior to the application of rail dampers, the effect of the rail dampers was uncertain. Nevertheless, the longer duration squeal events were reduced after the application of the rail dampers.

Jiang et al. [77] found that curve squeal noise was more severe for track with concrete sleepers than with timber sleepers. This indicated that the track dynamics may play an important role in curve squeal noise. The authors compared the track decay rate, the dynamic gauge and the point mobility of the two types of tracks. They claimed that the timber sleeper track was more flexible and thus can increase the dynamic gauge, which may change the contact conditions of the wheel and rail. They also found that the track mobility with concrete sleepers had a sharper resonance. The track decay rates were higher for timber sleepers in the squeal frequency range (above 1 kHz in this case).

1.2.3.4 Curving behaviour, rail profiles

Curve squeal usually occurs in tight curves as the bogie cannot align the wheels tangentially to the rail. Hence, improving the curving performance to make the wheel roll radially in the curve can reduce the squeal noise or even eliminate it.

In [61, 62], Anderson et al. found that at some sites certain freight trains were the main source of squeal due to poor steering. This was caused by ineffective centre-bowl lubrication leading to high angle of attack. By improving the centre-bowl lubrication the squeal was eliminated.

Bruni et al. [78] gave an extensive survey of control and monitoring for railway vehicle dynamics. They introduced the concepts of 'actuated solid wheelset' and 'actuated independently rotating wheels'. These can improve the vehicle curving behaviour while maintaining the vehicle stability. They also introduced control strategies for curving and the idea of 'perfect curving'. These can be achieved by controlling the yaw angles or by minimizing the longitudinal creep.

Elbers and Verheijen [79] introduced the effect of asymmetrical rail profiles on squeal noise. This was tested in a 200 m radius curve. It was found that the average sound pressure level was 3 dB lower after applying the design although the number of squeal events was not reduced. A second test was also performed with the same profile. In this case the rail head of the inner rail had also been impregnated with tungsten carbide. It was found that the squeal events were reduced from 74% to 26% and the average sound pressure level was reduced by 4 dB.

1.3   Objectives and layout of this thesis

The aim of this thesis is to provide a better understanding of the mechanism of curve squeal. It has been shown in the previous section that two mechanisms for curve squeal have been proposed in the literature but usually they have been studied separately. Moreover insufficient attention has been paid to the role played by the track dynamics. Hence, the objectives of this work are set below:

1) To develop a track model based on modal superposition and use it in the time domain part of the existing curve squeal model developed by Huang [27].

2) To investigate the role of the Coulomb friction coefficient, friction characteristics and rail dynamics by making use of the existing curve squeal model.

3) To assess the respective roles of the mode-coupling and falling-friction instability mechanisms in curve squeal by developing a reduced modal model.

4) To investigate the role of rail dynamics under constant friction force.

5) To design a laboratory measurement to verify the features of mode coupling or falling friction.

In order to meet these objectives, this thesis consists of the following chapters:

The curving behaviour of a free wheelset and a bogie are presented in Chapter 2. This will present how lateral sliding motion arises at the contact when the train is curving. The normal and tangential contact models adopted in the thesis are introduced in this chapter.

Chapter 3 explains three different friction-induced instability mechanisms by making use of simple mass-on-belt models. Stick-slip, falling friction and mode coupling are illustrated in this chapter.

In Chapter 4 an existing curve squeal model is first described and then an equivalent track model, based on modal analysis of multi-degree-of-freedom (mdof) mass-spring systems, is developed and implemented in the curve squeal model.

By making use of this curve squeal model, Chapter 5 presents a parametric study using both the frequency domain and the time domain versions of the model. The effects of the friction coefficient, friction curve characteristics and rail dynamics are analysed. By comparing the results, phenomena associated with mode coupling and the importance of rail dynamics are observed and highlighted.

Chapter 6 describes the development of a reduced modal model of wheel-rail contact systems. By making use of this model, the respective roles of mode-coupling and falling-friction mechanisms are investigated. A parametric study is performed in this chapter and basic features of mode coupling are shown. Some qualitative comparisons with field measurements of wheel acceleration during squeal are also presented.

In Chapter 7, both the Nyquist criterion and eigenvalue analysis approach are used to investigate the effect of rail dynamics. Various effects are considered that may introduce additional resonant behaviour into the rail dynamics. Also, by means of a reduced model, the main characteristics of the rail dynamics that can result in squeal are assessed.

A simple measurement campaign performed by adapting an existing pin-on-disc rig is presented in Chapter 8 and squeal noise is observed on a scaled wheel. It is deduced from the measurement results that falling friction or stick slip are the mechanisms behind this squeal case.

Finally, Chapter 9 summarises the conclusions obtained from this thesis; some recommendations for future work are also given.

1.4   Original contributions

The main original contributions in this thesis can be summarised as follows:

1) An existing curve squeal model is improved by developing and implementing an equivalent model for track dynamics. This equivalent track model is based on modal analysis of a multi-degree-of-freedom (mdof) mass-spring model and can be used in both time and frequency domain calculations for curve squeal.

2) Different origins of the instability of the system are observed by making use of the updated curve squeal model. They are falling friction, wheel mode coupling, and wheel/rail coupling. The effects of wheel rotation and rolling velocity are investigated.

3) A two-mode model is developed which can be used to assess mode-coupling and falling-friction mechanisms together. Parametric studies are performed including varying the adhesion coefficient, contact angle, lateral offset, wheel damping, and friction curve slope. The frequency shift and phase difference are observed from the simulation results of this model, which are two important indicators for mode coupling.

4) A field measurement from reference [60] is used to make qualitative comparisons with the results from the two-mode model. Available data have been re-analysed during this work to highlight the presence of frequency shift and phase difference.

5) A reduced model is developed to study the effect of rail dynamics on curve squeal. It is shown that the rail can play an important role in curve squeal by means of a form of coupling between the rail dynamics and a single wheel mode. However, it is not necessarily by introducing 'modes' in the rail that wheel modes can couple with the rail; instead the mass and/or damper behaviour of an infinite rail is responsible for wheel-rail coupling.

6) Laboratory measurements results suggested that falling friction or stick slip is responsible for the squealing in this measurement. The findings from these measurements give more evidence about the characteristics to distinguish the falling friction and mode coupling.

2 Railway curving behaviour and rolling contact

The wheels of railway vehicles are usually joined by a rigid axle to form a wheelset and two such wheelsets are mounted in a frame known as the bogie. When a train is travelling in a curve, the wheels cannot pass through the curve freely and instead the wheelset exhibits a non-zero angle of attack to the rail and consequently there is a lateral sliding velocity at the wheel-rail contact. This lateral sliding motion, causing a lateral creep force, is believed to be the main cause of curve squeal noise.

This chapter starts by describing the curving behaviour of a free wheelset and a bogie and then defines the creepage. It is explained how the lateral creepage arises during curving. Vertical and lateral models of the wheel-rail contact are also presented, which will be used in the subsequent chapters.

2.1 Curving behaviour

2.1.1 Curving of a free wheelset

A wheelset consists of two wheels connected by an axle. The running surface of a train wheel has an approximately conical geometry to keep the train's motion aligned with the track. Schematic views of a single wheelset running on a curved track are shown in Figure 2-1.
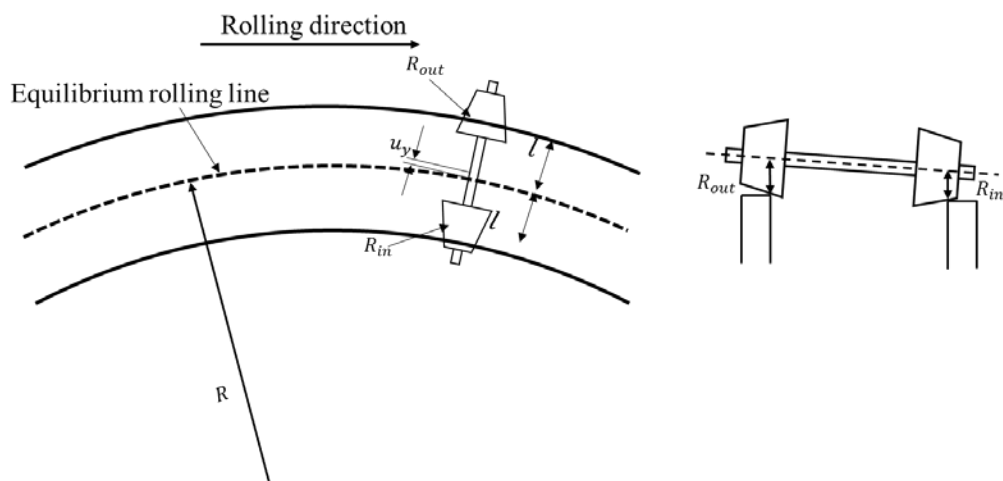
Figure 2-1. Radial steering of a free wheelset with conical profiles in a curve

It can be seen that, to achieve radial steering, i.e. the wheelset axis pointing towards the centre of the curve, the outer wheel needs to roll a longer distance than the inner wheel. This

will balance the difference in the lengths of the rails that the wheels roll over. For such free rolling the ratio of the radii between outer and inner wheels must satisfy [5]:

$$\frac{R_{out}}{R_{in}} = \frac{R + l}{R - l} \tag{2-1}$$

where R_{out} and R_{in} are the rolling radii of the outer and inner wheels, respectively, l is half the lateral distance between the points of contact of the wheels with the rails and R is the curve radius.

For conical profiles:

$$R_{out} = r_0 + \delta_0 u_y;$$
$$R_{in} = r_0 - \delta_0 u_y \tag{2-2}$$

where r_0 is the nominal wheel radius, u_y is the lateral displacement of the wheelset, and δ_0 is the conicity of the wheel (see Figure 2-2 as an example for the outer wheel).
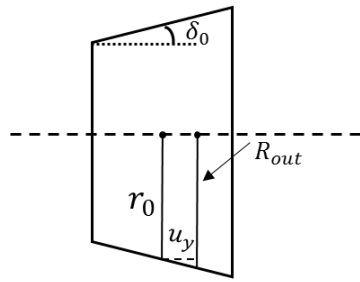
Figure 2-2. Outer wheel rolling radius when running in a curve.

Substituting Eq.(2-2) into Eq.(2-1), the lateral displacement of the wheelset can be obtained as:

$$u_y = \frac{r_0 l}{\delta_0 R} \tag{2-3}$$

If this lateral displacement is achieved exactly, the unconstrained wheelset will curve freely by running along the equilibrium rolling line.

2.1.2 Curving of a bogie

According to the observation by Stephenson [5], the free wheelset will exhibit a kinematic oscillation when running on a straight track instead of running stably (see Figure 2-3). To solve this problem, railway vehicles are mounted on bogies; these usually consist of two

wheelsets connected by a rigid frame [5] to ensure the stability. However, this also makes the curving behaviour of a bogie with two wheelsets differ from the ideal steering.
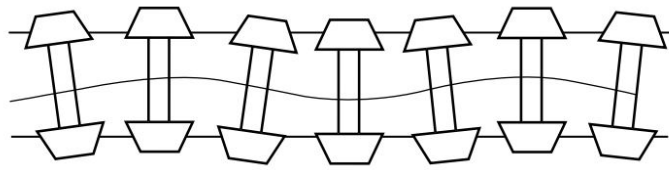
Figure 2-3. Kinematic oscillation of free wheelset on a straight track (from [5]).

If, the bogie is assumed to have a rigid frame, the wheelsets are fixed in the longitudinal direction of this frame. The attitude of the bogie in plan view is shown in Figure 2-4. It can be seen that the two axles are constrained and they cannot take up a radial position in the curve. This will make the wheelsets exhibit a considerable angle of attack (yaw angle of the wheelset relative to the rail). In practice, the wheelsets and vehicle are connected by vertical suspension springs while in the lateral and longitudinal directions the wheelsets and the frame are also connected by suspensions including springs and dampers. These are intended not only to stabilise the tendency of the wheelsets to oscillate but also to facilitate the motion of the vehicle in curves [5].
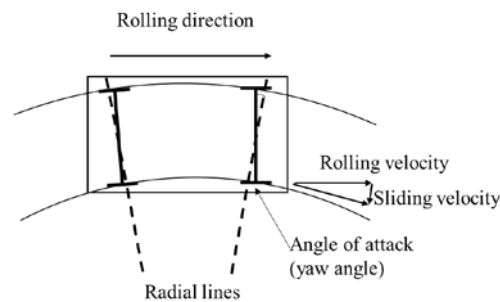
Figure 2-4. Plan view of a rigid bogie in a curve.

There are a number of factors that can affect the attitude of a two-axle vehicle or bogie in a curve. These mainly include the curve radius, the cant deficiency[2], and the speed of the vehicle [5]. The attitudes of a bogie in a curve for different speeds and radii are shown in Figure 2-5. At low speed and in a small radius curve, the leading wheelset moves outwards in the curve whereas the trailing wheelset moves inwards. Hence the outer wheel of the leading wheelset and the inner wheel of the rear wheelset tends to have flange contact. When the speed is increased (or the curve radius is increased), the rear wheelset tends to move

---

[2] Cant deficiency is present when a vehicle's speed on a curve is greater than the speed at which the components of wheel to rail force are normal to the plane of the track. The amount of cant deficiency is expressed in terms of required superelevation to be added in order to bring the resultant force acts normal to the plane of the track.

outwards. Therefore, the angle of attack of the leading wheelset in a small-radius curve is larger than it is in a larger-radius curve [1].

<div align="center">(a)   (b)</div>
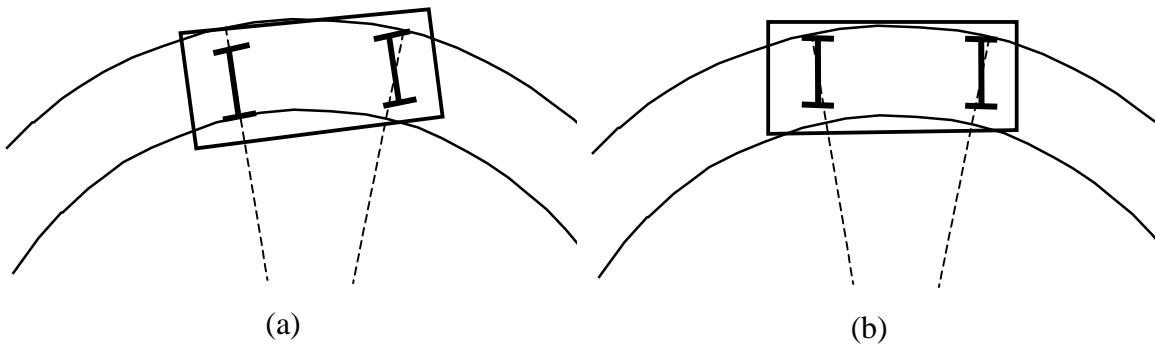
Figure 2-5. Plan view of a bogie in a curve: (a) low speed/small radius; (b) high speed/large radius.

A wheelset with a non-zero angle of attack cannot run straight ahead; due to the constraint of the flange it will roll around the curve. Hence a lateral sliding velocity exists especially at the inner wheel (see Figure 2-4). It is believed that this lateral sliding velocity is the main cause of curve squeal noise [1].

2.2 Creepages

As defined by Johnson [80], rolling is a relative angular motion between two bodies in contact about an axis parallel to their common tangent plane (see Figure 2-6). In the contact frame, the contact surfaces 'flow' through the contact zone with tangential velocities in the longitudinal (x) and lateral (y) directions (v_x and v_y). The bodies may also have angular velocities about the normal (z) direction (ω_{rz}). If the tangential velocities of the two bodies are unequal, i.e. $v_{x,1} \neq v_{x,2}$ and/or $v_{y,1} \neq v_{y,2}$, the rolling motion is accompanied by sliding. If the angular velocities about the z direction of the two bodies are unequal, i.e. $\omega_{rz,1} \neq \omega_{rz,2}$, the rolling motion is accompanied by spin. For rolling without sliding or spin, the motion is called 'pure rolling'.
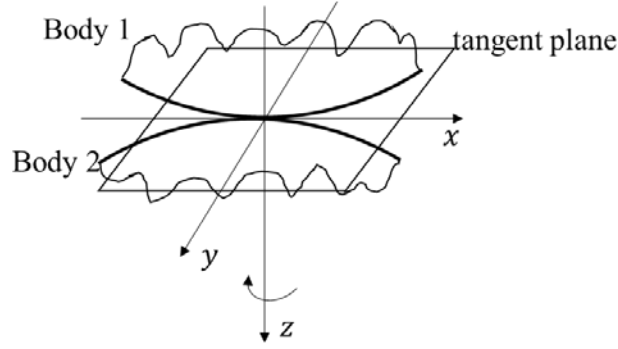
Figure 2-6. Rolling contact surface of two elastic bodies.

The relative velocities or spin of the two bodies normalised by the rolling velocity, which is the average absolute velocity of the two bodies, are defined as the creepage. Specifically, the longitudinal, lateral and spin creepages are defined as:

$$\gamma_x = \frac{v_{x,1} - v_{x,2}}{V_0}, \gamma_y = \frac{v_{y,1} - v_{y,2}}{V_0}, \gamma_{rz} = \frac{\omega_{rz,1} - \omega_{rz,2}}{V_0} \tag{2-4}$$

where V_0 is the rolling velocity and γ_x, γ_y, γ_{rz} are the longitudinal, lateral and spin creepages respectively.

The longitudinal and lateral creepages are dimensionless whereas the spin creepage has a dimension of m^{-1}.

In the context of wheel-rail contact (see Figure 2-7), the longitudinal, lateral and spin creepages can be written as:

$$\gamma_x = \frac{v_x^w - v_x^r}{V_0}, \gamma_y = \frac{v_y^w - v_y^r}{V_0}, \gamma_{rz} = \frac{\omega_{rz}^w - \omega_{rz}^r}{V_0} \tag{2-5}$$

where the subscripts x, y, z represent the directions and the superscripts w and r represent wheel and rail respectively.
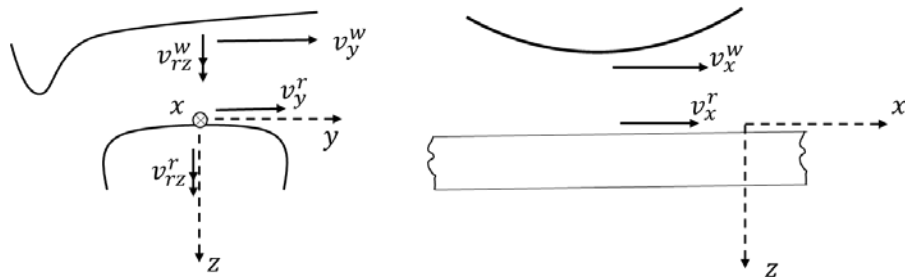
Figure 2-7. Velocities and creepages in the wheel/rail contact.

Although these creepages can all exist, it can be found from literature that the lateral creepage is usually associated with curve squeal [4]. As introduced in Section 2.1.2, when a

31

bogie is travelling in a curve, an angle of attack can arise; this will then result in a relative lateral velocity between the wheel and rail (see Figure 2-4). According to Eq. (2-5), this relative velocity normalized by the rolling velocity is the lateral creepage. Hence, the lateral creepage is approximately equal to the angle of attack.

2.3 Rolling friction

First sliding friction is introduced as shown in Figure 2-8. It is a body resting on the ground. The normal force F_N cancels out the gravity force of the body. The applied force F_{ext} tends to move the body. The static friction force F_s is equal in magnitude and opposite in direction to the external force until the maximum possible friction force between two surfaces is reached, which is the product of the coefficient of static friction and the normal force $\mu_s F_N$. Therefore, when there is no sliding, the friction force can have any value from zero up to the maximum friction force $\mu_s F_N$. If the friction force becomes larger than the limit of the static friction, sliding motion occurs. At this point, the friction force is static friction. It is recognised that static friction coefficient μ_s is usually larger than the dynamic friction coefficient μ_d (see Figure 2-9) and both are assumed to be independent of velocity according to the Coulomb friction law [81].
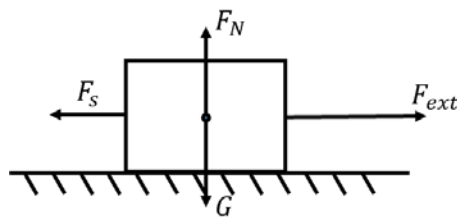
Figure 2-8. A block moving.
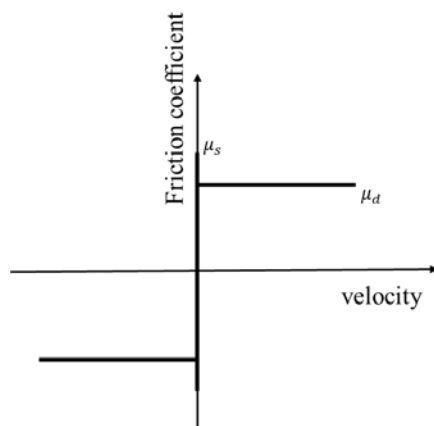
Figure 2-9. Static friction and dynamic friction.

32

For a rolling wheel, the wheel and rail are not rigid and under the contact of two elastic bodies, a deformation in the contact area exists. This deformation is fundamental to rolling friction [81]. In the contact area, there is local slip before gross sliding occurs. This phenomenon is named micro-slip or micro-displacement [82]. At this micro-slip stage, there are areas of both adhesion and slip in the contact area. This is shown in Figure 2-10. When entering the contact area, the surface particles of the wheel and rail lock together and move towards the rear; this front zone is the adhesion area. In the trailing zone of the contact area, where surface particles leave the contact area, a slip region occurs. The friction force usually grows gradually with increasing creepage and finally reaches its saturation value, where gross sliding occurs (see dashed line in Figure 2-11).
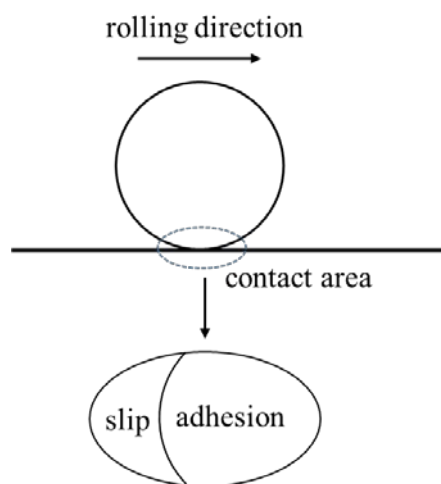
Figure 2-10. Slip and adhesion area in wheel-rail contact
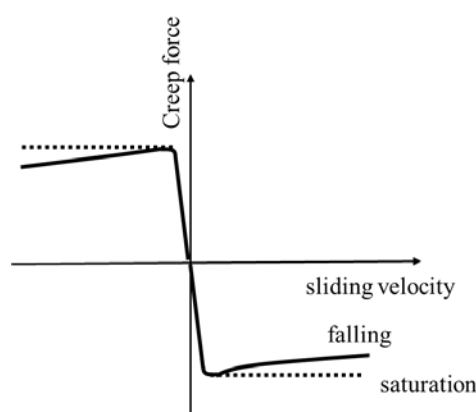
Figure 2-11. Creep force with micro-slip and saturation.

In analysing the parameters that influence the friction force in rolling, Stribeck demonstrated experimentally that the coefficient of friction in different bearings is dependent on the sliding velocity under gross sliding and it drops continuously with increasing small velocity [83]. He presented the friction-velocity curves, which are called "Stribeck curves" [84], of

different bearings including journal bearings, plain bearings and roller bearings. The results show a similar trend as Figure 2-12. It can be seen that the friction first decreases with increasing sliding velocity and then increases at higher velocities.
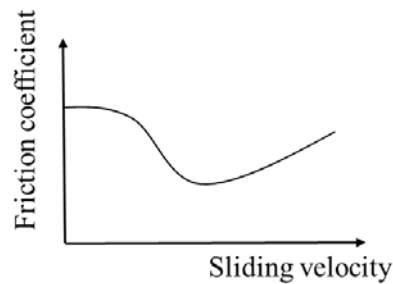
Figure 2-12. A typical Stribeck curve

In general, the friction between the wheel and rail is a combination of "micro slip" and a Stribeck curve (see solid line in Figure 2-11). However, friction depends on a number of factors. These can include molecular adhesion, surface roughness, deformation, temperature, etc. Hence, there is no universal friction-velocity function, and instead the relation is application-dependent and can vary under different conditions [85]. Different friction models used for curve squeal will be introduced in the next section.

2.4 Contact models

2.4.1 Normal contact model

The wheel-rail normal contact can be modelled approximately with Hertz contact theory [1]. This theory is based on some assumptions such as:

1) The contact surfaces can be represented by constant radii of curvature.

2) The strains are small and within the elastic limit.

3) Each body can be considered as an elastic half-space, i.e., the area of contact is much smaller than the dimensions and the characteristic radius of each body.

4) The surfaces are continuous and non-conforming. A non-conforming contact is one in which the shapes of the bodies are sufficiently dissimilar that, under zero load, they only touch at a point (or possibly along a line).

5) The two bodies are in frictionless contact.

The results are presented here, which can also be found in [1].

Assuming the wheel has radii of curvature R_w in the rolling direction and R_{wt} in the transverse direction, the rail has radius R_r in the rolling direction and transverse radius R_{rt}, an effective radius of curvature of the surface in contact is:

$$\frac{1}{R_0} = \frac{1}{2}\left(\frac{1}{R_w} + \frac{1}{R_{wt}} + \frac{1}{R_r} + \frac{1}{R_{rt}}\right) \tag{2-6}$$

In the wheel-rail contact area, the semi-axes a in the rolling direction, the semi-axes b in the transverse direction, and the normal approach u_0 are given by:

$$a = \sigma_1 \left(\frac{3N_0 R_0}{2E'}\right)^{1/3} \tag{2-7}$$

$$b = \sigma_2 \left(\frac{3N_0 R_0}{2E'}\right)^{1/3} \tag{2-8}$$

$$u_0 = \frac{\xi}{2R_0}\left(\frac{3N_0 R_0}{2E'}\right)^{1/3} \tag{2-9}$$

where N_0 is the normal load and E' is the plane strain elastic modulus defined as:

$$E' = \frac{E}{1 - v^2} \tag{2-10}$$

in which E is the Young's modulus and v is the Poisson's ratio. Both bodies are assumed to have the same elastic properties.

The parameters σ_1, σ_2 and ξ given by:

$$\sigma_1 = \left(\frac{2g^2 \mathbf{E}(e)}{\pi}\right)^{1/3} \tag{2-11}$$

$$\sigma_2 = \left(\frac{2\mathbf{E}(e)}{\pi g}\right)^{1/3} \tag{2-12}$$

$$\xi = \frac{4\mathbf{K}(e)}{\pi}\left(\frac{\pi}{2g^2 \mathbf{E}(e)}\right)^{1/3} \tag{2-13}$$

where $\mathbf{K}$ is the complete elliptic integral of the first kind, $\mathbf{E}$ is the complete elliptic integral of the second kind, g is the ratio of a and b, i.e. $g = \frac{a}{b}$, and $e = 1 - 1/g^2$.

An intermediate parameter, θ, is defined by:

$$\cos\theta = -\frac{R_0}{2}\left(\frac{1}{R_w} - \frac{1}{R_{wt}} + \frac{1}{R_r} - \frac{1}{R_{rt}}\right)$$

It is used to obtain σ_1, σ_2 and ξ using a pre-calculated table (see e.g. [1]).

It can be seen from Eq.(2-9) that the relationship between the normal approach and the normal load is non-linear. In order to apply the model in a frequency-domain analysis, this

35

expression is linearized for small displacement amplitudes about a nominal approach distance u_0 or normal load N_0. Thus the reciprocal of vertical contact stiffness $1/k_H$ is:

$$\frac{1}{k_H} = \frac{du_0}{dN_0} = \frac{\xi}{2}\left(\frac{2}{3E'^2 N_0 R_0}\right)^{1/3}$$ (2-14)

According to [86], the contact between two static bodies has a compliance in the transverse direction. The transverse contact stiffness is given by:

$$\frac{1}{k_L} = \frac{\chi}{k_H}$$ (2-15)

where χ is a value between about 1 and 1.4, given by:

$$\chi \approx 1 + \frac{\upsilon}{1-\upsilon}\left(\frac{1}{4} + \frac{1}{\pi}\tan^{-1} g\right)^{1/3}$$ (2-16)

where υ is Poisson's ratio and g is equal to a/b for the stiffness in the longitudinal direction or b/a for the lateral direction.

The Hertz normal contact model may not be accurate at flange contact. This is because the flange's thickness and the radius of curvature at the gauge corner are of the same order of magnitude as the contact length [87] and half space assumption is not satisfied. Also, in Hertz normal contact model, the surface roughness is not included, which could change the geometry of the contact surfaces.

2.4.2 Tangential contact model

2.4.2.1 Saturation of creepage

The wheel-rail contact requires a rolling friction model. This is different from the Coulomb friction model in which the friction force is independent of velocity. Under rolling contact, the friction force (or creep force) is a function of the relative speed between the wheel and rail, i.e. creepage. The creepage describes the overall relative motion of the wheel and rail (normalised by the rolling velocity), while in the contact patch both slip and stick may exist. With increasing creepage, the adhesion zone reduces. When the slip zone covers the whole contact patch, saturation of the creep force is achieved [1].

Kalker has given a detailed survey of rolling contact theories in [6]. Two of them will be introduced here and will be used in the calculations in later chapters. One is an approximate model by Vermeulen and Johnson [88], which considers longitudinal and lateral creepage but without spin creepage. According to Vermeulen and Johnson [88], the tangential force F_i can be formulated as:

$$F_i = \begin{cases} \mu_0 N_0 \left(\Gamma_i - \dfrac{1}{3}\Gamma_i^2 + \dfrac{1}{27}\Gamma_i^3 \right) & for\ \Gamma_i < 3 \\ \mu_0 N_0 & for\ \Gamma_i > 3 \end{cases} \qquad (2\text{-}17)$$

where μ_0 is the Coulomb friction coefficient, N_0 is the normal force, F_i is the longitudinal or lateral creep force and Γ_i is a normalised creepage given by:

$$\Gamma_i = \frac{GC_{ii}ab}{\mu F_0}\gamma_i \quad for\ i = 1,2 \qquad (2\text{-}18)$$

in which a and b are the semi-axis lengths of the contact patch, γ_i is the creepage in the longitudinal or lateral direction, G is the shear modulus of the wheel and rail material (assumed identical) and C_{ii} is the creep coefficient which is tabulated by Kalker [6].

The other one is given by Kalker. He gave three exact theories in [89, 90], but these theories require a large amount of computation time. Thus he developed a numerical method called FASTSIM [30] based on his simplified theory [91]. In FASTSIM, Kalker replaced the elastic half-space, which is assumed in the exact theory CONTACT [89, 90], by a bedding of uncoupled springs. Also, the displacement difference between wheel rand rail in one point is assumed proportional to the surfaced traction in the same point and independent of the surface traction in all other points [87].

This algorithm offers a quick approach to calculate the total tangential forces in rolling contact from given creepages (including spin) and is now widely used. In this algorithm, the elliptical contact area is divided into independent parallel longitudinal strips with equal width and each strip is divided equally into the same number of elements. The traction on each element can be calculated from the averaged deformation of this element and a series of equivalent springs.

The adhesion coefficient $\mu(\gamma)$ is defined as the ratio of lateral or longitudinal force to normal force. After the creep force reaches the full saturation regime, the absolute value of the lateral adhesion coefficient is equivalent to the friction coefficient μ_0 (which may be velocity dependent). Figure 2-13 shows a comparison of adhesion coefficient against creepage calculated using these two methods, neglecting the longitudinal and spin creepage. It can be seen that they are in good agreement. The parameters used are shown in Table 2-1.

Table 2-1. Parameters for non-dimensional friction curves by FASTSIM and Vermeulen and Johnson formula.

Parameters	Symbol (units)	Value
Normal contact force	N_0 (kN)	62
Longitudinal semi-axis of contact ellipse	a (mm)	5
Lateral semi-axis of contact ellipse	b (mm)	5
Shear modulus	G (Pa)	8.1×10^{10}
Coulomb friction coefficient	μ_0	0.4
Kalker's coefficient	C_{22}	3.699
Number of elements in each strip in FASTSIM	N_x	30
Number of strips in FASTSIM	N_y	20
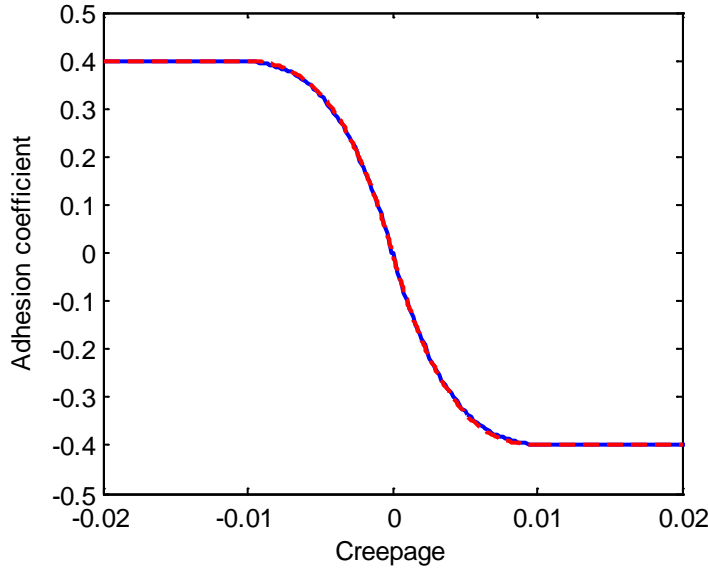
Figure 2-13. Comparison of friction curves calculated by FASTSIM and Vermeulen and Johnson formula for parameters in Table 2-1, ——— FASTSIM without longitudinal and spin creepage, — — — Vermeulen and Johnson's formula.

2.4.2.2 Falling friction at large creepages

It is recognized that the 'dynamic' or 'sliding' friction coefficient is smaller than the 'static' one. Usually when the creepage exceeds the saturation point, the friction coefficient decreases in magnitude with increasing creepage [1], see Figure 2-11.

Different falling functions at large creepage have been developed in previous studies. In [9], Rudd gives a model as:

$$\mu(\gamma) = \mu_0 \frac{\gamma}{\gamma_0} e^{(1-\frac{\gamma}{\gamma_0})} \tag{2-19}$$

where $\mu(\gamma)$ is the adhesion coefficient, μ_0 is the maximum friction coefficient, γ_0 is the creepage for this maximum friction coefficient and γ is the creepage. This falling model was compared with measurement results performed by Remington [14] using a test rig and good agreement was found.

Périard [20] considered two friction laws in his study. They were obtained from an overview of various laws given by Kragelskii [92]. One is from Poiré and Bochet and has the form of:

$$\mu = \mu_0 \frac{1}{1 + 0.03v} \tag{2-20}$$

The other one is from Galton and has the form of:

$$\mu = \mu_0 \frac{1 + 0.018v}{1 + 0.03v} \tag{2-21}$$

where v is the sliding velocity.

These two friction laws, Eq. (2-20) and (2-21), are empirical laws obtained by performing experiments with a train wheel sliding over a rail at a very large sliding velocity.

Kraft [16] proposed a semi-analytical expression as:

$$\mu_0(v) = \mu_0\{1 - 0.5e^{-0.138/|v|} - 0.5e^{-6.9/|v|}\} \tag{2-22}$$

This model was used by Schneider et al. [15] and Fingberg [17].

Huang [27] developed a heuristic formula for the falling friction in sliding, which is:

$$\tau(\gamma) = 1 - \lambda e^{-\kappa/|\lambda|} \tag{2-23}$$

where τ is the falling function which is used to account for the falling characteristics for large creepage, κ is the saturation coefficient, γ is the creepage, and λ is the falling ratio defined as:

$$\lambda = \frac{\mu_0 - |\mu_d(\gamma)|_{\gamma \to \infty}}{\mu_0} \tag{2-24}$$

where μ_d is the dynamic friction coefficient.

Figure 2-14 gives a comparison of friction curves from the different models given above. The rolling velocity is assumed to be 10 m/s for each case, and the static friction coefficient is set as 0.4. In particular, for Rudd's model in Eq. (2-19), $\gamma_0 = 0.009$ and $\mu_0 = 0.4$; for Huang's model in Eq. (2-23), $\lambda = 0.5$ and $\kappa = 0.05$. It can be seen from Figure 2-14 that

the two friction laws used by Périard (Eq. (2-20) and Eq. (2-21)) change very little in this creepage range. Rudd's model has a much steeper slope than others. Huang's model gives a steeper slope than Kraft at small creepage but at high creepage his friction curve tends to a constant value. Here, rolling is included in Rudd's model with the adhesion regime at small creepage while the other curves represent only sliding friction.
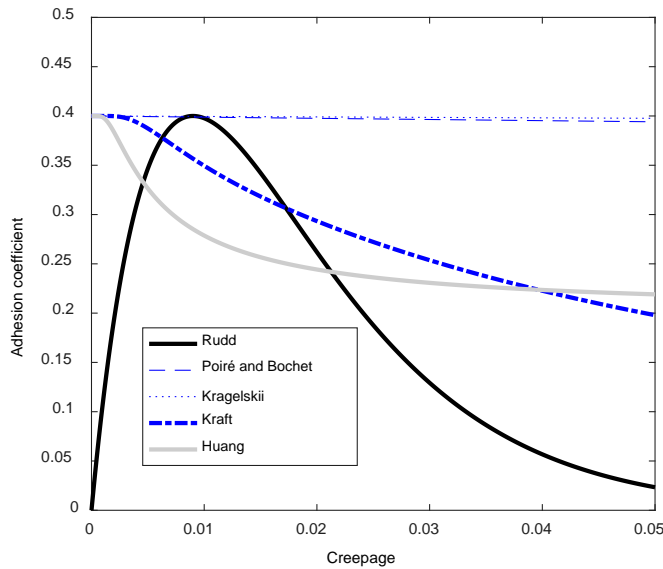
Figure 2-14. Comparison of friction or adhesion coefficients from different models of a wheel on a rail for a rolling velocity of 10 m/s. Rudd ($\gamma_0 = 0.009$, $\mu_0 = 0.4$); Huang ($\lambda = 0.5$, $\kappa = 0.05$).

In this thesis, Huang's falling function Eq. (2-23) will be adopted for those cases involving falling friction. Figure 2-15 shows the friction curves obtained based on FASTSIM together with the falling part from Eq. (2-23) with different combinations of λ and κ. It can be seen that the falling ratio λ mainly influences the friction curve at large creepages, whereas the saturation coefficient κ has an effect at small creepages. Other parameters are the same as shown in Table 2-1.
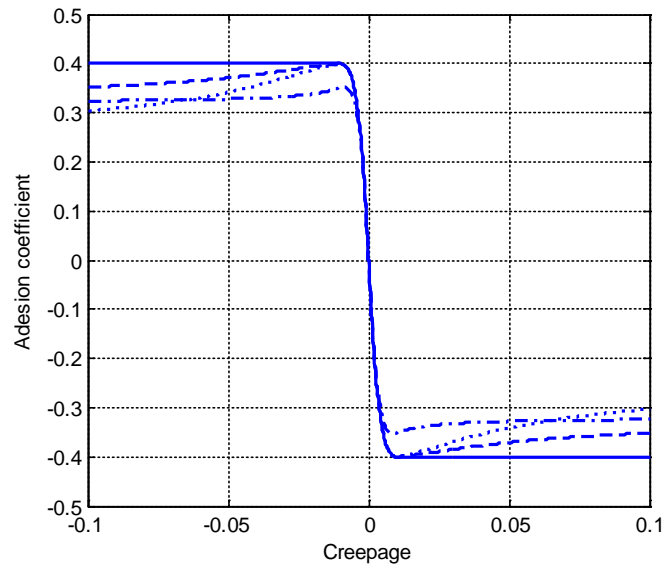
Figure 2-15. Friction curves with different combinations of λ and κ. Solid line: $\lambda = 0, \kappa = 0.005$; dashed line: $\lambda = 0.2, \kappa = 0.005$; dotted line: $\lambda = 0.4, \kappa = 0.005$; dash-dot line: $\lambda = 0.2, \kappa = 0.05$.

2.5 Summary

The lateral sliding motion of the wheel on the rail is considered to be the main cause of curve squeal noise. This chapter shows how this lateral sliding occurs when a train negotiates a curve, by introducing the curving behaviour of a free wheelset and a bogie. The definition of creepage is also introduced and applied to wheel-rail contact. The difference between static and dynamic friction is explained and will be used in the next chapter to explain stick-slip phenomena. The wheel-rail contact models in vertical and lateral directions are also presented. The Hertz contact model [1] is used in the vertical direction and Kalker's FASTSIM [6] is applied for the lateral direction.

3 Friction induced vibration and instability

Curve squeal noise is usually attributed to friction-induced instability. In this chapter, to assist in the interpretation of the mechanisms of different friction-induced instabilities, simple mass-on-belt models are introduced and different friction models are considered to represent each type of instability. These are: stick-slip, falling friction and mode coupling. The equations of motion for these different systems are shown and then the stabilities of these systems are investigated with different methods.

3.1 Stick-slip with constant dynamic and static friction coefficient

The simple model shown in Figure 3-1 will be studied first to explain the 'stick-slip' phenomenon. In this model a mass m_1 is resting on a belt that moves with a velocity V_b. The mass is restrained by a spring with stiffness k_1 and damping c_1. In this single-degree-of-freedom model the mass can only oscillate in the horizontal direction described by the coordinate y_{tot}. In this model, the dynamic friction coefficient μ_d is assumed to be smaller than the static friction coefficient μ_s. This friction model is shown in Figure 2-9. Both the dynamic and static friction coefficients are assumed as constant values [1] and, as an example, they are set equal to 0.4 and 0.3, respectively.
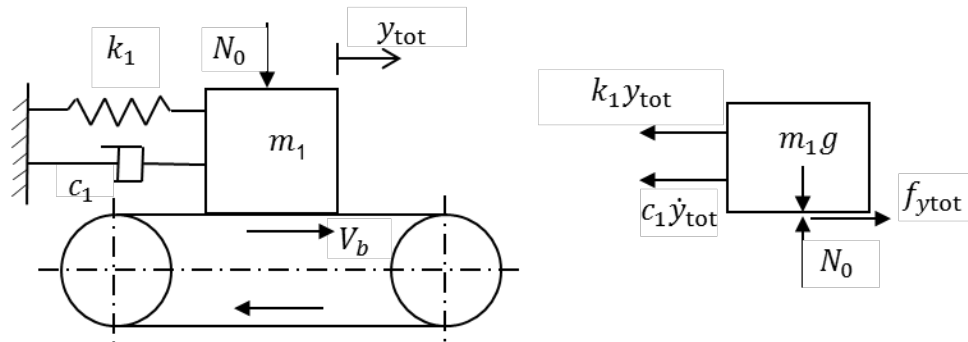
Figure 3-1. Schematic view of a restrained mass on a moving belt and forces acting on the mass.

First the damping is neglected. The static friction force at the contact between the body and the belt, $F \leq \mu_s N_0$, initially causes the mass to move with the belt. As long as the friction force F is sufficient to balance the reaction force exerted by the spring, $k_1 y_{tot}$, the mass moves with the belt. This is referred to the stick phase of the mechanism. The motion of the mass satisfies:

$$y_{tot} = V_b t \qquad\qquad (3\text{-}1)$$

where t is the time and the notation tot is used here for consistency with later sections. As the spring becomes extended, the friction force is eventually overcome by the opposing force of the spring, when $k_1 y_{tot} = \mu_s N_0$. Then the body slips relative to the belt and the friction coefficient drops to μ_d. The equation of motion of the mass becomes:

$$m_1 \ddot{y}_{tot} + k_1 y_{tot} = \mu_d N_0 \qquad\qquad (3\text{-}2)$$

The contact surfaces will continue to slip and the mass undergoes harmonic motion with natural frequency $\omega_0 = \sqrt{k_1/m_1}$. When the relative velocity $v_{y0}^S = (\dot{y}_{tot} - V_b)$ returns to zero, the contact surfaces regain adhesion and the system returns to the stick phase.

Eq. (3-2) has a solution of the form:

$$y_{tot} = A \sin\big(\omega_0(t - \tau)\big) + \frac{\mu_d N_0}{k_1} \qquad\qquad (3\text{-}3)$$

for some constants A and τ. The velocity in the slip phase is then:

$$\dot{y}_{tot} = A\omega_0 \cos\big(\omega_0(t - \tau)\big) \qquad\qquad (3\text{-}4)$$

Assuming the start of the slip phase corresponds to $t = 0$, and by using the initial condition $y_{tot}(t = 0) = \frac{\mu_s N_0}{k_1}$ and $\dot{y}_{tot}(t = 0) = V_b$, it can be found that:

$$A = \frac{v_0}{\omega_0}\sqrt{1 + \beta^2}$$

where β a non-dimensional parameter given by

$$\beta = \frac{(\mu_s - \mu_d)N_0}{V_b m_1 \omega_0} \qquad\qquad (3\text{-}5)$$

It can also be found that the lag τ depends on β. This non-dimensional parameter β determines the relative importance of stick and slip.

Figure 3-2 shows examples of the stick-slip motion for three values of β. These are shown in the 'phase plane' in which velocity is plotted against displacement. The velocity is normalised by the belt velocity V_b whereas the displacement is normalised by V_b/ω_0. These results illustrate the formation of a 'limit cycle': a stable periodic motion that is reached from a variety of initial conditions. It is found that, for small values of β the slip phase

predominates; the motion is close to elliptical on the phase plane and the oscillation frequency is close to the natural frequency. Conversely, for large values of β the stick phase predominates. The oscillation frequency always is lower than the natural frequency.

Figure 3-3 gives the velocity spectra for three different values of β. The frequency is normalised by ω_0. The amplitude of velocity is normalised by V_b. It can be seen that the oscillation frequency becomes lower as the value of β is increased. Higher harmonics are contained in the spectrum as the motion is not purely sinusoidal; this is often seen in squeal measurements. For railway applications, β is usually in the range of 0.1 to 1 for a single wheel mode [1].
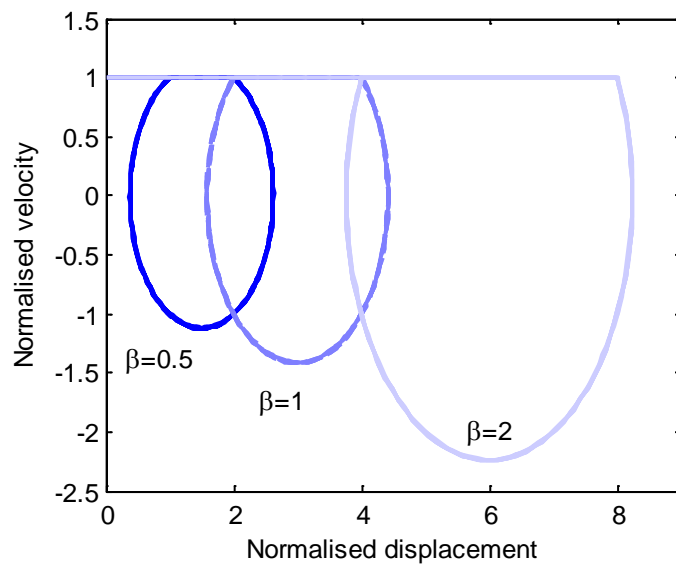
Figure 3-2. Phase plane plot for different values of β.
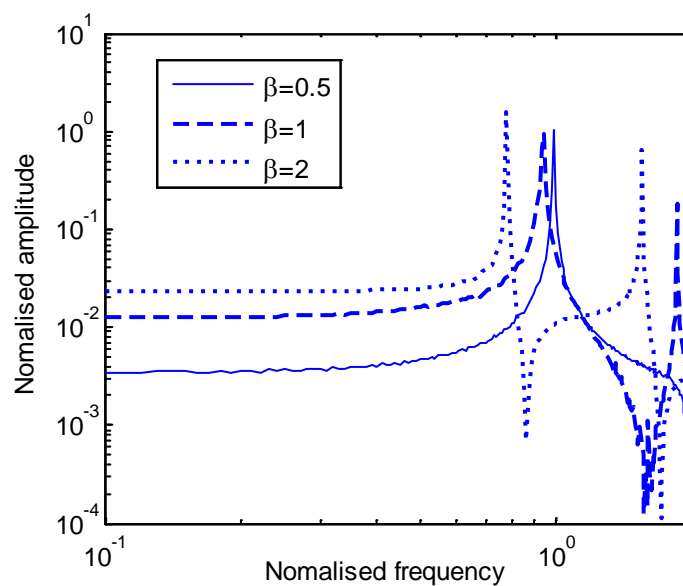
Figure 3-3. Velocity spectra for different different values of β.

45

According to this model the instability occurs because of the difference between the static and dynamic friction coefficients. However if damping is included and is high enough to prevent the velocity returning to V_b, stick-slip can be eliminated.

Figure 3-4 shows results for $\beta = 1$ for three values of damping ratio ζ. It can be seen that for $\zeta = 0.05$, a limit cycle response is still obtained, and the amplitude is close to the case with zero damping. However, when the damping ratio reaches 0.1, the oscillation is suppressed. Therefore, there should be a critical damping ratio value between 0.05 and 0.1 above which the unstable vibration can be eliminated. According to [1], the critical value of damping ratio can be approximated as:

$$\zeta \cong \frac{\beta^2}{4\pi} \qquad\qquad (3\text{-}6)$$

The minimum damping ratio calculated by Eq.(3-6) is compared with the result of the numerical solution of the system in Figure 3-5. It can be seen that the approximate result from Eq.(3-6) matches well with the numerical result when β is smaller than 1, but when β is larger than this, Eq.(3-6) produces an overestimate of the damping ratio required to overcome instability.

From this stick-slip motion it can be demonstrated that the difference between the static and dynamic friction coefficients is the reason for the occurrence of stick-slip motion. It is a periodic oscillation with a frequency that is lower than the natural frequency of the system. Adding damping can eliminate this motion but a minimum value of damping needs to be exceeded.
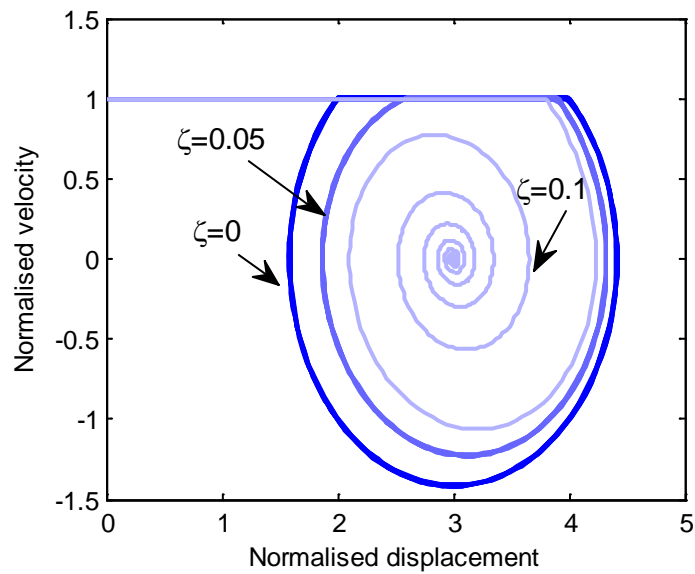
Figure 3-4. Phase plane plot with different damping ratio for $\beta = 1$.
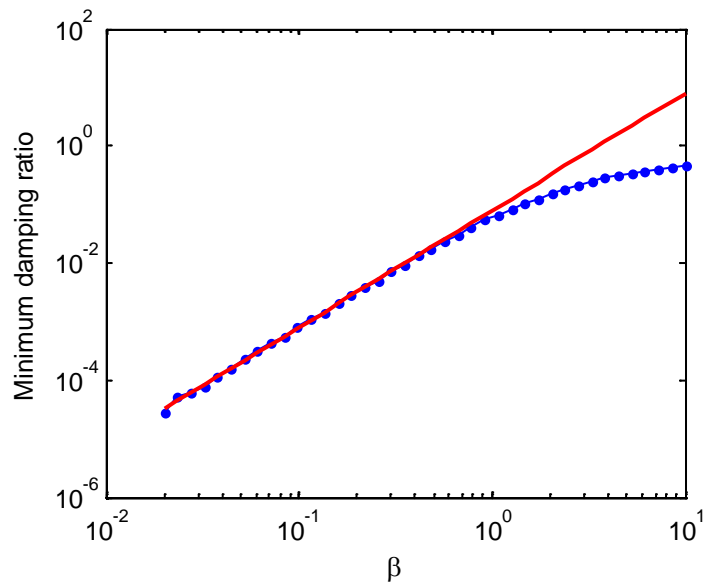
Figure 3-5. Minimum damping ratio required to prevent instability. ——, approximation for small values of β, —•—, numerical solution from damped stick-slip model.

3.2   Falling friction mechanism

3.2.1 Equation of motion

Next, the same model will be used with a friction coefficient that varies with sliding velocity (see Figure 2-11). Consider again the model shown in Figure 3-1. Here, y_{tot} is the total displacement of the mass m_1, and f_{ytot} represents the friction force acting between the mass and the belt.

The governing equation of this mass-spring-damper system is:

$$m_1 \ddot{y}_{tot} + c_1 \dot{y}_{tot} + k_1 y_{tot} = f_{ytot} \tag{3-7}$$

The sliding velocity between the mass and the belt is

$$v_{ytot}^S = \dot{y}_{tot} - V_b \tag{3-8}$$

If the normal contact force between the mass and belt is N_0, the sliding friction force acting on the mass can be obtained:

$$f_{ytot} = N_0 \mu(v_{ytot}^S) \tag{3-9}$$

where the non-dimensional friction force μ includes a sign opposite to that of the sliding velocity.

If the system is under equilibrium conditions, the mass has a velocity of $\dot{y}_{tot} = 0$. Thus, according to Eq.(3-8), the equilibrium sliding velocity v_{y0}^S is related only to the velocity of the moving belt:

$$v_{y0}^S = -V_b \tag{3-10}$$

Consequently, the equilibrium friction force f_{y0} given from Eq.(3-9) is:

$$f_{y0} = N_0 \mu(v_{y0}^S) \tag{3-11}$$

To balance the friction force, the spring k_1 should stretch an equilibrium length y_0 from its relaxed position, giving:

$$f_{y0} = N_0 \mu(v_{y0}^S) = k_1 y_0 \tag{3-12}$$

If there is a disturbance, which moves the mass away from its equilibrium position, the mass will start to oscillate. The displacement of the mass can be written as two parts. One is the equilibrium part y_0 and the other is the dynamic part y:

$$y_{tot} = y_0 + y \tag{3-13}$$

The first and second derivatives of Eq.(3-13) give the velocity and acceleration of the mass:

$$\dot{y}_{tot} = \dot{y} \tag{3-14}$$
$$\ddot{y}_{tot} = \ddot{y} \tag{3-15}$$

Then, combining Eq.(3-8), (3-10), and (3-14) gives:

$$v_{ytot}^S = \dot{y} - V_b = v_{y0}^S + \dot{y} \tag{3-16}$$

From Eq.(3-16), it can be seen that the sliding velocity is the sum of an equilibrium part v_{y0}^S and a dynamic part $\dot{y}$. Also, the friction force can be written as the sum of an equilibrium part f_{y0} and a dynamic part f_y :

$$f_{ytot} = f_{y0} + f_y \tag{3-17}$$

Substituting Eq.(3-13), (3-14), (3-15), (3-16) and (3-17) into (3-7), gives the following result after the equilibrium parts are eliminated:

$$m_1\ddot{y} + c_1\dot{y} + k_1 y = f_y \tag{3-18}$$

According to Eq. (3-9), (3-12), (3-16), the following equations can be obtained:

$$f_y = N_0\mu\left(v_{y_{tot}}^s\right) - N_0\mu\left(v_{y0}^s\right) \tag{3-19}$$

$$m_1\ddot{y} + c_1\dot{y} + k_1 y = N_0\left(\mu\left(v_{y0}^s + \dot{y}\right) - \mu\left(v_{y0}^s\right)\right) \tag{3-20}$$

3.2.2 Equivalent damping effect of friction force

After deriving the equations of the system, this mass-on-moving-belt system can be described as a positive feedback loop, see Figure 3-6. The input of the loop is a dynamic friction force, the output is the vibration of the mass, which can give a feedback to the dynamic friction force (see Eq.(3-18), (3-19) and (3-20)).
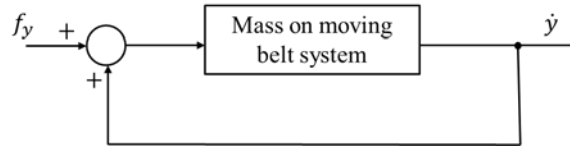
Figure 3-6. Positive feedback loop of mass-belt system.

To study the stability of the mass-on-moving-belt system at one possible equilibrium sliding velocity v_{y0}^s, the system can be linearized around this equilibrium point. Eq.(3-20) shows that only the dynamic friction force is nonlinear:

$$f_y = f_{ytot} - f_{y0} = N_0\left(\mu\left(v_{y_{tot}}^s\right) - \mu\left(v_{y0}^s\right)\right) \tag{3-21}$$

Thus, assuming small amplitudes and according to the first order term from the Taylor series, the dynamic friction force can be evaluated at the equilibrium point as:

$$f_y \approx \dot{y}\left.\frac{\partial f_y}{\partial \dot{y}}\right|_{v_{y0}^s} = \dot{y}N_0\left.\frac{\partial \mu}{\partial \dot{y}}\right|_{v_{y0}^s} \tag{3-22}$$

The form of the dynamic friction force in Eq. (3-22) is similar to the definition of viscous damping in which the restoring force is proportional to the velocity. Therefore, the dynamic friction force can be written as:

$$f_y = -c_e\dot{y} \tag{3-23}$$

where c_e is the equivalent damping coefficient defined as:

$$c_e = -N_0 \frac{\partial \mu}{\partial \dot{y}}\bigg|_{v_{y0}^s} \tag{3-24}$$

which is the product of the normal force and the slope of the friction curve at the equilibrium point. Substituting Eq.(3-23) into Eq.(3-18) gives:

$$m_1 \ddot{y} + (c_e + c_1)\dot{y} + k_1 y = 0 \tag{3-25}$$

Now, the stability of this system can be judged from the sign of the damping term $(c_e + c_1)$. If $(c_e + c_1)$ is positive, the damping will reduce the vibration energy, from a given initial condition, and make this system stable. According to Eq.(3-24), the equivalent damping can be either negative or positive depending on the sign of $\frac{\partial \mu}{\partial \dot{y}}$, so the criterion of the stability can also be written as:

$$\begin{cases} c_1 \geq 0, \text{if } c_e > 0 \\ c_1 > -c_e, \text{if } c_e \leq 0 \end{cases} \tag{3-26}$$

In railway application, the sliding velocity $\dot{y}$ is:

$$\dot{y} = \gamma V_0 \tag{3-27}$$

where V_0 is the rolling velocity and γ is creepage. Hence Eq. (3-24) can be written

$$c_e = -\frac{N_0}{V_0} \frac{\partial \mu}{\partial \gamma}\bigg|_{\gamma_0} \tag{3-28}$$

where γ_0 is the steady state creepage.

The minimum damping ratio ζ_e required to stabilise the system can be calculated as

$$\zeta_e = \frac{c_e}{2\omega_0 m} \tag{3-29}$$

where ω_0 is the natural frequency.

3.2.3 Self-excited vibration of a single wheel mode with falling friction

3.2.3.1 Parameters

The model shown in Figure 3-1 can be used to simulate the self-excited vibration of a single wheel mode. The parameters of the wheel mode used here are given in Table 3-1. This mode

is related to a mode considered in a later chapter (the 1102 Hz mode of Class 158 wheel in Chapter 5). It should be noticed that the belt velocity in Figure 3-1 does not represent the rolling velocity. It is instead equivalent to the equilibrium sliding velocity of the system (see Eq. (3-10).

Table 3-1. Parameters of a single mode of the wheel

Modal mass	78 kg
Natural frequency, $\omega_0/2\pi$	1102 Hz
Damping ratio	0.0001
Normal contact force, N_0	42 kN
Rolling velocity, V_0	10 m/s

The simplified creep force model proposed by Vermeulen and Johnson [88] is adopted (see Eq. (2-17) in Chapter 2). To introduce the falling regime, the heuristic formula, Eq. (2-23) and (2-24) in Section 2.4.2.2, proposed by Huang [27] is employed.

The parameters used for the falling function are $\lambda = 0.7$, $\kappa = 0.005$; the friction curve applied is shown in Figure 3-7. The slope turning point is at $\gamma_c = 0.004$, which can be called the critical creepage.
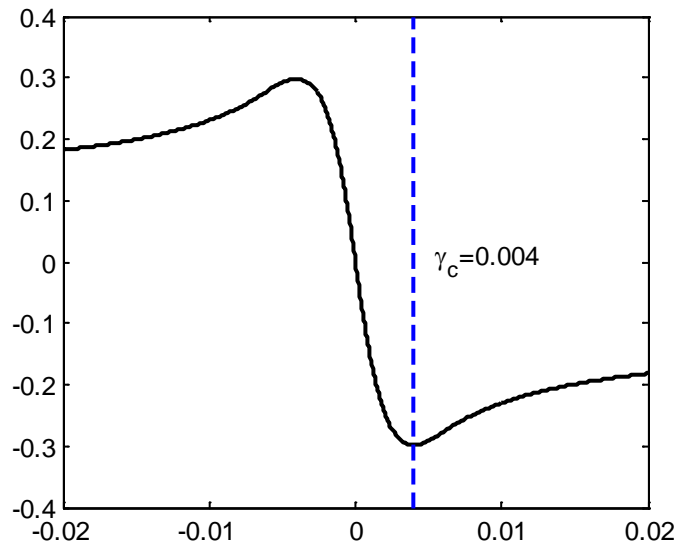
Figure 3-7. Friction law assumed in current section.

3.2.3.2 Stable results

As has been introduced in Section 3.2.2, if the steady state creepage is chosen below the critical creepage, the slope of the friction curve will be positive and lead to a positive damping effect. This, together with the structural damping, will stabilize the system. Figure 3-8 shows an example of a stable response result for a steady state creepage γ_0 of 0.0001. In

this example, the mass starts with a disturbance at the initial point and it end up at the steady state, which has zero displacement and creepage of 0.0001
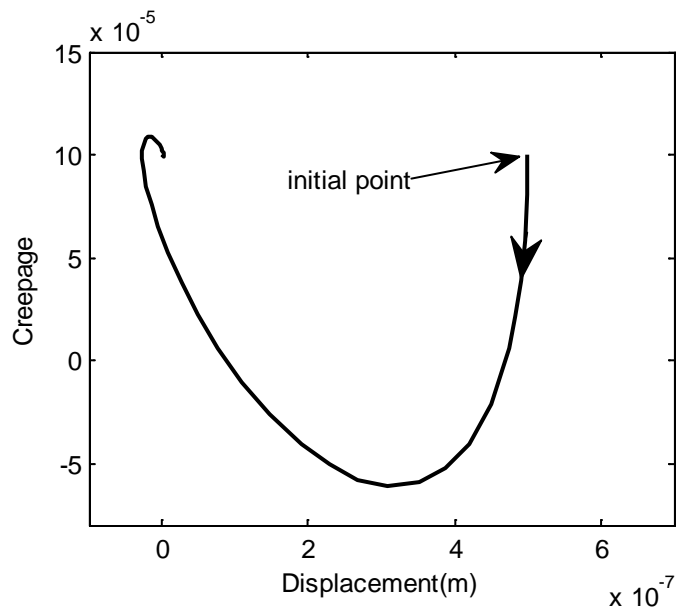
Figure 3-8. Phase plane plot of a stable response ($\gamma_0 = 0.0001$).

3.2.3.3 Limit cycle response

However, if the steady state creepage is larger than the critical creepage and the equivalent negative damping is larger than the structural damping, the system will be unstable.

The motion trajectory of a limit cycle response is shown as a phase-plane plot in Figure 3-9. It can be observed that the motion ends with a limit cycle response. In addition, when the creepage becomes smaller than the critical creepage (area under the red line in Figure 3-9), the friction force tends to stabilise the system and this leads to distortion of the limit cycle curve.
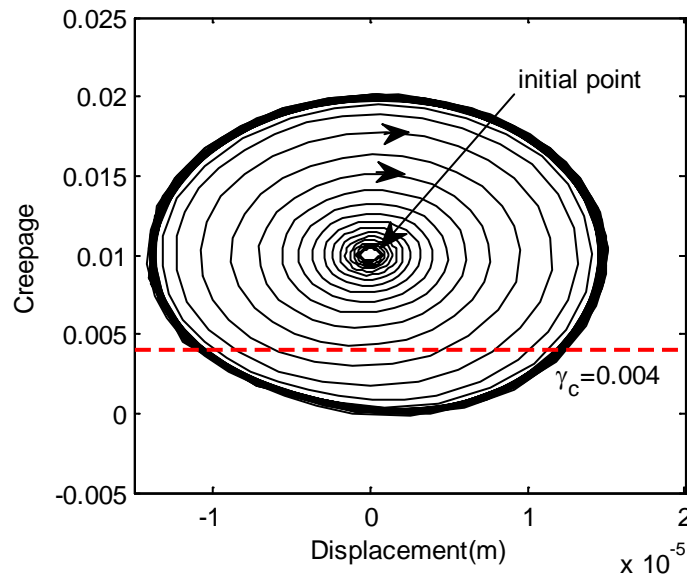
Figure 3-9. Phase plane plot of a limit cycle response ($\gamma_0 = 0.01$).

3.2.3.4 Effects of damping ratio

According to Section 3.2.2, if the structural damping ratio of the wheel is increased to be larger than the absolute value of the equivalent damping, the wheel should be stable. Figure 3-10 shows the effect of increasing the damping ratio of the wheel.

Four different damping ratios are considered. They are 0.0001, 0.001, 0.01, and 0.07. It can be seen from Figure 3-10 that, even if the damping ratio is increased from 0.0001 to 0.01, the system is still unstable. Moreover, the amplitudes of the limit cycle are very similar for all these three damping ratios. However, when damping ratio becomes 0.07, the system is stable. The slope of μ at steady state creepage γ_0 can be obtained from the friction curve used. The minimum damping ratio can be calculated From Eq. (3-28) and Eq. (3-29). After getting the slope of μ at the steady state creepage γ_0 from the friction curve it is found to be 0.033.
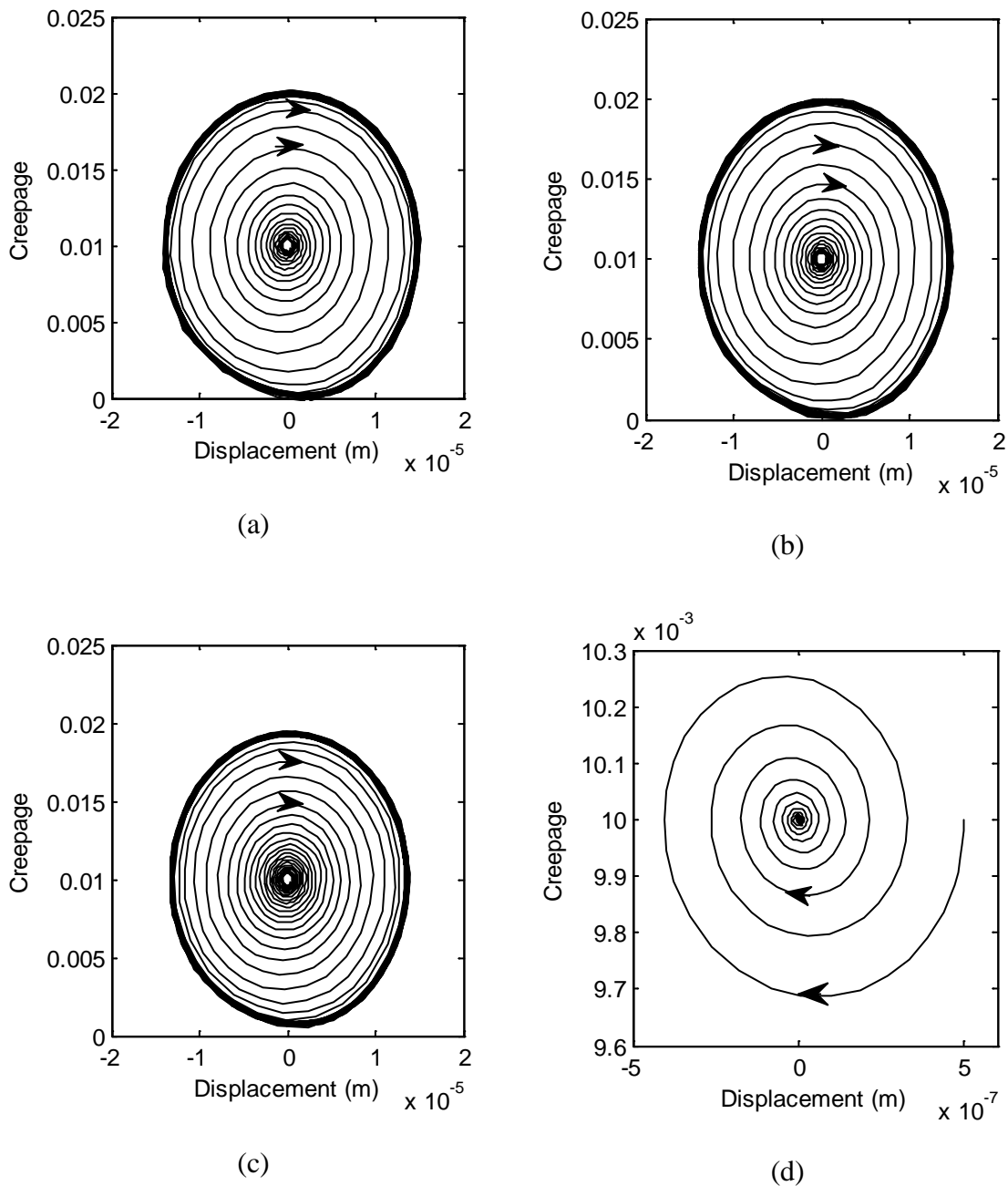
Figure 3-10. Phase plane plots of limit cycle responses with different damping ratios (for $\gamma_0 = 0.005$): (a) $\zeta = 0.0001$; (b) $\zeta = 0.001$; (c) $\zeta = 0.01$; (d) $\zeta = 0.07$.

3.3 Mode coupling

3.3.1 Equation of motion

As discussed in Section 1.2, mode coupling is another type of friction-induced self-excited vibration. In [38, 39], Hoffman et al. developed a two-degree-of-freedom mass-belt model to explain the mode coupling instability. This two-degree-of-freedom model is briefly introduced here (see Figure 3-11).
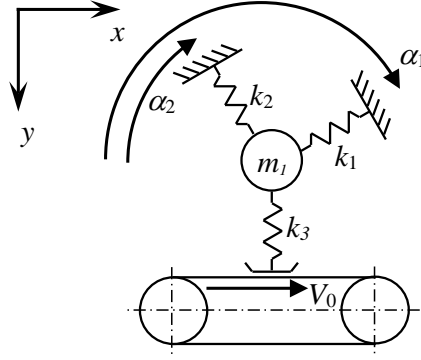
Figure 3-11. Two-degree-of-freedom system on moving belt [38].

Figure 3-11 shows that the mass has two degrees of freedom x and y. The belt is assumed to have a constant sliding velocity V_0. By assuming a constant friction coefficient between the mass and belt, the friction force will be $\mu k_3 y$. Hence, the equation of motion of the system in Figure 3-11 is:

$$\begin{bmatrix} m_1 & 0 \\ 0 & m_1 \end{bmatrix} \begin{bmatrix} \ddot{x} \\ \ddot{y} \end{bmatrix} + \begin{bmatrix} k_{11} & k_{12} - \mu k_3 \\ k_{21} & k_{22} \end{bmatrix} \begin{bmatrix} x \\ y \end{bmatrix} = 0 \tag{3-30}$$

where the elements in the stiffness matrix are:

$$k_{11} = k_1 \cos^2 \alpha_1 + k_2 \cos^2 \alpha_2 \tag{3-31}$$

$$k_{12} = k_{21} = -k_1 \sin \alpha_1 \cos \alpha_1 - k_2 \sin \alpha_2 \cos \alpha_2 \tag{3-32}$$

$$k_{22} = k_1 \sin^2 \alpha_1 + k_2 \sin^2 \alpha_2 + k_3 \tag{3-33}$$

The stiffness matrix in Eq. (3-30) is asymmetric and this can lead to instability [93]. The term $k_{12} - \mu k_3$ can introduce coupling between the normal and tangential dynamics. Thus when the normal displacement of the mass varies the tangential friction force will also change.

3.3.2 Features of mode coupling

In [38], the features of mode coupling were discussed by using a simple case. This will be briefly introduced again here with different parameters.

In this case, m_1 is assumed to be 50 kg, k_1, k_2, and k_3 are assumed to be 1.8×10^8 N/m, 2.5×10^9 N/m and 1.33×10^9 N/m, respectively. α_1 and α_2 are equal to $150°$ and $30°$, repectively. These values are randomly choose here but it can give a squeal frequency around 1 kHz (see calculations below) which is close to real application.

By performing eigenvalue analysis of this equation, the stability of this system can be investigated: a positive real part of one of the eigenvalues indicates instability. The imaginary part (frequency) and real part (growth rate) are plotted against the friction coefficient μ in Figure 3-12. It can be seen that the real part starts at 0 and, when μ becomes larger than 0.75, one of the real parts becomes positive and the other one becomes negative. For the imaginary part, when $\mu = 0$, there are two modes with different frequencies. They become closer and closer with increasing friction coefficient and finally merge to a single value, in this case 1 kHz, which is not equal to neither of the frequencies of the two modes with $\mu = 0$. This frequency shift is one of the basic features of mode coupling [38].

(a)   (b)
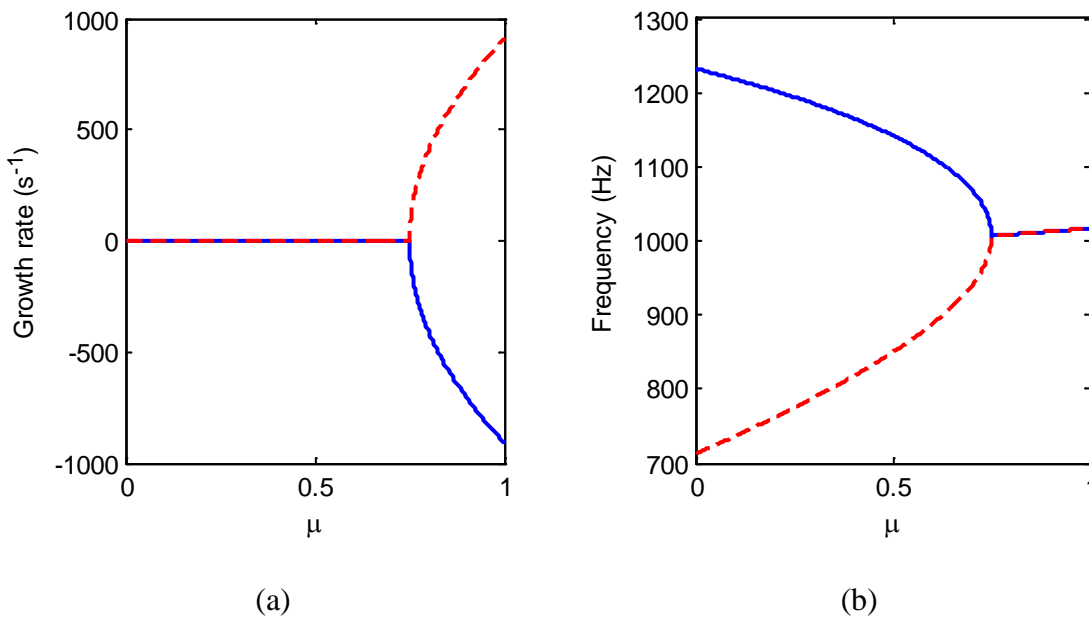
Figure 3-12. Real part (growth rate) and imaginary part (frequency) against the friction coefficient.

Time domain analysis is performed here to study the vibration in vertical and lateral directions. Results are shown in Figure 3-13 for two different friction coefficients. One is 0.7, which is just below 0.75 where the real part becomes positive and the other is 0.8 which is just above 0.75.
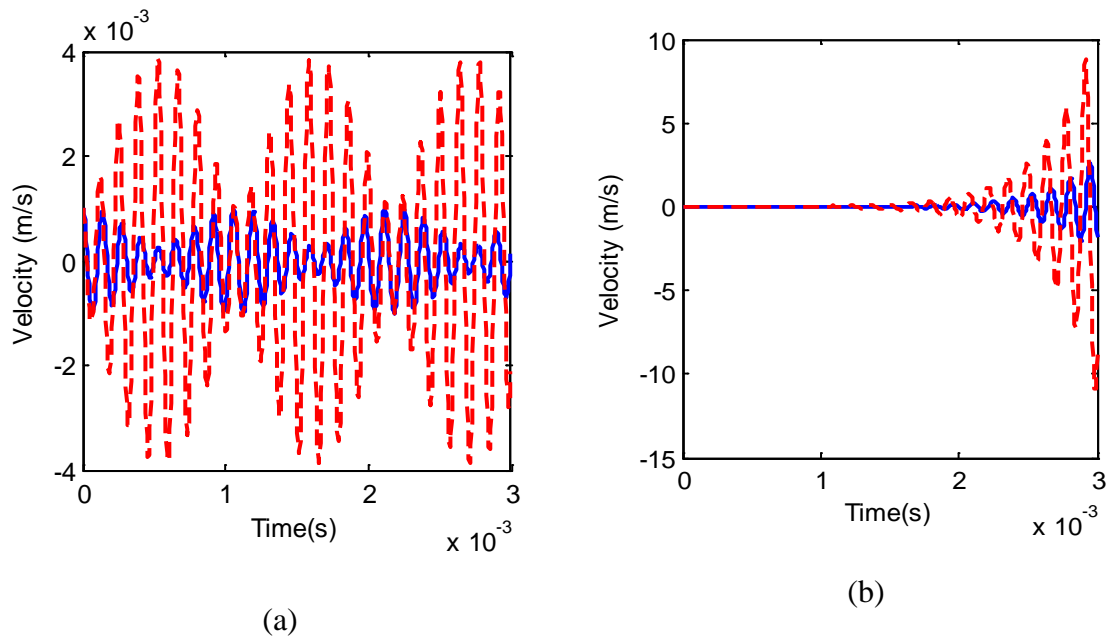
Figure 3-13. Time histories with (a) $\mu = 0.7$ and (b) $\mu = 0.8$; blue solid line: lateral direction; red dashed line: vertical direction.

It can be seen that with $\mu = 0.7$, the time domain results show repeated oscillations for both directions. A 'beating' phenomenon can be seen in Figure 3-13(a). When $\mu = 0.8$, it can be seen that the system is unstable: the vibration in both directions keeps increasing. A phase difference between the velocities in the two directions exists. This is also a sign of coupling between the two directions [38]. This phase difference is necessary to transfer energy from one direction to the other one and generate the instability.

The results here are not necessarily representative of a curve squeal situation but illustrate the phenomenon in a simplified manner. In railway curve squeal, coupling could occur between wheel modes or between wheel and rail modes. Damping is not included here but in [39, 94] this mass-on-belt model is used to investigate the effect of damping on mode coupling. In addition, this model will be applied to more specific curve squeal cases in Chapter 6 including a detailed parametric study.

3.4 Summary

In this chapter, three different friction-induced instabilities have been presented by making use of simple mass-on-belt models. These models are then used to explain the stick-slip phenomenon with different values of dynamic and static friction coefficients, the negative damping effect due to falling friction, and the mode coupling effect related to asymmetries

in the stiffness matrix. It is also shown that frequency shift, phase difference and beating can be observed in the vertical and lateral vibration in the presence of mode coupling.

4 A curve squeal model

In this chapter, the curve squeal model developed by Huang [27] is presented and extended. This model includes wheel dynamics, rail dynamics and contact dynamics. In the frequency domain, a self-excited vibration loop based on the mobilities of the wheel, rail and contact dynamics is established and then stability can be investigated using the Nyquist criterion [95]. In the time domain, state-space models of the wheel and rail dynamics are used and a step-by-step integration method (Runge-Kutta method [96]) is applied. The rail model in the time domain is updated with a newly developed track model, which is based on equivalent mass-spring systems. The modal parameters of these systems are obtained after curve fitting with the results from analytical models. From this a state-space model for rail dynamics can be developed which can be used in time domain calculations.

4.1 Wheel dynamics

The wheel is modelled by finite element method (FEM) analysis. This is used to provide the modal parameters including natural frequencies and mode shapes. Modal damping ratios are included according to prior experience [1] or from measurements of wheel mobilities, where available. Then, according to the superposition principle of modal summation [97], the frequency response function between a force at a location k and the velocity response at a location j can be found as:

$$Y_{jk} = \sum_n \frac{\mathrm{i}\omega\phi_{jn}\phi_{kn}}{m_n(\omega_n^2 - \omega^2 + 2\mathrm{i}\zeta_n\omega\omega_n)} \tag{4-1}$$

where ϕ_{jn} is the modeshape of mode n at location j, m_n is the modal mass, ζ_n is the damping ratio of mode n, ω_n is the angular natural frequency of mode n and ω is the frequency of the external force.

As an example, the cross-section of the wheel from a Class 158 multiple unit train is shown in Figure 4-1. The wheel is assumed to be clamped of the inner edge of the hub. The rigid body modes with non-zero natural frequencies of the wheelset are included but no axle modes are included. The wheel mobilities at the nominal contact point of the Class 158 wheel in different directions (as defined in Figure 4-2) are shown in Figure 4-5 to Figure 4-6. Indices 1, 2 and 3 are longitudinal, lateral and vertical directions, respectively. Indices 4, 5, 6 are the rotations about the 1, 2, 3 directions, respectively. Rotation about the vertical

direction (index 6) is the spin direction. Various cross mobilities also exist but are not shown here.
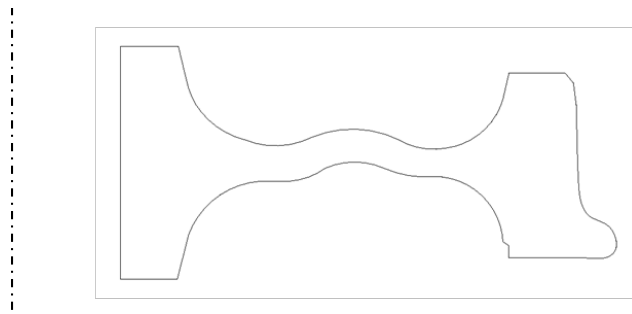
Figure 4-1. Cross-section of Class 158 wheel (radius 420 mm)

(a)   (b)
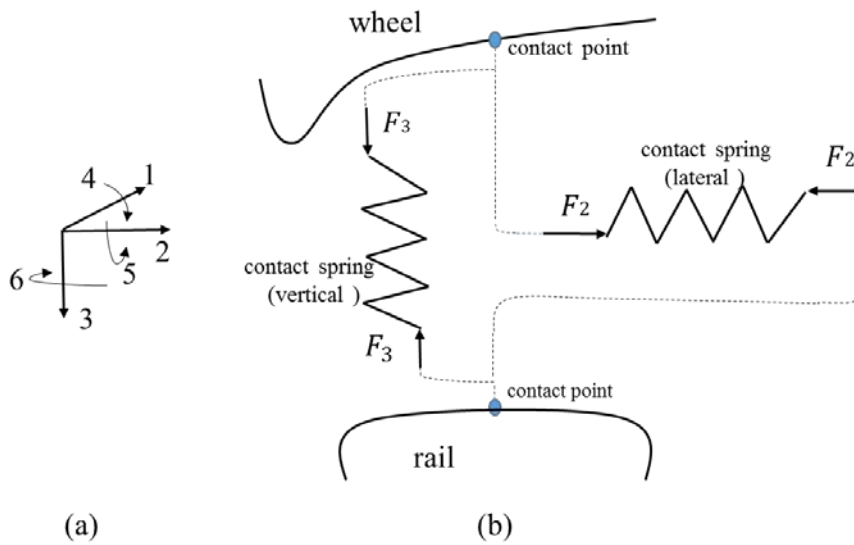
Figure 4-2. Schematic diagram of the wheel/rail contact system and the reference frame: (a) reference frame; (b) wheel/rail contact system.
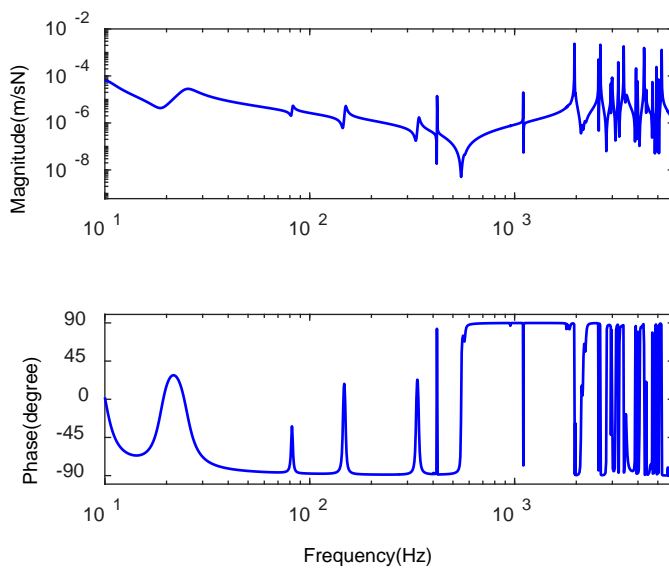
Figure 4-3. Wheel mobility in the vertical direction.
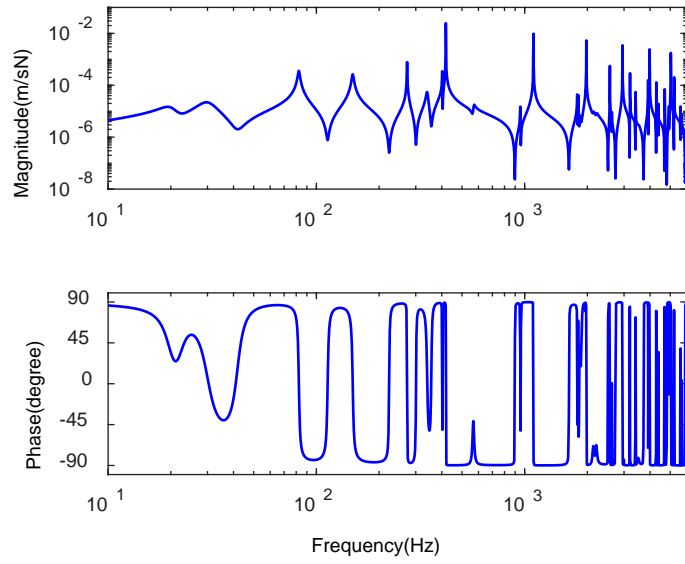
Figure 4-4. Wheel mobility in the lateral direction.
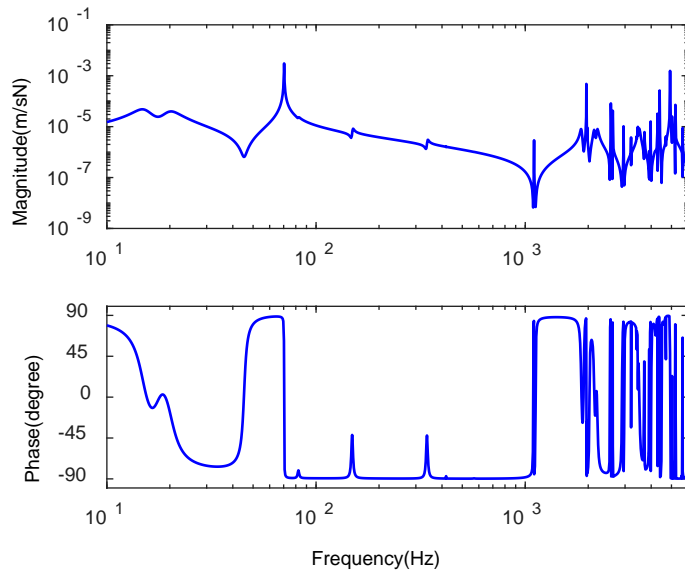
Figure 4-5. Wheel mobility in the longitudinal direction.
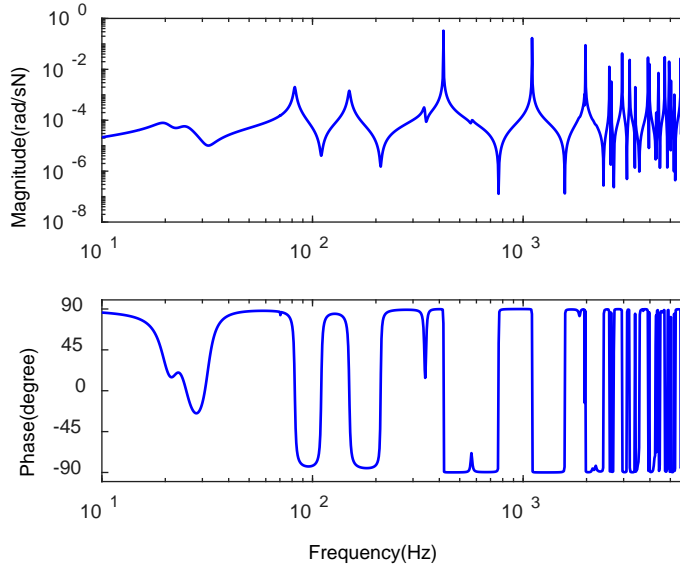
Figure 4-6. Wheel mobility in the spin direction.

These mobilities of the wheel can be used in a frequency domain analysis of curve squeal. This frequency domain analysis model will be introduced in Section 4.3.2. For time domain analysis, however, a state-space model of the wheel is required.

Consider a wheel with N modes, J input dynamic forces $\mathbf{f}^w = \left[f_1^w, f_2^w, f_3^w, \dots, f_J^w\right]^T$, and I output dynamic velocities $\mathbf{V}^w = \left[v_1^w, v_2^w, v_3^w, \dots, v_I^w\right]^T$. This can be represented by a state equation and an output equation,

$$\dot{\mathbf{W}} = \mathbf{A}^w \mathbf{W} + \mathbf{B}^w \mathbf{f}^w \tag{4-2}$$

$$\mathbf{V}^w = \mathbf{C}^w \mathbf{W} \tag{4-3}$$

where the state variable vector $\mathbf{W}$ consists of the modal velocities $\dot{q}_i$ and the modal displacements q_r of modes r (1 to N)

$$\mathbf{W} = [\dot{q}_1, \ \dot{q}_2, \dots, \dot{q}_N, q_1, q_2, \dots, q_N]^T \tag{4-4}$$

The system matrix $\mathbf{A}^w$ is:

$$\mathbf{A}^w = \begin{bmatrix} -2\zeta_1\omega_1 & 0 & \cdots & 0 & | & -\omega_1^2 & 0 & \cdots & 0 \\ 0 & -2\zeta_2\omega_2 & \cdots & 0 & | & 0 & -\omega_2^2 & \cdots & 0 \\ \vdots & \cdots & \ddots & 0 & | & \vdots & \cdots & \ddots & 0 \\ 0 & 0 & \cdots & -2\zeta_N\omega_N & | & 0 & 0 & \cdots & -\omega_N^2 \\ - & - & - & - & - & - & - & - & - \\ 1 & 0 & \cdots & 0 & | & 0 & 0 & \cdots & 0 \\ 0 & 1 & \cdots & 0 & | & 0 & \cdots & \cdots & 0 \\ \vdots & \cdots & \ddots & 0 & | & \vdots & \cdots & \ddots & \vdots \\ 0 & 0 & \cdots & 1 & | & 0 & 0 & \cdots & 0 \end{bmatrix} \qquad (4\text{-}5)$$

where ζ_r is the damping ratio of mode r and ω_r is the natural frequency (in radians/sec) of mode r. The input matrix $\mathbf{B}^w$ is used to transform the external forces into modal forces for each mode, while the output matrix $\mathbf{C}^w$ sums the modal velocities of each mode into output velocities. Both matrices are formed of mode shapes as:

$$\mathbf{B}^w = [\mathbf{C}^w]^\mathrm{T} = \begin{bmatrix} \phi_{11} & \phi_{12} & \cdots & \phi_{1N} & | & 0 & 0 & \cdots & 0 \\ \phi_{21} & \phi_{22} & \cdots & \phi_{2N} & | & 0 & 0 & \cdots & 0 \\ \vdots & \vdots & \ddots & \vdots & | & \vdots & \vdots & \ddots & \vdots \\ \phi_{I1} & \phi_{I1} & \cdots & \phi_{IN} & | & 0 & 0 & \cdots & 0 \end{bmatrix}^\mathrm{T} \qquad (4\text{-}6)$$

where ϕ_{ir} is the mass-normalised modeshape of mode r in the i direction. For example, ϕ_{12} is the mass-normalised modeshape of the second mode in the 1 direction (i.e. longitudinal direction as defined in Figure 4-2).

4.2 Rail dynamics

4.2.1 Analytical rail model

The dynamic behaviour of the track can be represented primarily by its frequency response functions (FRFs). Since the rail is quasi-symmetrical in its cross-section, four point FRFs and no cross FRF are adopted to describe the dynamic properties at the nominal contact position. These FRFs are in the longitudinal, lateral, vertical and spin directions [27].

Different analytical models are adopted in this work for the rail response in different directions. The vertical vibration response was derived by Grassie in [98] by using a Timoshenko beam on a two-layer support. Wu and Thompson [99] derived a model for the

lateral vibration response of a railway track based on multiple beams. Lurcock [100] studied the longitudinal motion using a model of a rod on a single layer support. Spin motion of the rail was modelled for squeal analyses by Huang [27] using a Timoshenko beam model.

In the analytical track models, either viscous or hysteretic damping models can be used. Of these two damping models, the hysteretic model can only be used in a frequency domain approach due to problems of causality if it is used in a time domain model. In the time domain, an equivalent track model based on mass-spring models will be derived in the next subsection, which is based on the rail dynamics with a viscous damping model. The difference between the rail dynamics obtained with these two damping models is introduced and the determination of the damping value for the viscous damping model is explained as follows.

According to [1], the mobility of the track is only influenced by the damping around the cut on frequencies of various waves. Hence a suitable choice of viscous damping coefficient C can be obtained by equating it to the required hysteretic damping value at the corresponding cut-on frequency of waves in the rail. This means:

$$s(1 + i\eta) = s + i\omega_0 C \qquad (4\text{-}7)$$

where s is the stiffness of the structure which corresponds to the different resonances of the system, and η is the damping loss factor. Solving Eq.(4-7) gives $C = \frac{s\eta}{\omega_0}$. This is the equation to get the equivalent viscous damping. However, for higher order bending waves in the rail this method is not valid. In this equation, s is either ballast or pad stiffness and first two cut-on frequencies are used to find the viscous damping for each of these components.

The mobility of a UIC60 rail with continuous double-layer support is shown in Figure 4-7 to Figure 4-10 for different directions. These graphs compare the results with the different damping models. For these results, a concrete sleeper and a soft rail pad are considered. The parameters used in the analytical models are listed in Table 4-1 and Table 4-2. The results show good agreement between these two damping models although there is some difference in the phase at low frequencies. For the viscous damping model, the phase always starts at 90° while for hysteretic damping the low frequency value of phase is lower than this.

In the vertical direction, the first and second peaks correspond to the vibration of the whole track mass on the ballast vertical stiffness and the vibration of the rail mass on the pad vertical stiffness, respectively. In the lateral direction, in [99] there are five cut-on frequencies. The first three correspond to the ballast lateral stiffness, pad lateral stiffness and

the rotational stiffness of the pad. The fourth and fifth correspond to web bending waves of the rail. In this example (Figure 4-8) only four peaks are observed. This is because the pad stiffness here is lower, so that the first and second peaks in [99] become very close together here. In the longitudinal direction, the only peak corresponds to the pad longitudinal stiffness. The only peak in the spin direction corresponds to the transverse stiffness of the rail pads.
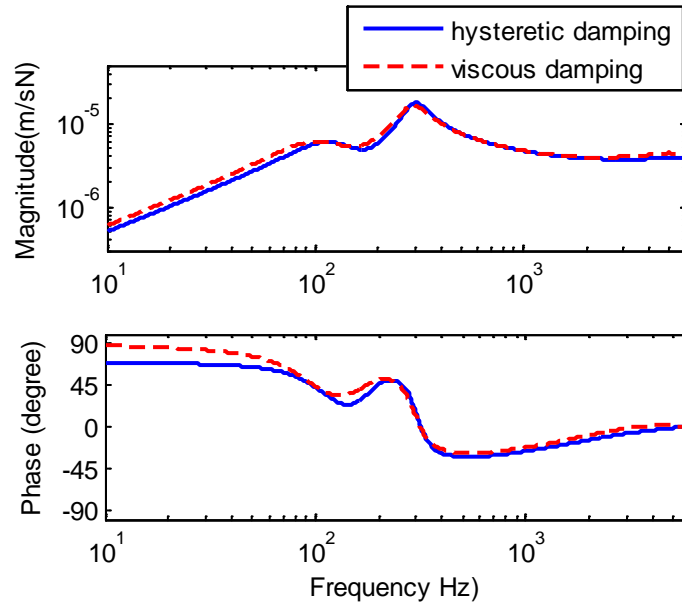
Figure 4-7. Vertical point mobility of the track.
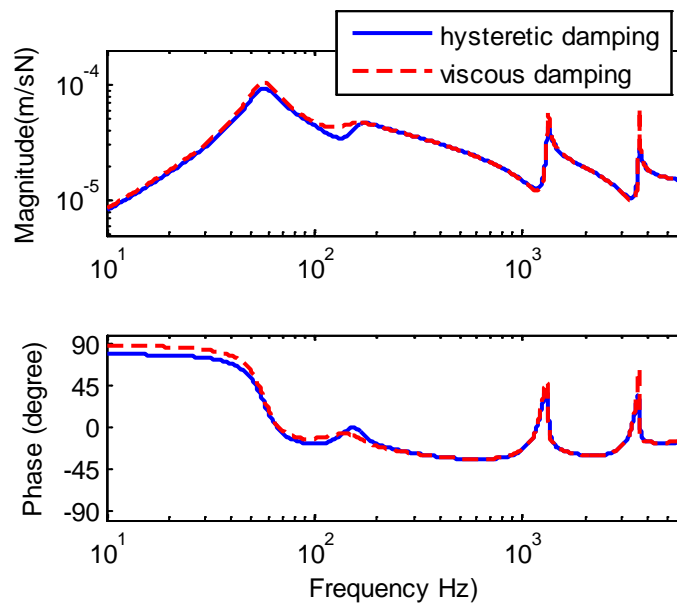
Figure 4-8. Lateral point mobility of the track.
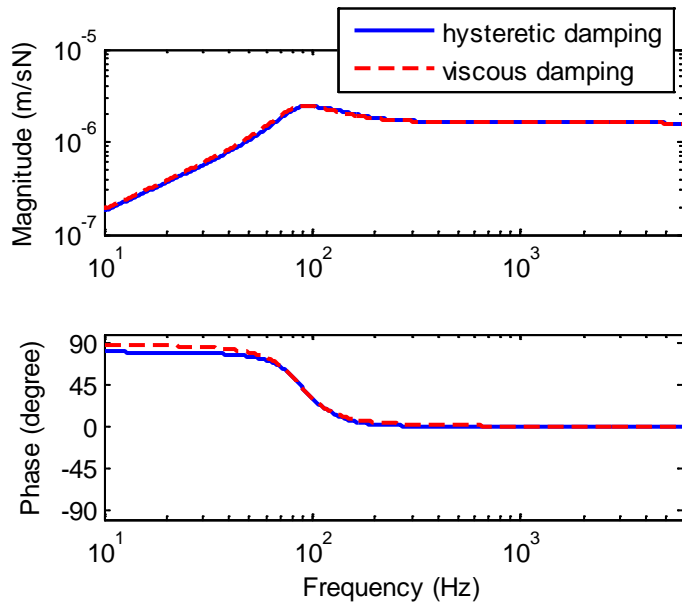
Figure 4-9. Longitudinal point mobility of the track.
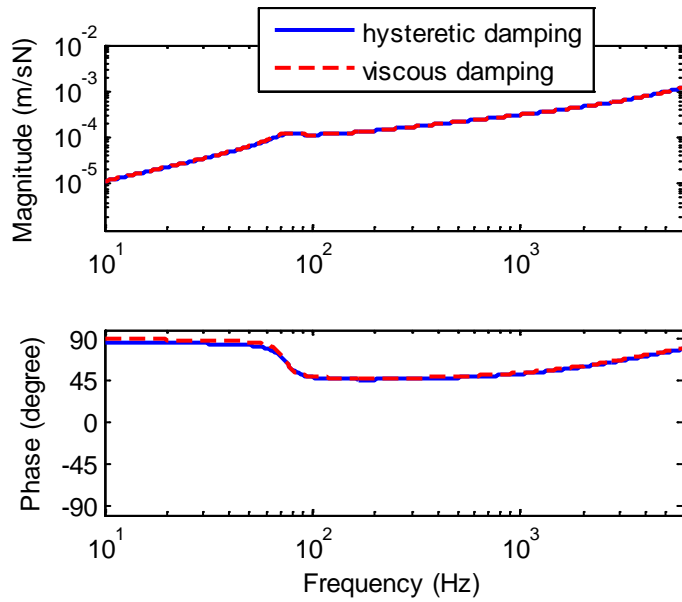
Figure 4-10. Spin point mobility of the track.

Table 4-1 Parameters used for track vertical mobility.

	Description	Value	Units
Rail	Density	7860	kg/m^3
	Young's modulus	210	GPa
	Poisson's ratio	0.3	/
	Shear coefficient	0.4	/
	Second moment of area	3.05×10^{-5}	m^4
	Cross-sectional area	7.60×10^{-3}	m^2
	Damping loss factor	0.02	/
Pad	Vertical stiffness	100	MN/m
	Damping loss factor	0.25	/
Sleeper	Sleeper spacing	0.6	m
	Sleeper mass (half)	162	kg
Ballast	Vertical stiffness	80	MN/m
	Damping loss factor	1.0	/

Table 4-2 Parameters for track mobility in lateral, longitudinal and spin directions.

	Description	Value	Units
Rail head	Cross-sectional area	2.847×10^{-3}	m^2
	Second moment of area	1.264×10^{-6}	m^4
	Polar moment of area	1.625×10^{-6}	m^4
	Torsional moment of area	1.033×10^{-6}	m^4
	Half height	0.0195	m
Rail foot	Cross-sectional area	2.625×10^{-3}	m^2
	Second moment of area	4.921×10^{-6}	m^4
	Polar moment of area	4.988×10^{-6}	m^4
	Torsional moment of area	0.403×10^{-6}	m^4
	Half height	0.00875	m
Rail web	Cross-sectional area	2.166×10^{-3}	m^2
	Second moment of area	6.3×10^{-5}	m^4
	Half height	0.057	m
Pad	Lateral stiffness	13	MN/m
	Rotational stiffness	0.18	MNm/rad
	Longitudinal stiffness	13	MN/m
	Damping loss factor	0.25	/
Ballast	Lateral stiffness	60	MN/m
	Longitudinal stiffness	60	MN/m
	Damping loss factor	1.0	/

This subsection together with Section 4.1 give the wheel and rail mobilities at the nominal contact point. However, in practice, under curving conditions, the contact point between the wheel and rail can differ from the nominal contact point. The translation and rotation matrices to transform the wheel and track dynamics at the nominal contact to the local contact point are provided in Appendix B.

4.2.2 Equivalent mdof track model

The analytical track models discussed above cannot be used directly in the step-by-step integration in the time domain due to their infinite length. In [101], it was shown that a simple system with a limited number of degrees can be used to represent an infinite track system. This method was also adopted in Huang's work [27]. However, this approach involved a system identification technique with system constants obtained by a least-squares fit to the frequency response functions over the frequency range of interest, which gives a

poor agreement in high frequencies. Moreover, it is difficult to relate these system constants to the physical properties of the track. In [102], an alternative approach was used for the vertical track dynamics based on a multi-degree-of-freedom (mdof) mass-spring system (see Figure 4-11).

This equivalent track model from [101] is adopted in this work. However, instead of expressing it in terms of physical parameters as in [101], modal parameters are used here. This will allow the model to have the same formulation as the wheel for use in a state-space formation for time domain calculations.
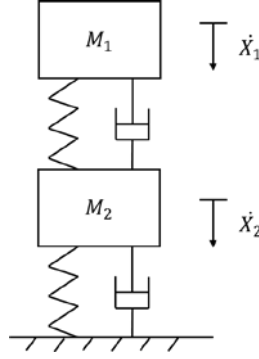
Figure 4-11. A two-degree-of-freedom mass-spring system representing the vertical rail dynamics.

According to the modal analysis method in [97], for a mdof system, the velocity at degree-of-freedom (dof) n due to a force at dof m is:

$$\dot{X}_n = F_m \sum_{j=1}^{N} i\omega \frac{\phi_{jn} \, \phi_{jm}}{-\omega^2 + \omega_j^2 + 2i\zeta_j\omega\omega_j} \qquad (4\text{-}8)$$

where ω_j is the natural frequency of the jth mode, ω is the excitation frequency, and ϕ is the mass-normalised mode shape. F_m is the external force at dof m.

The driving point mobility is then:

$$\frac{\dot{X}_n}{F_n} = \sum_{j=1}^{N} i\omega \frac{\phi_{jn}^2}{-\omega^2 + \omega_j^2 + 2i\zeta_j\omega\omega_j} \qquad (4\text{-}9)$$

To use this formulation, the modal parameters must be derived by comparison or curve fitting with the mobilities calculated with the analytical models of the track.

The mobilities from the analytical models, which are based on an infinite track, contain peaks at the cut-on frequencies of waves in the rail. According to the number of cut-on frequencies in the frequency range considered, the number of modes included in the

equivalent modal model can be defined. Their natural frequencies are chosen to be equal to the cut-on frequencies from the analytical model. A curve fitting method (lsqnonlin in Matlab) is used to obtain an appropriate combination of the other unknown parameters in Eq. (4-9).

Taking the vertical point mobilities of the track as an example, Figure 4-12 shows a comparison between the rail vertical mobility of the analytical model and a modal model with two modes. From the analytical model, it can be seen that there are two peaks at 80 Hz and 300 Hz, which are also chosen as the natural frequencies in the modal model. These two models match well up to 1 kHz, but at higher frequency the agreement is less good. This is because, for an infinite track, energy is carried away from the driving point at high frequency due to free wave propagation along the rail. Consequently the mobility of a Timoshenko beam behaves like a damper and it tends to a phase of 0 and a constant magnitude at high frequency, whereas the modal model tends to a phase of $-\pi/2$ and a slope of $1/\omega$, equivalent to a mass.

In order to get a better match at high frequency, an additional spring/damper set together with a small mass is included in series with the mass/spring model, see Figure 4-13. This can be considered as adding an additional mode to the system; its natural frequency is set equal to 20 kHz which is beyond the frequency range considered in the current study.
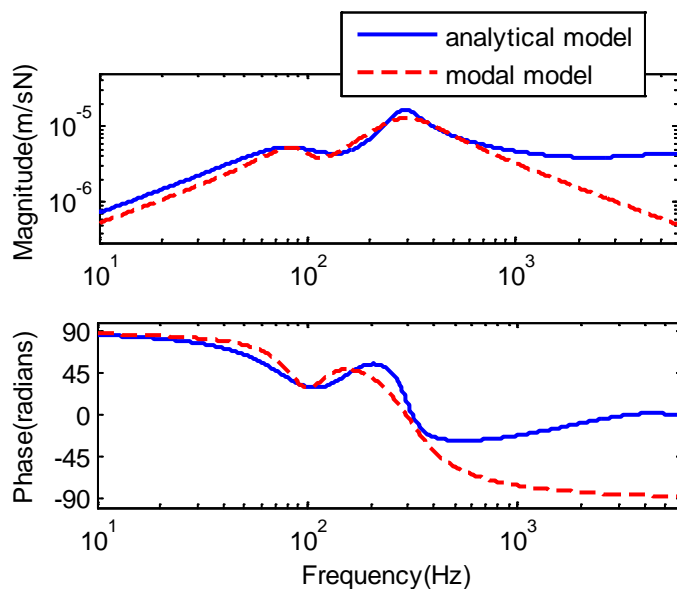
Figure 4-12. Comparison of track vertical mobility between analytical model and modal model with two degrees of freedom.
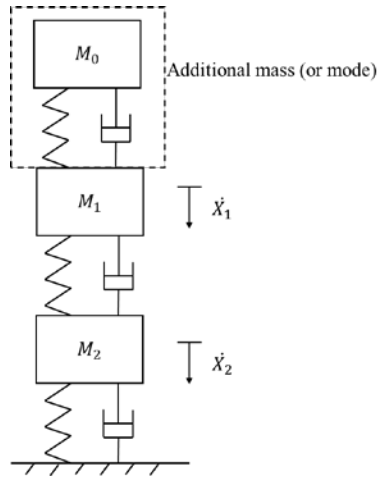
Figure 4-13. Mass-spring equivalent representation for track vertical mobility including additional mode.

The mobility of this new system can be written as:

$$\frac{\dot{X}_1}{F_1} = \sum_{j=1}^{2} i\omega \frac{\phi_{j1}^2}{-\omega^2 + \omega_j^2 + 2i\zeta_j\omega\omega_j} + i\omega \frac{\Psi^2}{-\omega^2 + \Omega^2 + 2i\omega\zeta_0\Omega} \quad (4\text{-}10)$$

where Ψ is the mass-normalised mode shape of the additional mode, Ω is its natural frequency and ζ_0 is the damping ratio of the additional mode. With this additional mode, it can be seen from Figure 4-14 that the model shows a better fit to the analytical model at high frequency. Table 4-3 gives the parameters used in the modal model.
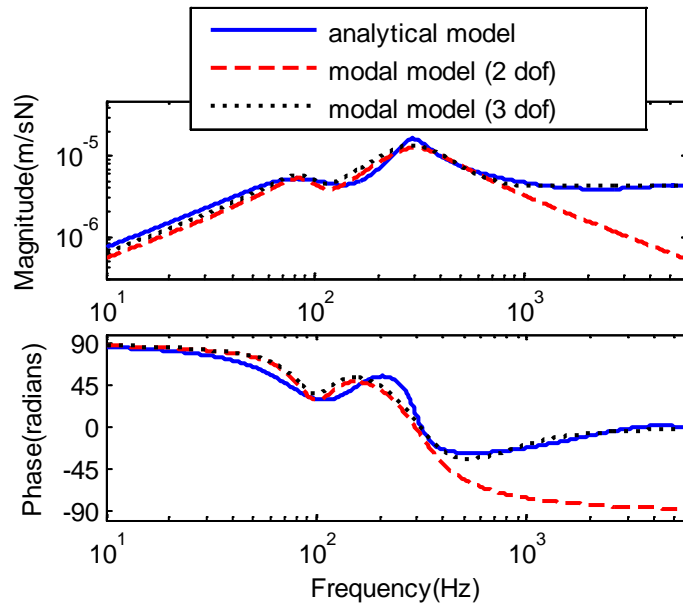
Figure 4-14. Comparison of track vertical mobility between analytical model and modal model with additional mode.

Table 4-3 Parameters used in modal model for track vertical mobility.

Parameters of modal model without additional mode	$\omega_1/2\pi$	$\omega_2/2\pi$	ϕ_1	ϕ_2	ζ_1	ζ_2
	80 Hz	300 Hz	0.03	0.14	0.26	0.39
Parameters of additional mode	$\Omega/2\pi$	Ψ	ζ_0			
	20000 Hz	4.48	18.47			

The equivalent mdof models for the longitudinal and lateral directions are shown in Figure 4-15 and Figure 4-16. These are obtained with a similar method. The parameters are listed in Table 4-4 and Table 4-5. It should be mentioned that, for the spin direction, see Figure 4-17, the modal model cannot match the results very well at high frequency as the mobility in the spin direction increases with increasing frequency.
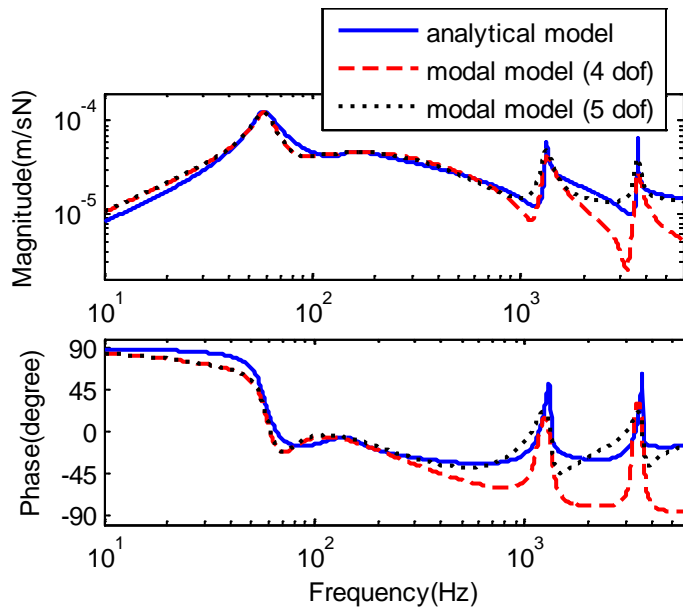
Figure 4-15. Comparison of track lateral mobility between analytical model and modal model.

Table 4-4 Parameters used in modal model for track lateral mobility.

	$\omega_1/2\pi$	$\omega_2/2\pi$	$\omega_3/2\pi$	$\omega_4/2\pi$
	60 Hz	160 Hz	1327 Hz	3630 Hz
Parameters of modal model without additional mode	ϕ_1	ϕ_2	ϕ_3	ϕ_4
	0.09	0.32	0.18	0.19
	ζ_1	ζ_2	ζ_3	ζ_4
	0.12	1.14	0.05	0.03
Parameters of additional mode	$\Omega/2\pi$	Ψ	ζ_0	
	20000 Hz	6.33	12.05	
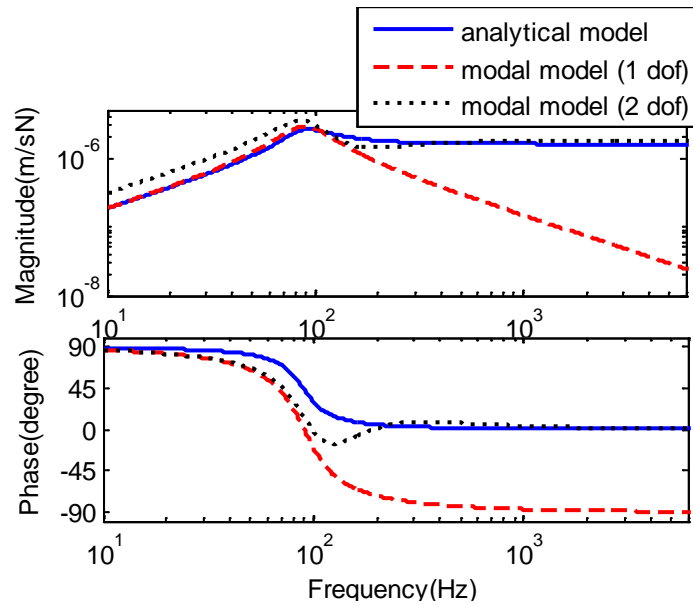
Figure 4-16. Comparison of track longitudinal mobility between analytical model and modal model.

Table 4-5 Parameters used in modal model for track longitudinal mobility

	$\omega_1/2\pi$	ψ_1	ζ_1
Parameters of modal model without additional mode			
	90 Hz	0.03	0.29
	$\Omega/2\pi$	Ψ	ζ_0
Parameters of additional mode			
	20000 Hz	5.46	66.11
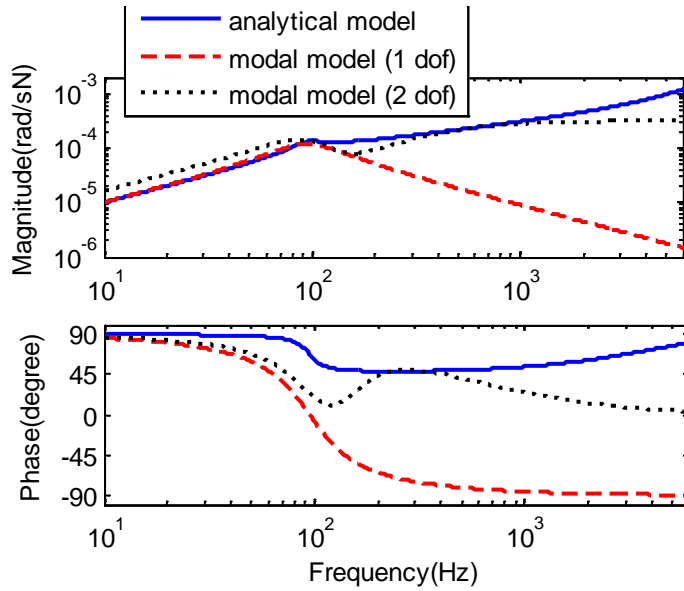
Figure 4-17. Comparison of track spin mobility between analytical model and modal model (same legend with Figure 4-14).

Table 4-6 Parameters used in modal model for track spin mobility

Parameters of modal model without additional mode	$\omega_1/2\pi$	ψ_1	ζ_1
	95 Hz	0.24	0.40

Parameters of additional mode	$\Omega/2\pi$	Ψ	ζ_0
	20000 Hz	40	20

4.2.3 State-space model for track dynamics

A state-space model of the rail is required for the step-by-step simulation in the time-domain calculation. After the equivalent mass-spring system has been built with the modal analysis method, a state-space model can be easily obtained for these mass-spring systems in four directions, vertical, longitudinal, lateral and spin. Each direction has a corresponding equivalent mass-spring model.

Now consider a mass-spring system with N modes, one input dynamic force f, and I output dynamic velocities $\mathbf{V}^r = [v_1^r, v_2^r, v_3^r, \dots, v_I^r]^{\mathrm{T}}$. Similar to the wheel in Section 4.1, this can be represented by a state equation and an output equation,

$$\dot{\mathbf{R}} = \mathbf{A}^r \mathbf{R} + \mathbf{B}^r f \tag{4-11}$$

$$\mathbf{V}^r = \mathbf{C}^r \mathbf{R} \tag{4-12}$$

where the state variable vector $\mathbf{R}$ consists of the modal velocity $\dot{q}_i$ and the modal displacement q_i of modes i (1 to N)

$$\mathbf{R} = [\dot{q_1}, \ \dot{q_2}, \ ..., \dot{q_N}, q_1, q_2, ..., q_N]^\mathrm{T} \tag{4-13}$$

The system matrix $\mathbf{A}^r$ is:

$$\mathbf{A}^r = \begin{bmatrix} -2\zeta_1\omega_1 & 0 & \cdots & 0 & | & -\omega_1^2 & 0 & \cdots & 0 \\ 0 & -2\zeta_2\omega_2 & \vdots & 0 & | & 0 & -\omega_2^2 & \cdots & 0 \\ \vdots & \cdots & \ddots & \cdots & | & \vdots & \vdots & \ddots & \vdots \\ 0 & 0 & \cdots & -2\zeta_N\omega_N & | & 0 & 0 & \cdots & -\omega_N^2 \\ - & - & - & - & | & - & - & - & - \\ 1 & 0 & \cdots & 0 & | & 0 & 0 & \cdots & 0 \\ 0 & 1 & \cdots & 0 & | & 0 & 0 & \cdots & 0 \\ \vdots & \cdots & \ddots & \vdots & | & \vdots & \vdots & \ddots & \vdots \\ 0 & 0 & \cdots & 1 & | & 0 & 0 & \cdots & 0 \end{bmatrix} \tag{4-14}$$

where ζ_i is the damping ratio of mode i and ω_i is the natural frequency (in radians/sec) of mode i. The input matrix $\mathbf{B}^r$ can transform external forces into modal forces for each mode, while the output matrix $\mathbf{C}^r$ sums modal velocities of each mode into external velocities. Both matrices are formed of mode shapes, for example for the 1 direction:

$$\mathbf{B}^r = [\mathbf{C}^r]^\mathrm{T} = [\phi_{11} \ \phi_{12} \ \cdots \phi_{1N} \ | \ 0,0\cdots0 \ ]^\mathrm{T} \tag{4-15}$$

where ϕ_{1n} is the mass-normalised modeshape of mode n in 1 direction.

Four directions are considered here, so by assembling all these four mass-spring state-space models, the total system matrix $\mathbf{A}$, input matrix $\mathbf{B}$ and output matrix $\mathbf{C}$ are given as follows:

$$\mathbf{A} = \begin{bmatrix} \mathbf{A}_{11}^r & & & \\ & \mathbf{A}_{22}^r & & \\ & & \mathbf{A}_{33}^r & \\ & & & \mathbf{A}_{66}^r \end{bmatrix} \tag{4-16}$$

$$\mathbf{B} = \begin{bmatrix} \mathbf{B}_{11}^r & & & \\ & \mathbf{B}_{22}^r & & \\ & & \mathbf{B}_{33}^r & \\ & & & \mathbf{B}_{66}^r \end{bmatrix} \tag{4-17}$$

$$C = \begin{bmatrix} C^r_{11} & & & \\ & C^r_{22} & & \\ & & C^r_{33} & \\ & & & C^r_{66} \end{bmatrix} \tag{4-18}$$

where the subscript 1 refers to the longitudinal direction, 2 to the lateral direction, 3 to the vertical direction and 6 to spin (also see Figure 4-2). The matrices **A**, **B** and **C** can be obtained using the parameter values given in Section 4.2.2.

4.3 Curve squeal model

4.3.1 Time domain curve squeal model

In this section, the time domain model developed by Huang [27] will be introduced. In his model, four degrees of freedom were considered, which are the longitudinal, vertical, lateral and spin directions. The reference frame and the indices for the different directions are shown in Figure 4-18.
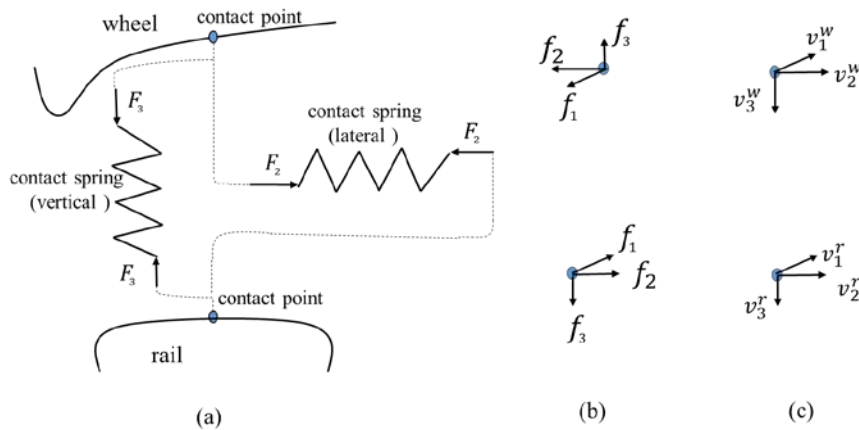
Figure 4-18. Forces and velocities at the wheel/rail contact frame: (a) wheel/rail contact system; (b) forces acting at the wheel and rail; (c) velocities of wheel and rail.

In the vertical direction, there is no sliding because the wheel and rail are assumed to maintain contact. The dynamic approach of the wheel and rail in the vertical direction can be considered as the compression of the contact spring. Expressing this in terms of velocities:

$$v^c_3 = \dot{d}^c_3 = -(\dot{d}^r_3 - \dot{d}^w_3) = -(v^r_3 - v^w_3) \tag{4-19}$$

where v^c_3 is the dynamic velocity of the vertical contact spring, d^c_3 is the relative displacement of the vertical contact spring; d^r_3 and d^w_3 are the dynamic displacements of the

rail and wheel, respectively; v_3^r and v_3^w are the dynamic velocities of the rail and wheel, respectively.

The vector of sliding velocities can be written as:

$$\begin{bmatrix} v_1^s \\ v_2^s \\ v_3^s \\ v_6^s \end{bmatrix} = \begin{bmatrix} v_1^r \\ v_2^r \\ v_3^r \\ v_6^r \end{bmatrix} - \begin{bmatrix} v_1^w \\ v_2^w \\ v_3^w \\ v_6^w \end{bmatrix} + \begin{bmatrix} v_1^c \\ v_2^c \\ v_3^c \\ 0 \end{bmatrix} \tag{4-20}$$

where v_i^r and v_i^w are the velocity of rail and wheel in i direction. v_i^c is the relative velocity of the contact spring in i direction.

The creepage vector is defined as:

$$\begin{bmatrix} \gamma_{1tot} \\ \gamma_{2tot} \\ \gamma_{6tot} \end{bmatrix} = \frac{1}{V_0} \begin{bmatrix} v_{1tot}^s \\ v_{2tot}^s \\ v_{6tot}^s \end{bmatrix} \tag{4-21}$$

where γ_{itot} are the total creepages in the respective directions. The total sliding velocities and corresponding creepages can be written as the sum of a steady-state part and a dynamic part:

$$\begin{bmatrix} \gamma_{1tot} \\ \gamma_{2tot} \\ \gamma_{6tot} \end{bmatrix} = \frac{1}{V_0} \begin{bmatrix} v_{10}^s + v_1^s \\ v_{20}^s + v_2^s \\ v_{60}^s + v_6^s \end{bmatrix} = \begin{bmatrix} \gamma_{10} + v_1^s/V_0 \\ \gamma_{20} + v_2^s/V_0 \\ \gamma_{60} + v_6^s/V_0 \end{bmatrix} \tag{4-22}$$

where v_{i0}^s and γ_{i0} are the steady-state sliding velocities and creepages, which are determined from the steady-state curving behaviour.

The creep forces can be written as the product of the normal contact force and the corresponding adhesion coefficients (see Section 2.4.2):

$$\begin{bmatrix} f_{1tot} \\ f_{2tot} \\ f_{6tot} \end{bmatrix} = \begin{bmatrix} \mu_1(\gamma_{1tot}, \gamma_{2tot}, \gamma_{6tot}, f_{3tot}) \\ \mu_2(\gamma_{1tot}, \gamma_{2tot}, \gamma_{6tot}, f_{3tot}) \\ \mu_6(\gamma_{1tot}, \gamma_{2tot}, \gamma_{6tot}, f_{3tot}) \end{bmatrix} f_{3tot} \tag{4-23}$$

$$\begin{bmatrix} f_{10} \\ f_{20} \\ f_{60} \end{bmatrix} = \begin{bmatrix} \mu_1(\gamma_{10}, \gamma_{20}, \gamma_{60}, N_0) \\ \mu_2(\gamma_{10}, \gamma_{20}, \gamma_{60}, N_0) \\ \mu_6(\gamma_{10}, \gamma_{20}, \gamma_{60}, N_0) \end{bmatrix} f_{30} \tag{4-24}$$

77

where μ_i is the adhesion coefficient, f_{itot} is the total friction force, f_{i0} is the steady-state friction force. The vertical contact force f_{3tot} can be also regarded as a sum of a steady-state part N_0 and a dynamic part f_3:

$$f_{3tot} = N_0 + f_3 \tag{4-25}$$

For the dynamic component of the vertical force f_3, linearized Hertzian contact theory (see Section 2.4.1) can be applied for small amplitudes of displacement [1]. This can be expressed through the contact stiffness as:

$$f_3 = k_H d_3^c \tag{4-26}$$

where k_H is the linearized Hertzian contact stiffness in the vertical direction.

Hence, the dynamic friction force can be written as:

$$\begin{bmatrix} f_1 \\ f_2 \\ f_6 \end{bmatrix} = \begin{bmatrix} f_{1tot} \\ f_{2tot} \\ f_{6tot} \end{bmatrix} - \begin{bmatrix} f_{10} \\ f_{20} \\ f_{60} \end{bmatrix} =$$

$$\begin{bmatrix} \mu_1(\gamma_{1tot}, \gamma_{2tot}, \gamma_{6tot}, f_{3tot}) \\ \mu_2(\gamma_{1tot}, \gamma_{2tot}, \gamma_{6tot}, f_{3tot}) \\ \mu_6(\gamma_{1tot}, \gamma_{2tot}, \gamma_{6tot}, f_{3tot}) \end{bmatrix} (N_0 + f_3) - \begin{bmatrix} \mu_1(\gamma_{10}, \gamma_{20}, \gamma_{60}, N_0) \\ \mu_2(\gamma_{10}, \gamma_{20}, \gamma_{60}, N_0) \\ \mu_6(\gamma_{10}, \gamma_{20}, \gamma_{60}, N_0) \end{bmatrix} N_0 \tag{4-27}$$

Eq.(4-27) is a nonlinear equation. Combining it with the state-space wheel and track models given in Sections 4.1 and 4.2, and the contact spring formulation in Eq. (4-26), the time domain squeal analysis can be carried out by using a step-by-step integration method.

4.3.2 Frequency domain curve squeal model

In this section, the frequency domain model developed by Huang [27] will be introduced.

In the quasi-steady condition, the dynamic contact forces f_k and velocities v_k can be converted into the frequency domain by assuming harmonic motion at some frequency ω. Thus, the dynamic components of the contact forces, wheel velocities, rail velocities, contact spring velocities, and sliding velocities can be written as:

$$f_i = F_i e^{i\omega t}, v_i^w = V_i^w e^{i\omega t}, v_i^r = V_i^r e^{i\omega t}, v_3^c = V_3^c e^{i\omega t}, v_i^s = V_i^s e^{i\omega t} \tag{4-28}$$

where F and V are the complex force and velocity amplitudes, the superscript w represents the wheel, the superscript r represents the rail, c is for contact, and s is for sliding. The subscript i is for different directions, as shown in Figure 4-18.

Hence, the dynamic components of velocity of wheel, rail and sliding can be written as:

$$
\begin{bmatrix} V_1^w \\ V_2^w \\ V_3^w \\ V_6^w \end{bmatrix} = \begin{bmatrix} Y_{11}^w & Y_{12}^w & Y_{13}^w & Y_{16}^w \\ Y_{21}^w & Y_{22}^w & Y_{23}^w & Y_{26}^w \\ Y_{31}^w & Y_{32}^w & Y_{33}^w & Y_{36}^w \\ Y_{61}^w & Y_{62}^w & Y_{63}^w & Y_{64}^w \end{bmatrix} \begin{bmatrix} F_1 \\ F_2 \\ F_3 \\ F_6 \end{bmatrix}
\tag{4-29}
$$

$$
\begin{bmatrix} V_1^r \\ V_2^r \\ V_3^r \\ V_6^r \end{bmatrix} = \begin{bmatrix} Y_{11}^r & Y_{12}^r & Y_{13}^r & Y_{16}^r \\ Y_{21}^r & Y_{22}^r & Y_{23}^r & Y_{26}^r \\ Y_{31}^r & Y_{32}^r & Y_{33}^r & Y_{36}^r \\ Y_{61}^r & Y_{62}^r & Y_{63}^r & Y_{64}^r \end{bmatrix} \begin{bmatrix} F_1 \\ F_2 \\ F_3 \\ F_6 \end{bmatrix}
\tag{4-30}
$$

$$
\begin{bmatrix} V_1^s \\ V_2^s \\ V_3^s \\ V_6^s \end{bmatrix} = \begin{bmatrix} V_1^r \\ V_2^r \\ V_3^r \\ V_6^r \end{bmatrix} - \begin{bmatrix} V_1^w \\ V_2^w \\ V_3^w \\ V_6^w \end{bmatrix} + \begin{bmatrix} V_1^c \\ V_2^c \\ V_3^c \\ 0 \end{bmatrix}
\tag{4-31}
$$

where Y_{ij}^w is the wheel mobility and Y_{ij}^r is the rail mobility from force in the j direction to response in the i direction.

the contact velocity can be expressed in terms of the contact spring mobility, which gives:

$$
V_i^c = Y_{ii}^c F_i
\tag{4-32}
$$

where the mobility of the contact spring can be found as:

$$
Y_{ii}^c = \frac{i\omega}{k_{ci}}
\tag{4-33}
$$

where the contact stiffness in different directions k_{ci} can be found in Section 2.4.1.

By substituting Eq.(4-29), (4-30), (4-33) into Eq.(4-31), the relationship between the sliding velocities and the mobilities is:

$$
\begin{bmatrix} V_1^s \\ V_2^s \\ V_3^s \\ V_6^s \end{bmatrix} = \begin{bmatrix} Y_{11} & Y_{12} & Y_{13} & Y_{16} \\ Y_{21} & Y_{22} & Y_{23} & Y_{26} \\ Y_{31} & Y_{32} & Y_{33} & Y_{36} \\ Y_{61} & Y_{62} & Y_{63} & Y_{64} \end{bmatrix} \begin{bmatrix} F_1 \\ F_2 \\ F_3 \\ F_6 \end{bmatrix}
\tag{4-34}
$$

where Y_{ij} is the sum of the wheel, rail and contact spring mobilities.

As there is no sliding velocity in the vertical direction:

$$
V_3^s = Y_{31}F_1 + Y_{32}F_2 + Y_{33}F_3 + Y_{36}F_6 = 0
\tag{4-35}
$$

Then the vertical dynamic component of force F_3 can be written in terms of the other components as:

$$F_3 = - \begin{bmatrix} \dfrac{Y_{31}}{Y_{33}} & \dfrac{Y_{32}}{Y_{33}} & \dfrac{Y_{36}}{Y_{33}} \end{bmatrix} \begin{bmatrix} F_1 \\ F_2 \\ F_6 \end{bmatrix} \tag{4-36}$$

Combining Eq. (4-34), (4-35) and (4-36) gives the relationship between the dynamic friction forces and the sliding velocities:

$$\mathbf{V_s} = \mathbf{G F^f} \tag{4-37}$$

where $\mathbf{V_s}$ is the sliding velocity vector, $\mathbf{G}$ is a matrix of mobility and $\mathbf{F^f}$ is the friction force vector. They are written as:

$$\mathbf{V_s} = [V_1^s \quad V_2^s \quad V_6^s]^{\mathrm{T}} \tag{4-38}$$

$$\mathbf{G} = \begin{bmatrix} Y_{11} - \dfrac{Y_{13}Y_{31}}{Y_{33}} & Y_{12} - \dfrac{Y_{13}Y_{32}}{Y_{33}} & Y_{16} - \dfrac{Y_{13}Y_{36}}{Y_{33}} \\ Y_{21} - \dfrac{Y_{23}Y_{31}}{Y_{33}} & Y_{22} - \dfrac{Y_{23}Y_{32}}{Y_{33}} & Y_{26} - \dfrac{Y_{23}Y_{36}}{Y_{33}} \\ Y_{61} - \dfrac{Y_{63}Y_{31}}{Y_{33}} & Y_{62} - \dfrac{Y_{63}Y_{32}}{Y_{33}} & Y_{66} - \dfrac{Y_{63}Y_{36}}{Y_{33}} \end{bmatrix} \tag{4-39}$$

$$\mathbf{F^f} = [F_1 \quad F_2 \quad F_6]^{\mathrm{T}} \tag{4-40}$$

By assuming small dynamic quantities and ignoring the terms of second order, Eq.(4-27) can be linearized as:

$$\begin{bmatrix} f_1 \\ f_2 \\ f_6 \end{bmatrix} = \frac{N_0}{V_0} \begin{bmatrix} \dfrac{\partial \mu_1}{\partial \gamma_1} & \dfrac{\partial \mu_1}{\partial \gamma_2} & \dfrac{\partial \mu_1}{\partial \gamma_6} & \dfrac{\partial \mu_1}{\partial f_3} \\ \dfrac{\partial \mu_2}{\partial \gamma_1} & \dfrac{\partial \mu_2}{\partial \gamma_2} & \dfrac{\partial \mu_2}{\partial \gamma_6} & \dfrac{\partial \mu_2}{\partial f_3} \\ \dfrac{\partial \mu_6}{\partial \gamma_1} & \dfrac{\partial \mu_6}{\partial \gamma_2} & \dfrac{\partial \mu_6}{\partial \gamma_6} & \dfrac{\partial \mu_6}{\partial f_3} \end{bmatrix} \begin{bmatrix} v_1^s \\ v_2^s \\ v_6^s \\ V_0 f_3 \end{bmatrix} + \begin{bmatrix} \mu_1 \\ \mu_2 \\ \mu_6 \end{bmatrix} f_3 \tag{4-41}$$

where in the convention adopted for this thesis the adhesion coefficient μ_i is negative for a positive creepage (see Figure 2-15).

According to Eq. (4-28), the amplitude of the harmonic friction forces can be also written as:

$$\begin{bmatrix} F_1 \\ F_2 \\ F_6 \end{bmatrix} = \frac{N_0}{V_0} \begin{bmatrix} \dfrac{\partial \mu_1}{\partial \gamma_1} & \dfrac{\partial \mu_1}{\partial \gamma_2} & \dfrac{\partial \mu_1}{\partial \gamma_6} & \dfrac{\partial \mu_1}{\partial f_3} \\ \dfrac{\partial \mu_2}{\partial \gamma_1} & \dfrac{\partial \mu_2}{\partial \gamma_2} & \dfrac{\partial \mu_2}{\partial \gamma_6} & \dfrac{\partial \mu_2}{\partial f_3} \\ \dfrac{\partial \mu_6}{\partial \gamma_1} & \dfrac{\partial \mu_6}{\partial \gamma_2} & \dfrac{\partial \mu_6}{\partial \gamma_6} & \dfrac{\partial \mu_6}{\partial f_3} \end{bmatrix} \begin{bmatrix} V_1^s \\ V_2^s \\ V_6^s \\ V_0 F_3 \end{bmatrix} + \begin{bmatrix} \mu_1 \\ \mu_2 \\ \mu_6 \end{bmatrix} F_3 \tag{4-42}$$

The terms related to F_3 can be brought together and then eliminated using Eq. (4-36), which then gives:

$$\mathbf{F^f} = \mathbf{H_1} \mathbf{V^s} + \mathbf{H_2} \mathbf{F^f} \tag{4-43}$$

where:

$$\mathbf{H_1} = \frac{N_0}{V_0} \begin{bmatrix} \dfrac{\partial \mu_1}{\partial \gamma_1} & \dfrac{\partial \mu_1}{\partial \gamma_2} & \dfrac{\partial \mu_1}{\partial \gamma_6} \\ \dfrac{\partial \mu_2}{\partial \gamma_1} & \dfrac{\partial \mu_2}{\partial \gamma_2} & \dfrac{\partial \mu_2}{\partial \gamma_6} \\ \dfrac{\partial \mu_6}{\partial \gamma_1} & \dfrac{\partial \mu_6}{\partial \gamma_2} & \dfrac{\partial \mu_6}{\partial \gamma_6} \end{bmatrix} = \begin{bmatrix} \dfrac{\partial f_1}{\partial v_1^s} & \dfrac{\partial f_1}{\partial v_2^s} & \dfrac{\partial f_1}{\partial v_6^s} \\ \dfrac{\partial f_2}{\partial v_1^s} & \dfrac{\partial f_2}{\partial v_2^s} & \dfrac{\partial f_2}{\partial v_6^s} \\ \dfrac{\partial f_6}{\partial v_1^s} & \dfrac{\partial f_6}{\partial v_2^s} & \dfrac{\partial f_6}{\partial v_6^s} \end{bmatrix} \tag{4-44}$$

$$\mathbf{H_2} = - \begin{bmatrix} \mu_1 + N_0 \dfrac{\partial \mu_1}{\partial f_3} \\ \mu_2 + N_0 \dfrac{\partial \mu_2}{\partial f_3} \\ \mu_6 + N_0 \dfrac{\partial \mu_6}{\partial f_3} \end{bmatrix} \begin{bmatrix} \dfrac{Y_{31}}{Y_{33}} & \dfrac{Y_{32}}{Y_{33}} & \dfrac{Y_{36}}{Y_{33}} \end{bmatrix} \tag{4-45}$$

$$\mathbf{F^f} = [F_1 \quad F_2 \quad F_6]^T \tag{4-46}$$

$$\mathbf{V^s} = [V_1^s \quad V_2^s \quad V_6^s]^T \tag{4-47}$$

By substituting Eq.(4-37) into Eq.(4-43):

$$\mathbf{F^f} = (\mathbf{H_1} \mathbf{G} + \mathbf{H_2}) \mathbf{F^f} \tag{4-48}$$

which gives a self-excitation loop (see Figure 4-19). The open loop transfer function matrix is $\mathbf{Q} = \mathbf{H_1} \mathbf{G} + \mathbf{H_2}$.
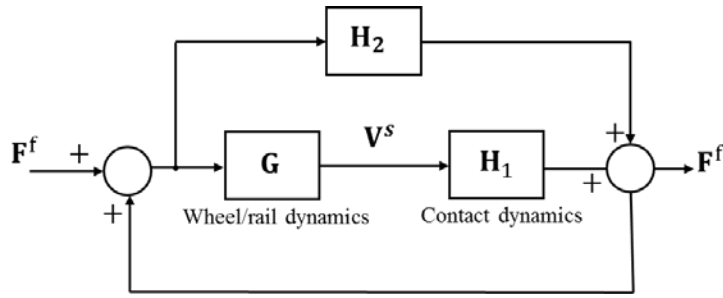
Figure 4-19. Frequency domain feedback loop of wheel/rail contact system.

After the open loop transfer function matrix $\mathbf{Q}$ is obtained, the generalised Nyquist criterion [95] can be used to analyse the stability. The closed-loop system will be stable if and only if the net sum of anti-clockwise encirclements of the critical point (-1/k, j0) by the set of eigenloci of the open-loop transfer function matrix (TFM) is equal to the total number of right-half plane poles of the TFM, where for negative feedback, $k = 1$, and for a positive feedback as here, $k = -1$. Since the open-loop system here (the dynamic response of the wheel/rail system in the absence of the feedback mechanism) is always stable, no pole of the open-loop TFM is located in the right-half plane, and the total number of right-half plane poles of the open-loop transfer TFM is zero. Thus, to ensure the closed-loop system is stable the eigenloci of the open-loop TFM must not encircle the critical point (1+j0) (positive feedback loop with k = -1). The physical meaning of this criterion can be explained as: if the open loop frequency response has a gain greater than unity at the frequency giving an open loop phase lag of 0°, the force amplitude will grow due to the positive feedback.

4.4 Summary

In this chapter, a curve squeal model based on [27] has been presented. This model includes wheel dynamics, rail dynamics, and contact dynamics. The wheel is modelled using a modal basis obtained from the FE method. The frequency response (mobility) for different directions of an example wheel has been shown. The state-space model of the wheel has also been presented which can be used for purpose of time domain calculation.

A new equivalent track model has been developed. This is based on the modal analysis method for mass-spring systems. According to the frequency response (mobility) from analytical models of the track dynamics, different numbers of dof are chosen for different equivalent track models in different directions. After obtaining the modal parameters for the equivalent track model using a curve fitting method, the state-space model can then be obtained and used in time domain calculation.

After the curve squeal model in [27] is updated, it will be used for a parametric study in next chapter to find out different mechanism for curve squeal.

5 Investigation on the origins of curve squeal

In the previous chapter, the curve squeal model from [27] was presented and adapted by introducing a newly developed track model. In this chapter, this curve squeal model is used to illustrate the effect of three main factors: the value of the Coulomb friction coefficient, the friction characteristics (falling or constant) and the track dynamics (with rigid or flexible track). Both frequency and time domain analyses are performed to give a detailed comparison of the effects of these factors on instability and on the limit cycle. Additionally, the effects of wheel rotation and rolling velocity are also investigated in the frequency domain.

5.1   Parameters and case descriptions

5.1.1 Friction curves

To see whether a constant friction coefficient can also lead to curve squeal, the two friction curves shown in Figure 5-1 are considered: these represent falling and constant friction in the saturation region. They are calculated according to Kalker's FASTSIM algorithm [30], which is modified to include the falling part as shown in Eq.(2-24). Some other important parameters used to obtain these friction curves are listed in Table 5-1.
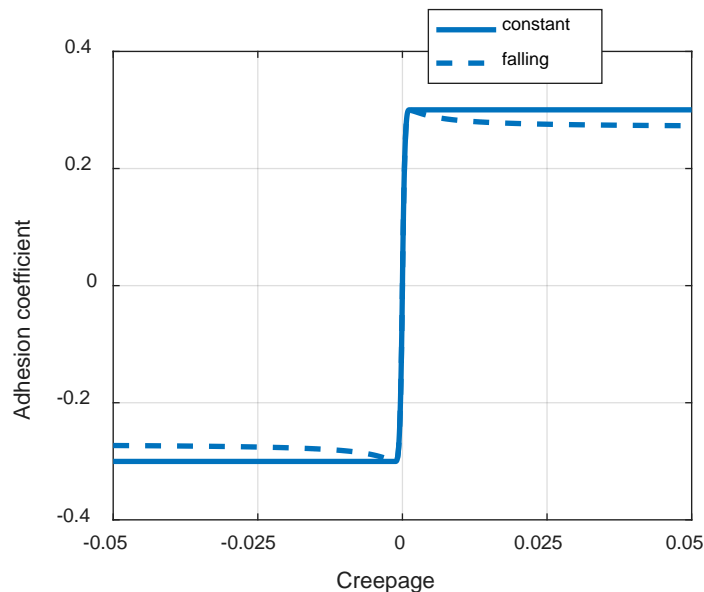
Figure 5-1. Two friction laws used in this chapter.

Table 5-1. Parameters used for friction force calculation.		
Description and Name	Value	Units
Coulomb friction coefficient μ_0	0.3	/
Falling ratio λ in Eq. (2-23)	$\begin{cases} 0.1 \text{ for with falling} \\ 0 \text{ for constant} \end{cases}$	/
Saturation coefficient κ in Eq.(2-24)	0.005	/
Longitudinal creepage	0	/
Spin creepage	0	/
Longitudinal semi-axis of contact ellipse a	6.1	mm
Lateral semi-axis of contact ellipse b	4.1	mm

5.1.2 Case descriptions

To study the roles of the friction coefficient, track dynamics and friction characteristics after saturation, five cases are considered which are described in Table 5-2. For Cases I to IV, the friction coefficient is set to 0.3. Cases I and II are with falling friction; rail dynamics is included in Case I but not in Case II. Meanwhile constant friction is adopted for Cases III and IV, again with and without the rail dynamics respectively. Like Case IV, Case V also has constant friction and the rail is assumed to be rigid, but the Coulomb friction coefficient is increased to 0.7.

The wheel and track considered are the ones introduced in Sections 4.1 and 4.2. The linearized vertical contact stiffness is calculated according to Section 2.4.1 and is equal to 1.12×10^9 N/m for a normal load 62 kN.

Some other important parameters used in these calculations are shown in Table 5-3. The wheel is assumed to be the right-hand wheel in a right-hand curve. For simplicity the contact position is assumed here to be located at the nominal wheel/rail contact point and the contact angle is set as -1.5° (it is always negative for the right wheel, see Figure 4-2) according to the wheel cross-section design. This is not necessarily representative of a train running around a curve but still can give insights into the stability of the system with different combinations of the parameters shown in Table 5-2. The effect of varying the contact position is studied in Chapter 6.

Table 5-2. Description of calculation cases.

Case number	Coulomb friction	Falling friction (✔) or constant friction(✘)	Include track (✔) or not (✘)
I	0.3	✔	✔
II	0.3	✔	✘
III	0.3	✘	✔
IV	0.3	✘	✘
V	0.7	✘	✘

Table 5-3. Some input parameters and their values.

Description	Unit	Value
Normal force N_0	kN	62
Rolling velocity V_0	m/s	10
Lateral steady state creepage γ_2	/	0.025
Longitudinal steady state creepage γ_1	/	0
Spin steady state creepage γ_6	m^{-1}	0

5.2   Frequency domain analysis

Frequency domain analysis is performed here to predict the potentially unstable frequencies. Figure 5-2 gives the Nyquist locus and Bode plot for Case I with falling friction and including the track. The unstable frequencies are marked by a '*' in both the Nyquist plots and the modulus graph of the Bode plot.

Before performing the calculations for other cases, the effect of the lateral and longitudinal contact spring is studied. It is found that adding the contact spring in these two directions has no effect. Hence for all calculations in this work, these two contact springs are omitted.

The plots for other cases are shown in Figure 5-3 to Figure 5-5. To compare all these cases, the results are summarised in Table 5-4. In this table, the 'wheel modes involved' are the wheel modes corresponding to the unstable frequencies. These are verified by including only these wheel modes in the analysis to check whether the unstable frequencies remain: i.e. if any of the wheel modes identified are deleted, the corresponding unstable frequency will disappear.

From the results shown in Table 5-4 and by analysing the mode(s) involved in the instabilities and considering whether the track is present or not, three different situations can be identified. They are the falling friction mechanism, coupling of pairs of wheel modes and coupling between the wheel and rail. These are discussed in more detail below.

Falling friction. It can be seen that both cases with falling friction can lead to instability (see Cases I and II). Only one wheel mode is responsible for each unstable frequency. Hence, these instabilities can be attributed to the negative damping effect induced by falling friction. In addition, most wheel modes involved are axial modes with zero nodal circles. This agrees with the results from many previous studies (see Table 1-3).

Wheel modes coupling. Case V, which has a higher friction coefficient than Case IV, has two unstable frequencies at 178.2 Hz and 1982.0 Hz. More than one wheel mode is involved in both of these instabilities. This indicates that wheel mode coupling exists in this case (the track is not included). In Chapter 6, a more detailed discussion about wheel mode coupling will be given. It is also found in Case V that unstable frequencies are not at the peaks of modulus of the open loop transfer function (see Figure 5-5).

Wheel/rail coupling. By comparing the results of Cases I and II in Table 5-4, it can be seen that with a falling friction characteristic, the unstable frequency at 150.5 Hz can be eliminated if the track is not included in this model. Also by comparing the results of Cases III and IV, it can be found that when rail is assumed to be rigid, the unstable frequencies in Case III no longer exist. This suggests that the rail dynamics is playing a significant role for these unstable frequencies. Moreover, only a single wheel mode is involved for each of these unstable frequencies. This means that these unstable frequencies are due to the coupling between a single wheel mode and the rail. This type of instability will be investigated further in Chapter 7.
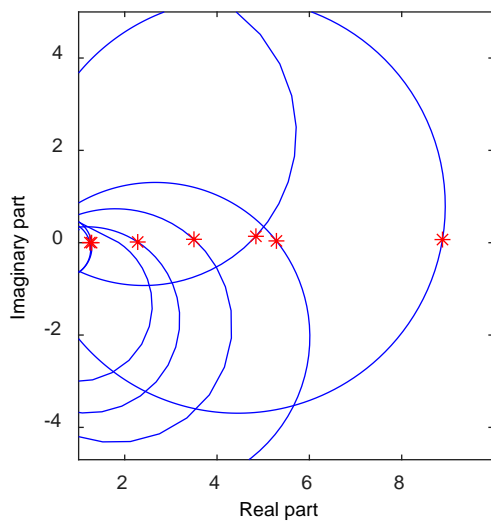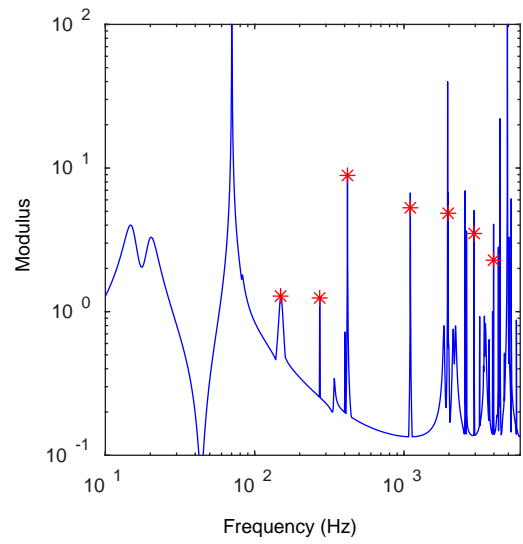
Figure 5-2. Results for Case I: Stability analysis of model including rail dynamics in frequency domain: (a) Nyquist locus; (b) modulus of the open loop transfer function. '*' unstable frequencies.
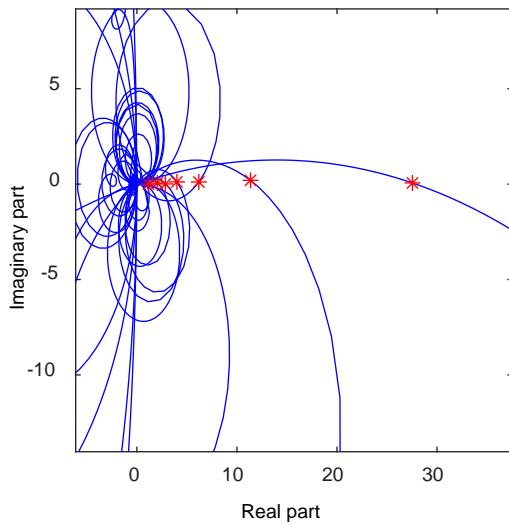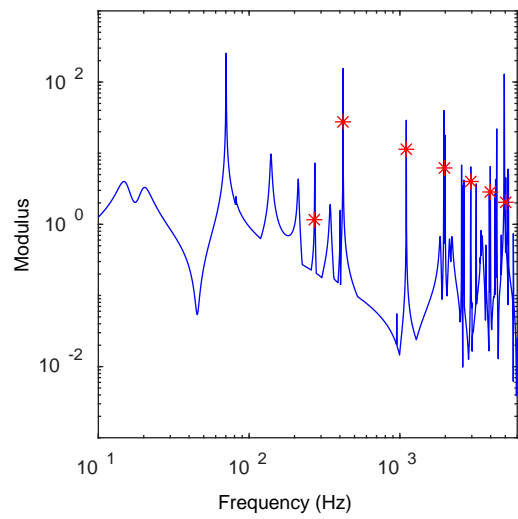
Figure 5-3. Results for Case II: Stability analysis of model excluding rail dynamics in frequency domain: (a) Nyquist locus; (b) modulus of the open loop transfer function. '*' unstable frequencies.
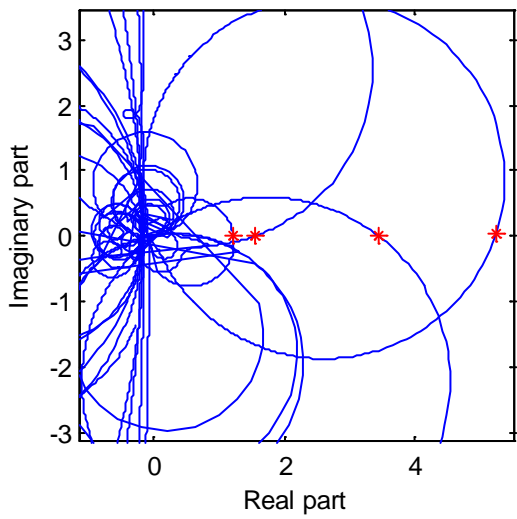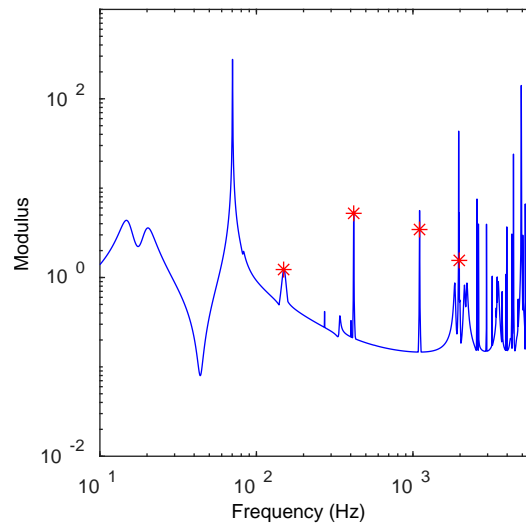
(a)   (b)

Figure 5-4. Results for Case III: Stability analysis of model including rail dynamics in frequency domain: (a) Nyquist locus; (b) modulus of the open loop transfer function. '*' unstable frequencies.
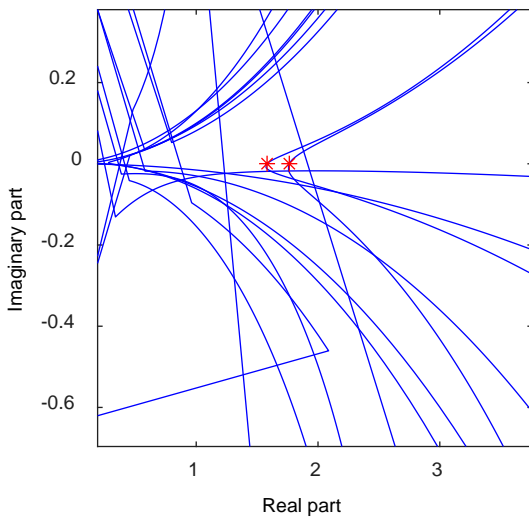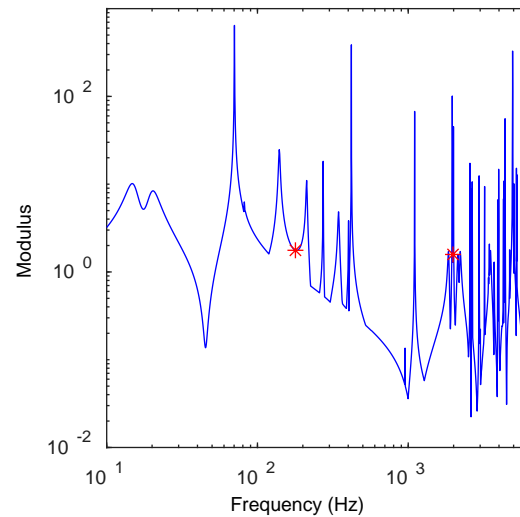
(a)   (b)

Figure 5-5. Results for Case V: Stability analysis of model including rail dynamics in frequency domain: (a) Nyquist locus; (b) modulus of the open loop transfer function. '*' unstable frequencies.

Table 5-4. Summary of frequency domain analysis for Cases I to V.

Case I (falling friction /rail included)	Unstable frequencies (Hz)	149.2	272.5	418.3	1102.0	1976.0	2951.0	3978.0	5032.0
	Loop gain	1.28	1.25	8.88	5.29	4.84	3.50	2.28	1.87
	Wheel modes involved (Hz)	149.4	272.5	418.3	1102.0	1976.2	2950.4	3977.4	5031.7
	(n, m)	(1,0)	(0,0)	(2,0)	(3,0)	(4,0)	(5,0)	(6,0)	(7,0)
Case II (falling friction/ rigid rail)	Unstable frequencies (Hz)		270.8	419.4	1102.0	1976.0	2951.0	3978.0	5032.0
	Loop gain		1.16	27.54	11.36	6.20	4.00	2.85	2.04
	Wheel modes involved (Hz)		272.5	418.3	1102.0	1976.2	2950.4	3977.4	5031.7
	(n, m)		(0,0)	(2,0)	(3,0)	(4,0)	(5,0)	(6,0)	(7,0)
Case III (constant friction /rail included)	Unstable frequencies (Hz)	149.2		418.4	1102.0	1977.0	.		
	Loop gain	1.23		5.22	3.44	1.55			
	Wheel modes involved (Hz)	149.4		418.3	1102.0	1976.2			
	(n, m)	(1,0)		(2,0)	(3,0)	(4,0)			
Case IV (constant friction / rigid rail)	stable								
Case V (constant friction /rail included)	Unstable frequencies (Hz)	178.6				1982.0			
	Loop gain	1.76				1.58			
	Wheel modes involved (Hz)	10, 15 149.4				1959.4 1976.2			
	(n, m)	Rigid modes (1,0)				(2, r) (4,0)			

5.3 Time domain analysis

The time histories of the response of the wheel and rail in different directions can be obtained by using step-by-step integration. Figure 5-6 shows the time history results for the lateral direction for different cases. Case IV is not shown as it is stable and would simply show a decaying trend. In each figure, the above subplot is the creepage (lateral velocity normalised by the rolling velocity) against the time. The below one is the corresponding spectra and they are evaluated over the limit cycle region using an FFT (fast Fourier transform) with a rectangular window and frequency resolution 2 Hz.
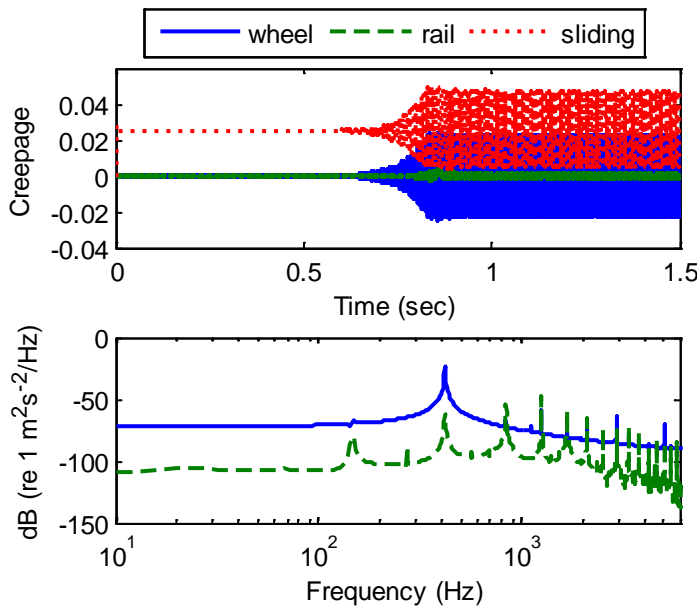
(a)
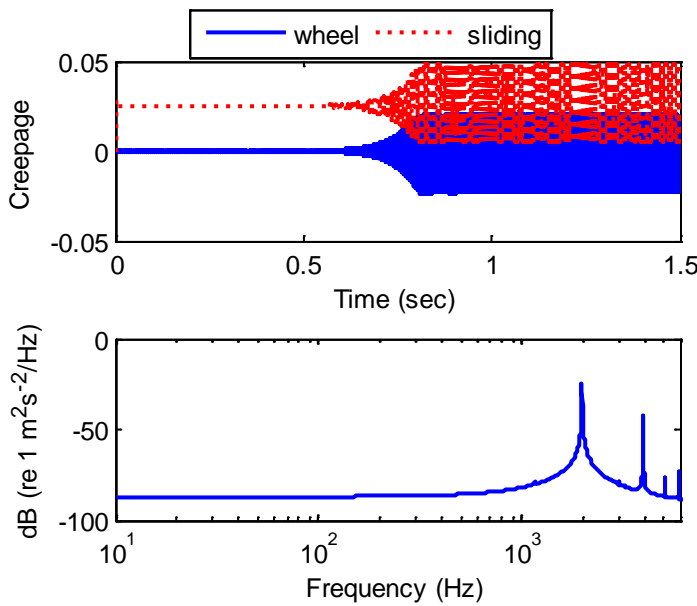
(b)
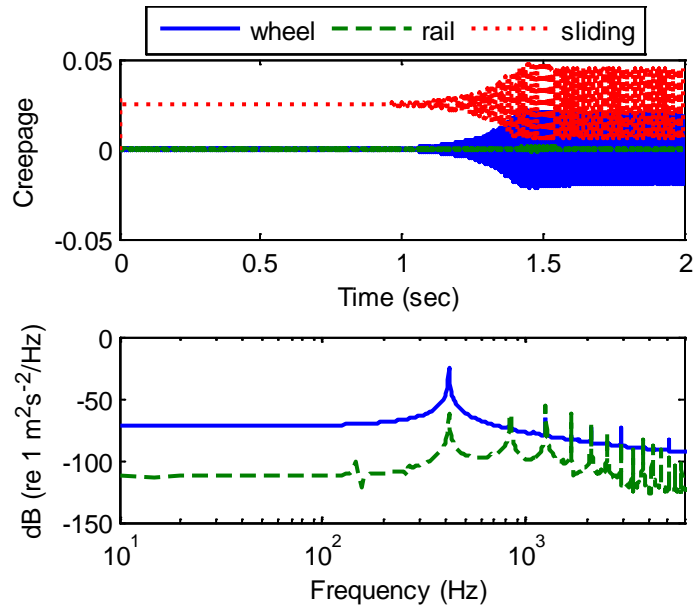
(c)
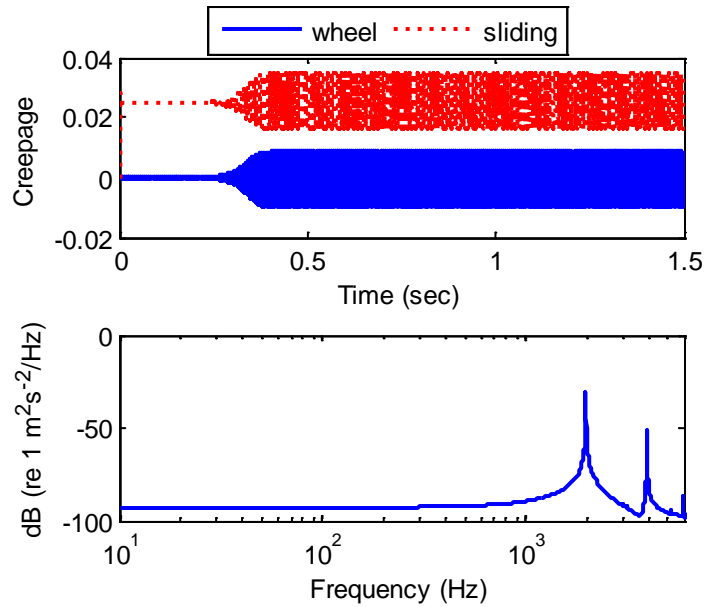
(d)

Figure 5-6 .Time histories: (a) Case I; (b) Case II; (c) Case III; (d) Case V.

The time histories for Case I show that a steady state response is obtained after 0.8 s. Moreover, it can be seen that for Cases I and III, the amplitude of vibration of the rail, when it is included, is much smaller than the response of the wheel. The ratio between the vibration amplitudes of the wheel and rail is about 9. The spectra show that, although several possible unstable frequencies were found in the frequency domain analysis, only one becomes dominant in the time domain. For Case I it is at 420 Hz which had the largest loop gain (but this is not always the case). Other peaks exist in the response spectrum and they are the higher harmonics of 420 Hz occurring due to non-linearities. The wheel vibration is close to sinusoidal at 420 Hz, showing the highest amplitude at this frequency, but the rail spectrum

can be greater than that of the wheel at the higher harmonics or at the frequencies of the rail modes.

The time histories for other Cases show similar characteristics. Meanwhile, it is found that the dominant frequency of the limit cycle can change when the rail is not included. For example, for Case II with a rigid rail, the dominant frequency is 1976 Hz whereas for Case I with a flexible track it is 420 Hz. Moreover, each of the dominant frequencies found here corresponds to one of those found in the frequency domain analysis in Table 5-4, although they are not necessarily the ones with the largest loop gain. For example, the largest loop gain in the frequency domain for Case II is 420 Hz whereas in the time domain analysis the dominant frequency of the limit cycle is 1976 Hz.

Figure 5-6 only gives the vibration in the lateral direction. In fact the vibration in the vertical direction shows similar characteristics. It also grows gradually and finally a limit cycle response is achieved. However, some interesting results can be found by comparing the vibration in the two directions. Figure 5-7 shows a comparison of the vibration in the limit cycle in the two directions for Case I and Case V. It can be seen that for Case I, which has an unstable frequency due to falling friction, the responses in the two directions are almost in phase. Meanwhile, for Case V, where wheel mode coupling exists, there is a phase difference (77˚) between the vibration in the two directions. This phase difference is a feature of mode coupling and has been introduced in Section 3.3.2. Further discussion of this phase shift in mode coupling will be given in Chapter 6.
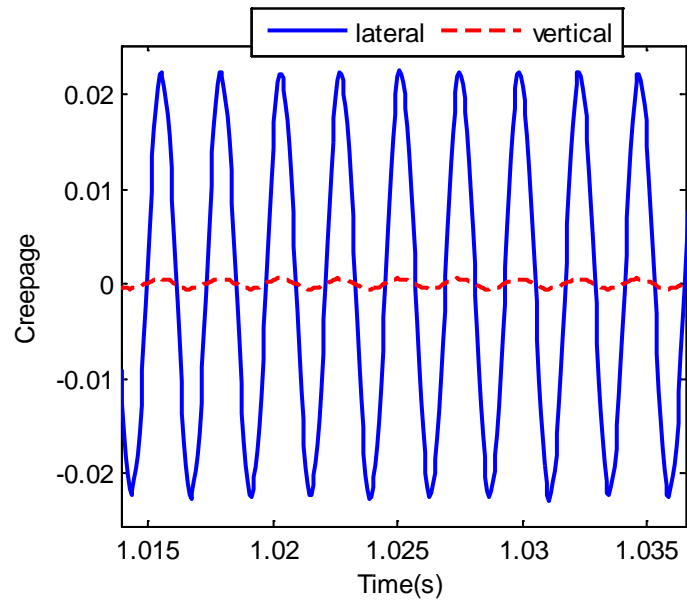
(a)
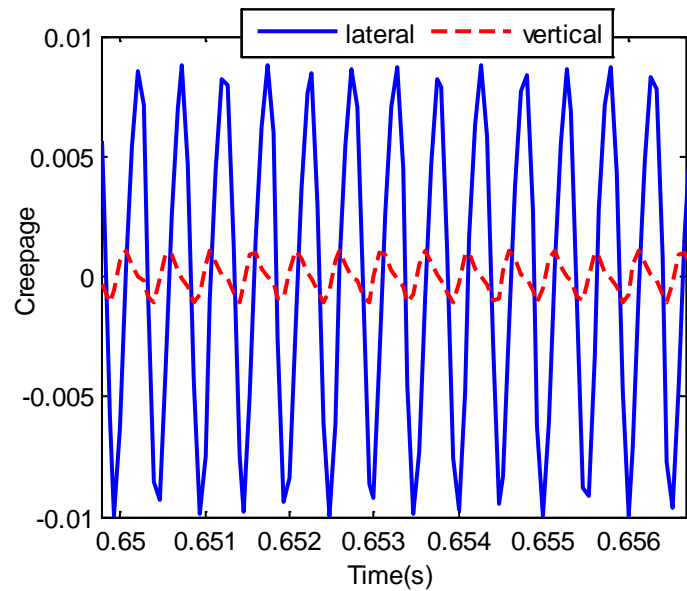
(b)

Figure 5-7. The close-up of the vibration at limic cycle in two directions: (a) Case I; (b) Case V.

5.4 The effects of wheel rotation

It was shown in Section 5.2 that in certain situations wheel mode coupling can lead to curve squeal (Case V). However, the wheel rotation has not been considered. In fact, when the wheel rolls along the track, the forcing point effectively moves around its circumference. This will make the natural frequencies of the wheel with one or more nodal diameters split

95

into pairs (these are also known as doublet modes) [103]. This section will investigate whether this splitting of wheel modes can affect the wheel coupling effect.

The theory describing the wheel rotation effect is described in [1] and is summarised in Appendix C. Here the wheel is assumed to have a rolling velocity of 10 m/s. The mobilities of the wheel in the lateral and vertical directions including the wheel rotation are shown in Figure 5-8 and Figure 5-9. Compared with Figure 4-5 to Figure 4-6, the modes with one or more nodal diameters are separated into dual peaks according to Eq. (C.18). For example, the axial mode at 1976 Hz is split into two peaks at 1961 and 1991 Hz (see Figure 5-8). The (2, r) radial mode at 1959 Hz is split into two peaks at 1952 Hz and 1967 Hz (see Figure 5-9).

To study whether this splitting of wheel modes affects the curve squeal prediction, the procedure and parameters of Case V in Section 5.2 are adopted here, replacing the wheel mobility with the one including the effect of wheel rotation. This is described as Case VI here. The unstable frequencies are shown in Table 5-5. The results of Case V are listed again for comparison. It can be seen from Table 5-5 that the wheel rotation does have an effect on the curve squeal. One more unstable frequency appears compared with the case without wheel rotation. However, the two modes within each doublet do not couple with each other; instead one of the doublet modes at 1959 Hz is coupling with one of the other doublet modes at 1976 Hz and the other modes in each doublet form another pair. Without wheel rotation, the two modes at 1959 Hz and 1976 Hz are coupled. Hence, the wheel rotation is considered to have no significant effect for this case.
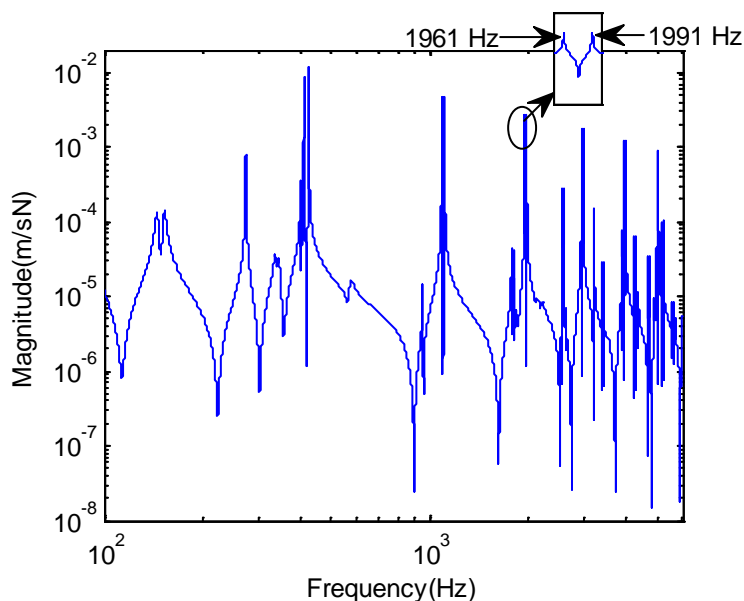
Figure 5-8. Class 158 wheel mobility in lateral direction including effect of wheel rotation.
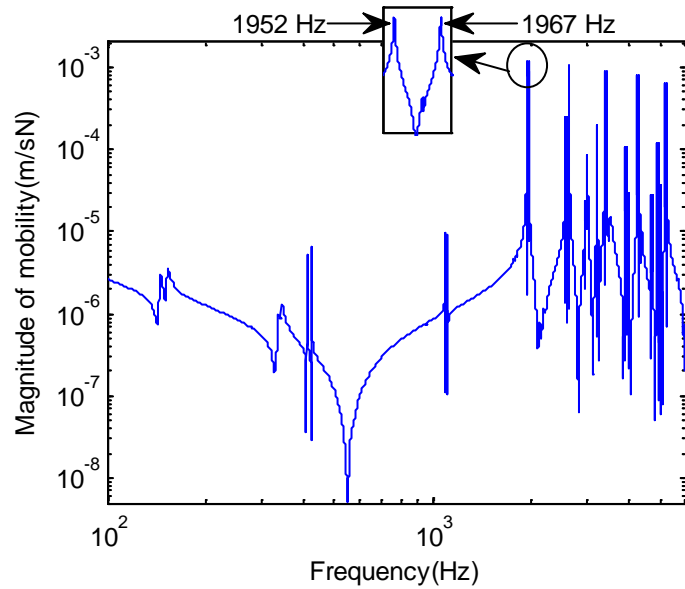
Figure 5-9. Class 158 wheel mobility in vertical direction including effect of wheel rotation.

Table 5-5. Frequency domain prediction with or without effect of wheel rotation.

Case V (without wheel rotation)	Unstable frequencies (Hz)	178.6		1982.0
	Loop gain	1.76		1.58
	Wheel modes involved (Hz)	10, 15 149.4		1959.4 1976.2
	(n, m)	Rigid modes (1,0)		(2, r) (4,0)
Case VI (including wheel rotation)	Unstable frequencies (Hz)	179.2	1959	1993
	Loop gain	1.78	1.37	5.38
	Wheel modes involved (Hz)	149.4	1952 1961	1967 1991
	(n, m)	(1,0)	(2,r) (4,0)	(2,r) (4,0)

Another wheel is considered here to investigate the effect of wheel rotation. This is also a regional train wheel but has brake discs mounted on the wheel web. The cross-section is shown in Figure 5-10. The mobility of this wheel in two directions is shown in Figure 5-11 and Figure 5-12, from which it can be seen that many of the modes are again split into two. For example, the axial mode at 3976 Hz splits into two peaks at 3954 Hz and 3999 Hz. The radial mode at 3963 Hz splits into two peaks at 3948 Hz and 3978 Hz. By using the same parameters as Case V and Case VI but with this different wheel, the curve squeal predictions in the frequency domain are given in Table 5-6 with and without effect of wheel rotation.
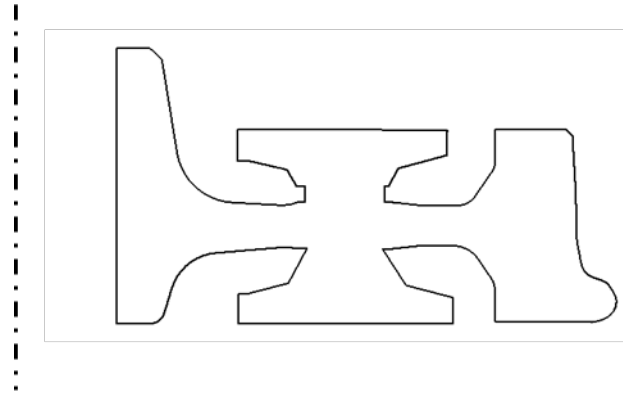
Figure 5-10. Cross-section of Coradia wheel (radius 420 mm).
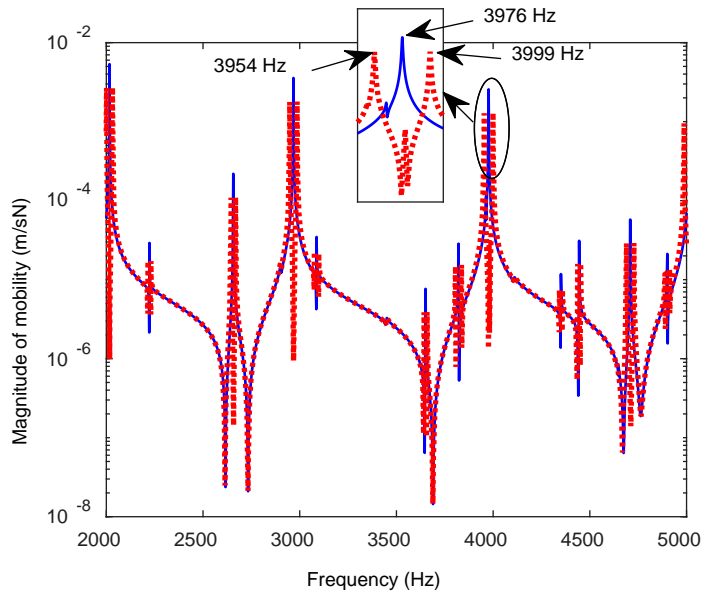
Figure 5-11. Coradia wheel mobility in lateral direction; blue solid line: without wheel rotation; red dotted line: with wheel rotation.
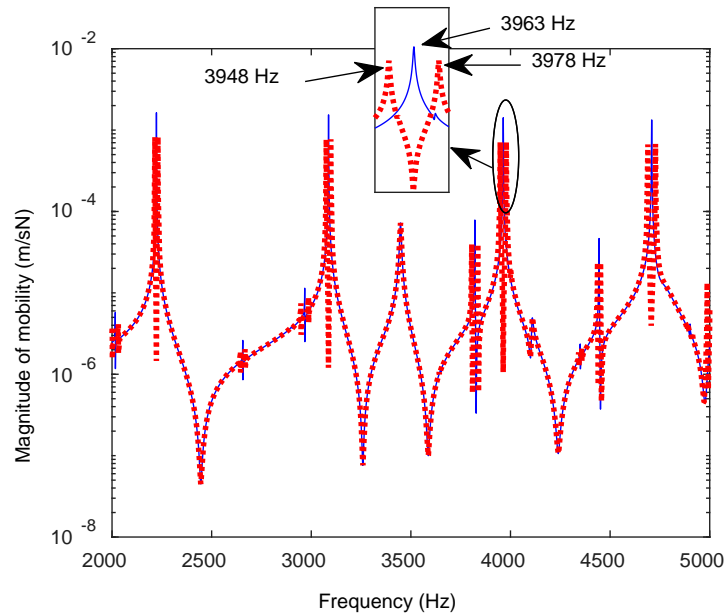
Figure 5-12. Coradia wheel mobility in vertical direction; blue solid line: without wheel rotation; red dotted line: with wheel rotation.

Table 5-6. Frequency domain prediction with or without effect of wheel rotation for Coradia wheel.

Coradia wheel (without wheel rotation)	stable		
Coradia wheel (including wheel rotation)	Unstable frequencies (Hz)	3955	3998
	Loop gain	1.46	4.30
	Wheel modes involved (Hz)	3954	3978
		3978	3999
	(n, m)	(4,r)	(4,r)
		(6,0)	(6,0)

It can be seen from Table 5-6 that when wheel rotation is not included the result is always stable whereas there are two unstable frequencies when including wheel rotation. This shows that wheel rotation has a significant effect for this case. In addition, for the unstable frequency at 3955 Hz, the two responsible wheel modes are 3954 Hz (one doublet of the 3976 Hz mode) and 3978 Hz (one doublet of the 3963 Hz mode). For the unstable frequency at 3998 Hz, the two responsible wheel modes are 3999 Hz (again one doublet of the 3976 Hz mode) and 3978 Hz (one doublet of the 3963 Hz mode). Hence, the coupled wheel modes are not the doublets of one mode, but instead one of the doublets is coupled with one of another doublets. This is similar to the case above (Case V and Case VI).

Hence, the results here indicate that the wheel rotation has a different effect on different wheels. Mode coupling can arise between modes of different doublets while the corresponding modes of the non-rotating wheel are not necessarily unstable.

5.5 The effects of rolling velocity

For all the cases calculated above, the rolling velocity is equal to 10 m/s. In this section, the effect of rolling velocity is investigated by changing it to 15 m/s and 20 m/s and then comparing the results to those above. Both non-rotating and rotating wheels are considered in this section.

5.5.1 Non-rotating wheel

First, a non-rotating wheel is adopted, which is again the Class158 wheel. To study whether the rolling velocity affects the curve squeal prediction, the procedure and parameters of Case I in Section 5.2 are adopted here but with different rolling velocities of 15 m/s and 20 m/s. For the cases with constant friction, it can be deduced from Eqs. (4-42) to (4-48) that the rolling velocity will not affect the results as the slope of friction curve is zero in Eq. (4-42).

The frequency domain results are summarized in Table 5-7. When the rolling velocity is increased from 10 m/s to 15 m/s, only one unstable frequency at 272.5 Hz disappears while all other unstable frequencies remain. The loop gains reduce slightly with increasing rolling velocity. Hence, the rolling velocity is considered to have insignificant effect on curve squeal with this non-rotating wheel.

Table 5-7. Frequency domain prediction with different rolling velocity with a non-rotating wheel.

Case I (falling friction /rail included) with rolling velocity 10 m/s	Unstable frequencies (Hz)	149.2	272.5	418.3	1102.0	1976.0	2951.0	3978.0	5032.0
	Loop gain	1.28	1.25	8.88	5.29	4.84	3.50	2.28	1.87
	Wheel modes involved (Hz)	149.4	272.5	418.3	1102.0	1976.2	2950.4	3977.4	5031.7
	(n, m)	(1,0)	(0,0)	(2,0)	(3,0)	(4,0)	(5,0)	(6,0)	(7,0)
Case I with rolling velocity 15 m/s	Unstable frequencies (Hz)	149.2		418.3	1102.0	1976.0	2951.0	3978.0	5032.0
	Loop gain	1.23		7.53	4.59	3.66	2.49	1.74	1.35
	Wheel modes involved (Hz)	149.4		418.3	1102.0	1976.2	2950.4	3977.4	5031.7
	(n, m)	(1,0)		(2,0)	(3,0)	(4,0)	(5,0)	(6,0)	(7,0)
Case I with rolling velocity 20 m/s	Unstable frequencies (Hz)	149.2		418.3	1102.0	1976.0	2951.0	3978.0	5032.0
	Loop gain	1.21		6.86	4.17	3.13	2.06	1.42	1.11
	Wheel modes involved (Hz)	149.4		418.3	1102.0	1976.2	2950.4	3977.4	5031.7
	(n, m)	(1,0)		(2,0)	(3,0)	(4,0)	(5,0)	(6,0)	(7,0)

5.5.2 Rotating wheel

When wheel rotation is considered, the rolling velocity can affect the frequency split according to Appendix C. Hence, the effect of the rolling velocity under constant friction with a rotating wheel is investigated in this section. Case VI from Section 5.4 is adopted here but with the rolling velocity changing from 10 m/s to 15 m/s and 20 m/s. The frequency domain results are summarised in Table 5-8. The natural frequencies of the doublet modes for some modes related with the unstable frequencies are given in Table 5-9.

From Table 5-8 it can be found that the rolling velocity has an effect on the curve squeal with a rotating wheel. When the rolling velocity is 15 m/s, one more unstable frequency at 3941 Hz appears compared with the results for 10 m/s. However, again the two modes within each doublet do not couple with each other; instead one of the doublet modes at 3915 Hz is coupling with one mode of the other doublet modes at 3977 Hz. When the rolling velocity is increased to 20 m/s, the unstable frequencies at 1954 and 3941 Hz disappear. This could be because of the change of the natural frequencies of the doublet modes at the corresponding wheel modes.

Table 5-8. Frequency domain prediction with different rolling velocity with a rotating wheel.

Case VI (including wheel rotation) rolling velocity 10 m/s	Unstable frequencies (Hz)	179.2	1959	1993	
	Loop gain	1.78	1.37	5.38	
	Wheel modes involved (Hz)	149.4	1952 1961	1967 1991	
	(n, m)	(1,0)			
Case VI with rolling velocity 15 m/s	Unstable frequencies (Hz)	180.1	1954	1999	3941
	Loop gain	1.80	3.35	6.53	2.21
	Wheel modes involved (Hz)	149.4	1948 1954	1970 1998	3938 3943
	(n, m)	(1,0)			
Case VI with rolling velocity 20 m/s	Unstable frequencies (Hz)	181	2004		
	Loop gain	1.83	3.63		
	Wheel modes involved (Hz)	149.4	1974 2006		
	(n, m)	(1,0)			

Table 5-9. The natural frequencies (in Hz) of the doublet modes with different rolling velocities.

Natural frequencies (Hz) (n, m)	10 m/s	15 m/s	20 m/s
1959 (2, r)	1952 and 1967	1948 and 1970	1944 and 1974
1976 (4, 0)	1961 and 1991	1954 and 1998	1946 and 2006
3915 (4, 1)	3900 and 3930	3892 and 3938	3885 and 3945
3977 (6, 0)	3954 and 4000	3943 and 4011	3932 and 4023

5.6 Summary

In this chapter, the curve squeal model presented in Chapter 4 is employed to perform frequency domain and the time domain analyses for an example wheel under different conditions. Results show that both falling and constant friction can lead to squeal due to different origins of the instabilities. Also, track dynamics can play an important role in curve squeal. Consequently three mechanisms have been identified: falling friction, wheel mode coupling and wheel/rail coupling. A more detailed investigation for the latter two mechanisms is performed in the next two chapters.

It is also found that inclusion of wheel rotation can have different effects on different wheels and can introduce instability where a non-rotating wheel may be stable. The effect of rolling velocity is found to have an influence on the curve squeal when a rotating wheel is considered.

6 Investigation of mode coupling effect based on a two-mode model

As introduced in the literature review, wheel mode coupling is a possible mechanism for curve squeal in addition to the traditional falling friction mechanism. Moreover, in Section 5.2 it has been shown that for Case V with constant friction and in the absence of track dynamics, instability still exist due to the coupling of two wheel modes. In this chapter, this mode coupling mechanism will be investigated by making use of a simplified two-mode model. This model is based on the model described in Section 3.3.1 (also in [38]). Different modes from different wheels are considered within this model. These wheels include a regional train wheel (Class 158 considered in Chapter 5), a wheel from a freight train and a resilient wheel from a tram. Parametric studies are performed including varying the adhesion coefficient, contact angle, lateral offset, and wheel damping. The effect of including falling friction is also studied. Some characteristics of the wheel response in the presence of the mode coupling instability are also presented. One is the frequency shift: the squealing frequency and the wheel natural frequency are different; the other is phase difference between the vibration in the axial and radial directions. Wheel vibration measurements of a squealing tram wheel [60] are analysed and qualitatively compared with the model to identify these features.

6.1   Description of the wheel/rail interaction model

The wheel is modelled through a modal approach; the modal parameters, i.e. mode shapes (ϕ_i) and natural frequencies (ω_i), are extracted from an axisymmetric finite element model. Modal damping ratios (ζ_i) are included according to prior experience [1] or from measurements of wheel mobilities, where available (i.e. for the tram wheel). At the contact point the interaction with the rail is assumed to excite the wheel in two directions: normal and tangential to the contact plane; the other directions are ignored. The contact in the normal direction is represented by a linearized contact spring while the lateral forces are modelled through creep forces with saturation and a possible falling regime at high creepages, as described in Section 2.4.2. Figure 6-1 shows a schematic representation of the system as considered here. The physical coordinates x and y are used to represent the lateral and vertical directions, while t and n represent the directions tangential and normal to the contact plane, forming a coordinate system rotated by an angle α with respect to x-y. In the context of

wheel-rail contact the angle α represents the direction of the plane tangential to the wheel and rail surfaces at the contact point relative to the lateral direction. In this simplified model the track is not included; for simplicity it is assumed to be rigid throughout this chapter. The motion of the belt in Figure 6-1 represents the sliding velocity in the transverse direction on the wheel (not the rolling velocity).

(a)   (b)
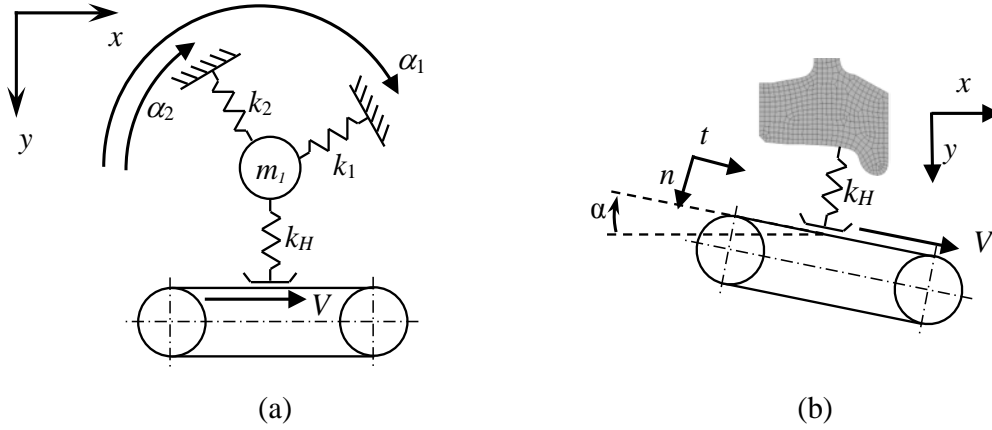
Figure 6-1. Two degree-of-freedom system on moving belt and its analogue to wheel/rail system.

For small amplitude vibration around the steady-state condition, the equations of motion in modal coordinates are:

$$\mathbf{I}\ddot{\mathbf{q}} + \mathbf{C}_q\dot{\mathbf{q}} + \mathbf{K}_q\mathbf{q} = \mathbf{\Phi}^{\mathrm{T}}\begin{Bmatrix} f_x \\ f_y \end{Bmatrix} = \mathbf{\Phi}^{\mathrm{T}}\mathbf{R}\begin{Bmatrix} f_t \\ f_n \end{Bmatrix} \qquad (6\text{-}1)$$

where $\mathbf{I}$ is the identity matrix; the modal damping matrix $\mathbf{C}_q$ and modal stiffness matrix $\mathbf{K}_q$ are diagonal with diagonal terms equal to $2\zeta_i\omega_i$ and ω_i^2 respectively. $\mathbf{\Phi}$ is the mode shape matrix and $\mathbf{R}$ represents a rotation matrix to transform the dynamic forces from directions tangential and normal to the contact $(f_t$ and $f_n)$ into the x and y directions. This transformation can be found in Appendix B. The modal coordinate transformation is defined as

$$\mathbf{q} = \mathbf{\Phi}^{\mathrm{T}}\begin{Bmatrix} u_x \\ u_y \end{Bmatrix} \qquad (6\text{-}2)$$

with u_x and u_y representing the dynamic displacements at the contact point in the x and y directions.

The forces in the right-hand term in Eq. (6-1) are themselves dependent on the displacement and velocity at the contact point. The system therefore does not consist of independent equations, despite being written in modal coordinates. It is required to solve the forcing terms

and will constitute the coupling between the modes considered and form a possible source of instability.

In the normal direction n, linearized Hertzian contact theory can be applied for small amplitudes of displacement [1]. The dynamic component of the normal force f_n can be expressed through the contact stiffness as:

$$f_n = -k_H u_n \tag{6-3}$$

where u_n is the dynamic displacement in the normal direction and k_H is the linearized Hertz contact stiffness in the normal direction (see Section 2.4.1).

The creep force is calculated as the product of the adhesion coefficient μ and the normal force N. In general the adhesion coefficient itself depends on both the sliding velocity and the normal load [26] but, in this simplified formulation, the dependence on the normal load is neglected. Hence, according to Eq. (4-41) the dynamic component of the creep force f_t can be found from

$$f_t \cong \mu(\gamma_0) f_n + \frac{\partial \mu}{\partial \gamma_0} \frac{N_0}{V_0} v_t \tag{6-4}$$

where the subscript 0 denotes the quasi-static quantities evaluated at the steady-state condition, V_0 is the rolling velocity and v_t is the sliding velocity in the tangential direction. Previous studies have shown that occurrence of squeal is dependent on the angle of attack (see e.g. [56, 66]). In this modelling approach, however, if a constant friction coefficient is considered and the angle of attack is large enough for the creep-adhesion curve to be in the saturated region, the actual value of the angle of attack is no longer important for stability. When including falling friction, the angle of attack is important in the whole creepage range as it affects the slope of the friction curve.

Introducing a modal coordinate transformation, the dynamic force vector becomes:

$$
\begin{aligned}
\begin{Bmatrix} f_t \\ f_n \end{Bmatrix} &= \begin{Bmatrix} \dfrac{\partial \mu}{\partial \gamma_0} \dfrac{N_0}{V} \\ 0 \end{Bmatrix} v_t + \begin{Bmatrix} (-\mu(\gamma_0) k_H) \\ -k_H \end{Bmatrix} u_n \\
&= \begin{bmatrix} \dfrac{\partial \mu}{\partial \gamma_0} \dfrac{N_0}{V} & 0 \\ 0 & 0 \end{bmatrix} \mathbf{R}^T \mathbf{\Phi} \dot{\mathbf{q}} + \begin{bmatrix} 0 & -\mu(\gamma_0) k_H \\ 0 & -k_H \end{bmatrix} \mathbf{R}^T \mathbf{\Phi} \mathbf{q}
\end{aligned}
\tag{6-5}
$$

Then the right hand term of Eq.(6-1) becomes:

$$\boldsymbol{\Phi}^{\mathrm{T}} \begin{Bmatrix} f_x \\ f_y \end{Bmatrix} = \boldsymbol{\Phi}^{\mathrm{T}} \mathbf{R} \begin{bmatrix} \dfrac{\partial \mu}{\partial \gamma_0} \dfrac{N_0}{V} & 0 \\ 0 & 0 \end{bmatrix} \mathbf{R}^{\mathrm{T}} \boldsymbol{\Phi} \dot{\mathbf{q}} + \boldsymbol{\Phi}^{\mathrm{T}} \mathbf{R} \begin{bmatrix} 0 & -\mu(\gamma_0) k_H \\ 0 & -k_H \end{bmatrix} \mathbf{R}^{\mathrm{T}} \boldsymbol{\Phi} \mathbf{q}$$

$$= \mathbf{C}_{qF} \dot{\mathbf{q}} + \mathbf{K}_{qF} \mathbf{q}$$

(6-6)

The overall linearized equation of motion can then be formulated as:

$$\mathbf{I} \ddot{\mathbf{q}} + \left(\mathbf{C}_q - \mathbf{C}_{qF} \right) \dot{\mathbf{q}} + \left(\mathbf{K}_q - \mathbf{K}_{qF} \right) \mathbf{q} = 0 \tag{6-7}$$

where the sizes of the matrices $\mathbf{C}_q$, $\mathbf{C}_{qF}$, $\mathbf{K}_q$, $\mathbf{K}_{qF}$ are $N_m \times N_m$ where N_m is the number of modes considered in the model. Unless otherwise stated, for all calculations presented in this chapter, only two modes are considered and the effect of other modes is neglected. This simplification is verified in Section 6.4.5, where, for some of the cases analysed, the effect of including other modes is also investigated. When only two modes are included, $\mathbf{K}_{qF}$ and $\mathbf{C}_{qF}$ can be expanded as:

$$\mathbf{K}_{qF} = \begin{bmatrix} -\phi_{t1}\phi_{n1}\mu(\gamma_0)k_H - \phi_{n1}^2 k_H & -k_H\phi_{n2}(\phi_{t1}\mu(\gamma_0)+\phi_{n1}) \\ -k_H\phi_{n1}(\phi_{t2}\mu(\gamma_0)+\phi_{n2}) & -\phi_{t2}\phi_{n2}\mu(\gamma_0)k_H - \phi_{n2}^2 k_H \end{bmatrix} \tag{6-8}$$

$$\mathbf{C}_{qF} = \begin{bmatrix} \phi_{t1}^2 \dfrac{\partial \mu}{\partial \gamma_0} \dfrac{N_0}{V_0} & \phi_{t1}\phi_{t2} \dfrac{\partial \mu}{\partial \gamma_0} \dfrac{N_0}{V_0} \\ \phi_{t1}\phi_{t2} \dfrac{\partial \mu}{\partial \gamma_0} \dfrac{N_0}{V_0} & \phi_{t2}^2 \dfrac{\partial \mu}{\partial \gamma_0} \dfrac{N_0}{V_0} \end{bmatrix} \tag{6-9}$$

where the effect of the coordinate rotation, $\mathbf{R}$, has been included by rotating the mode shapes instead of the forces as:

$$\boldsymbol{\Phi}^{\mathrm{T}} \mathbf{R} = \begin{bmatrix} \phi_{t1} & \phi_{n1} \\ \phi_{t2} & \phi_{n2} \end{bmatrix} \tag{6-10}$$

Here ϕ_{t1}, ϕ_{t2} are the mode shapes of the first and second modes in the tangential direction, while ϕ_{n1}, ϕ_{n2} are the corresponding mode shapes in the normal direction.

Thus, the total stiffness matrix can be written as:

$$\mathbf{K}_{\mathrm{tot}} = \mathbf{K}_q - \mathbf{K}_{qF} = \begin{bmatrix} K_{11} & K_{12} \\ K_{21} & K_{22} \end{bmatrix} \tag{6-11}$$

with

$$K_{11} = \omega_1^2 + \phi_{t1}\phi_{n1}\mu(\gamma_0)k_H + \phi_{n1}^2 k_H \tag{6-12}$$

$$K_{12} = k_H\phi_{n2}(\phi_{t1}\mu(\gamma_0) + \phi_{n1}) \tag{6-13}$$

$$K_{21} = k_H\phi_{n1}(\phi_{t2}\mu(\gamma_0) + \phi_{n2}) \tag{6-14}$$

$$K_{22} = \omega_2^2 + \phi_{t2}\phi_{n2}\mu(\gamma_0)k_H + \phi_{n2}^2 k_H \tag{6-15}$$

6.2 Stability analysis

There are several factors in Eqs. (6-11) to (6-15) that can affect the values of the upper and lower off-diagonal terms of the total stiffness matrix and therefore the stability of this system. These are the directions and the amplitudes of the rotated mode shapes, the directions of the friction forces, the value of the adhesion coefficient and the contact stiffness. Also, it can be seen from Eq. (6-9) that the slope of the friction characteristic $\frac{\partial\mu}{\partial\gamma_0}$ in the matrix $\mathbf{C}_{qF}$ can modify the total damping matrix $(\mathbf{C}_q - \mathbf{C}_{qF})$.

The stability of the system is studied in this chapter by analysing the eigenvalues of Eq. (6-7). Instability occurs when one of the eigenvalues has a positive real part.

Alternatively, the analytical expressions of the Routh–Hurwitz coefficients [94, 104] can be adopted to show how the different elements of the stiffness and damping matrix need to be combined together for the system to be unstable. The characteristic equation of the system under constant friction (i.e. $\mathbf{C}_{qF} = \mathbf{0}$) is:

$$\lambda^4 + (c_1 + c_2)\lambda^3 + (K_{11} + K_{22} + c_1c_2)\lambda^2 + (c_1K_{22} + c_2K_{11})\lambda + K_{11}K_{22} - K_{12}K_{21} = 0 \tag{6-16}$$

where λ are the eigenvalues of the system; $K_{11}, K_{12}, K_{21}, K_{22}$ can be found from Eq. (6-12) to Eq. (6-15) while c_1 and c_2 are equal to $2\zeta_1\omega_1$ and $2\zeta_2\omega_2$ respectively.

According to the Routh–Hurwitz criterion [94, 104], the system is stable if all the following coefficients are positive:

$$H_1 = c_1 + c_2 \tag{6-17}$$

$$H_2 = K_{11}c_1 + c_1^2c_2 + K_{22}c_2 + c_1c_2^2 \tag{6-18}$$

$$H_3 = (c_1 K_{11} + c_1^2 c_2 + c_2 K_{22} + c_1 c_2^2)(c_1 K_{22} + c_2 K_{11}) - (c_1 + c_2)^2 (K_{11} K_{22} \\ - K_{12} K_{21}) \tag{6-19}$$

$$\begin{aligned} H_4 &= K_{11} K_{22} - K_{12} K_{21} \\ &= \omega_1^2 \omega_2^2 + \omega_1^2 \phi_{t2} \phi_{n2} \mu(\gamma_0) k_H + \omega_1^2 \phi_{n2}^2 k_H \\ &+ \omega_2^2 \phi_{t1} \phi_{n1} \mu(\gamma_0) k_H + \omega_2^2 \phi_{n1}^2 k_H \end{aligned} \tag{6-20}$$

When at least one of the coefficients H_i is negative, this system is unstable. It is clear that H_1 is always positive as the damping ratios of the two modes are positive. A necessary condition for H_2 to be negative is that K_{11} and/or K_{22} are negative. However in railway applications they are usually positive for modes above 500 Hz. This can be illustrated as follows, if in Eq. (6-12), k_H is assumed to be in the order of 10^9 N/m and μ is set to 1, the sign depends on the value of the mass normalised mode shapes in relation to the circular frequency squared. By means of the FE model it is found that the magnitude of the mass-normalised mode shape at the contact point is less than 0.15 for all the modes of all the wheels analysed in this chapter. Given this constraint, K_{11} and K_{22} are positive above 500 Hz. Following similar reasoning, H_4 can be found to be always positive above 500 Hz.

Hence, the stability of the system above 500 Hz is governed only by H_3 and the system is unstable if:

$$K_{12} K_{21} < K_{11} K_{22} - \frac{(c_1 K_{11} + c_1^2 c_2 + c_2 K_{22} + c_1 c_2^2)(c_1 K_{22} + c_2 K_{11})}{(c_1 + c_2)^2} \tag{6-21}$$

The right-hand side of the above inequality can be simplified as:

$$\frac{-c_1 c_2 (K_{11} - K_{22})^2 - c_1^3 c_2 K_{22} - c_1^2 c_2^2 K_{22} - c_1 c_2^3 K_{11}}{(c_1 + c_2)^2} \tag{6-22}$$

which is always negative. Therefore a necessary condition for instability is that K_{12} and K_{21} have different signs.

The stability of the system is then defined by any possible combination of the physical variables that satisfies Eq. (6-21). In particular, these variables are: (i) the mode shapes at the contact point, (ii) the natural frequencies, (iii) the damping ratios, (iv) the adhesion coefficient and (v) the contact stiffness. Eq. (6-21) can be used, as an alternative to the eigenvalue analysis, to study the stability of the system and can provide, in some cases, a clearer physical understanding of the problem; an example is shown below in Section 6.4.3.

However, in general, all five parameters play a combined role and need to be analysed together.

6.3   Description of the cases studied

Different pairs of modes from different wheels are considered as examples. As well as the wheel considered in Chapter 5 (Class158), a wheel from a freight train and a resilient wheel from a tram are also considered. Their cross-sections are shown in Figure 6-2. The FE model of regional train wheel and the resilient wheel are from previous studies [27, 31]. The FE model of the freight train wheel is developed here. ANSYS Finite Element (FE) software is used for the FE analysis. Only the cross-section is modelled and the element used here is Plane83, which is used for 2-D modelling of axi-symmetric structures with non-axisymmetric loading. The translations for three degree of freedom (X, Y, and Z) are constrained at the inner edge of the wheel hub. The total element number is 591 and the element size is approximately 5 mm. To select the pairs of modes for use in the parametric study, some preliminary calculations have been performed by making use of the model introduced in Chapter 4.

| (a) | (b) | (c) |
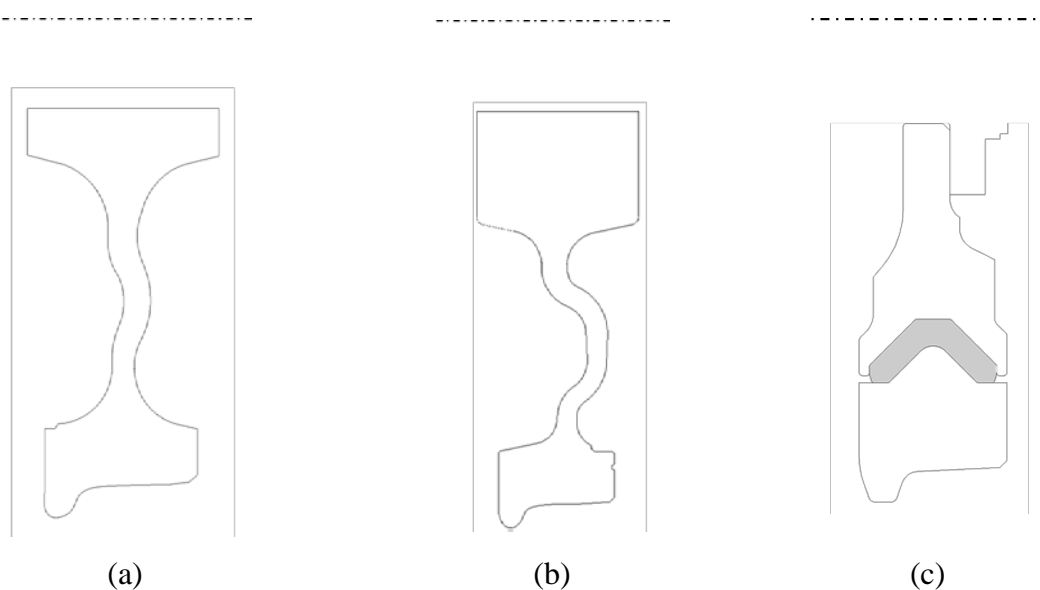
Figure 6-2. Cross-sections for the wheels considered. (a) UK Class 158 regional train wheel for Case 1, radius 420 mm; (b) freight train wheel type BA319 for Case 2, radius 460 mm; (c) resilient tram wheel for Cases 3, 4 and 5, radius 330 mm.

Five cases have finally been selected and they are summarised in Table 6-1. These are not the only possible unstable modes but are selected either because they were related to measured squealing frequencies (Cases 3-5) or are just taken as examples (Cases 1-2). There are some other unstable frequencies in these wheels which are due to the coupling between

rigid modes with low frequency modes. These are not discussed here. Case 1 is the pair of modes found to exhibit mode coupling in Chapter 4.4. Case 2 is formed of a pair of modes from a freight train wheel of type BA319. Cases 3, 4 and 5 consist of three different pairs of modes from the same resilient tram wheel. In these last three cases the Finite Element (FE) model developed and validated in [31] has been adopted and the modal damping ratios have been obtained from measurements, while the parameters representing the rubber elements in the FE model have been updated in [60] so that the natural frequencies and modal damping ratios could match those found in measured data. The radial and axial mobilities of this wheel up to 5 kHz at the nominal contact point are shown in Figure 6-3, in which the FE results (after model tuning) are compared with measured data.

The mode shapes of the chosen modes and their vector representations at the nominal contact point are shown in Figure 6-4 to Figure 6-6. For Case 3 the presence of the rubber layer in the resilient wheel makes it more difficult to assign a simple description to the mode shape based on the numbers of nodal diameters and nodal circles. With the normalisation applied in the FE model, the modal masses of the selected modes are all equal to 0.5 kg.

In all the calculations performed for this chapter, the wheel is assumed to be the left-hand wheel of a leading wheelset of a bogie, while the curve can be a left-hand or right-hand curve depending on whether the inner or outer wheel is considered. For the left-hand wheel, the contact angle is assumed to be always positive (see Figure 6-1) and the steady-state creepage is always positive for a right-hand curve and negative for a left-hand curve.

Table 6-1. Parameters of two-mode model used for different cases

		(n,m)	Natural frequency (Hz)	Mode shape at nominal contact point (normal direction) (m)	Mode shape at nominal contact point (axial direction) (m)	Rotation mode shape about longitudinal direction (rad)	Original Damping ratio
Case 1	Lower mode	(2, r)	1959	5.4×10^{-2}	-3.5×10^{-3}	-3.1×10^{-1}	1.0×10^{-4}
	Higher mode	(4, 0)	1976	6.2×10^{-3}	-8.2×10^{-2}	-6.2×10^{-1}	1.0×10^{-4}
Case 2	Lower mode	(3, r)	1983	5.5×10^{-2}	2.1×10^{-2}	1.4×10^{-1}	1.0×10^{-4}
	Higher mode	(1, 2)	1993	2.7×10^{-3}	3.5×10^{-2}	1.1×10^{0}	1.0×10^{-2}
Case 3	Lower mode	(4, 1)	2474	-6.8×10^{-2}	-1.1×10^{-1}	-9.5×10^{-1}	4.2×10^{-3}
	Higher mode	$n =1$; See Figure 6-3	2536	1.5×10^{-2}	7.9×10^{-2}	3.5×10^{0}	5.9×10^{-3}
Case 4	Lower mode	(4, 0)	2223	8.1×10^{-2}	-7.9×10^{-2}	-6.0×10^{-1}	5.0×10^{-3}
	Higher mode	(4, 1)	2474	-6.8×10^{-2}	-1.1×10^{-1}	-9.5×10^{-1}	4.2×10^{-3}
Case 5	Lower mode	(3, 0)	1271	6.0×10^{-2}	-1.0×10^{-1}	-7.2×10^{-1}	7.2×10^{-3}
	Higher mode	(3, 1)	1417	-8.7×10^{-2}	-8.0×10^{-2}	-6.4×10^{-1}	1.2×10^{-2}
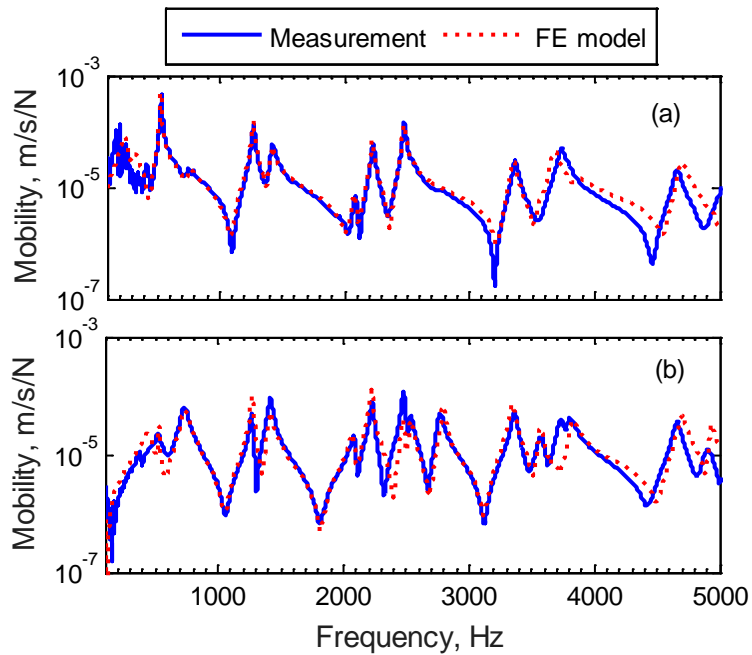
Figure 6-3. Tram wheel mobilities at nominal contact point: (a) axial direction; (b) radial direction.
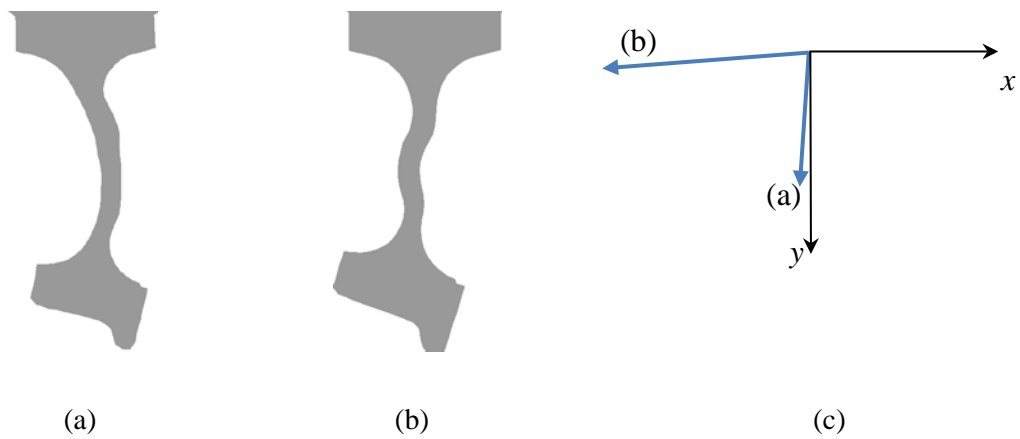
Figure 6-4. Mode shapes of Class 158 wheel (a) *n*=2 at 1959 Hz; (b) *n*=4 at 1976 Hz; (c) mode shape vectors for mode (a) and mode (b) at nominal contact point.
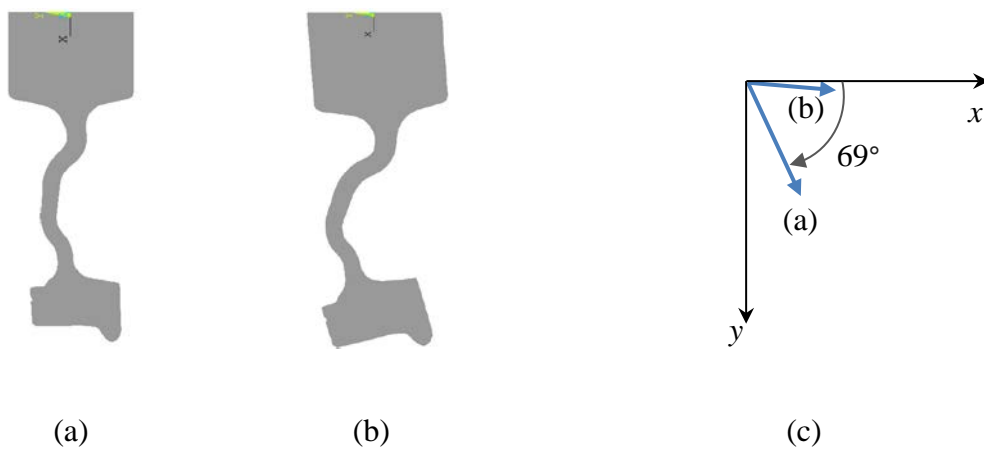
Figure 6-5. Mode shapes of BA319 freight wheel (a) *n*=3 at 1983 Hz; (b) *n*=1 at 1993 Hz; (c) mode shape vectors for mode (a) and mode (b) at nominal contact point.
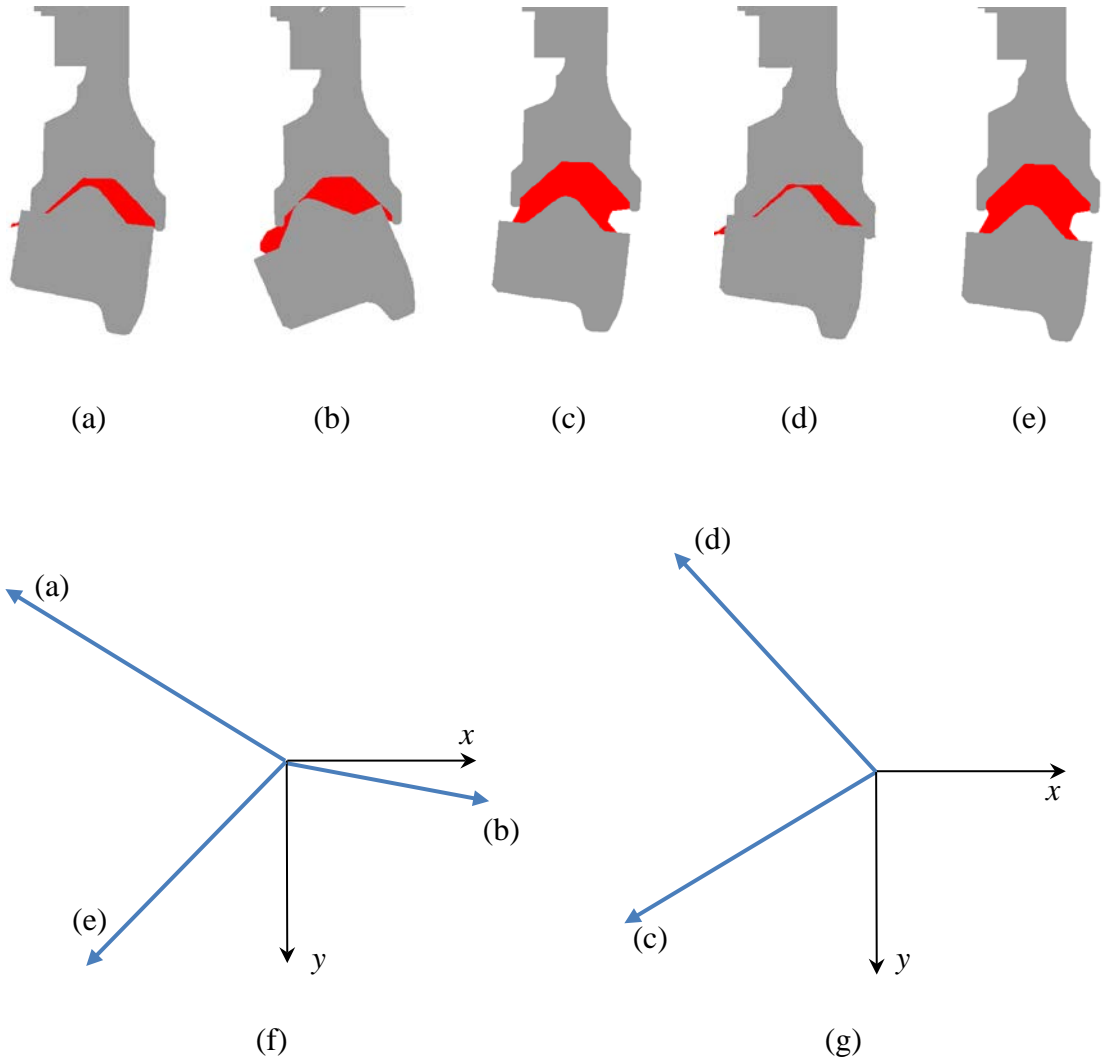
Figure 6-6. Mode shapes of resilient wheel (a) $n=4$ at 2476 Hz; (b) $n=1$ at 2536 Hz; (c) $n=3$ at 1271 Hz; (d) $n=3$ at 1417 Hz; (e) $n=4$ at 2223 Hz; (f) mode shape vectors for modes (a), (b) and (e) at nominal contact point; (g) mode shape vectors for modes (c) and (d) at nominal contact point.

6.4   Frequency-domain results from two-mode model

Results from the frequency-domain model are shown in this section by evaluating the real part of the eigenvalues; positive values indicate instability. Results are presented as a function of the quasi-static adhesion coefficient $\mu(\gamma_0)$, as well as the lateral offset of the contact position Δ_x , the contact angle α, the damping ratio ζ_i. Although these parameters are not completely independent of each other, they are assessed here independently to give a more complete overview of their effect on the stability of the system described in Eq. (6-7). A constant friction model is assumed throughout this section.

6.4.1 Effect of the adhesion coefficient on stability and unstable frequency

First, an example is presented for two cases to show the effect of the adhesion coefficient on the stability. For Case 1, a left-hand curve is considered (the wheel is the inner wheel) and the contact is assumed to be at the nominal contact point. Figure 6-7 shows the results. For an adhesion coefficient of 0.66 one of the two eigenvalues becomes positive and the system is unstable. The imaginary parts, when converted into Hz correspond to the frequency of oscillation, start at certain values related to the natural frequencies and become closer with increasing adhesion coefficient. The starting value of the imaginary parts are not the same with the natural frequencies because the presence of k_H in Eq. (6-12). From the imaginary part of the eigenvalue, the corresponding unstable frequency is found to be 1986 Hz when $\mu = 0.66$. This has a good agreement with Case V in Section 5.2.
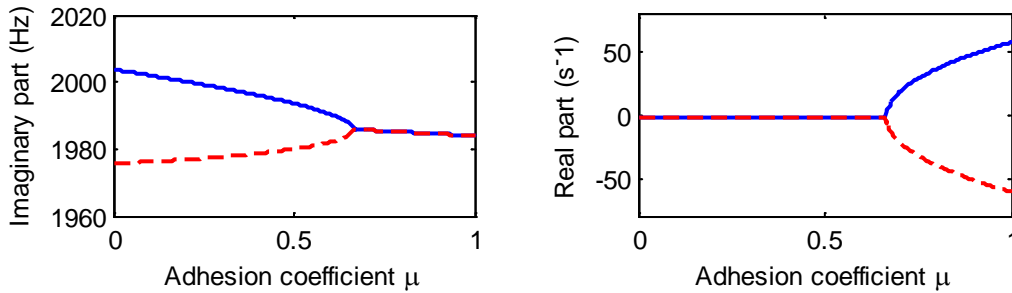
Figure 6-7. Imaginary part and real part (growth rate) of eigenvalues for Case 1.

For Case 5, the imaginary part and the real part of the eigenvalues of this system are shown in Figure 6-8 for a right-hand curve (the wheel is an outer one), with an offset of 20 mm and a contact angle of 20˚. Instability occurs for adhesion coefficients greater than about 0.6 when the real part of one eigenvalue becomes larger than zero. The squealing frequency is predicted to be around 1470 Hz and varies slightly with adhesion coefficient.
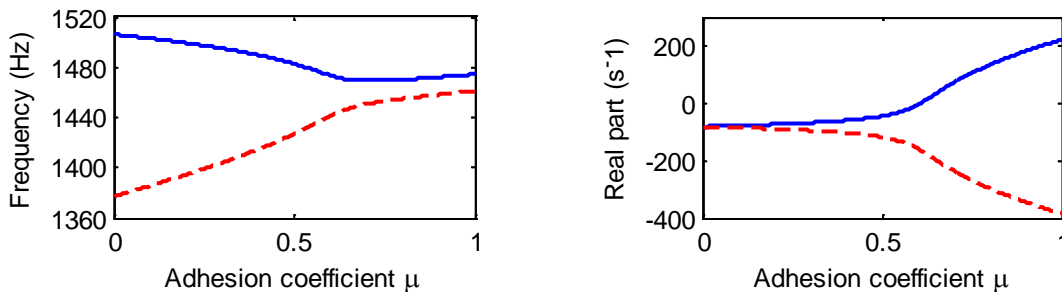
Figure 6-8. Imaginary part (frequency) and real part (growth rate) of eigenvalues for Case 5.

6.4.2 Combined effect of the adhesion coefficient and lateral offset

In this section, the effect of varying the lateral contact position on the wheel is determined for a left-hand curve (the wheel is the inner wheel) with the contact point assumed to be on the wheel tread. For the different wheels, the range of offset values is different and varies according to the wheel section design while the contact angle is assumed to remain constant. Specifically, the contact angle is assumed to be 1.5˚ for Case 1, 2˚ for Case 2 and 3˚ for Cases 3, 4 and 5. The nominal contact point is defined as 0 mm in each case. A negative offset means that the contact point moves away from the flange; a positive offset means it moves towards the flange.

The effect of varying the adhesion coefficient and the offset for those cases that show instability is presented in Figure 6-9 in the form of stability maps. The adhesion coefficient μ is varied between 0 and 1. The stability maps are divided into stable and unstable areas by studying the sign of the real part of the eigenvalues of Eq. (6-7). Instability can be found in Cases 1, 2 and 3. For Cases 4 and 5 the system was found to be stable for any contact position across the wheel tread so these are not shown here. For Cases 2 and 3, only positive offsets will give instability although there are other pairs of modes that are unstable for negative offsets. For Case 1, the instability can occur for offsets between -7 mm and 20 mm for sufficiently high μ. The minimum value of adhesion coefficient necessary for instability is found in Case 2 and is as low as 0.3 for an offset of 5 mm.
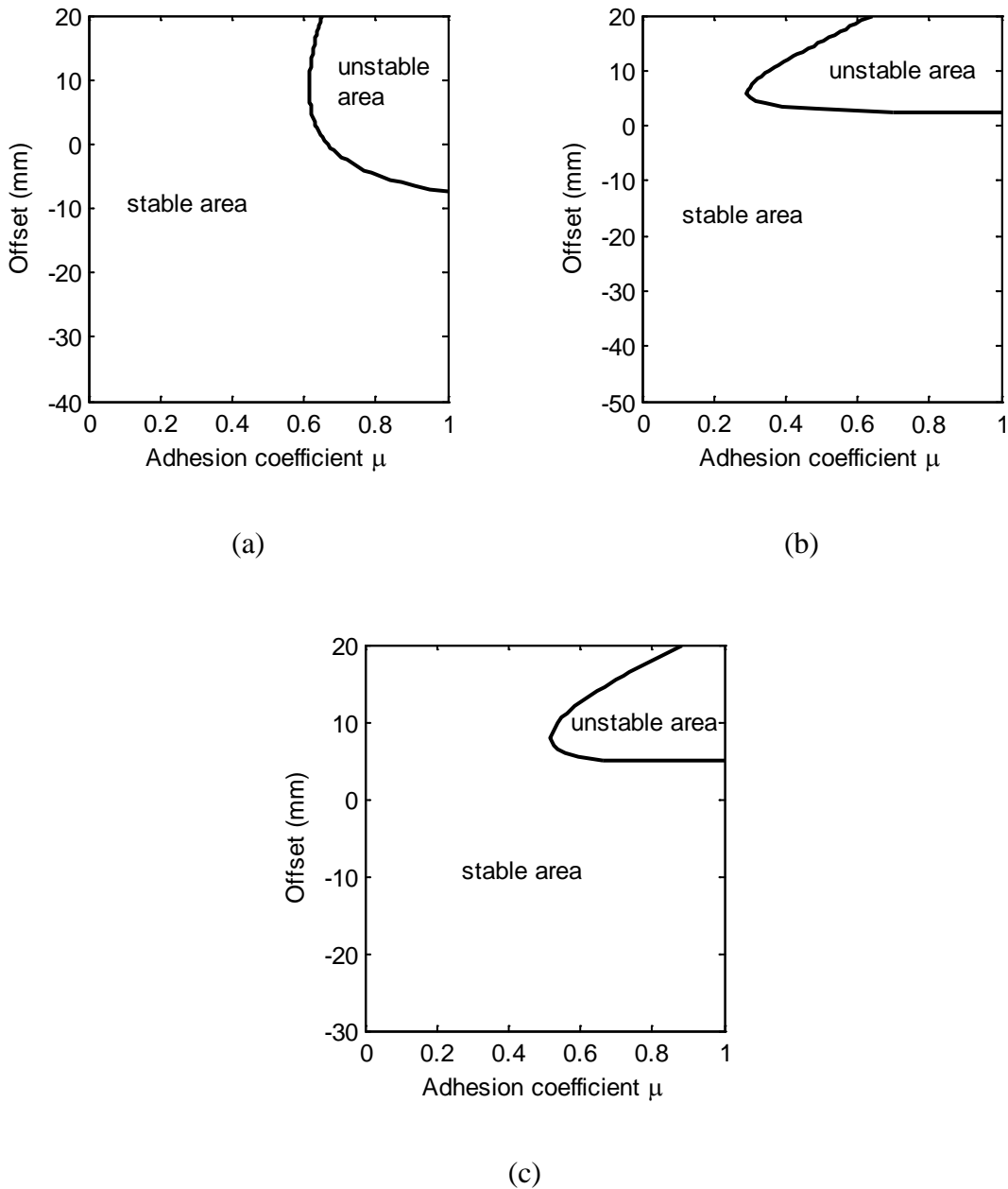
Figure 6-9. Stability maps for the inner wheel for contact on the tread. Effect of the offset of the contact point from the nominal position and of the adhesion coefficient. (a) Case 1; (b) Case 2; (c) Case 3.

6.4.3 Combined effect of the adhesion coefficient and contact angle

To study the effect of the contact angle, the wheel is assumed to be traversing a right-hand curve (i.e. it is the outer wheel) and the contact point is assumed to be on the flange. For simplicity, for the different cases, the offset is assumed to remain constant, with the contact position set in the middle of the flange, whilst the contact angle is varied between 0˚ and 90˚. Specifically, for Case 1 the lateral offset is 30 mm, for Case 2 it is 40 mm and for Cases 3, 4 and 5 it is 20 mm. The rotation of the contact plane is implemented by means of a rigid

rotation from *x-y* to *n-t* coordinates as shown in Figure 6-10. Clearly, the range of rotations considered is exaggerated compared with railway applications but it allows the instability trends to be captured in a wider area.

Again the adhesion coefficient μ is varied between 0 and 1. The corresponding stability maps are shown in Figure 6-10. Instability is found for Cases 2, 4 and 5. Cases 1 and 3 are always stable and are not shown here. In Case 2, instability extends over a range of contact angles between 22˚ and 66˚. There is also a small unstable area for contact angles between 85˚ and 90˚ but the adhesion coefficient required for instability here is larger than 0.85. The unstable area is small for Case 4; squeal is predicted for small contact angles, below about 20˚, and with adhesion coefficients above 0.76. Finally the pair of modes at 1.2 and 1.4 kHz (Case 5) can lead to instability for angles less than 30˚ with adhesion coefficients above 0.6. According to previous studies in literature review, curve squeal is often attributed to the inner wheels (see Table 1-5). However, the findings here suggest that the outer wheel may also squeal and mode coupling is a possible mechanism behind this phenomenon. The modes involved are not necessarily the same as for the inner wheel.

A feature in defining the shape of the stability map is the orientation of the rotated/translated mode shapes with respect to the contact plane. In particular, when the mode shape of one of the two modes is parallel to the contact plane, one of the off-diagonal terms of the stiffness matrix will be equal to zero (see Eq. (6-13) and (6-14)). In this condition the system is always stable as the criterion in Eq. (6-21) cannot be satisfied. For example, for Case 2 (see Figure 6-10(a)), the system becomes stable when the contact angle approaches 69˚. From the mode shape shown in Figure 6-5(c), at this contact angle, the mode at 1983 Hz is parallel to the contact plane. This finding suggests that the wheel modes prone to have mode coupling should have significant modeshape components in both lateral and vertical directions (for example, see mode at 1271 and 1417 Hz in Figure 6-6).

In the other situations considered, all the other system parameters are also playing an important role in defining stability and it is difficult to define a priori a set of necessary conditions that an unstable pair of modes should exhibit.
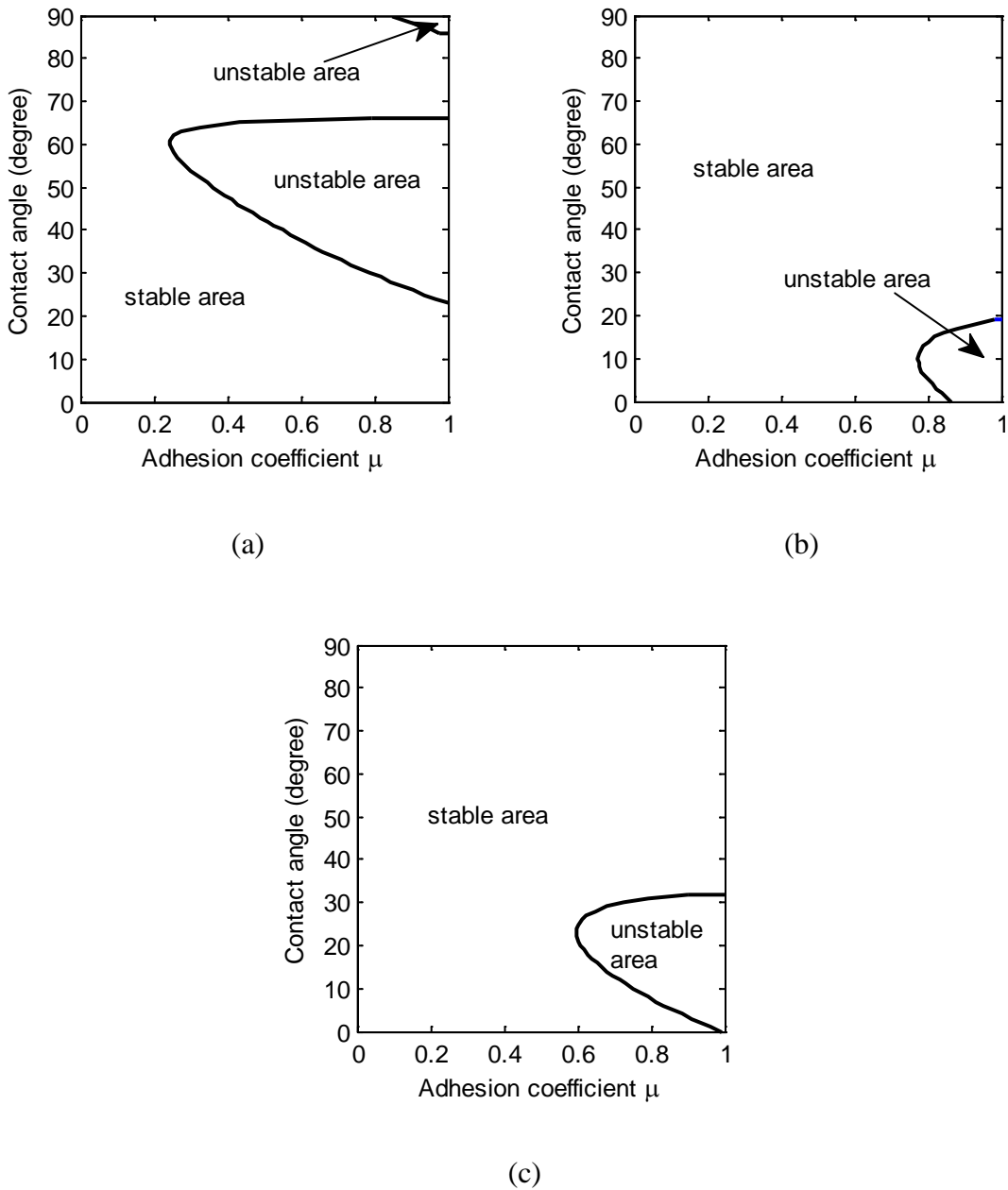
Figure 6-10. Stability maps for the outer wheel for contact on the flange. Effect of the contact angle and of the adhesion coefficient. (a) Case 2; (b) Case 4; (c) Case 5.

6.4.4 Effect of wheel damping

Increased wheel damping is often proposed as a solution for curve squeal, although in practice it is not always found to be successful [4]. In this section, Cases 1 to 4 described in Section 6.3, are adopted to discuss the effect of changing the damping ratios of the two modes. In order to do this, for Cases 1, 2 and 3, contact on the wheel tread is considered and a single value of lateral offset within the corresponding unstable regions shown in Figure 6-9 is chosen for each case. This is equal to 0 mm for Case 1, 8 mm for Case 2 and 10 mm

for Case 3. For Case 4, flange contact is considered and a single contact angle in the unstable region shown in Figure 6-10(b) is chosen, which is 10˚.

First, the damping of the higher frequency mode is varied between 10^{-4} and 10^{-1} while the damping of the lower frequency mode is kept equal to the original value shown in Table 6-1. Figure 6-11 shows the corresponding stability maps. For Case 3, it can be seen that increasing the damping ratio of the higher frequency mode always has a beneficial effect in terms of the stability of the system. However, for Cases 1, 2 and 4, there is a range of damping ratios in which increasing the damping can make the system more unstable.

When the damping ratio of the lower frequency mode is changed, it is found that, for Cases 1, 3 and 4, the stability maps are similar to the corresponding ones in Figure 6-11. Hence they are not shown here. Only for Case 2 are there differences as increasing the damping ratio of the lower mode stabilizes the system (see Figure 6-12). The reason for this is that the original damping ratios of these two modes are considerably different, and the results in both Figure 6-11(b) and Figure 6-12 are calculated using the original damping for the mode that is not changed. Specifically, in Figure 6-11(b), when the damping of the higher frequency mode changes, the damping ratio of the lower frequency mode remains as 10^{-4}, whereas in Figure 6-12, the damping ratio of the higher frequency mode remains as 10^{-2} when the damping of the lower mode is changed. This, and other results in Figure 6-11, indicate that the instability is greater when the modes have very dissimilar damping ratios.
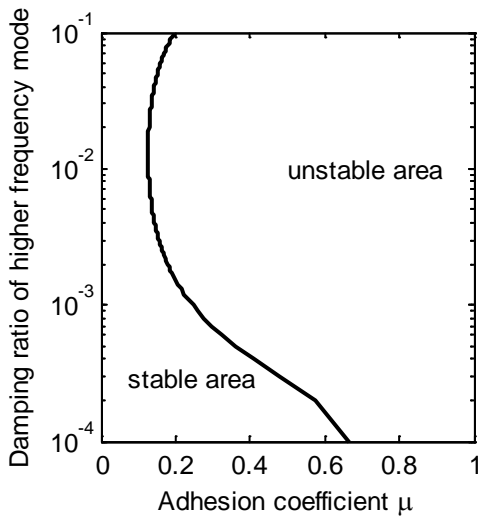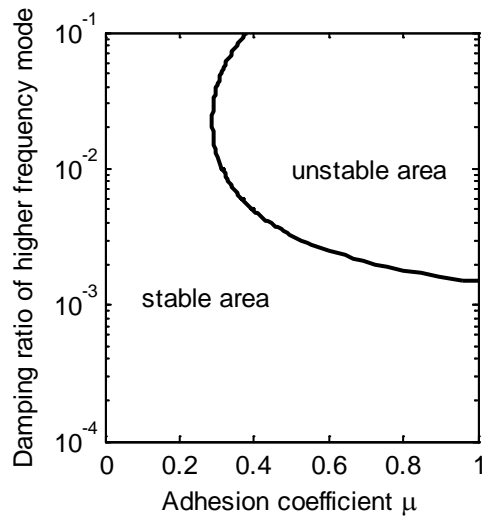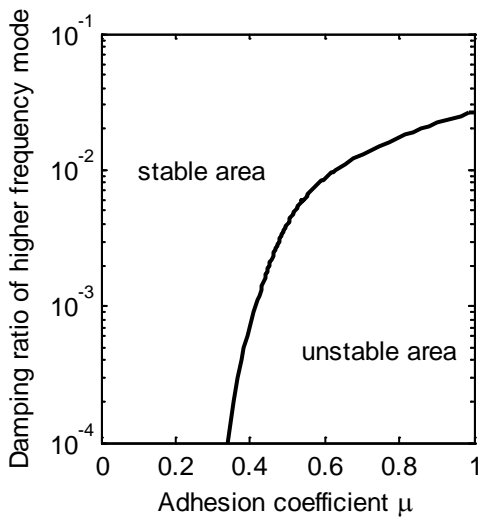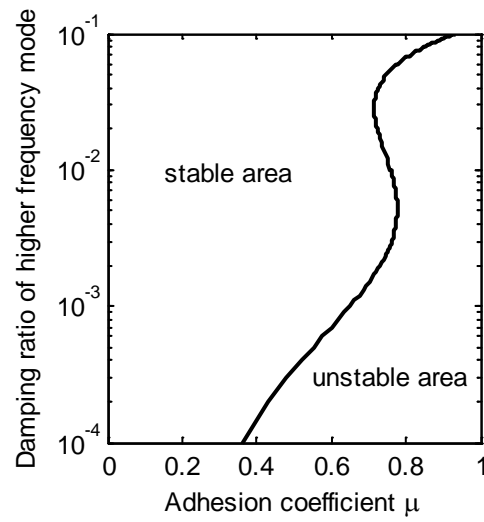
Figure 6-11. Effect of changing the damping ratio of the higher frequency mode. (a) Case 1, 0 mm offset; (b) Case 2, 8 mm offset; (c) Case 3, 10 mm offset; (d) Case 4, contact angle 10˚.
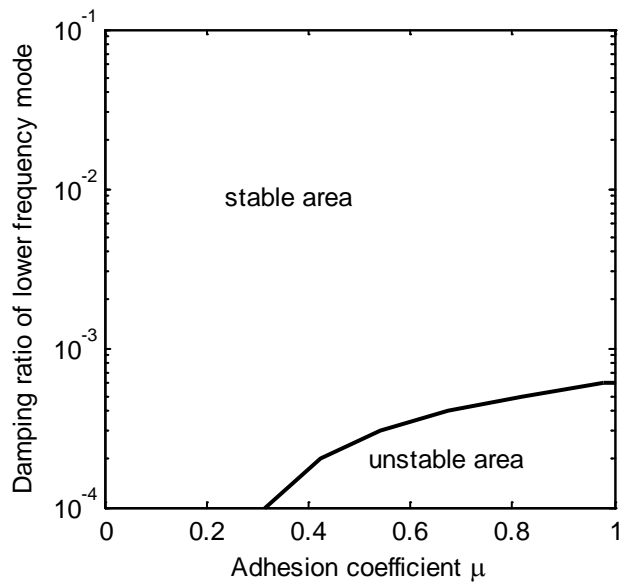
Figure 6-12. Effect of changing the damping ratio of the lower frequency mode of Case 2.

The effect of changing the damping of both modes simultaneously is shown in Figure 6-13. In this case, when the damping ratio of the higher frequency mode increases, the ratio of the two damping ratios (ξ_1/ξ_2) is kept constant. In Figure 6-13 the stable areas are always to the left of the corresponding lines. It can be seen that now the results for these four cases have the same trend. For values of damping below a certain limit, the stability of the system is not affected by changes in the damping ratios. This limit value is different for the different cases, being as low as 0.04% for Case 1 and almost 0.4% for Case 2.

In summary, adding damping to the wheel does not automatically eliminate the possibility of curve squeal. If the mechanism responsible for the instability is mode coupling, as here, in the extreme case that the damping of a single mode is increased, the system can even become more unstable in certain situations. This behaviour has been observed previously by other authors and has often been described as the "destabilisation paradox", see e.g. [105]. Even for a more realistic case where the damping is increased for both modes, a limit value needs to be exceeded for the added damping to have a significant effect in eliminating the instability.
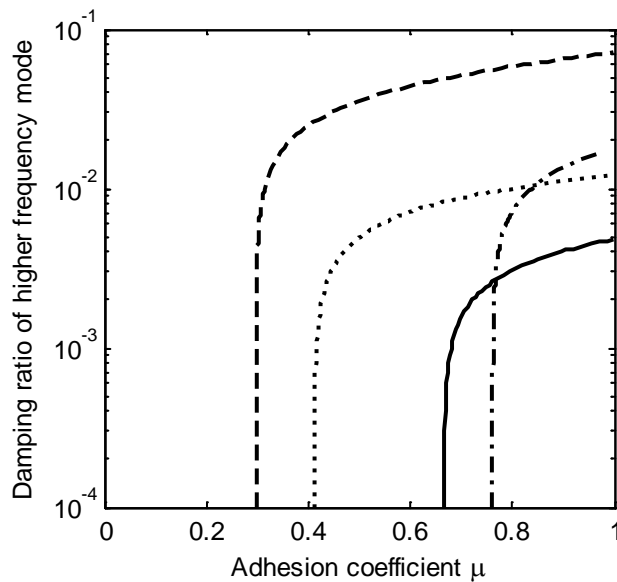
Figure 6-13. Effect of damping (keeping the ratio between the two modes ζ_1/ζ_2 constant). Solid line: Case 1, 0 mm offset; dashed line: Case 2, 8 mm offset; dotted line: Case 3, 10 mm offset; dash-dot line: Case 4, contact angle 10˚.

6.4.5 Effect of other modes

For all the cases considered so far, only pairs of modes have been selected. In this section, additional neighbouring modes are included in the model to verify whether this has an effect on stability.

Figure 6-14(a) shows the stability map for Case 1 with different numbers of modes included. Here, 'two modes' corresponds to the original two coupled modes (1959 Hz and 1976 Hz) given in Figure 6-9(a). Then the modes at the following natural frequencies are added, one at a time: 1853 Hz, 2136 Hz and 2210 Hz. When the number of modes is increased from 2 to 5, the unstable region is extended to slightly lower adhesion coefficients, but has a very similar shape.

Similarly, Figure 6-14(b) shows the stability map with different numbers of modes for Case 2. The added modes are: 1923 Hz, 2254 Hz, 2374 Hz. In this case the stability map is affected only slightly by the additional modes, although the trend is the opposite to the previous case, as the unstable area decreases when more modes are included in the system. Similar results can be found for other cases. It is therefore justified to use only two modes at a time in the current study of mode coupling.
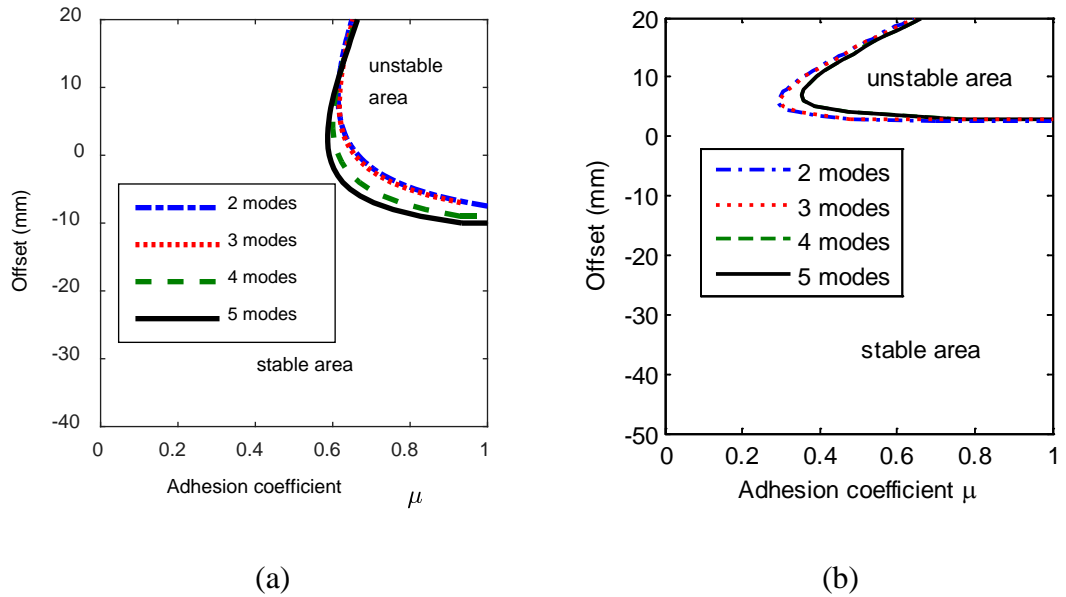
Figure 6-14. Stability map including different number of modes. (a) Case 1; (b) Case 2.

6.5 Frequency domain analysis with presence of both falling friction and mode coupling

Unlike previous section, this section introduce a falling friction in this two-mode model and will study falling friction and mode coupling together.

If a falling region is introduced in the friction model, the effective damping of the system is modified by the friction force. With a single-mode model of the wheel, a limit value of the friction slope for stability can be calculated. According to [44], this can be found as:

$$\frac{\partial \mu}{\partial \gamma_0} = \frac{2\omega_i \xi_i V}{N \Phi_{xi}^2} \tag{6-23}$$

where Φ_{xi} is the mass-normalised mode shape in the tangential direction of the ith mode. However, for a two-mode system this simple estimate no longer applies.

To show the effect of friction slope, Case 2 is considered here and the maximum friction coefficient μ_0 is set to equal to 0.4. The stability map with different friction slopes and contact angles is shown in Figure 6-15, with a close-up in Figure 6-15(b). The solid line shows the division between stable and unstable areas for the two-mode system. As shown already in Figure 6-10(a) the system with constant friction is unstable at this value of friction coefficient between about 48° and 64°. Figure 6-15 also shows the minimum friction slopes that would result in instability when each wheel mode is considered as a single degree of

125

freedom (dof) system (i.e. Eq. (6-23)) in the axial direction (dashed line and dotted line). For all the curves, the stable region is always below the corresponding line and the unstable region is above it.

The line representing the limit value for the lower frequency mode (dashed line) crosses the line of stability of the whole system at around 45˚ and again at 65˚ whereas the line corresponding to the higher frequency mode (dotted line) never crosses the solid line. In the region above both the solid and dashed/dotted lines the system is considered to be unstable due to the negative slope of the friction curve.
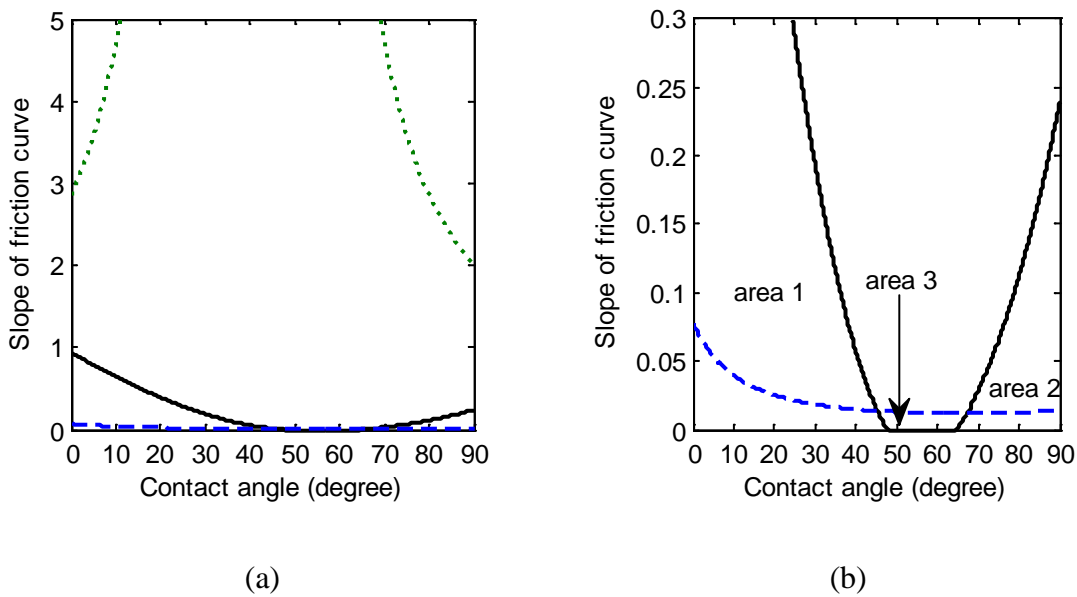
Figure 6-15. Stability map with different contact angles and friction curve slopes for Case 2 with $\mu = 0.4$. (a) Stability map; (b) close-up. (Solid line: mode coupling; dashed line: lower frequency mode; dotted line: higher frequency mode).

Three interesting areas can be identified between the continuous and broken lines. They are highlighted as 'area 1', 'area 2' and 'area 3' in the figure. Inside both area 1 and area 2, the two-mode system is stable, even although the slope of the friction curve is above the limit value of the lower frequency mode. However, inside area 3, the system is unstable due to mode coupling as the slope of the friction curve is below the limit value for the single mode. Nevertheless the shape of area 3 changes as the slope of the friction curve is increased which suggests that the negative slope is modifying the damping of the system, and consequently affecting the mode-coupling instability.

Another example is shown in Figure 6-16. This corresponds to Case 5 with the maximum friction coefficient set to 0.8. As seen in Figure 6-10(c), for constant friction at this level this system is unstable between about 8° and 30°. Similar trends to the previous results can be

seen. Analogous results are also found for other cases and in general they can be summarized as follows. Sometimes the single dof approach indicates stability where the two-mode system is actually unstable due to mode coupling (e.g. area 3 in Figure 6-15 and Figure 6-16). For other combinations of parameters the single dof approach would give instability due to a negative damping term, but the two-mode system is actually stable (e.g. areas 1 and 2 in Figure 6-15, area 2 in Figure 6-16). In these cases the presence of an additional coupled degree of freedom stabilises the single dof instability.
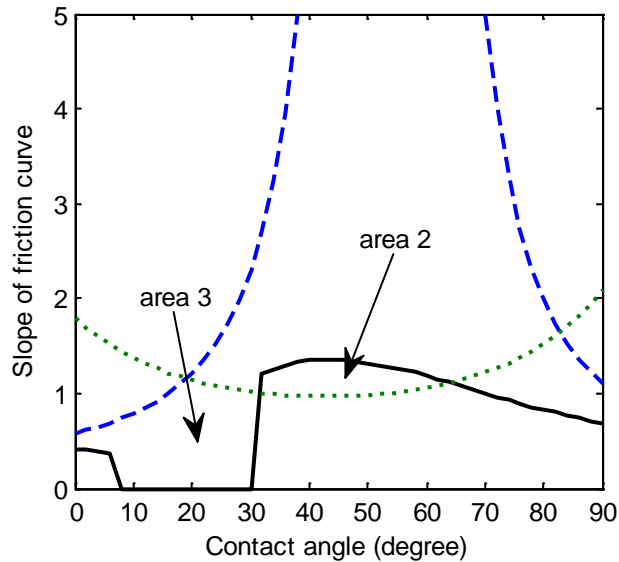
Figure 6-16. Stability map with different contact angles and friction curve slopes for Case 5 with $\mu = 0.8$ (solid line: mode coupling; dashed line: lower frequency mode; dotted line: higher frequency mode).

6.6 Time-domain results for two-mode model

In the frequency-domain analysis performed above, the friction force is linearized around the steady-state creepage. To include the nonlinearities of the friction force, in this section time-domain simulations are also carried out by using a step-by-step integration method (Runge-Kutta method [96]). This allows the nonlinearity to be fully considered and the limit cycle to be calculated. Case 5, based on the tram wheel modes, is adopted as an example for time-domain analysis. The wheel is represented by the same two modes only. First, a particular combination of friction coefficient and contact angle in the unstable region according to Figure 6-10 is chosen. Here, for this case, the contact angle and friction coefficient are chosen as 20° and 0.8 respectively.

Figure 6-17 shows the time-domain solutions for this two-mode system. It can be seen that the responses in both tangential and normal directions increase until the limit cycle is reached. The close-up of the limit cycle shows a phase difference (135°) between the responses in the two directions. The spectrum shows that the frequency of the limit cycle is at 1496 Hz. This is not equal to either of the natural frequencies of the two modes considered (i.e. 1271 Hz and 1417 Hz). The higher frequency peaks in the spectrum correspond to harmonics of this fundamental frequency appearing due to the non-linearity in the creep force.
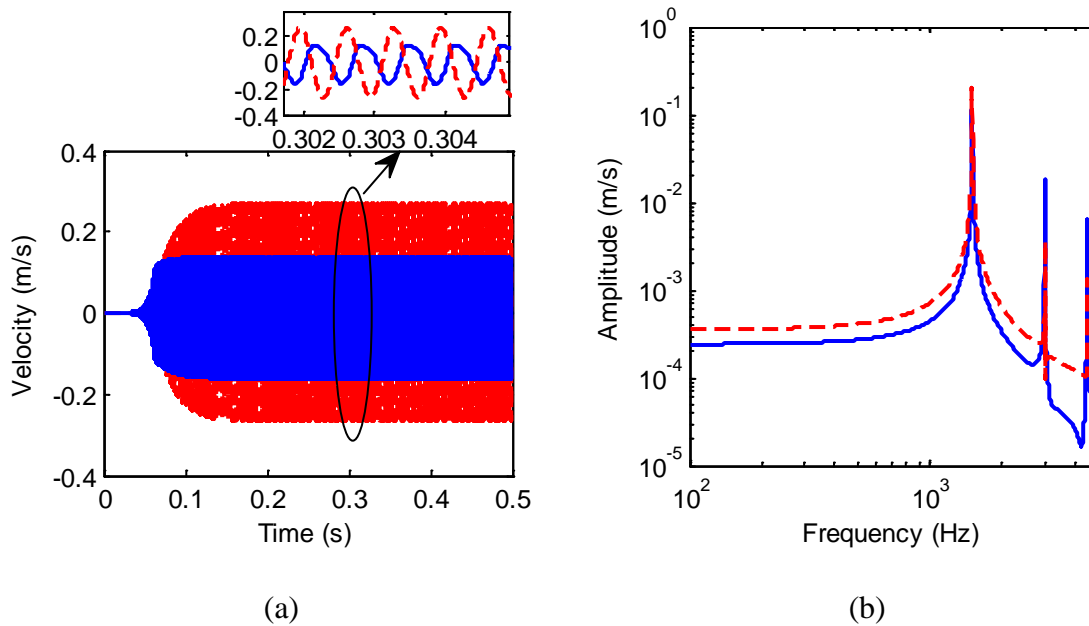
Figure 6-17. Time-domain solution for Case 5 with angle of 20˚, friction coefficient of 0.8 and offset of 20mm. (a) Complete solution; (b) spectrum of the responses. solid line: tangential direction; dash line: normal direction.

Next, the phase shift is investigated when both mode coupling and falling region are included. Again, Case 5 is adopted and three different combinations of contact angle and adhesion coefficient are used. A falling friction law is considered with different friction curve slopes at the steady-state creepage value.

From the time-domain simulations, the phase difference in the limit cycle between the two directions is calculated by taking the Fourier transforms of the limit cycle responses. The results are shown in Figure 6-18. It can be seen that with larger slopes where falling friction is expected to dominate, the phase difference tends to 0˚. This is aligned with the results shown in Figure 6-16, where a slope of 2 or more was found to be above the single mode stability lines. In the absence of mode coupling, where a single (real) mode is responsible for squeal, the phase difference is expected to be zero. Figure 6-18(b) gives the squealing frequency from the limit cycle; it starts from around 1500 Hz and tends to the frequency of

the higher mode (1417 Hz) with increasing slope. In the absence of mode coupling the instability is due to negative damping and is associated with a single wheel mode. The presence of a phase difference and frequency shift are indicators of the presence of mode coupling although they do not exclude the influence of falling friction, as both mechanisms may be acting together, as illustrated in Section 6.5.

(a)   (b)
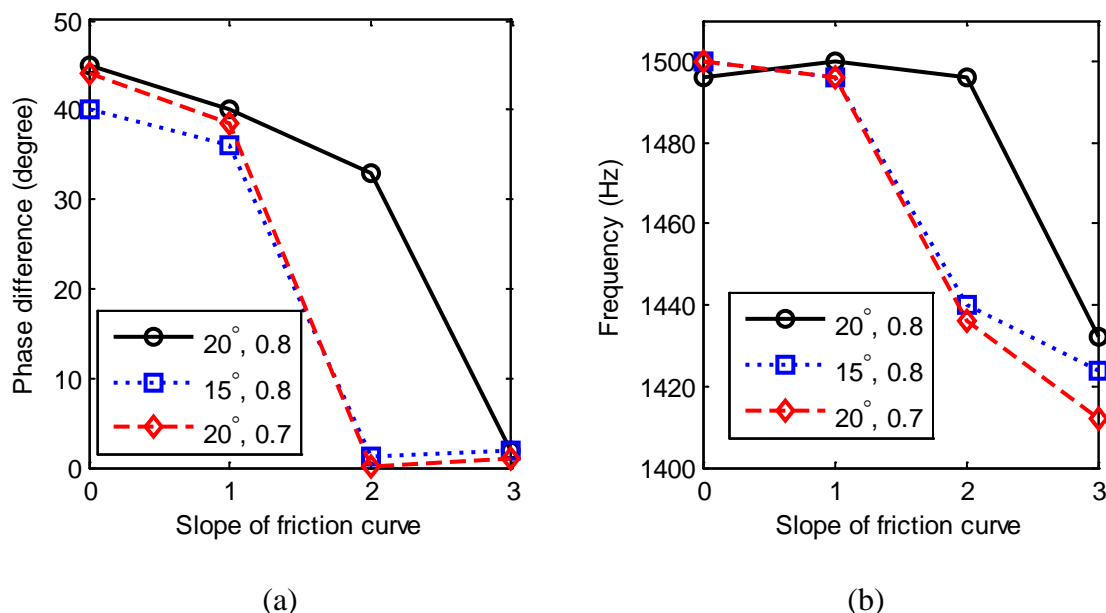
Figure 6-18. Phase difference and squealing frequency with different friction slopes for Case 2: (a) phase difference; (b) squealing frequency.

The examples shown in this chapter are all taken from an unstable region of the stability map (see Figure 6-9(c)); the response is unstable and builds up to a limit cycle. If the system is solved for input parameters taken from the stable areas the response decays with time. However, there are some combinations of input data, within the stable regions but close the unstable ones, which result in beating. This has been demonstrated in Section 3.3.2 using the model from [38] for the case of a two dof mass on a moving belt.

6.7 Frequency shift and phase difference in a measurement campaign

The tram wheel adopted in the calculations of Cases 3, 4 and 5 is an example of a resilient wheel used for trams. Field experiments have been presented in [60] with this type of wheel running on a curve with severe squeal noise problems. The selected test section had a very small radius of 18 m with grooved rails and ballasted track (see Figure 6-19); as a result the angle of attack was found to be around 2.5° [31] and it can be fully expected that the contact is in the saturated region. The wheel was fitted with accelerometers and the vibration in both

axial and radial directions on the wheel tyre was recorded. A detailed description of the measurements is given in [60]; this wheel was also used in [31] to study the effect of the presence of two-point contact on squeal noise. In fact it is likely that during running in the curve, both outer and inner wheels had two contact points. The outer wheel was in contact on the tread and flange whereas for the inner wheel the gauge side of the flange could touch the grooved rail head which was showing wear on its surface. Despite the study presented in [31], the effect of having two contact points during squeal is not yet fully understood and addressing it is beyond the scope of the present work.

Figure 6-19. The tram running on the test curve for the measurements described in [60].

In [60], the authors only showed the whole time history data of the wheel vibration response during the test and its spectrogram, which was used to find the dominant frequency during the test. No further investigation were made. In this section, these measurement data were used again with more analysis. In addition to the spectrogram, the vibration responses of the measured wheel in two directions are compared and the squeal frequencies are also compared with the natural frequencies of the wheel modes. These can provide some useful understanding in analysing the possible mechanism behind curve squeal and results are presented here to allow a qualitative comparison with the simplified models described above.

An example of the measured wheel vibration is shown in Figure 6-20. In this example the instrumented wheel was the front inner one and the tram running speed was 2.78 m/s. It can be seen that the wheel vibrates at a relatively high level in the time period from about 13 s to 25 s. From the spectrograms, it is found that there are two dominant frequencies for both

axial and radial directions. They are around 1.5 kHz and 2.5 kHz and these broadly correspond to the squealing frequencies in Cases 3 to 5 analysed above.

A close-up plot of part of the acceleration signal from Figure 6-20 is shown in Figure 6-21 along with the corresponding frequency spectra. The most important features of squeal are evident, with the vibration being intermittent, mono-tonal and of very high levels. The squealing frequency in this time window was at 2517 Hz, as shown in Figure 6-21(b).

(a) (b)
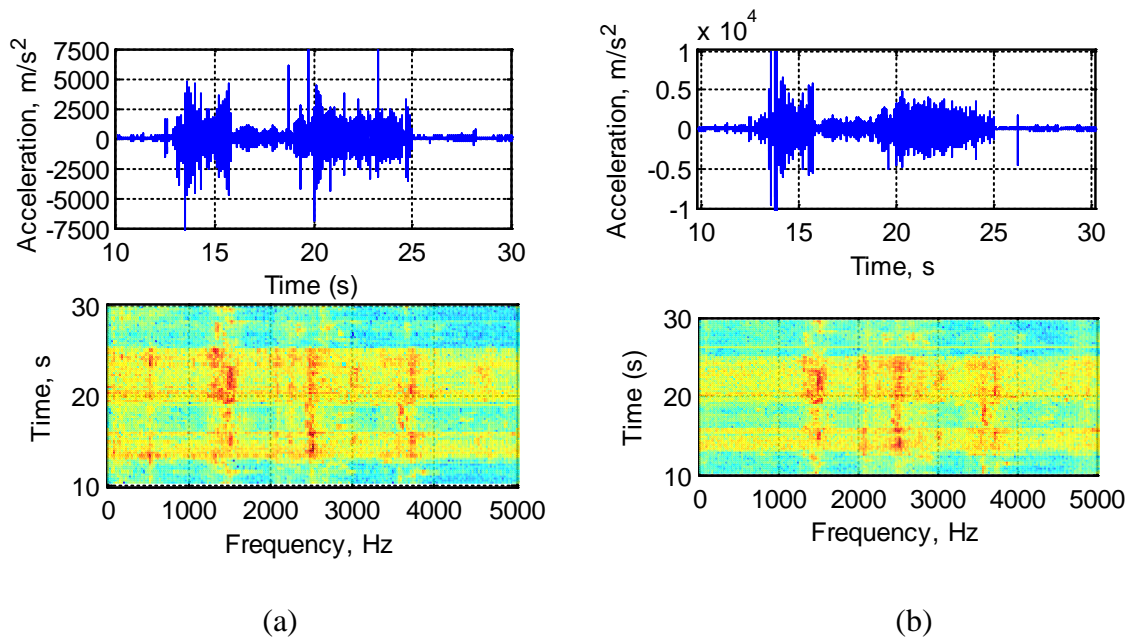
Figure 6-20. Measured wheel vibration acceleration and the corresponding spectrograms: (a) axial direction; (b) radial direction.
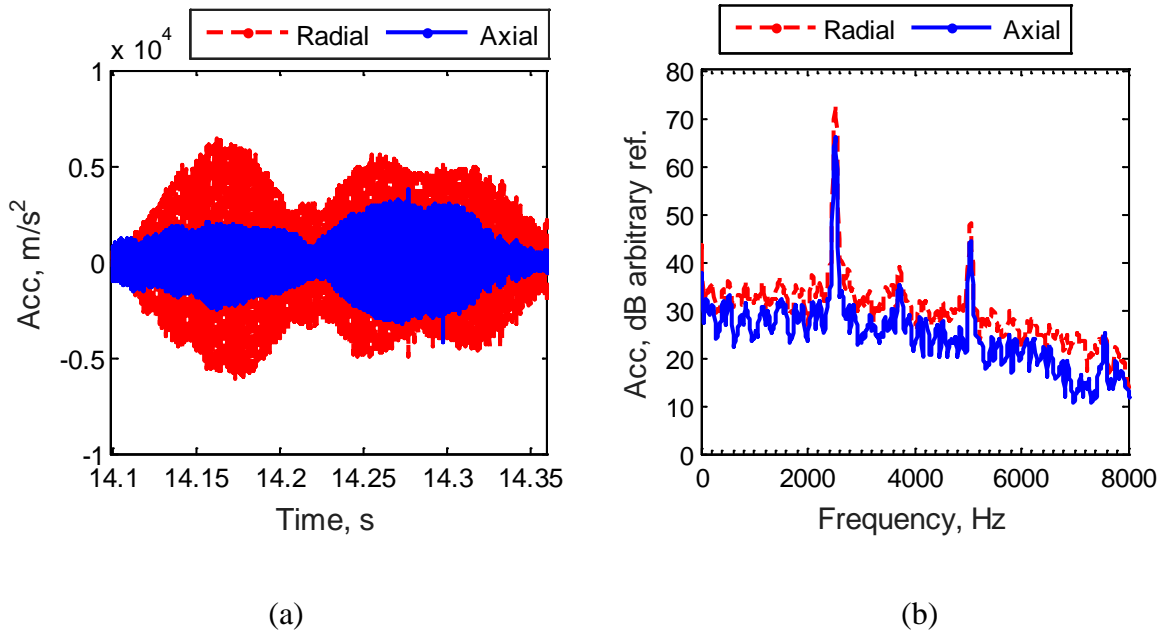
Figure 6-21. Wheel vibration measured during squeal at 2522 Hz. (a) Example of time history data (b) frequency spectrum.

At around this frequency, this wheel has the two vibration modes included in Case 3 above: the first mode (2476 Hz) has 4 nodal diameters and is predominantly in the radial direction, but also with an important component in the axial direction; the outer rim rocks on the rubber layer (Figure 6-6(a)). At a slightly higher frequency (2536 Hz) there is a mode with one nodal diameter and a mode shape with the outer rim in torsion on the rubber layer (Figure 6-6(b)). These two modes have been studied with the simplified approach in the sections above and it has been shown that for an offset of around +5 mm mode coupling instability can arise (Figure 6-9(c)).
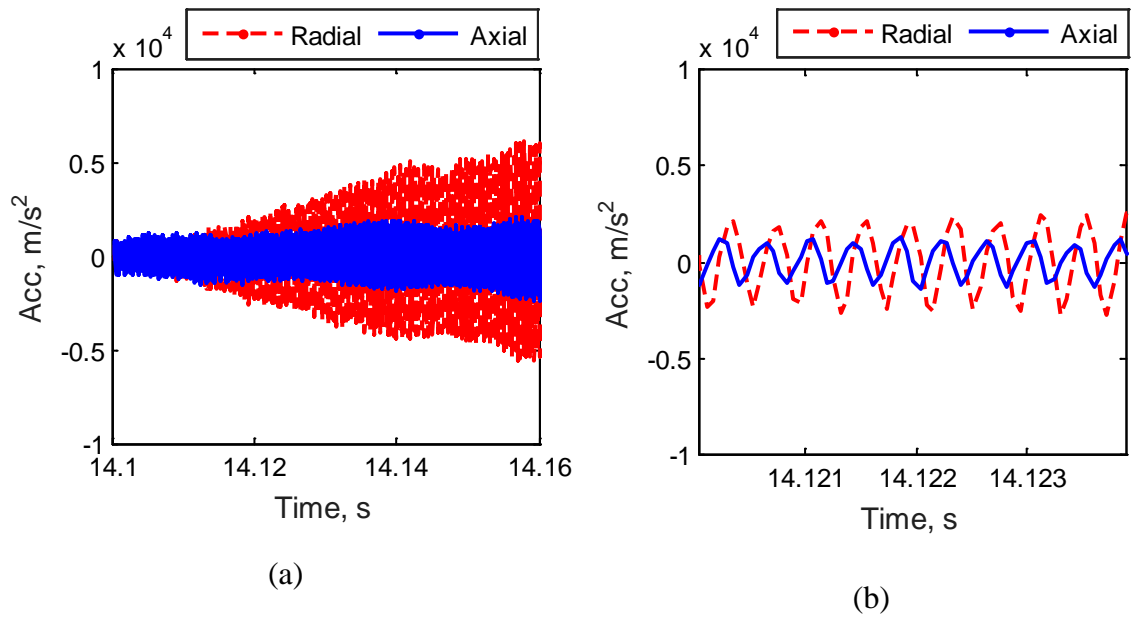
Figure 6-22. Close-up of Figure 6-21. (a) Initial build-up (b) enlargement over a few vibration cycles to show phase lag between axial and radial directions.

In addition, in Section 6.5 it was shown that another important feature of mode coupling is a phase lag between the radial and axial vibration. Figure 6-22 shows two additional close-up plots of the vibration data presented in Figure 6-21. Clearly both directions are involved in the vibration and increase together in this region.

An additional example showing a similar outcome is shown in Figure 6-23. The squealing frequency is 1515 Hz and does not correspond closely to any of the modes in Figure 6-3, the nearest modes being at 1271 and 1414 Hz. This has also been found in the modelling (Figure 6-8). Moreover, again there is a phase lag of about 30° between the two directions that qualitatively resembles the one obtained with the model in Figure 6-17(a).
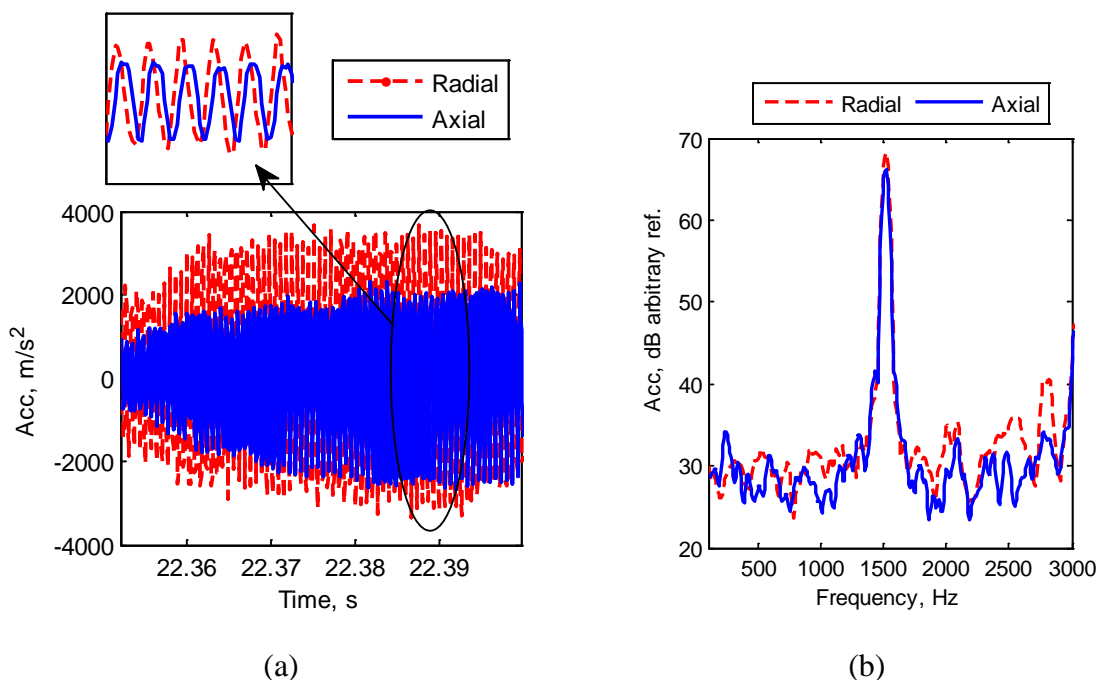
Figure 6-23. Wheel vibration during squeal at 1515 Hz. (a) time data and (b) frequency spectrum.

The measurement data shown here therefore include two important characteristics of mode coupling: the squealing frequency is different from the natural frequencies of the modes involved and there is a phase lag between the radial and axial directions. Both features have also been found earlier in this chapter with the simplified model with constant friction by including only two modes.

A further phenomenon that may be related to the presence of mode coupling in the measurement campaign is shown in Figure 6-24. In this case the interaction between two modes results in beating at about 15 Hz; the modes involved are the two at around 3750 Hz (see Figure 6-3). Both the time domain data and the frequency spectrum show the typical behaviour of beating. The amplitude changes periodically in time from one direction to the other one while a fine frequency spectrum, such as the one shown in the close-up in Figure 6-24(b), reveals the presence of two distinct, but close, peaks (at 3707 and 3720 Hz respectively). In reference [38] this type of vibration was shown in the response of a two dof system characterised by a friction coefficient close to, but slightly smaller than, what is needed for instability.
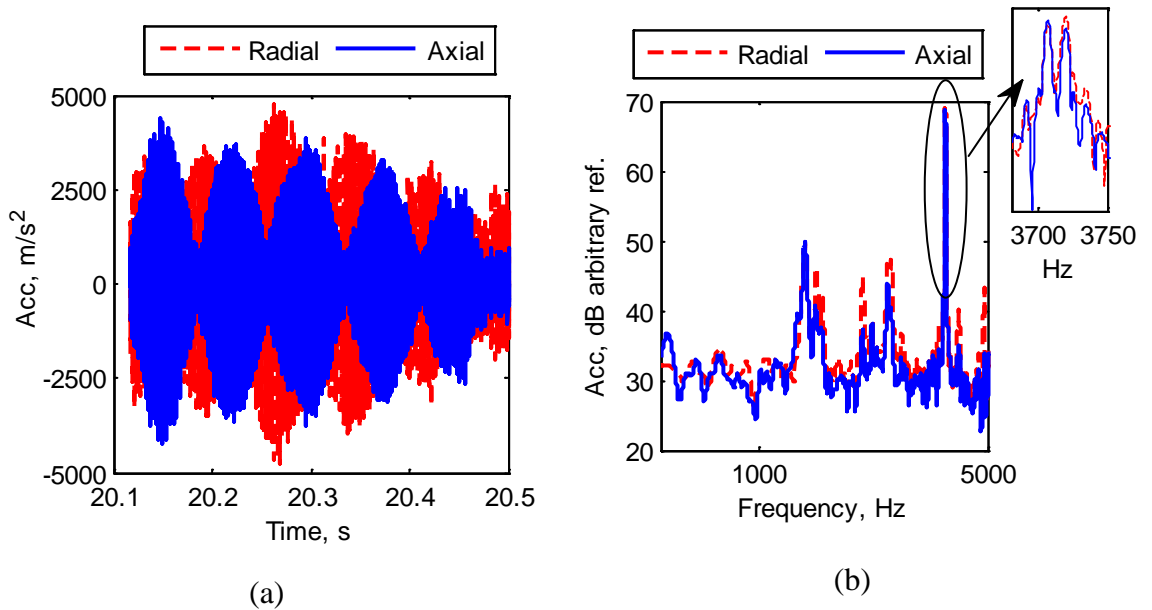
Figure 6-24. Wheel vibration measured during squeal with the presence of beating at around 3.7 kHz. (a) Time data (b) frequency spectrum.

The wheel acceleration data from a number of pass-bys have been analysed statistically to determine the distribution of the squealing frequency and the phase difference between the axial and radial directions. Three main squealing frequencies were observed, at around 1.5, 2.5 and 3.7 kHz as seen in Figure 6-20. The phase difference has been calculated at every oscillation period after applying a band-pass filter around the squealing frequency. Only those time windows with acceleration levels above 800 m/s^2 (rms) have been selected to compute the phase difference. The average squealing frequencies were calculated over the same cycles and found to be 1489 Hz, 2514 Hz and 3713 Hz with standard deviations of 47 Hz, 21 Hz and 48 Hz, respectively.

A summary of the measured phase difference for these three squealing frequencies is shown in Figure 6-25. The horizontal axis represents the absolute value of the phase difference in degrees while the vertical axis indicates the number of times the difference occurs in a certain 10˚ range. To obtain these results, three different pass-bys at 2.78 m/s have been considered. It can be seen that the phase difference can vary between 0˚ and 180˚ with the greatest tendency for the phase differences to be in the range between 10˚~40˚ and 120˚~160˚, especially for the squealing frequency of 1489 Hz. This broadly agrees with the results from the model in Figure 6-18 for small values of friction slope.
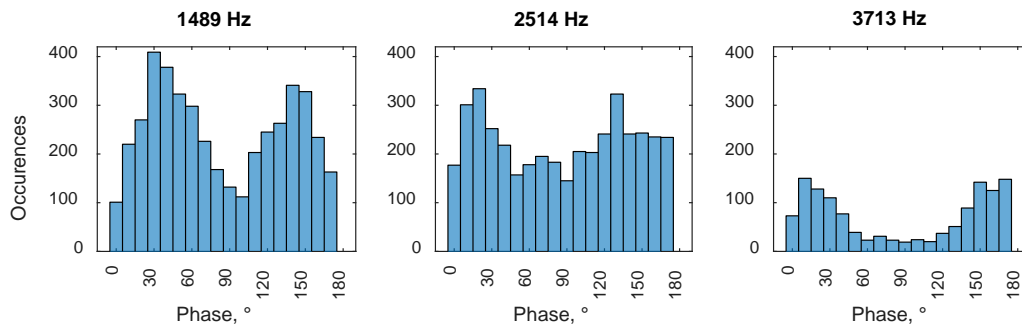
Figure 6-25. Phase difference for three squealing frequencies.

The experimental results therefore show the same features as the model. The squealing frequencies of 1489 Hz and 2514 Hz are similar to those found in Section 6.4 and the non-zero phase difference corresponds to that found for the case of mode coupling. There are too many uncertainties in the measurement campaign to allow a full quantitative comparison between the model and measurements. In particular, it was not possible to determine the actual friction coefficient or the exact contact position. Nevertheless, the evidence presented here gives additional indications that mode coupling is a possible mechanism behind curve squeal at least in some situations.

6.8 Summary

A two-mode model has been used to illustrate the mode-coupling mechanism, which can be a cause of curve squeal noise in addition to the traditional falling friction mechanism. This model can also be used to assess mode coupling and falling friction together. Different pairs of modes have been considered, including modes from a regional train wheel, a freight train wheel and a resilient tram wheel.

By carrying out a parametric study using frequency-domain stability analysis, it has been shown that the offset of the contact point and the contact angle can both have an effect on the squeal noise. It is confirmed that both inner and outer wheels in the curve can result in squeal noise due to mode coupling. Moreover, it is shown that the modal damping ratio can play an important role. Increasing the damping of a single mode does not always have a beneficial effect on squeal noise and in some cases can actually make the system more prone to squeal. Increasing the damping of both modes simultaneously has no effect until a certain limit is reached.

Frequency shift and phase difference are two basic features of mode coupling. In the literature review, it was shown that in [46, 60, 106], the authors observed a frequency shift in field measurements. However, only in [54] was mode coupling mentioned in relation to

this. A phase shift was only mentioned in [65] and it was observed in the vibration signal from the rail. In this chapter, frequency shift and phase difference are both observed by analysing the system in the presence of a mode-coupling instability. Some qualitative comparisons with field measurements of tramway wheel acceleration have also been presented. Measured data show similar characteristics to those that were attributed to mode coupling in the modelling, as both frequency and phase shift are detected in the wheel signals. This provides additional evidence that mode coupling can be a possible mechanism for curve squeal at least in some situations.

7 Effect of track dynamics on curve squeal under constant friction

Although the rail plays an important role in the wheel/rail interaction, the track dynamics has been paid only limited attention in studies of curve squeal so far. Most previous models neglect the track dynamics or they include it without evaluating its role and importance.

It was shown in Chapter 5 that the track dynamics potentially can play an important role in the occurrence of curve squeal. From Table 5-4, it can be found that the system can be unstable with only one wheel mode in the presence of track dynamics. In this chapter, the effect of the track is investigated with a reduced model and only constant friction is considered to exclude the negative damping effect due to the negative slope of the friction curve.

The track is first modelled as an infinite beam over a continuous elastic foundation and, in contrast with the wheel, it is not characterised by any vibration modes. Various effects are then considered that may introduce additional resonant behaviour into the track dynamics. These include the rail pad stiffness, the periodic or continuous support of the rail, multiple wheels resting on the rail, the rail cross-section deformation and the rail cross mobility. Finally, a reduced model is developed to identify what aspects of the dynamic behaviour of the track can cause instability. In this model, only a single wheel mode is included and the track is represented as a mass, a spring or a damper.

7.1 Curve squeal prediction with and without the rail using a mobility approach with reduced model

7.1.1 Transfer function

To simplify the problem and to exclude other factors, the open loop transfer function of the frequency domain model for curve squeal in Chapter 4, $\mathbf{Q} = \mathbf{H}_1\mathbf{G} + \mathbf{H}_2$, is simplified to have only two degrees of freedom: vertical and lateral directions. The effects of fluctuation of the normal force on the friction force is neglected ($\frac{\partial \mu}{\partial f}$ in Eq.(4-45) are all zero). Hence, from Section 4.3.2, the transfer function under constant friction now becomes:

$$Q = \pm \mu_0 \frac{Y_{VL}^w + Y_{VL}^r}{Y_{VV}^w + Y_{VV}^r + Y_{VV}^c} \tag{7-1}$$

where for a positive lateral creepage (right-hand curve), the plus sign is taken. μ_0 is the friction coefficient; Y^w, Y^r and Y^c are the mobilities of the wheel, the rail and the contact spring. Indices L and V represent lateral and vertical directions; subscript LL represents lateral point mobilities, while LV indicates the coupling between the two directions; mobilities of this type are referred to as cross mobilities. The cross mobility for the contact spring, Y_{LV}^c, is equal to 0.

It can be seen that, with a constant friction coefficient, three factors can affect the transfer function. They are the value of the friction coefficient, the combined cross mobility between the lateral and vertical directions and the combined point mobility in the vertical direction. The lateral point mobility does not appear in the above equation.

7.1.2 Frequency domain results

The method of obtaining wheel and rail mobilities has been introduced in Chapter 3. Here, again, the Class 158 wheel is used. The track also has the same parameters as the one in Chapter 4; however in addition to the soft rail pad (vertical stiffness 100 MN/m) used in Chapter 4, a stiffer rail pad is also considered with vertical stiffness 600 MN/m.

The vertical and cross mobilities of the wheel for frequencies up to 6 kHz are shown in Figure 7-1(a) and rail mobility and contact mobility are shown in Figure 7-1(b). The vertical contact mobility is obtained from the linearized Hertzian contact stiffness [1], which has the same value as used in Chapter 5, i.e. 1.12×10^9 N/m. The rail cross mobility is neglected in this section but will be considered in Section 7.2.4 using an alternative model.
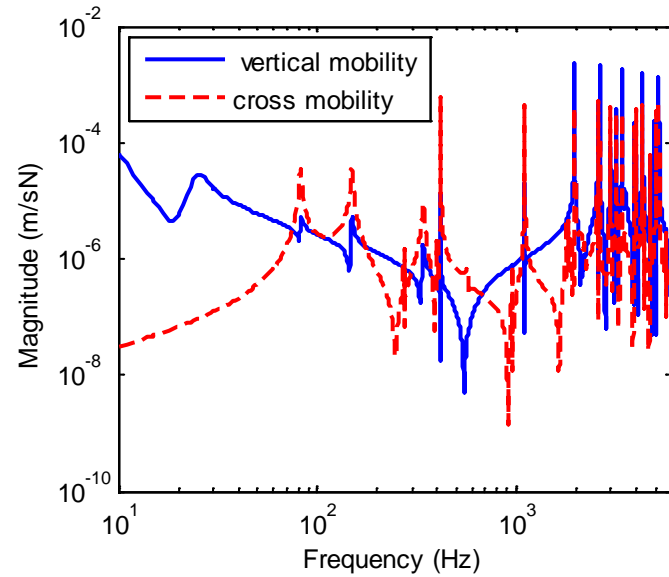
(a)
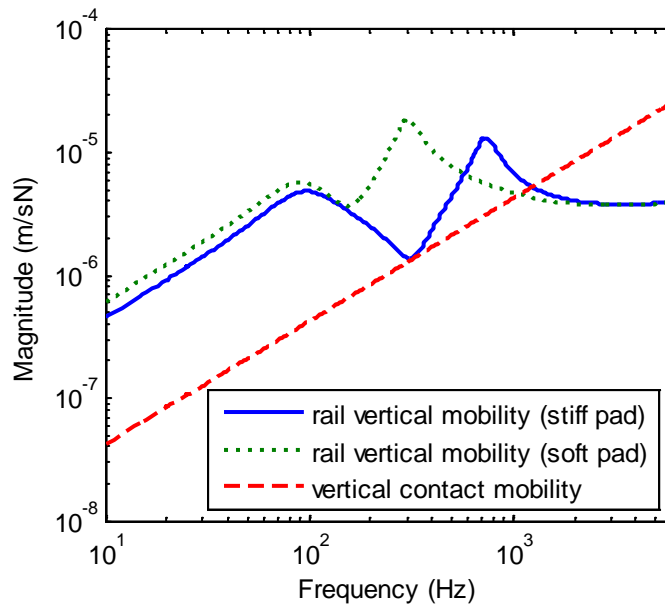
(b)

Figure 7-1. The mobilities: (a) wheel vertical and vertical-to-lateral cross mobility, (b) rail and contact vertical mobilities.

To evaluate stability, the Nyquist criterion [95] is again used and applied to Eq.(7-1). In the calculations presented in this section, the contact is assumed to be at the nominal position and the wheel is assumed to be the right-hand wheel of the leading wheelset of a bogie, on a right-handed curve. The Coulomb friction coefficient μ_0 is set to 0.3 and rolling velocity is assumed to be 10 m/s.

When track dynamic properties are included, there are four unstable frequencies, as summarised in Table 7-1, for both soft and stiff rail pads. For the soft pad case, the results are almost identical to the results from Case III in Table 5-4. This means that the simplified transfer function Eq. (7-1) introduced in this chapter is acceptable. It is also found that the

pad stiffness only affects the loop gain by a small amount but does not change the unstable frequencies.

Table 7-1. Summary of curve squeal prediction for the case including the track.

Unstable frequencies (Hz)	Stiff pad	150.3	418.2	1102.0	1977.0
	Soft pad	149.2	418.4	1102.0	1977.0
Loop gain	Stiff pad	1.14	5.61	4.43	1.58
	Soft pad	1.29	7.58	4.28	1.53
Wheel modes involved (Hz)		149.4	418.3	1102.0	1976.2
Mode shape (n, m)		(1, 0)	(2, 0)	(3, 0)	(4, 0)

7.2 Introduction of additional features into the track dynamics

The rail mobility considered so far corresponds to the response of an infinite beam over most of the frequency range, with two highly damped resonant peaks at low frequencies (see Figure 7-1(b)). In this section, various additional features are introduced into the track dynamics that can contribute additional resonant-like behaviour, in order to investigate their possible effects on the likelihood of instability. In each case only the track with the soft rail pad is considered.

7.2.1 Effect of pinned-pinned resonance on curve squeal

In practice, the track is not supported continuously but rather on discrete sleepers. This will result in a pinned-pinned resonance at around 1 kHz for the current parameters, at which half the bending wavelength corresponds to the support spacing [1]. Figure 7-2 shows a comparison of the rail mobility with continuous and discrete supports for excitation at mid-span based on the model shown in [1]. It can be seen that the response is hardly affected by the discrete support at low frequencies, but a lightly damped resonant peak is observed at 1072 Hz.

To study whether this pinned-pinned resonance affects the curve squeal predictions, the same procedure described in previous section is adopted here by replacing the rail mobility with the one from the discretely supported rail. The unstable frequencies are shown in Table 7-2. By comparing these with the results from the continuous support, it can be seen that the results are almost identical. Only the loop gain is different, noticeably for the 1102 Hz mode which is closest to the pinned-pinned frequency. Hence, the addition of the pinned-pinned resonance does not significantly affect the curve squeal prediction results.
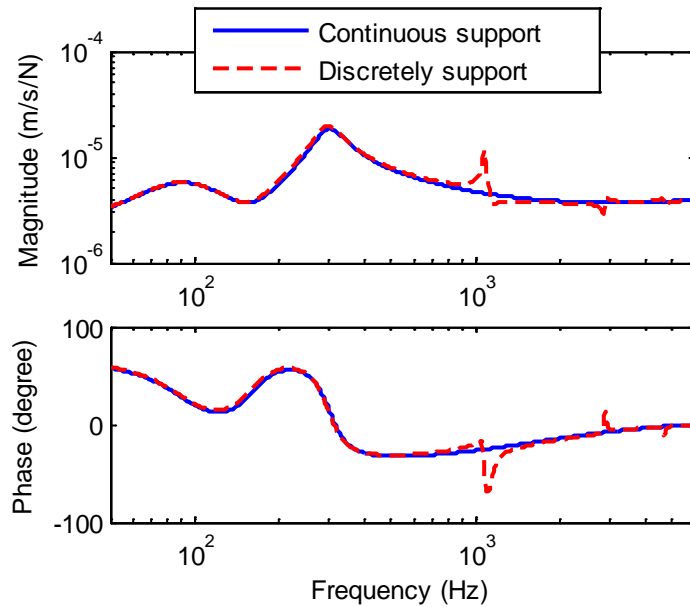
Figure 7-2. Comparison of rail mobility with continuous and discrete support.

Table 7-2. Summary of curve squeal prediction results for different cases

Unstable frequencies (Hz)	Continuous support	149.2	418.4	1102.0	1977.0
	Discrete support	149.0	418.4	1102.0	1977.0
	Multiple wheels	149.0	418.4	1102.0	1977.0
	With cross-section deformation	-	418.4	1102.0	1977.0
Loop gain	Continuous support	1.29	7.58	4.28	1.53
	Discrete support	1.28	7.49	5.74	1.53
	Multiple wheels	1.28	7.68	4.31	1.59
	With cross-section deformation	stable	7.74	4.06	1.64
Wheel modes involved (Hz)		149.4	418.3	1102.0	1976.2
Mode shape (n, m)		(1, 0)	(2, 0)	(3, 0)	(4, 0)

7.2.2 Effect of multiple wheels on curve squeal

In the previous sections, to calculate the rail mobility, the presence of the other wheels on the rail has been neglected. In practice, there are multiple wheels rolling on the track which result in reflections of waves in the rail. In [107] Wu and Thompson have shown that, in the presence of multiple wheels, the point receptance of the rail fluctuates around that of the rail without additional wheels. These additional peaks are equivalent to additional modes in the rail which could increase the likelihood of mode coupling.

For a track with a continuous support, the point mobility of the rail with multiple wheels on it can be written as [107]:

$$Y_w^r = Y_F^r - \sum_{n=1}^{N_w} \frac{[Y_{rT}^F(z_n)]^2}{Y^w + Y^c + Y_F^r} \tag{7-2}$$

where Y_w^r is the point mobility of the track with wheels on the rail, Y_F^r is the driving point mobility of the track without wheels, Y^w and Y^c are the mobilities of the wheel and contact spring, $Y_{rT}^F(z_n)$ is the transfer mobility of the track at a distance z_n from the forcing point (the location of the nth wheel relative to the forcing point) and N_w is the number of additional wheels considered.

The train geometry is chosen to represent a Class 158 regional multiple unit train. Only two bogies are considered, located at the adjacent ends of two carriages (see Figure 7-3). The wheels are numbered from 1 to 4 as shown in Figure 7-3. The dimensions shown are given by $d_1 = 2.6$ m and $d_2 = 4.4$ m.
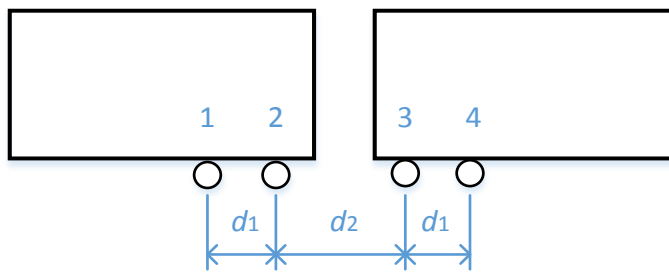
Figure 7-3. Wheel distances of a regional train Class 158.

The excitation is assumed to be at wheel 3; other parameters are the same as those used in Section 7.1. The rail point mobilities obtained by including the other three wheels are shown in Figure 7-4. It can be seen that at low frequencies, where the track decay rate is high (see Figure 7-5), the rail mobility is almost unaffected by the wave reflection due to the additional wheels. Meanwhile, at higher frequencies, when multiple wheels are taken into account, the mobility fluctuates around the one without additional wheels. It can be also observed that the maximum fluctuation exists between about 600 and 1000 Hz. This is because the low decay rate in this frequency range. Above 1000 Hz, there are less fluctuation due to the isolation by the contact stiffness.

The stability of the system is studied when the rail mobility used in Section 7.1.2 is replaced by the one that includes the effect of the other wheels, shown in Figure 7-4. The resulting unstable frequencies are summarised in Table 7-2 from which it can be seen that in the presence of the additional wheels, the predicted frequencies are the same and the loop gain changes only very little. This suggests that the effect on curve squeal of the fluctuations in the rail mobility due to the presence of other wheels is small and can generally be neglected

144

despite the additional peaks in the rail mobility. This also suggests that adding damping treatments to the rail, which could increase the track decay rate and hence suppress these additional peaks, would also not significantly affect curve squeal.
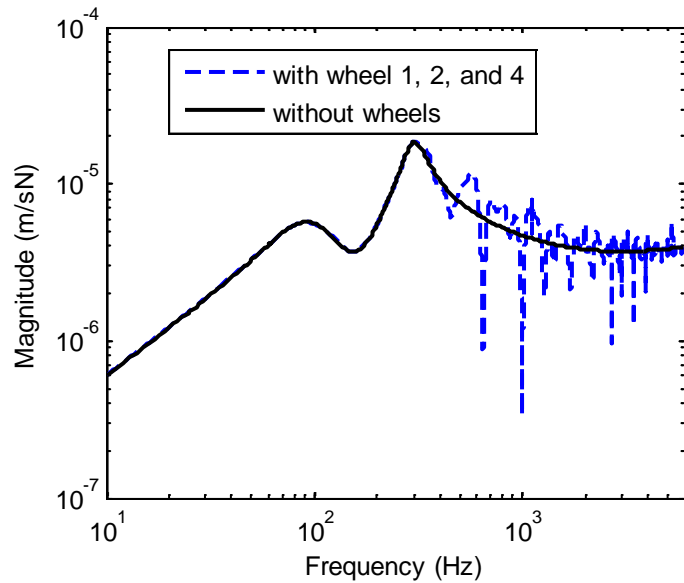
Figure 7-4. The vertical rail point mobilities with and without multiple wheels on it.
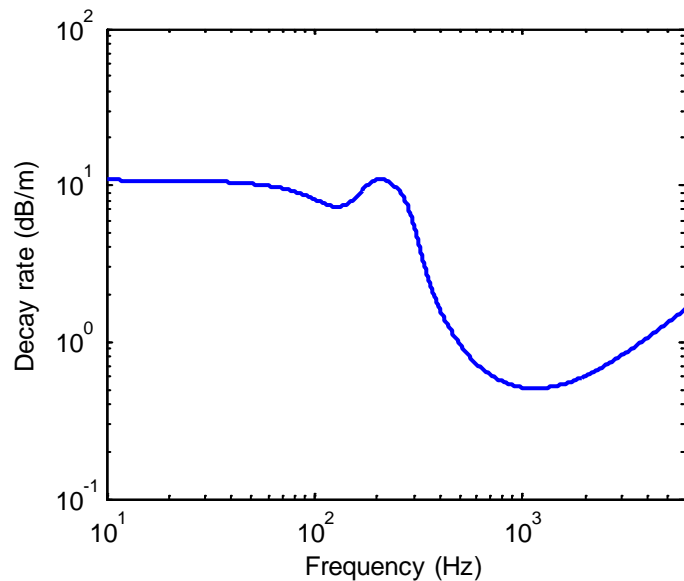
Figure 7-5. The track decay rate.

7.2.3 Effect of rail cross-section deformation on curve squeal

At high frequencies, the rail no longer behaves as a simple beam and cross-section deformation occurs [1]. In the lateral direction, web bending occurs above about 1.5 kHz. In the vertical direction, foot flapping motion starts progressively from above about 2 kHz, leading to a strong peak in the mobility at around 5 kHz.

To explore the effect of rail cross-section deformation, a waveguide finite element (WFE) model, based on the method developed by Nilsson and Jones [108], is adopted to calculate the rail mobilities. This method, also known as semi-analytical finite element (SAFE) or 2.5D finite element, has been used previously in [109] to calculate the dynamic response of a rail and its sound radiation; it was also used by Pieringer [47].

The rail profile used here is again that of a UIC60 rail, and for simplicity only a single-layer support is considered in the WFE model. The FE mesh of the cross-section is shown in Figure 7-6. The shaded areas represent the rail pads which are constrained at their base. The rail and pad material properties used here are given in Table 7-3. The pad is assumed massless. The Young's modulus used for the pad corresponds to a vertical support stiffness of 100 MN/m per pad, which is the same as that used in Section 7.1 for the soft pad.

The driving point mobility at point A (rail head centre, see Figure 7-6) for this WFE model is shown in Figure 7-7. It is compared with the results from the Timoshenko beam model with a double layer support. The first peak in the WFE model corresponds to the rail bouncing vertically on the pad stiffness; the lower frequency peak is missing due to the omission of the sleeper in this model. At high frequencies, in the WFE model the response increases to a peak at around 5.4 kHz; this is due to foot flapping motion [1]. The cross mobility is zero in this case as the rail cross-section is symmetric about the centreline; it will be studied separately below.
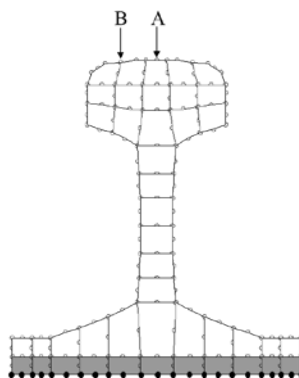
Figure 7-6. FE mesh of the rail cross-section.

Table 7-3. Material properties used for WFE model.

	Rail	Pads
Young's modulus	210 GPa	0.32 MPa
Density	7860 kg/m^3	-
Poisson's ratio	0.3	0.45
Damping loss factor	0.02	0.25
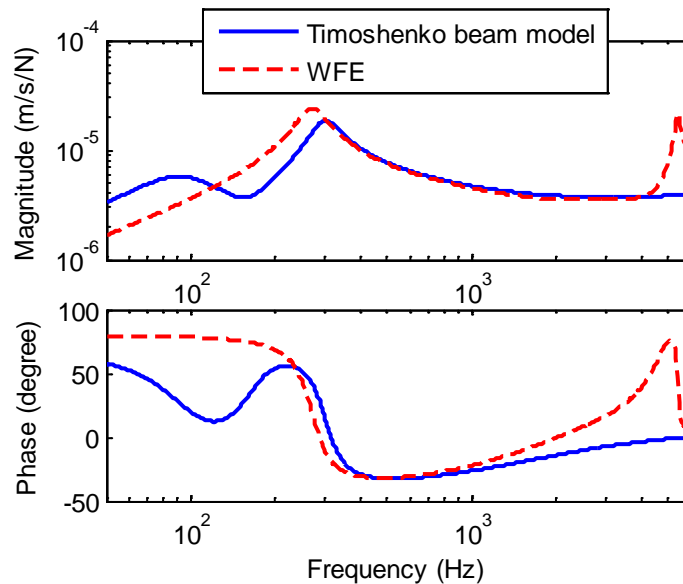
Figure 7-7. The vertical point mobility at the rail head centre.

With this newly calculated rail point mobility, the stability analysis is carried out using the Nyquist criterion, as in the previous examples. The results are again presented in Table 7-2. Compared with the earlier results, the unstable frequency at 150 Hz disappears. This may be associated with a change in the track dynamic behaviour; in this frequency region the rail mobility has changed to become stiffness-controlled whereas previously the phase was close to 0. The other three unstable frequencies are almost identical and the loop gain only changes small amount. No additional unstable frequencies are introduced. Hence, the rail cross-section deformation has a negligible influence on curve squeal when the excitation force is at the rail centre.

7.2.4 Effect of rail cross mobility on curve squeal

The rail cross mobility has been neglected in the beam model of Section 7.1.2. Moreover, the rail cross mobility is zero at the nominal contact point considered above in the WFE model. However Eq. (7-1) showed that the cross mobility of the rail can possibly play a role. In this section, the rail cross mobility is included by considering the contact to be at Point B

in Figure 7-6, which is 18.5 mm away from the rail centre; a contact angle of 3.5° is also introduced. The rail mobilities are again calculated using the WFE method [108].

The rail mobilities at point B are shown in Figure 7-8 for the input parameters in Table 7-3; these are shown in the vertical-lateral coordinate system. Due to the lateral offset the three mobilities show additional peaks representing the cut-on frequencies of higher order waves. In the lateral direction the first and second peaks (70 Hz and 220 Hz) correspond to the rail bouncing on the lateral and rotational stiffness of the pad, while the third and fourth peaks (1360 Hz and 3910 Hz) correspond to web bending waves [1]. Because of the coupling introduced by the lateral offset, the vertical mobility contains peaks at some of the cut-on frequencies of the lateral waves in addition to the two main cut-on frequencies associated with waves in the vertical direction: the vertical bending wave that cuts-on at 270 Hz and foot flapping at 5.4 kHz.

To perform stability analysis, the wheel mobilities are also required at point B and should be expressed in the normal-tangential coordinate system. For simplicity the lateral offset of the wheel is kept the same as that of the rail, i.e. 18.5 mm.

Two different cases are considered. First, the stability is evaluated by accounting for the two rail mobilities (normal Y_{NN} and normal-to-tangential Y_{NT}) as obtained from the numerical model (Figure 7-8) after applying a rigid rotation. Second, the cross term Y_{NT} is set to zero while Y_{NN} is kept the same. Table 7-4 reports the unstable frequencies and loop gains in both cases. By comparing these results with the earlier ones, it can be seen that the instability at 2 kHz disappears while the loop gain at the others reduces. This also occurs in the case where the rail cross mobility term is suppressed, indicating that the changes in the wheel and rail point mobilities and the wheel cross mobility due to the translation and rotation are responsible for this behaviour rather than the introduction of the rail cross mobility term. The only effect of introducing the rail cross mobility is the addition of a low frequency instability at 78 Hz.
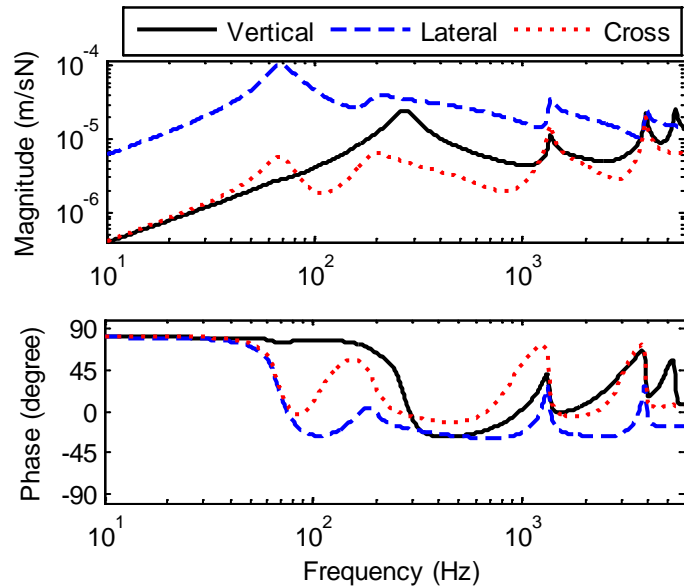
Figure 7-8. The rail mobilities at point B.

Table 7-4.Summary of curve squeal predictions with and without rail cross mobility.

Unstable frequency (Hz)	78.2	418.3	1102.0	1977.0
With no offset (from Table 5)	Stable	7.74	4.06	1.64
With offset (including rail cross mobility)	1.60	1.64	1.26	Stable
With offset (without rail cross mobility)	Stable	1.64	1.26	Stable
Wheel mode involved (Hz)	25	418.3	1102.0	1976.2
Mode shape (*n, m*)	Rigid modes	(2, 0)	(3, 0)	(4, 0)

7.3 A reduced model to represent wheel and rail dynamics

It has been shown in the previous sections that, for a constant friction coefficient, curve squeal can occur with only a single wheel mode coupled to the rail vertical dynamics through the contact stiffness; the lateral rail mobility makes no contribution to the open loop transfer function. To give further insight into the role of the rail dynamics in the instability, a reduced model is presented here. A lumped parameter representation of this model is shown in Figure 7-9. This system is mathematically equivalent to the model presented by Hoffmann et al. in [38]. The wheel and rail are simplified as single-mode systems and a contact spring is used to represent the contact force in the normal direction. The rail mode contains only vertical (or normal) motion whereas the wheel mode contains motion at some angle relative to the normal direction and can therefore be excited by the friction force as well as the normal force.

It is assumed that the mass-spring system representing the wheel is sliding to the right on the rail at a speed corresponding to the lateral sliding velocity during curving.
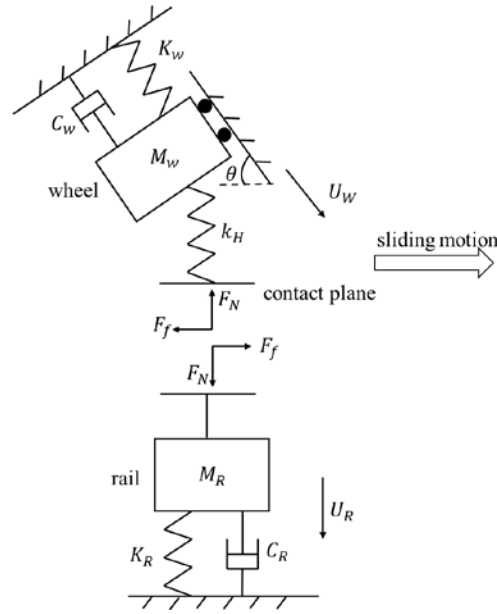
Figure 7-9. Schematic of a reduced model for wheel and rail mode

7.3.1 Equations of motion

For the system shown in Figure 7-9 the equations of motion are:

$$M_w \ddot{u}_w + C_w \dot{u}_w + K_w u_w = -F_N \sin \theta - F_f \cos \theta \qquad (7\text{-}3)$$

$$M_r \ddot{u}_r + C_r \dot{u}_r + K_r u_r = F_N \qquad (7\text{-}4)$$

where M, K, C are the mass, stiffness and damping in each case, u is the displacement, the subscripts w and r represent the wheel and rail, respectively. F_N is the normal contact force, F_f is the friction force, θ is the angle between the direction of u_w and the lateral direction. In the subsequent analysis, the rail will be represented by only one of the terms (mass, stiffness or damping) but all three are retained here for simplicity.

The normal force F_N and the friction force F_f in the contact plane are:

$$F_N = k_H(u_w \sin \theta - u_R) \qquad (7\text{-}5)$$

$$F_f = \mu(\gamma_0)F_N \qquad (7\text{-}6)$$

Hence, writing the equations in matrix form gives:

$$\mathbf{M\ddot{u} + C\dot{u} + Ku} = 0 \qquad (7\text{-}7)$$

where the mass matrix **M**, damping matrix **C** and stiffness matrix **K** are given by:

150

$$\mathbf{M} = \begin{bmatrix} M_w & 0 \\ 0 & M_R \end{bmatrix} \tag{7-8}$$

$$\mathbf{C} = \begin{bmatrix} C_w & 0 \\ 0 & C_R \end{bmatrix} \tag{7-9}$$

$$\mathbf{K} = \begin{bmatrix} K_w + k_H \sin^2 \theta + \mu_0 k_H \sin \theta \cos \theta & -k_H \sin \theta + \mu_0 k_H \cos \theta \\ -k_H \sin \theta & K_R + k_H \end{bmatrix} \tag{7-10}$$

In can be seen from Eq. (7-10) that the friction force results in an asymmetric stiffness matrix which can lead to instabilities [38].

By assuming a solution of the form $\mathbf{u} = \mathbf{u}_0 \exp(st)$, the characteristic equation of this system is found as:

$$\begin{aligned} M_w M_R s^4 + (M_w C_R + M_R C_w) s^3 &+ (M_w k_{22} + C_R C_w + M_R k_{11}) s^2 \\ &+ (C_w k_{22} + C_R k_{11}) s + k_{11} k_{22} - k_{12} k_{21} = 0 \end{aligned} \tag{7-11}$$

where $k_{11}, k_{12}, k_{21}, k_{22}$ represent the four elements of the stiffness matrix in Eq. (7-10). Eigenvalue analysis can then be performed by solving the characteristic equation Eq. (7-11); if one of the eigenvalues has a positive real part, the system can be unstable.

7.3.2 Parameters

Two wheel modes are chosen to be used here, one has a natural frequency of 418.3 Hz and the natural frequency of the other is at 1102.0 Hz. The modal parameters for these two modes (natural frequency f_n, modal displacements in axial and radial directions ϕ_a and ϕ_r, modal mass m_w and modal damping ratio ζ_w) and the corresponding equivalent parameters M_w, K_w and C_w are listed in Table 7-5. These equivalent parameters are derived from the modal quantities as:

$$M_w = \frac{m_w}{\phi_a^2 + \phi_r^2}; \quad K_w = (2\pi f_n)^2 M_w; \quad C_w = 2\zeta_w \sqrt{K_w M_w} \tag{7-12}$$

Table 7-5. Modal parameters of a single wheel mode.

Description and Name		Value		Units
		Mode 1	Mode 2	
	Natural frequency f_n	418.3	1102.0	Hz
Parameter for single wheel mode	Modal mass m_w	0.5	0.5	kg
	Modal displacement in axial direction ϕ_a	0.0809	0.0819	m
	Modal displacement in radial direction ϕ_r	0.0019	0.0037	m
	Modal damping ratio ζ_w	0.0001	0.0001	/
Equivalent parameters	Mass M_w	76.4	74.5	kg
	Damping C_w	40.1	103.2	Ns/m
	Stiffness K_w	0.53×10^9	3.57×10^9	N/m
	θ	1.35	2.58	°

Although the rail is shown in Figure 7-9 as a mass-spring-damper system, its behaviour will be simplified here to that of solely a mass, a stiffness, or a damper separately. This means that three different cases are considered for each wheel mode, as shown in Table 7-6. The values of K_R, M_R and C_R are determined to ensure that, for each case, the rail mobility amplitude is the same as the value in Figure 7-1(b) at the frequency of interest (418 Hz and 1102 Hz), which are equal to 4.53×10^{-6} m/s/N and 9.83×10^{-6} m/s/N, respectively. The linearized Hertzian contact stiffness k_H has the same value as used in Section 7.1.2, which is 1.12×10^9 N/m.

Table 7-6. Parameters of mass-spring-damper system for rail

		M_R	C_R	K_R
Stiffness case	418 Hz	0	0	2.67×10^8 N/m
	1102 Hz	0	0	1.53×10^9 N/m
Mass case	418 Hz	39 kg	0	0
	1102 Hz	32 kg	0	0
Damper case	418 Hz	0	1.02×10^5 Ns/m	0
	1102 Hz	0	2.21×10^5 Ns/m	0

7.3.3 Eigenvalue analysis results

Considering the wheel mode at 1102 Hz, the eigenvalues for the three cases are calculated and shown in Figure 7-10 for friction coefficients μ_0 varying between 0 and 1. For the case in which the rail is represented by a stiffness, the real parts of the eigenvalues are always negative and the system is always stable. For the other two cases, the system can be unstable

and the real parts of the eigenvalues can become positive even with a very small friction coefficient (see Figure 7-10).

The characteristic equation, Eq. (7-11), becomes a quadratic for the stiffness case. The roots are a complex conjugate pair of numbers with the same negative real part (see Figure 7-10(a)); only the positive imaginary part is shown in Figure 7-10(a). When M_R and C_R are set to zero, K_R and k_H act as two springs in series; the whole system is still a single-mode system and cannot become unstable under the constant friction considered here. For comparison Figure 7-11(b) shows the eigenvalue of a system with a rigid rail which also shows a constant and negative real part.

For the mass case, C_R and K_R are set to zero and M_R is non-zero. This makes Eq. (7-11) a quartic equation. The roots (i.e. eigenvalues) are two pairs of complex conjugate numbers (see Figure 7-10(c), again only the positive imaginary parts are shown). The whole system becomes a two-mode system, equivalent to the one introduced in [38], and this can potentially become unstable due to mode coupling. From Figure 7-10(c), it can be seen that, when the friction coefficient becomes larger than 0.05, the real part of one of the eigenvalues can be positive although initially with very small values.

For the damper case, M_R and K_R are set to zero and C_R is non-zero; Eq. (7-11) becomes a cubic equation. One of the eigenvalues is a purely negative real number (the solid line in Figure 7-10(d)) while the other two form a pair of complex conjugate numbers with the same real part (the dashed line in Figure 7-10(d)). Only the positive imaginary part is shown here and it gives an unstable frequency at around 1100 Hz. The close-up figure shows that the real part of the complex number can become positive when the friction coefficient becomes larger than about 0.1. In this case the rail does not introduce another mode to the system, yet instability can still occur.

The same calculations have been carried out with the wheel mode at 418.3 Hz; the results are shown in Figure 7-11. These are similar to the results of Figure 7-10 to wheel mode at 1102 Hz. Again, the system is always stable when the rail is represented by a stiffness, whereas it can be unstable when the rail is represented by a mass or a damper.

From this analysis it can be concluded that the mass and damping behaviour of the rail can induce coupling-type instabilities between the rail and the wheel. When the rail is represented by a mass, this is analogous to the mode-coupling already observed in the literature between pairs of wheel modes. For the case with the rail modelled as a damper, however, the situation is slightly different and it would be incorrect to call this instability

'mode coupling' as the damper representing the rail connected in series with the contact stiffness is not adding an additional mode. The importance of this damping-like behaviour of the rail has practical significance: as can be seen from the mobility in Figure 4-7, the rail behaves in reality like a damper for frequencies above 1 kHz, which is where curve squeal often occurs. the mobility has a constant modulus and a phase close to 0.

In other applications it has been found that a single degree-of-freedom system moving at a constant speed over an infinite beam [110] could become unstable due to the interaction between its own vibration and the structural waves propagating along the infinite beam ('radiation damping'). The calculations presented above show a similar phenomenon although treated from a different perspective and suggest that the damping-like behaviour of the rail could be the source of an instability mechanism behind curve squeal.
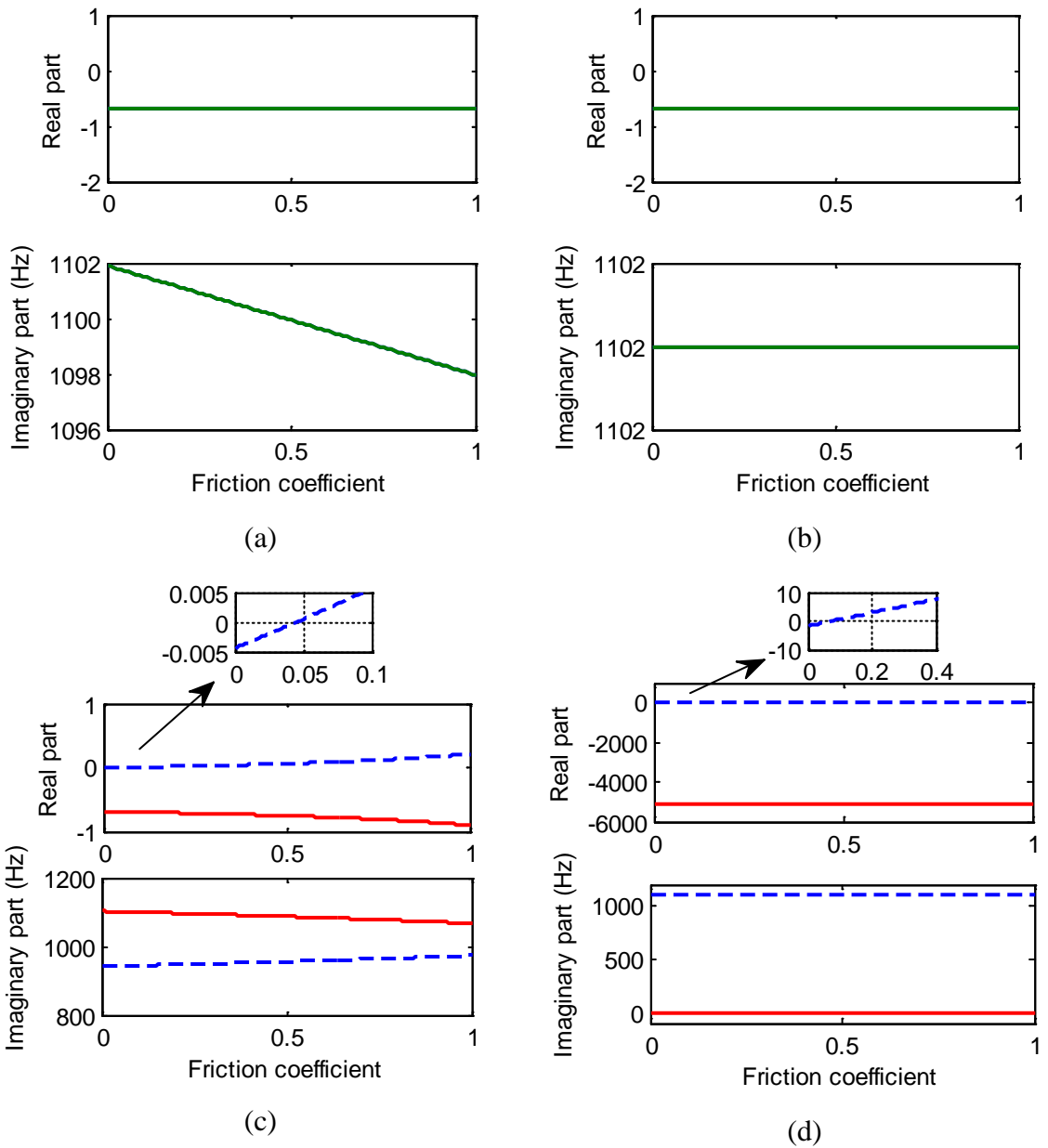
Figure 7-10. Eigenvalue results with 1102 Hz wheel mode: (a) rail represented as stiffness; (b) rigid rail; (c) rail represented as mass; (d) rail represented as damper.
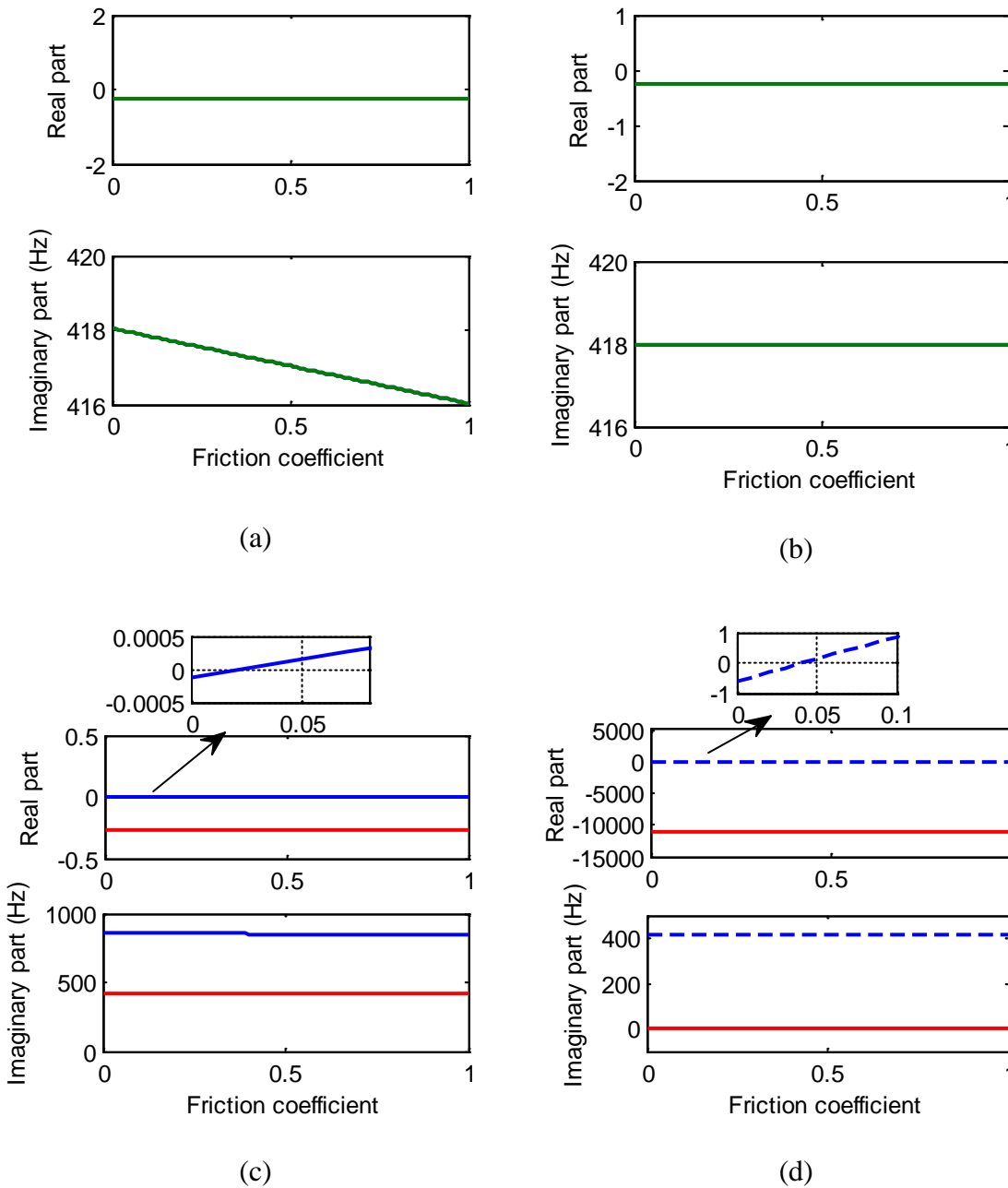
Figure 7-11. Eigenvalue results with 418.3 Hz wheel mode: (a) rail represented as stiffness; (b) rigid rail; (c) rail represented as mass; (d) rail represented as damper.

7.3.4 Time domain analysis

It has been shown for the mass and damper cases above that the reduced model potentially gives unstable response according to eigenvalue analysis. Time domain analysis can be used to evaluate the relative amplitude between the wheel and rail vibration and to study the behaviour in the limit cycle. The friction curve adopted here is based on a constant friction coefficient as shown in Figure 5-1 and the steady state creepage is set to 0.025. The time

domain results are obtained by numerically integrating Eq. (7-3) using a Runge-Kutta method. The FASTSIM routine is used to evaluate $\mu(\gamma)$ at each integration step.

Results are only calculated for the case in which the rail is modelled as a damper with the 418.3 Hz wheel mode. It is found in Section 5.2, with a curve squeal model, for constant friction and including the rail (Case III in Section 5.2), this 418.3 Hz wheel mode is dominant in the time domain response (see Figure 5-6(c)).

The results are shown in Figure 7-12 with the friction coefficient μ_0 set to 0.3. The solution reaches the steady-state condition after 1.1 s where the wheel and rail velocity amplitude are in a ratio of around 40. These results are very close to those shown in Figure 5-6(c). The squealing frequency is at 417 Hz and there is a 15° phase lag between wheel and rail velocities. Another feature of this simulation is that if μ is in the range between 0.1 and 0.2, although the eigenvalue analysis gives instability with a small positive real part, the time domain solution is mildly stable and/or results in a limit cycle after a much longer time. This is because that the real part (growth rate) of the eigenvalue is too small to make the system response achieve a limit cycle in a short time.

Time domain results are not presented for the case in which the rail is modelled as a mass as this is an extreme case and it is not representative of the track in any situation. Results (not shown here) show exaggerated fluctuations of the normal load that would cause the total vertical forces to become negative.
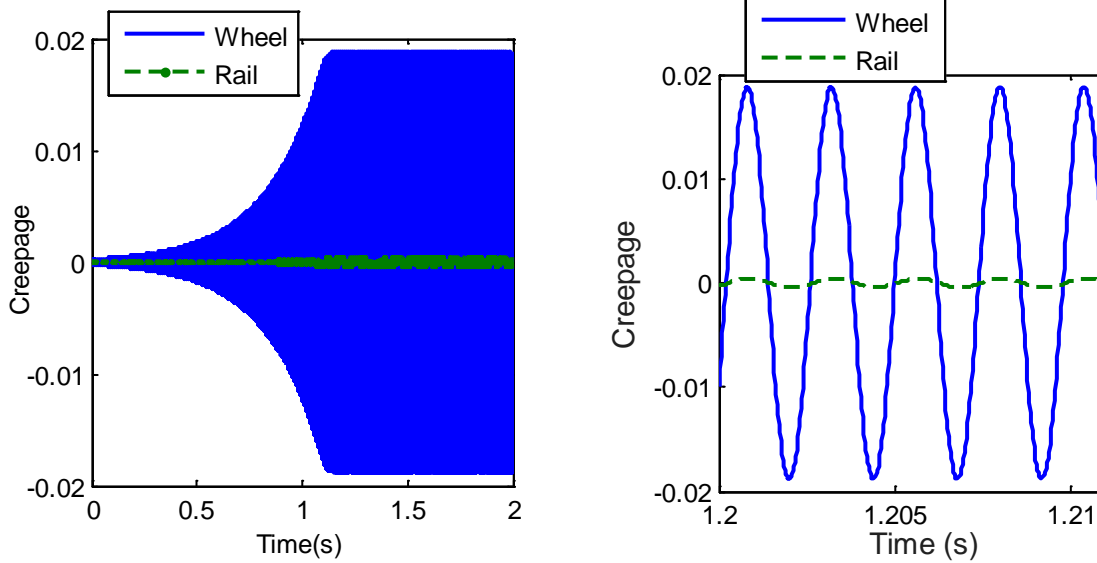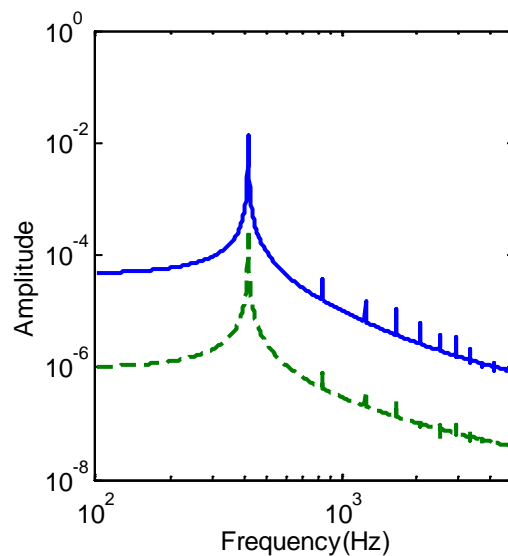
Figure 7-12. Time history results of case with the rail represented as a damper with 418.3 Hz wheel mode: (a) time domain solution; (b) close-up; (c) spectra of limit cycle.

7.3.5 Stability map for a single wheel mode with simplified rail dynamics

In the previous subsections the rail was represented as a mass, a spring or a damper. In this section, intermediate cases are considered in the frequency domain by assuming the following generic form for the rail mobility:

$$Y_{VV} = 4.53 \times 10^{-6} \times \left(\frac{i\omega}{2\pi \times 1102} \right)^{\alpha} \tag{7-13}$$

where ω is the angular frequency, and α is in the range between -1 to 1.

With this expression, the magnitude of the rail mobility will be always 4.53×10^{-6} m/s/N at 1102 Hz, as in Figure 7-1(b). The slopes of the mobility, and the corresponding phase angle, are different for different values of α. Figure 7-13 shows the magnitude and phase of the mobility for five different values of α. When α is equal to -1, 0 or 1, the rail dynamics are equal to those of a mass, a damper or a stiffness, as considered in Section 7.3.3. To study the stability of this system, the mobility approach is adopted to evaluate how the coefficient α affects the stability of the system. For the wheel, only the mode at 1102 Hz is included.
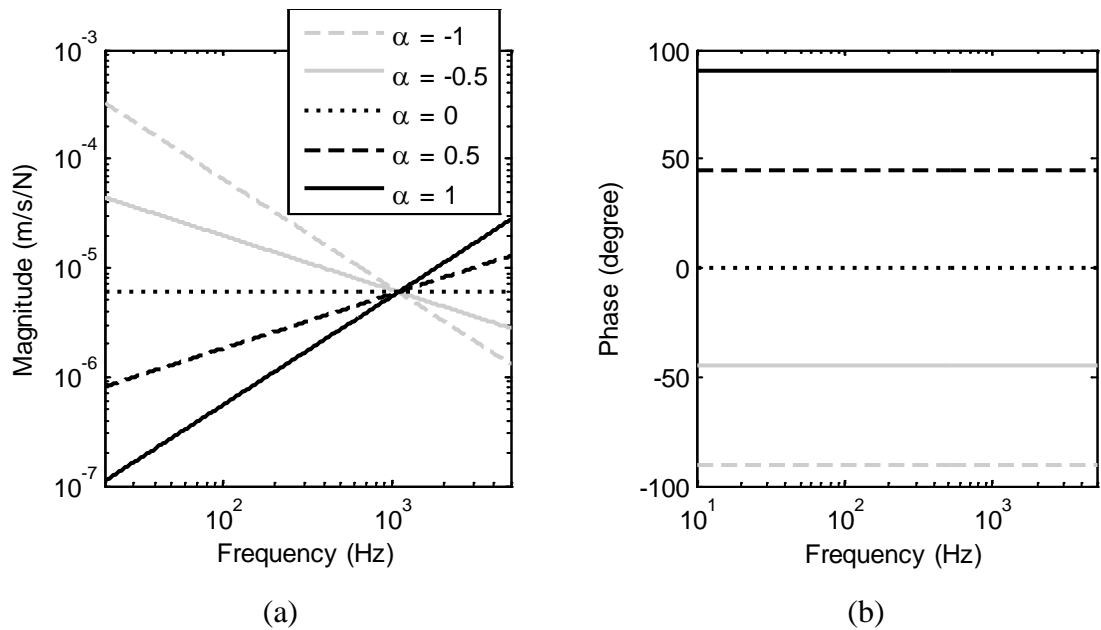
Figure 7-13. Magnitude and phase of simplified rail point mobility with different values of α: (a) magnitude; (b) phase.

Figure 7-14 shows the stability map of the system obtained by varying both α and μ_0 for different values of the wheel damping ratio. The stable areas are always to the left of the corresponding lines. When α is equal to -1 or 0, the system can be unstable with very small friction coefficient. However, when α is equal to 1, it is always stable. These results agree with those given in Section 7.3.3. For other values of α, the system can be unstable although a high value of friction coefficient is needed when α is close to 1.

Increasing the wheel damping ratio stabilises the system, except for the case of $\alpha = -1$, in which the transition between stable and unstable areas is always at $\mu = 0.05$; this is equal to $\tan \theta$ from the mode shape of the 1102 Hz wheel mode (compare the upper right term in

Equation (7-10)). This phenomenon is also found for the 418 Hz mode although not shown here.
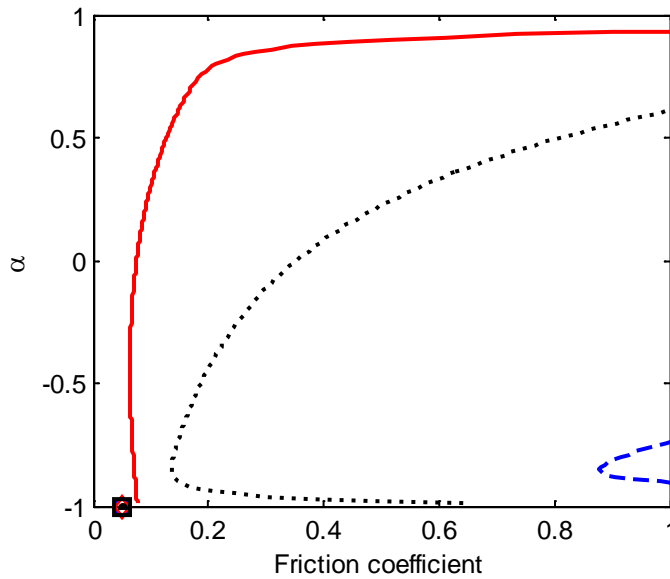
Figure 7-14. Stability map for different combinations of α and μ: solid line: $\zeta_w = 0.0001$; dotted line: $\zeta_w = 0.001$; dashed line: $\zeta_w = 0.01$.

7.4 Summary

The role played by the track dynamics in curve squeal has been investigated in this chapter. Attention has been focused on the situation with a constant friction coefficient. The track has been represented by various models of increasing complexity. Initially it is modelled as an infinite Timoshenko beam on a two-layer elastic foundation. It has been demonstrated that even with this track model single wheel modes can couple with the rail and give squeal.

Subsequently, various effects have been considered that may introduce additional resonant behaviour into the rail dynamics. These include the effect of varying the rail pad stiffness, the influence of the periodic support of the rail, reflections between multiple wheels on the rail, and rail cross-section deformation. The effect of the rail cross mobility has also been explored. However, the results show that all these factors have little influence on the predicted curve squeal instabilities.

By introducing a reduced model, in which the wheel and rail are represented by single-degree-of-freedom systems, the main characteristics of the rail dynamics that can result in squeal are then assessed. It is shown that the mass and damping-like behaviour of the infinite rail are at the origin of the instabilities associated with wheel-rail coupling rather than any modal or pseudo-modal behaviour of the track. Curve squeal may occur for a single wheel mode even if the rail is represented by a damper, which is a close approximation to the real

behaviour of the track at high frequencies. This indicates that it is not necessarily the introduction of 'modes' in the rail that causes the wheel modes to couple with the rail; instead the equivalent mass and especially damper behaviour of an infinite rail is the origin of the wheel-rail coupling phenomenon.

Although the number of the cases analysed is limited, thus not allowing for general conclusions, it is unlikely that the changes in the track dynamic parameters will affect the results and comments given before significantly.

8 Laboratory measurements

8.1 Introduction

Throughout this thesis it has been shown that mode coupling can be another possible cause for curve squeal noise in addition to falling friction. It has been demonstrated that, where this is the case, phase difference and frequency shift are important indicators of mode coupling. This has been observed from both numerical modelling and field test results. For the purpose of further investigating curve squeal instabilities, a laboratory measurement has also been designed and some simple tests have been performed. The initial aim of this test was to reproduce, in a controlled environment, a mode coupling instability on a scale model of a railway wheel. An available machine, originally designed to perform pin-on-disc tests [111], has been adapted to fit a 1:5 model of a railway wheel.

Modal tests have first been performed on the free wheel and on the wheel resting on the disc. These are described in Section 8.2. The measurement set-up and results are presented in Section 8.3. A comparison between measurements and an equivalent model is shown in Section 8.4.

The analysis of the experimental results presented in this chapter is focused around the following topics. (i) Is it possible from these tests to demonstrate whether the mechanism in this situation is mode coupling or falling friction? (ii) Is there phase shift between the axial and radial vibration response? (iii) At what frequency does wheel squeal occur and how does this differ from the natural frequency of the free wheel?

8.2 Impact test of a wheel disc

8.2.1 Measurement set-up

Before the squeal test was carried out, impact tests of the wheel disc were performed to obtain its modal parameters. The wheel is in 1:5 scale (20 cm in diameter actual size). This wheel disc was used in [112] for rolling noise and railway squeal test rig measurement; in this case the wheel was set to roll on a circular track with a diameter equal to 3 m[3]. In the current set-up the wheel was clamped at the wheel hub on the vertical arm of the pin-on-disc

---

[3] This measurement rig is no longer available at the University Of Southampton.

machine using bolts and nuts (see Figure 8-1(a)). Two accelerometers (type: PCB 352C22) were fixed at point 1 to measure vibration in the radial and axial directions (see Figure 8-1(b)). Eighteen measured positions were chosen, as shown in Figure 8-1(b), with positions 1 to 16 evenly distributed around the circumference with a 22.5° angular interval. Three impacts were given for both axial and radial directions at points 1 to point 16. Positions 17 and 18 are lateral along a radial line and only axial impacts have been carried out to help identify the nodal circles. The type of the hammer is PCB 086C03 with a steel tip. Time domain data were acquired with a PXI-4496 card and analysed separately in Matlab.
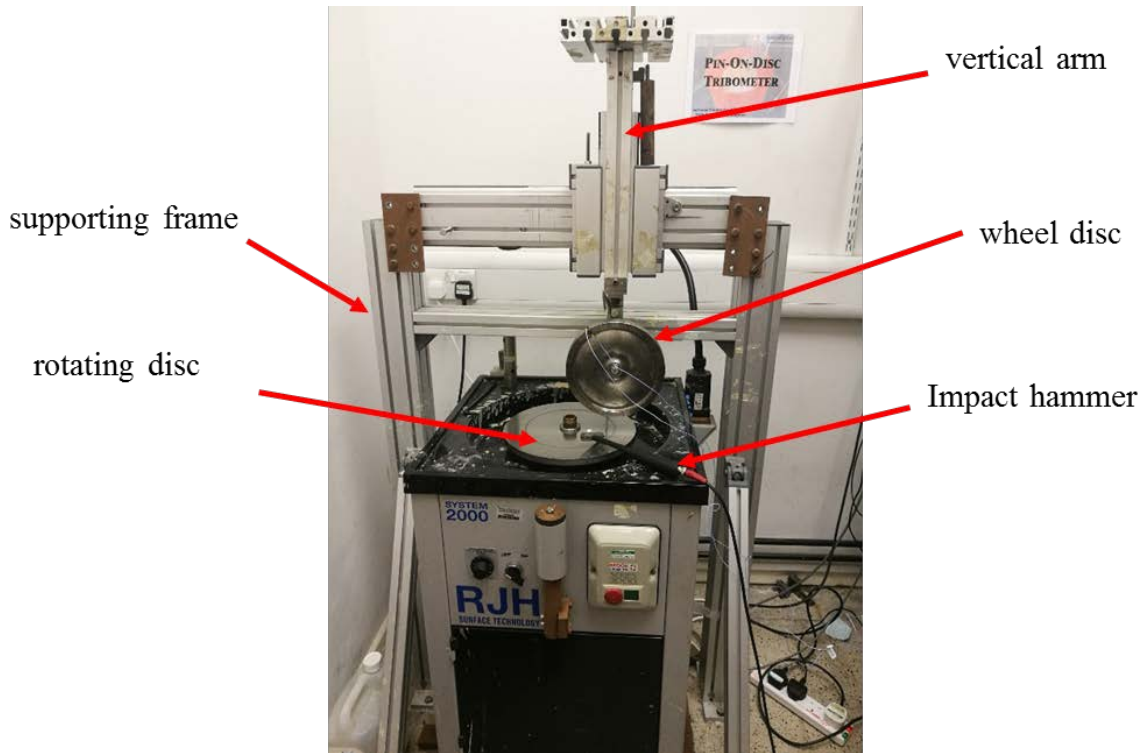
(a)
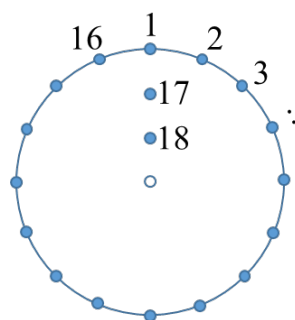
(b)

Figure 8-1. Impact test set-up and the measurement points in the wheel disc. (a) wheel disc and rotating disc; (b) measured positions.

The time signals were post-processed and averaged by applying a Fourier transform to obtain the frequency response functions (FRFs). After the FRFs are obtained, a modal analysis software (developed in-house) was used to identify the modal parameters. This software is based on curve fitting the modal superposition equation and the measured FRFs. The superposition equation is [97]:

$$Y_{jk} \cong \sum_{n}^{N} \left(\frac{i\omega\phi_{jn}\phi_{kn}}{(\omega_n^2 - \omega^2 + 2i\zeta_n\omega\omega_n)} \right) \tag{8-1}$$

where Y_{jk} is the mobility between a force at location k and the reponse at location j, ϕ_{jn} is the mass-normalised modeshape of mode n at location j, ζ_n is the damping ratio of mode n, ω_n is the angular natural frequency of mode n and ω is the angular frequency. Residuals terms are not included in the analysis as the main goal was initially to identify the modes. However, the effect of the mass-like residual term is analysed separately below.

8.2.2 Measurement results

The measured driving point mobilities of the clamped wheel (at the hub) are shown in Figure 8-2. It can be seen that in the frequency range 1 kHz to 6 kHz, there are three axial modes at 1026 Hz, 2884 Hz, and 5428 Hz, which also have a small radial component. There is also a radial mode at 3838 Hz, the axial component of which is extremely small. From this mobility result, it can be deduced that mode coupling is not likely to exist for this wheel. This is because the important modes above 1 kHz only have a significant mode shape in one direction whereas according to the studies in Chapter 6 modes that are prone to couple with each other should have a significant component of the mode shapes in both directions.

The modal parameters for the four important modes after curve fitting of the modal superposition equation are summarised in Table 8-1. The mode shapes for different modes are plotted in Figure 8-3 to Figure 8-6, where the dashed line indicates the undeformed wheel and the solid line is the deformed mode shape. The x and y coordinates are the components of radial modal displacements while the z coordinate is the axial modal displacement. It can be seen that there are 2, 3, and 4 nodal diameters for the modes at 1026 Hz, 2884 Hz and 5428 Hz respectively, while the mode at 3838 Hz is a radial mode with 2 nodal diameters. The modal parameters for the modes are summarised in Table 8-1, these will be used to represent the dynamic behaviour of this wheel in Section 8.4.
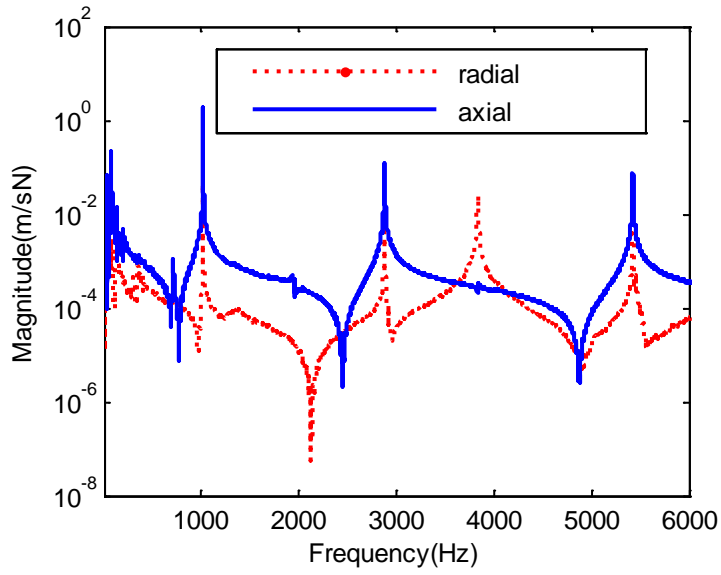
Figure 8-2. Measured driving point mobilities of the clamped wheel disc.
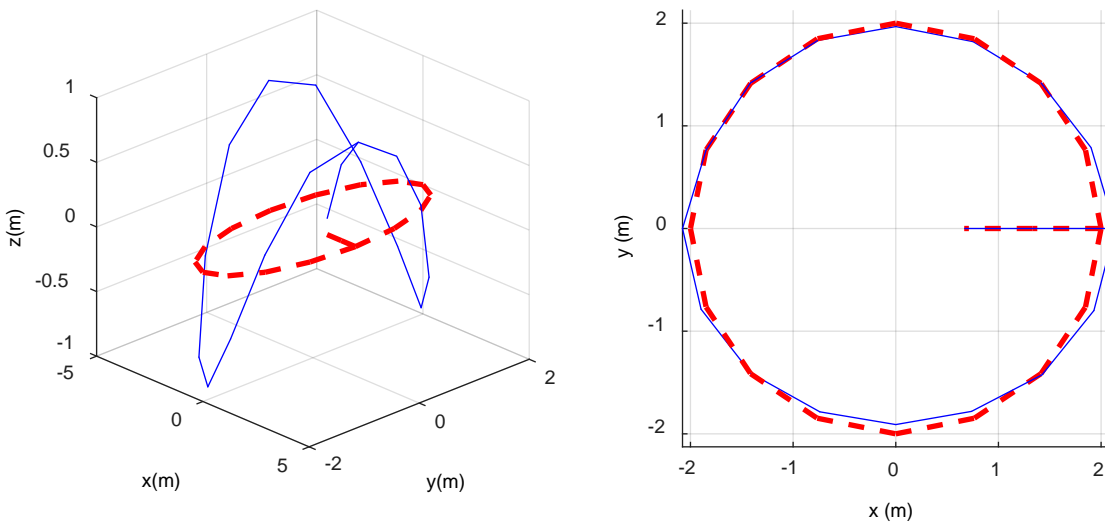
Figure 8-3. The modeshape of the mode at 1026 Hz for 3-D view and top view: red dashed line: undeformed; blue solid line: deformed.
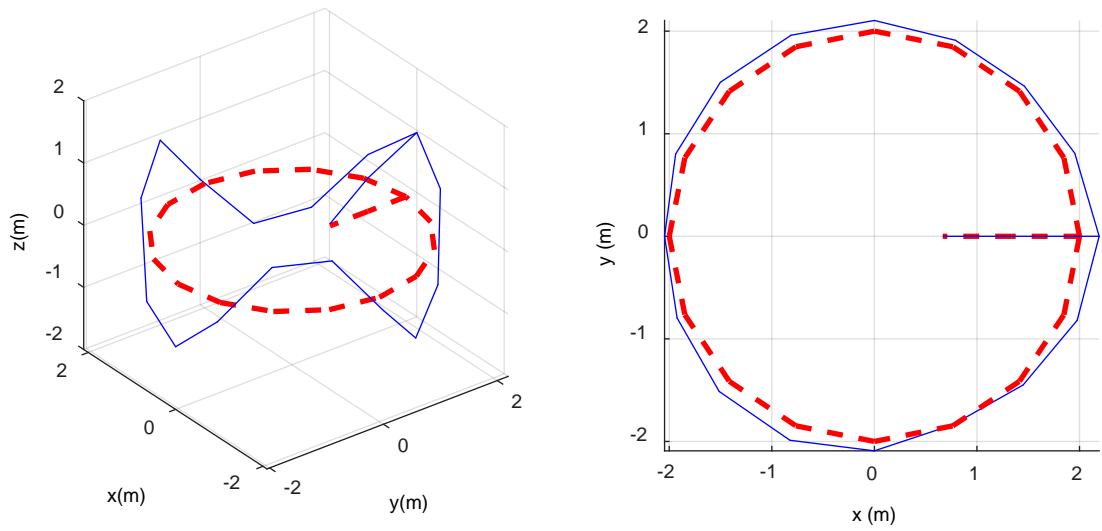
Figure 8-4. The modeshape of the mode at 2884 Hz for 3-D view and top view: red dashed line: undeformed; blue solid line: deformed.
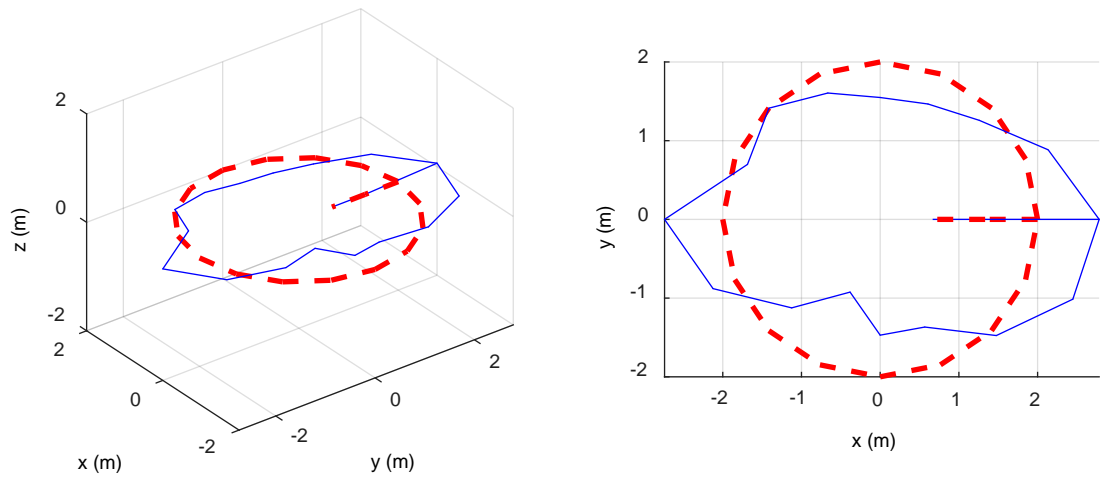
Figure 8-5. The modeshape of the mode at 3838 Hz for 3-D view and top view: red dashed line: undeformed; blue solid line: deformed.
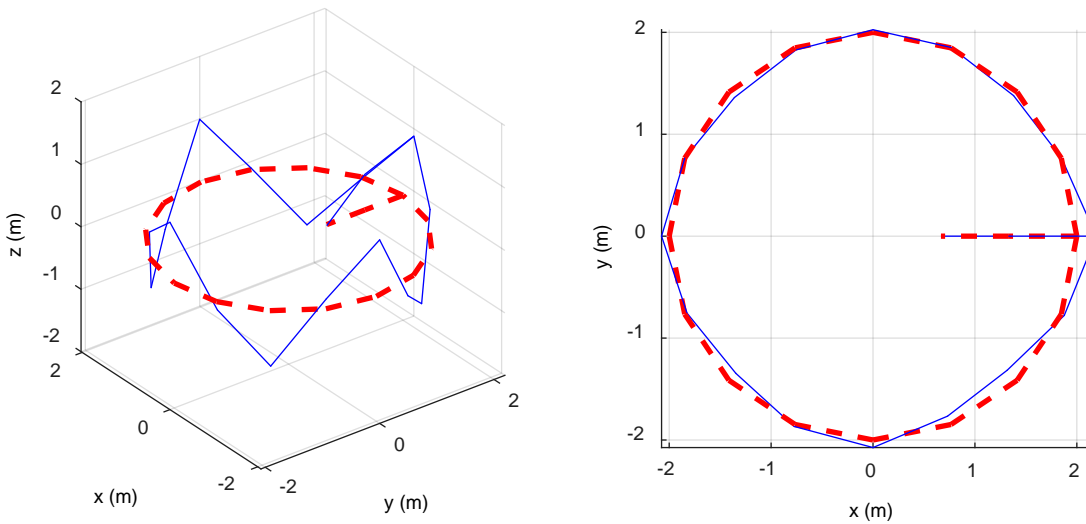
Figure 8-6. The modeshape of the mode at 5428 Hz for 3-D view and top view: red dashed line: undeformed; blue solid line: deformed.

Table 8-1. Modal parameters from measurement.

Frequency (Hz)	(n, m)	Modal mass (kg)	Axial Mode shape (m)	Radial mode shape (m)	Damping ratio
1026	(2, 0)	1	1.31	0.21	6.0×10^{-5}
2884	(3, 0)	1	0.97	0.18	1.5×10^{-4}
3838	radial	1	0.08	0.95	8.1×10^{-4}
5428	(4, 0)	1	0.98	0.22	1.5×10^{-4}

The impact test for the wheel suspended on elastic bungees and for the clamped wheel (at the hub) resting on the disc of the pin-on-disc machine were also performed to assess the effect of these different boundary conditions. For the wheel resting on the disc, the excitation point was selected to be at the top of the wheel, which is 180° from the contact point. The results are compared in Figure 8-7. It can be seen that for frequencies above 1 kHz, the results for the clamped wheel and the clamped wheel resting on the disc are almost the same. However, for this frequency range, two modes at 1183 Hz and 1917 Hz found for the free wheel no longer exist when the wheel is clamped. This is because the wheel is now constrained at the hub. The frequency of the radial mode at 3.8 kHz changes when the wheel is resting on the disc.
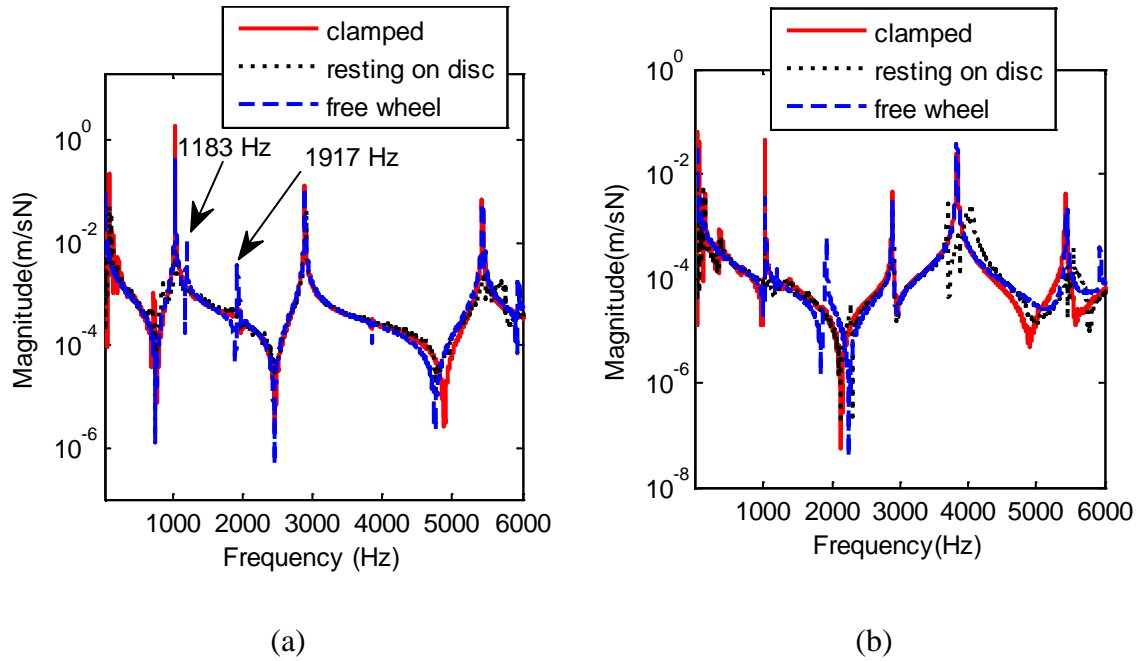
Figure 8-7. The comparison of wheel mobilities of clamped wheel, wheel resting on the disc and free wheel: (a) axial direction; (b) radial direction.

8.3 Vibration test of the reduced scaled wheel on the rotating disc

8.3.1 Measurement set-up

The 1:5 scale wheel disc is clamped at the hub and located on a rotating disc as shown in Figure 8-8. The rotating disc is made of stainless steel and it lies in the horizontal plane whereas the wheel is in the vertical plane with its axis tangential to the rotating disc. Note that in this configuration the wheel is not rolling and the arrangement is intended to represent a situation where pure lateral sliding occurs. The rotating disc is driven by a motor and the rotating speed is controlled by an existing feedback algorithm implemented in LabVIEW. The angular velocity of the disc sets the amount of lateral sliding at the disc/wheel interface. The surface of the disc was cleaned before the test to make sure the surface contact condition is generally the same when the disc starts to rotate. The distance between the contact point and centre of the rotating disc is 10 cm. The normal load is the weight of the wheel plus the arm, which was measured to be 30.4 N and is therefore taken as the nominal normal load. The lateral force was measured using a force transducer (OBBS Bending Beam Load Cell) placed on the arm that connects the wheel hub to the rig frame. Because the transducer is fitted away from the contact point, its results can only be used in an average sense and cannot

169

give information on the local instantaneous contact force. The wheel vibration at the contact is measured in the vertical and axial directions using the same two accelerometers adopted for modal testing. A water pipe can be used to add water onto the rotating disc to create a watered contact condition between the wheel and the rotating disc.

It is important to note that the vibration measurement designed here has a number of simplifications and assumptions: i) the wheel is not rolling; ii) only the lateral sliding velocity is known while the creepage is undefined; iii) the rail dynamics is not present; iv) the normal load fluctuation is not measured and only a constant nominal load is used to estimate the friction coefficient. For these reasons, this rig is not fully representative of a realistic case. However, the fundamental features of squeal can be captured to help understand and explore the effects of the different mechanisms behind curve squeal.

force transducer

touch position in Series B measurement

contact position

plastic water pipe

(a)

force transducer
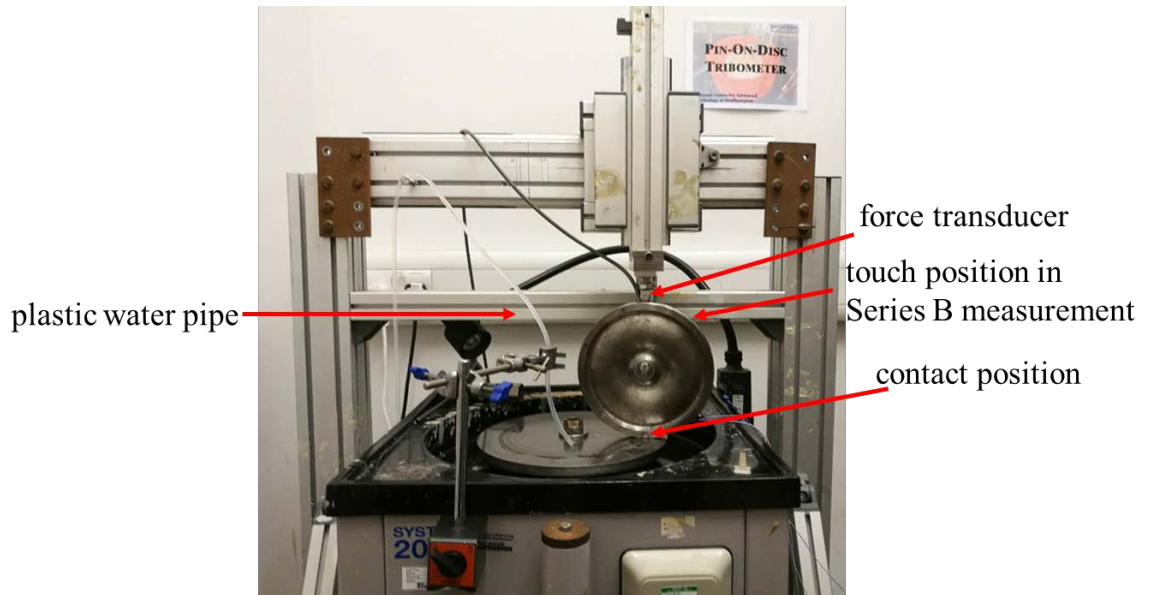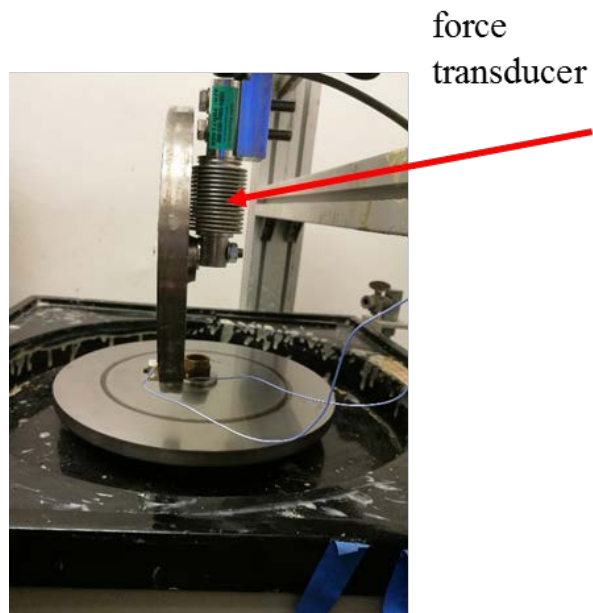
(b)

Figure 8-8. The measurement set-up of the wheel on the pin-on-disc machine: (a) front view; (b) side view

8.3.2 Measurement results

8.3.2.1 Vibration response data

For entirely dry contact conditions squeal noise was not found. Instead, in this situation a low frequency rattling noise was always present, probably due to the flexibility of the rig frame. However, after applying some water at the contact area, squeal occurred. Two different squealing frequencies were found in two different sets of measurements.

- Series A: a constant thin film of water was always present on the rotating disc in the region in front of the contact area, and the rotating speed was varied between 2.9 rev/min and 13.5 rev/min. In this configuration the wheel was squealing at 1 kHz.

- Series B: as it was found that occasionally the wheel was starting to squeal at 2.9 kHz in this second series the wheel was forced to vibrate according to the mode at 2.9 kHz. This was achieved by touching the wheel at the position corresponding to the nodal diameter of this mode. This position is marked in Figure 8-8 (a).

For each series, an example of acceleration data in the time domain is shown in Figure 8-9 and Figure 8-10. It can be seen that the acceleration amplitudes for Series B are higher than those for Series A. However, the velocity amplitude for both series at the same rotational speed are similar due to the different squealing frequency of the two series, as will be shown in the next section.
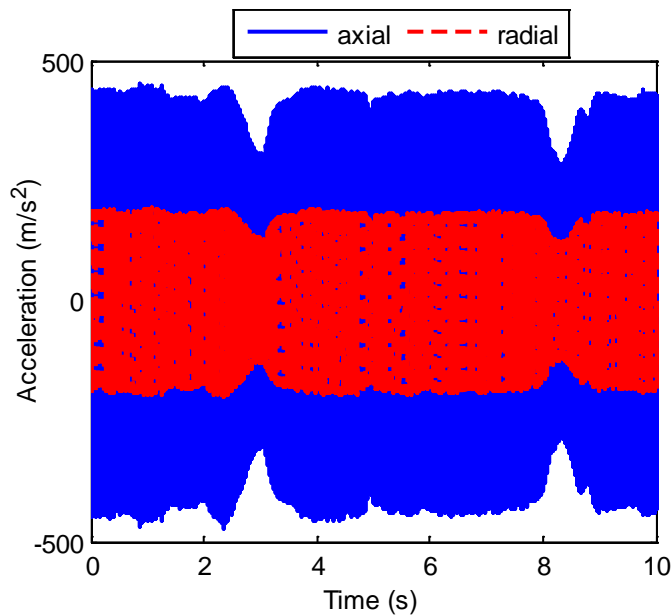
Figure 8-9. An example of vibration time history for rotational speed of 6.8 rev/min from Series A
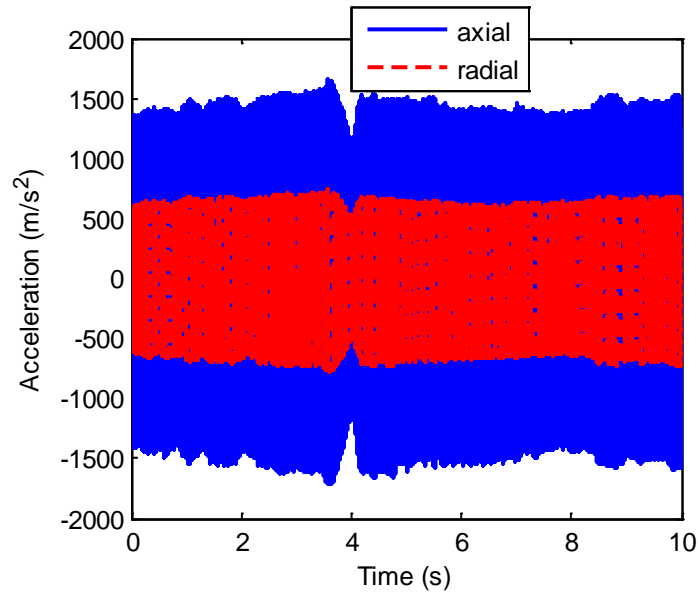
Figure 8-10. An example of vibration time history for rotational speed of 8.2 rev/min from Series B

8.3.2.2 Friction data

The lateral force measured by the force transducer is assumed to be equal to the average friction force. Some examples of the force time history are shown in Figure 8-11 and Figure 8-12. They are from the same measurement series. A low-pass filter (Butterworth filter) has been applied to both examples with a cut-off frequency of 20 Hz and order of 2. To achieve this, first the butter function in Matlab is used to get the transfer function coefficients and then filtfilt function is used to get the output data after filtering. It can be seen that the force signal is noisy and that it is fluctuating during the measurement. This fluctuation can be because the fluctuation of the normal load in the measurement. In Figure 8-11 the rotational speed is 6.8 rev/min and this means the period of this rotating disc is around 9 s. It can be seen from Figure 8-11 that the lateral force also has a period of around 9 s. This means that similar values of lateral force always correspond to the same angular position on the disc. The same features can found in Figure 8-12 for a different rotational speed.

173
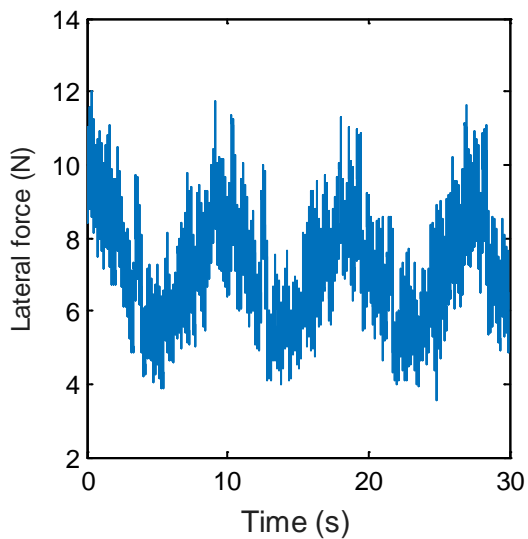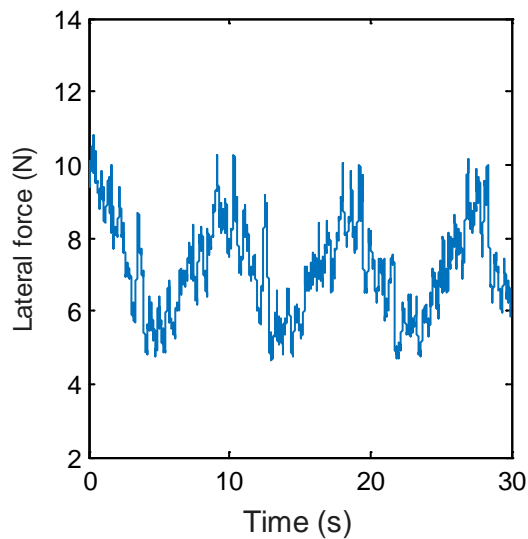
(a)   (b)

Figure 8-11. An example of lateral force time history for rotational speed of 6.8 rev/min for Series A: (a) original time data; (b) after applying low pass filter (20 Hz).
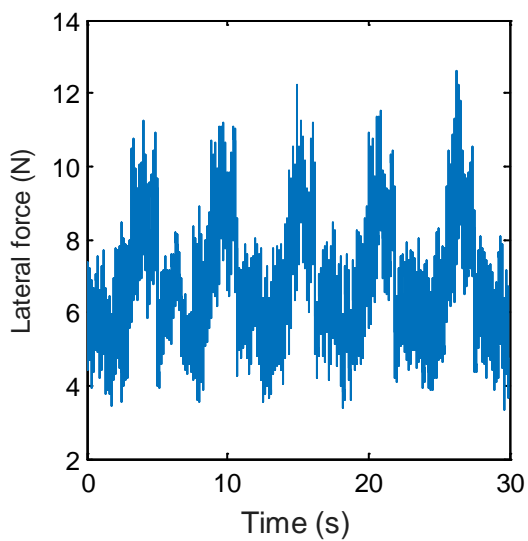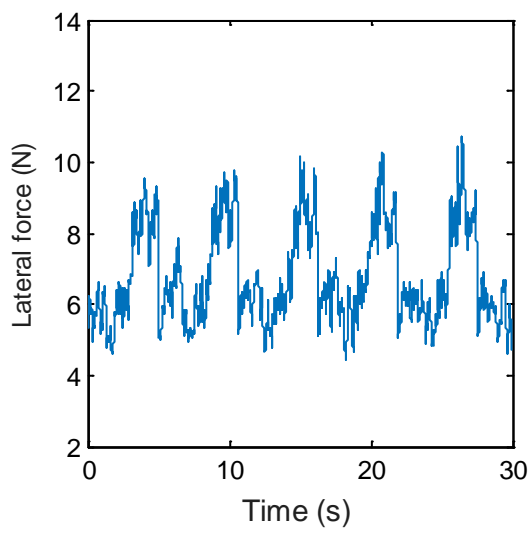
(a)   (b)

Figure 8-12. An example of lateral force time history for rotational speed of 10.8 rev/min of Series A: (a) original time data; (b) after applying low pass filter (20 Hz).

8.3.3 Discussion

8.3.3.1 Mechanism

The spectra of the lateral acceleration in squeal window are shown in Figure 8-13 and Figure 8-14. It is found that the squealing frequency for Series A is at around 1 kHz, while for Series B the squealing frequency is about 2.9 kHz. Higher harmonics can be found due to nonlinearities. Similar results are found for other rotational speeds for each series of measurement. The squealing frequencies for each rotational speed are summarised in Table 8-2. The local sliding velocity can be calculated according to:

$$v = \frac{\omega_{RPM} 2\pi}{60} R_c$$

where ω_{RPM} is the rotational speed in rev/min and R_c is the distance from the centre of the rotating disc to the contact position(R_c =0.1 m).

For either of these two squealing frequencies, there is only a single wheel mode nearby. According to the impact test, the wheel mode (2, 0) at 1026 Hz is close to squealing frequency of the Series A measurements. For the squealing frequency of Series B, there is a single wheel mode (3, 0) at 2884 Hz nearby. Hence mode coupling seems not to be present in these measurements. Other alternatives are therefore falling friction or a simple stick-slip. The squealing frequency for each run are summarised in Table 8-2 and Table 8-3. By comparing the squealing frequencies (see Table 8-2 and Table 8-3) with the natural frequencies of the wheel, it is found that the frequency is almost the same as the natural frequency of the corresponding wheel mode.

By looking at the close-up of the acceleration time histories, it can be seen that the vibration response in the axial and radial directions are always in phase (see examples in Figure 8-15). The phase shifts have been calculated and are shown in Table 8-2 and Table 8-3. They are calculated in a similar way as described in Section 6.7. The threshold of lateral vibration level to be considered as squealing is 100 m/s^2 (rms) for Series A and 500 m/s^2 (rms) for Series B. It can be seen that they are all close to 0° and this means that for these measurements, the phase shift is almost absent. In Chapter 6 it is also shown that phase shift is one of the characteristics of mode coupling and by introducing the falling friction, the phase shift tends to become 0 (or 180°) with increasing the slope of friction curve.
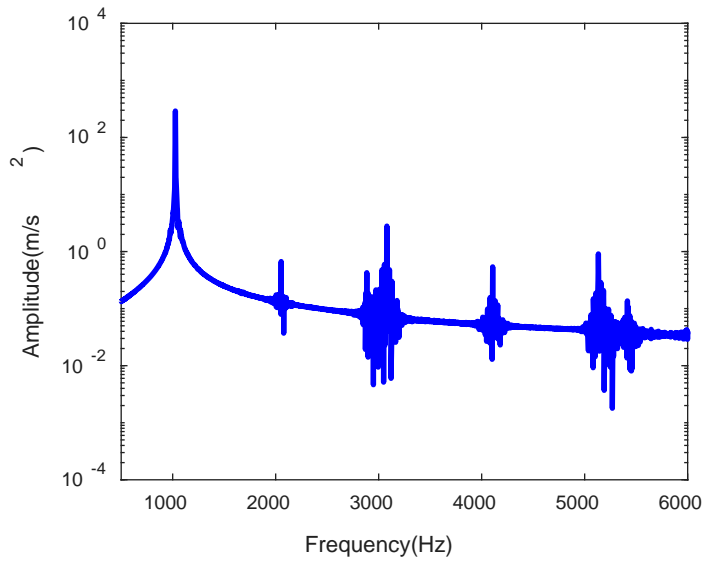
Figure 8-13. Spectrum of the lateral acceleration in a squeal window with rotational speed as 6.8 rev/min of Series A
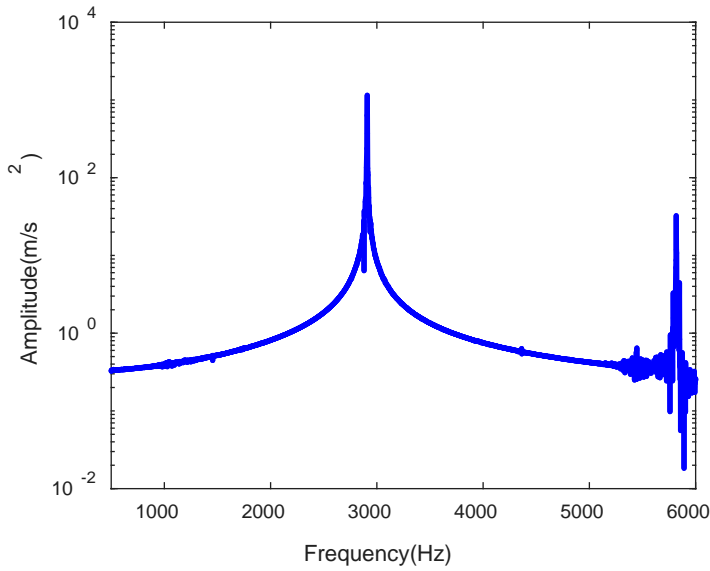
Figure 8-14. Spectrum of the lateral acceleration in a squeal window with rotational speed as 8.2 rev/min from Series B
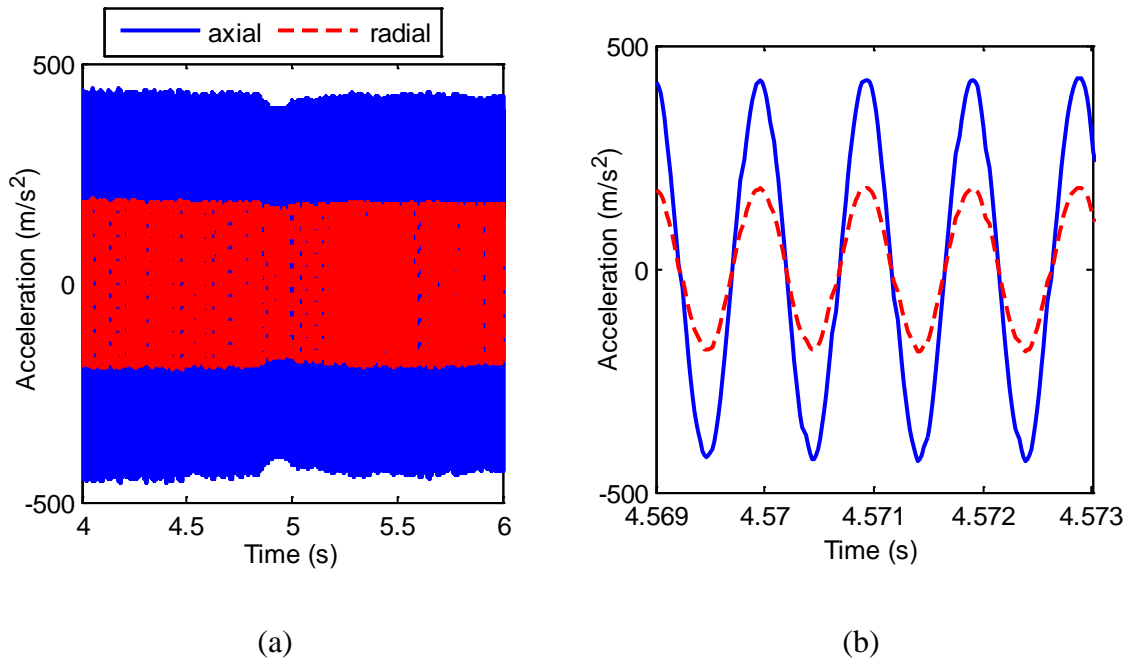
Figure 8-15. An example acceleration time history with rotational speed 6.8 rev/min and its close-up from Series A: (a) acceleration time history; (b) close-up.

Table 8-2. The average squealing frequency and phase difference of Series A.

Rotational speed (rev/min)	Sliding velocity at the contact (m/s)	Average squealing frequency and its standard deviation (Hz)		Difference between squealing frequency and the 1026 Hz mode (Hz)	Average phase difference and its standard deviation (degrees)		Wheel axial velocity (m/s)
2.9	0.030	1026.7	4.5	0.7	-0.08	1.50	0.026
4.2	0.044	1026.2	0.8	0.2	0.01	0.40	0.038
5.5	0.058	1027.2	1.0	1.2	-0.14	0.40	0.056
6.8	0.071	1028.0	1.2	2.0	-0.16	0.25	0.064
8.2	0.086	1026.6	1.4	0.6	0.02	0.03	0.071
9.5	0.099	1026.7	0.4	0.7	0.18	0.23	0.090
10.9	0.114	1028.0	3.3	2.0	-0.18	0.15	0.100
12.2	0.128	1026.7	0.4	0.7	-0.35	0.24	0.118
13.5	0.141	1026.7	4.4	0.7	0.21	0.19	0.130
20.1	0.211	1027.3	0.9	1.3	-0.02	0.24	0.245

Table 8-3. The average squealing frequency and phase difference of Series B.

Rotational speed (rev/min)	Sliding velocity at the contact (m/s)	Average squealing frequency and its standard deviation (Hz)		Difference between squealing frequency and the 2884 Hz mode (Hz)	Phase difference and standard deviation (degrees)		Wheel axial velocity (m/s)
4.2	0.044	2907.0	3.4	23.0	0.16	0.12	0.035
5.5	0.058	2891.1	3.9	7.1	0.01	0.02	0.053
6.8	0.071	2894.5	4.2	10.5	0.13	0.03	0.066
8.2	0.086	2895.6	2.4	11.6	0.06	0.04	0.077
9.5	0.099	2893.8	4.2	9.8	0.11	0.03	0.086
10.9	0.114	2888.8	3.7	4.8	0.06	0.02	0.096
12.2	0.128	2904.8	3.4	6.8	0.07	0.08	0.103
13.5	0.141	2888.7	3.2	4.7	0.09	0.13	0.093
26.8	0.281	2890.1	4.2	6.1	-0.04	0.25	0.086
33.4	0.349	2889.8	3.9	5.8	0.21	0.04	0.083
40.0	0.419	2898.0	4.9	14.0	0.12	0.05	0.071
53.4	0.559	2892.6	4.4	8.6	0.14	0.05	0.060
67	0.702	2901.6	2.1	7.6	0.20	0.04	0.060

It has been seen that the acceleration amplitude is higher in the Series B measurement. To investigate the mechanism at the origin of these squealing events it is interesting also to compare the vibration velocity with the nominal sliding velocity. If the vibration velocity equals the sliding velocity, stick may occur and a stick-slip phenomenon may also be involved. The velocity is integrated from the acceleration after using a high pass Butterworth filter, in this case the cut-off frequency is 400 Hz for Series A and 1000 Hz for Series B. Three examples are shown in Figure 8-16 to Figure 8-18 for different rotational speed in different series of measurements. The horizontal line in these figures defines the estimate for rotational speed (sliding velocity) of each case. It can be seen from Figure 8-16 and Figure 8-17 that with a low rotational speed, the maximum wheel axial velocity are very close to the sliding velocity but never exceeds it. Especially from Figure 8-16(b) it can be observed that in some cycles the maximum wheel velocity is just equal to the sliding velocity. This is a sign of stick slip which has been shown in Chapter 3. However, when the rotational speed becomes higher, the maximum wheel axial velocity are below the sliding velocity (see example in Figure 8-18).
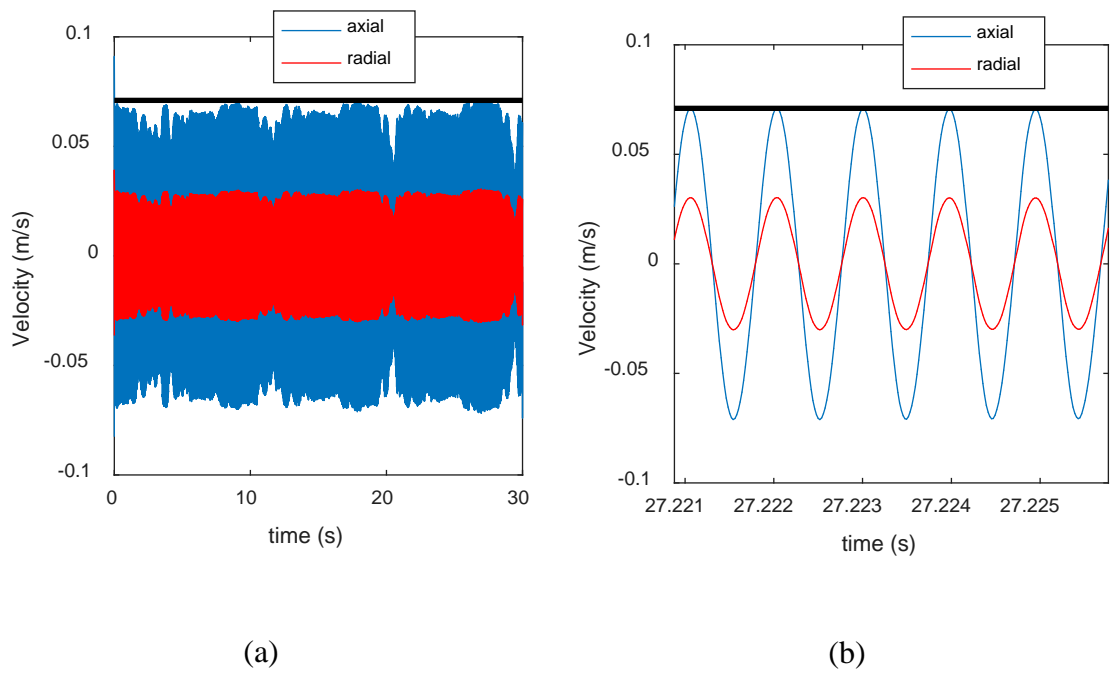
Figure 8-16. Velocity after integration from acceleration with rotational speed 6.8 rev/min of Series A; (a) whole time history; (b) close-up of a few cycles.
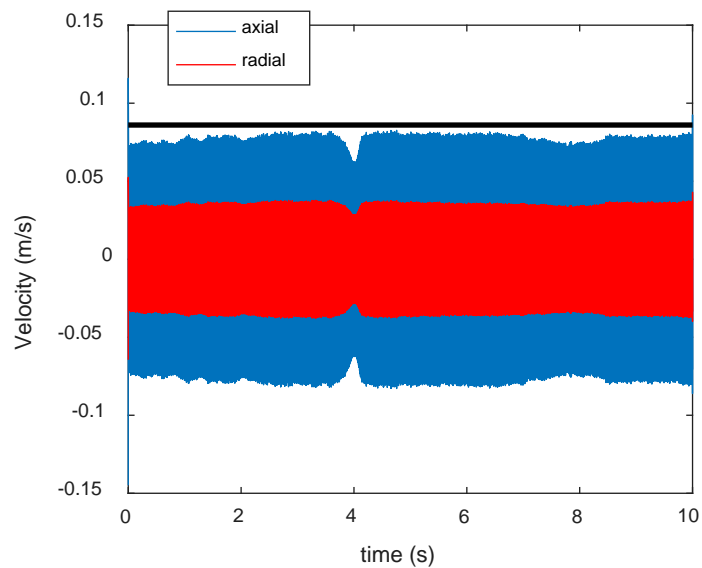
Figure 8-17. Velocity after integration from acceleration with rotational speed 8.2 rev/min of Series B
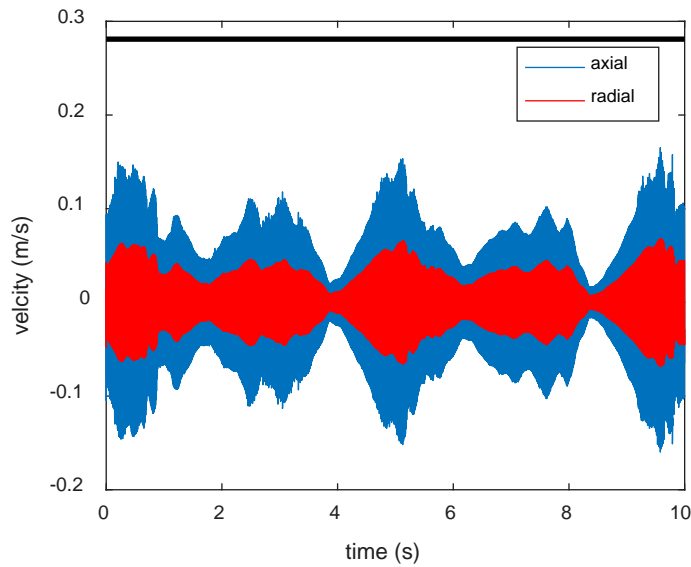
Figure 8-18. Velocity after integration from acceleration with rotational speed 40 rev/min of Series B

For all the cases, the velocity vibration amplitude is estimated here according to

$$|v| = \frac{|a|}{\omega} \tag{8-2}$$

where ω is the average squealing frequency and can be found in Table 8-2 and Table 8-3 (in Hz), a is obtained by multiplying $\sqrt{2}$ by the root-mean-square value of the acceleration data in each test. The vibration amplitudes in the axial direction are also shown in Table 8-2 and Table 8-3. They are also plotted in Figure 8-19.
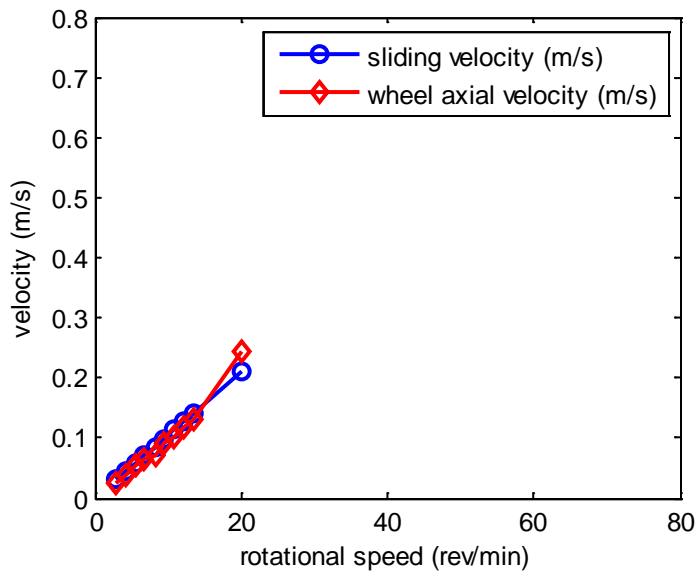
(a)
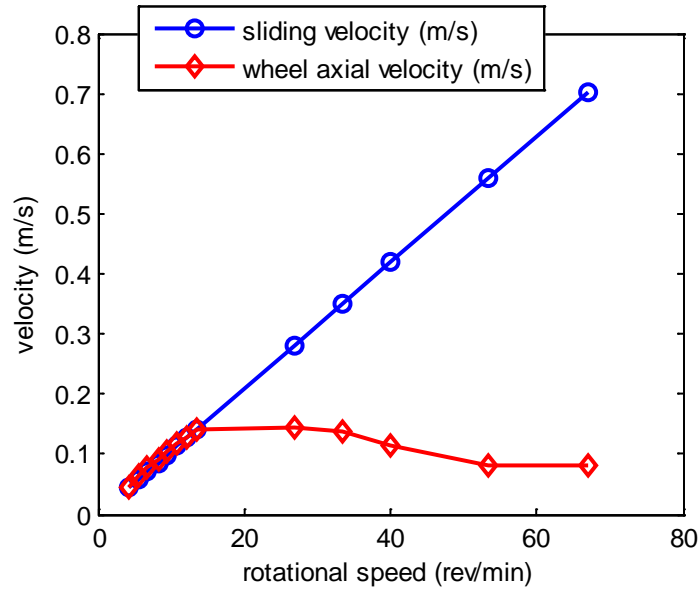
(b)

Figure 8-19. Comparison of the sliding velocity and the maximum wheel axial velocity: (a) Series A; (b) Series B

It can be found that when the sliding velocity is smaller than 0.15 m/s, the maximum wheel axial velocity is very similar to the sliding velocity. However, when the sliding velocity becomes larger than 0.15 m/s, the maximum wheel axial velocity is always smaller. According to the results in Section 3.1 for a mass-on-belt systems, in the stick-slip phenomenon, when the velocity of the mass becomes the same as the sliding velocity (belt velocity), it is in the stick phase. When the velocity of the mass is smaller than the sliding velocity, it is in the slip phase. The mass velocity will not exceed the velocity of the belt. The comparison of the sliding velocity and the maximum wheel axial velocity suggests that, with small sliding velocity, stick-slip may exist in these measurements.

8.3.3.2 Friction coefficient

In these measurements, the total static normal load (including the wheel and the arm) is 30.4 N. From the measured lateral force, the average friction coefficient can be estimated. However, the dynamic normal load is not measured so this friction coefficient is only an approximate value. For each rotating speed, the friction coefficient is averaged during the measurement time. The friction curves for both series are then shown in Figure 8-20 with error bars (±standard deviation) included. It can be seen that the friction coefficient during the squealing time window for each sliding velocity fluctuates and the error bar is very large (around ±30% of the average value). A mild falling trend of the average friction coefficient with increasing sliding velocity can be observed.

181

Another approach is adopted here to reduce the effect of the slow fluctuations in the normal load. In this approach, only the time periods with a relatively steady lateral force are used to determine the friction coefficient. Specifically, for each rotational speed, two sets of data are chosen from the whole time window of the lateral force. They satisfy the following conditions,

$$f_{min} < f < f_{min} + 0.2(f_{max} - f_{min}), \qquad (8\text{-}3)$$

$$f_{max} - 0.2(f_{max} - f_{min}) < f < f_{max} \qquad (8\text{-}4)$$

where f_{max} and f_{min} are the maximum and the minimum lateral forces in the time window for each rotational speed. This means that only the time windows corresponding to the lateral force close to the minimum, or the maximum value, are selected to calculate the friction coefficient. In other words this would correspond to using always the same angular sector on the rotating disc for the analysis. After this selection, the friction coefficient obtained is shown in Figure 8-21. It can be found that the error bar is smaller now but there is a large difference between the two average values. The difference between the maxima and minima are likely to be related to fluctuations in the normal load.

Because the lateral force does not decrease in every case with increasing velocity and because the standard deviation is large, these friction force measurements are not conclusive.
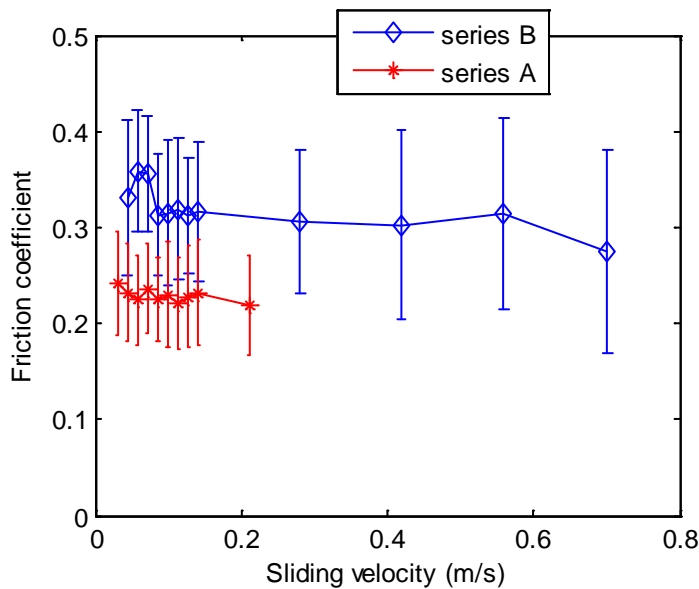
Figure 8-20. Friction-velocity curves of Series A and B
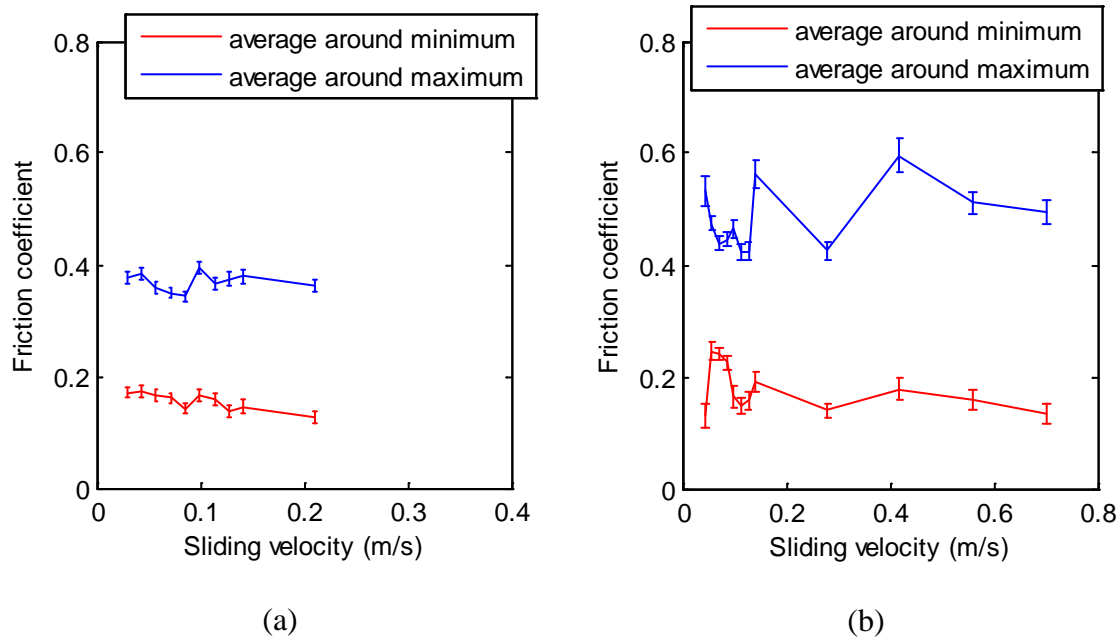
Figure 8-21. Friction-velocity curves of Series A and B after selection of the lateral force around minimum or maximum values. (a) Series A; (b) Series B.

8.4 Comparison with simulation results

8.4.1 Parameters

The curve squeal model described in Chapter 4 is used here to investigate whether the two squealing frequencies observed in these measurements can be predicted with the modelling approach described in Chapter 4. Only the four modes listed in Table 8-1 are included to represent the wheel dynamics. The mobilities including only these four modes are shown in Figure 8-22. For radial direction, a mass term is also included to fit the first anti-resonance with the measurement.

For the friction curve, only the falling regime after saturation is considered because in this measurement the wheel is not rolling. Therefore, the heuristic equation Eq. (2-23) is used to get the friction curve. Two combinations of the parameters in Eq. (2-23) as listed in Table 8-4 are used to fit the two friction curves in Figure 8-20. The results are shown in Figure 8-23 and Figure 8-24. Other parameters used in this curve squeal prediction are given in Table 8-5. The rail is assumed to be rigid.

(a)   (b)
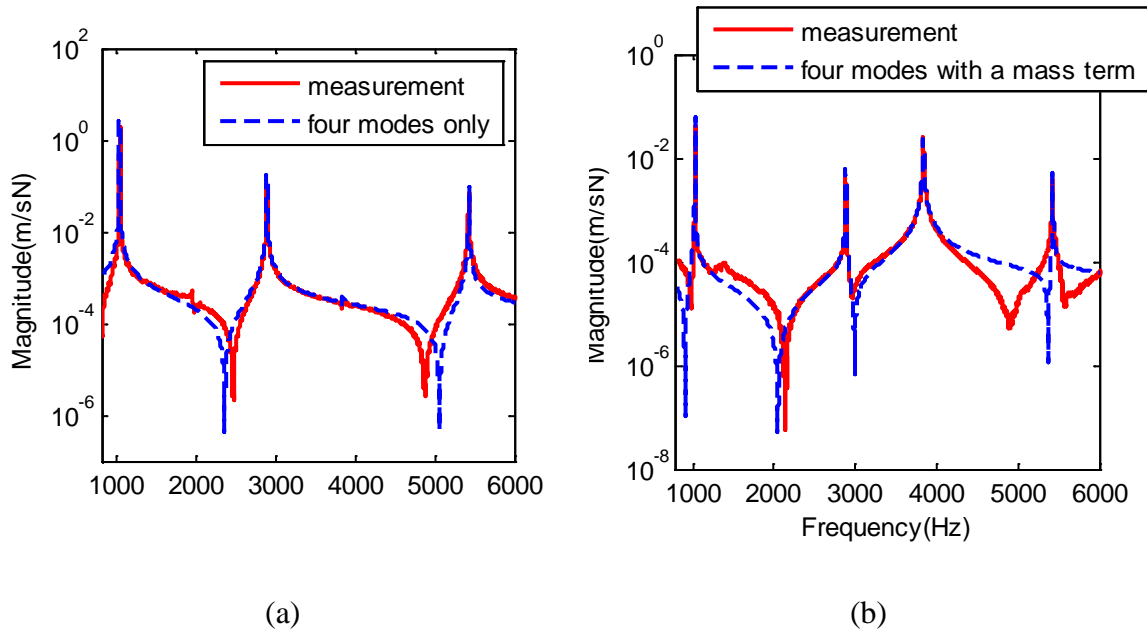
Figure 8-22. The mobility of wheel including four modes only and its comparison with the measuremet of the clamped wheel: (a) axial direction; (b) radial direction.

Table 8-4. The parameters for friction curves.

	Coulomb friction μ_0	λ in Eq. (2-23)	κ in Eq. (2-23)
Friction A for Series A measurement	0.26	0.25	0.005
Friction B for Series B measurement	0.4	0.3	0.005
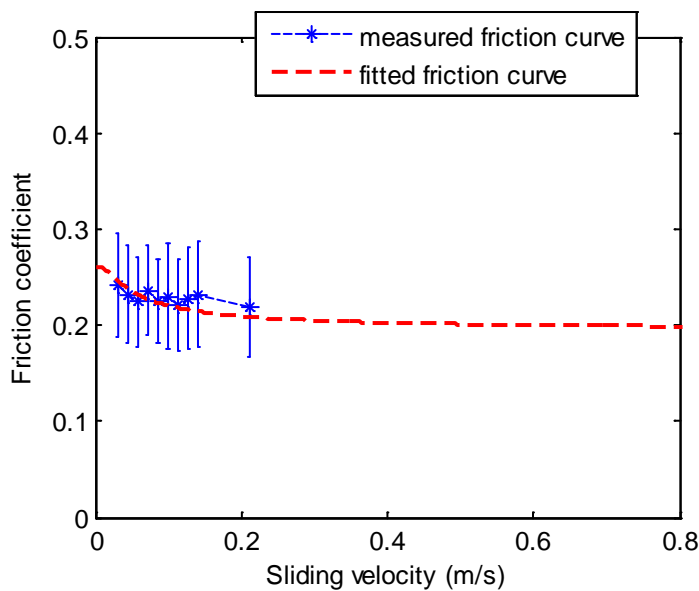
Figure 8-23. Measured and theoretical friction curve A
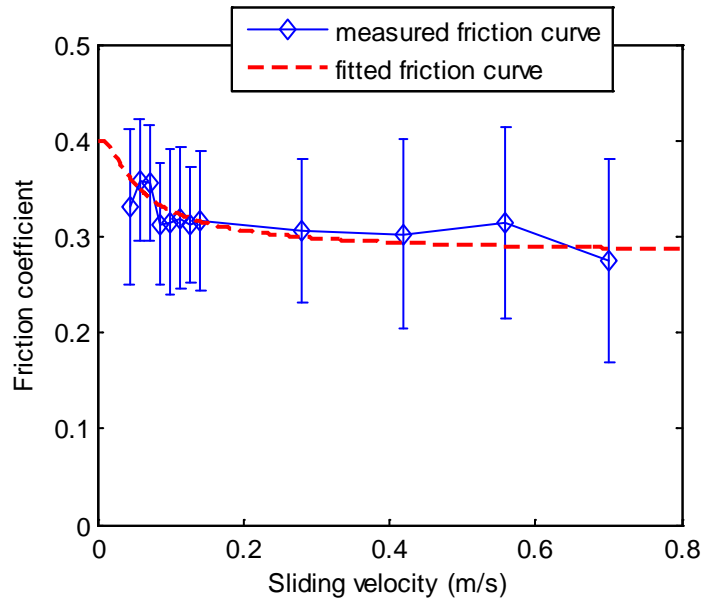
Figure 8-24. Measured and theoretical friction curve B

Table 8-5. Other parameters for prediction of curve squeal

Parameters	Values
Normal load	34 N
Rolling velocity	10 m/s
Steady state creepage	0.02
Wheel disc radius	10 cm

8.4.2 Frequency domain results

Two cases are calculated with these two friction curves. The Nyquist plot and bode plot for both cases are shown in Figure 8-25 and Figure 8-26. It can be seen that for the case with friction curve A only one unstable frequency, at 1076 Hz, appears, while for friction curve B, there are two unstable frequencies at 1078 Hz and 2877 Hz. The wheel modes responsible are 1026 Hz and 2884 Hz respectively. These agrees well with the measurements although the squealing frequencies are not exactly the same.
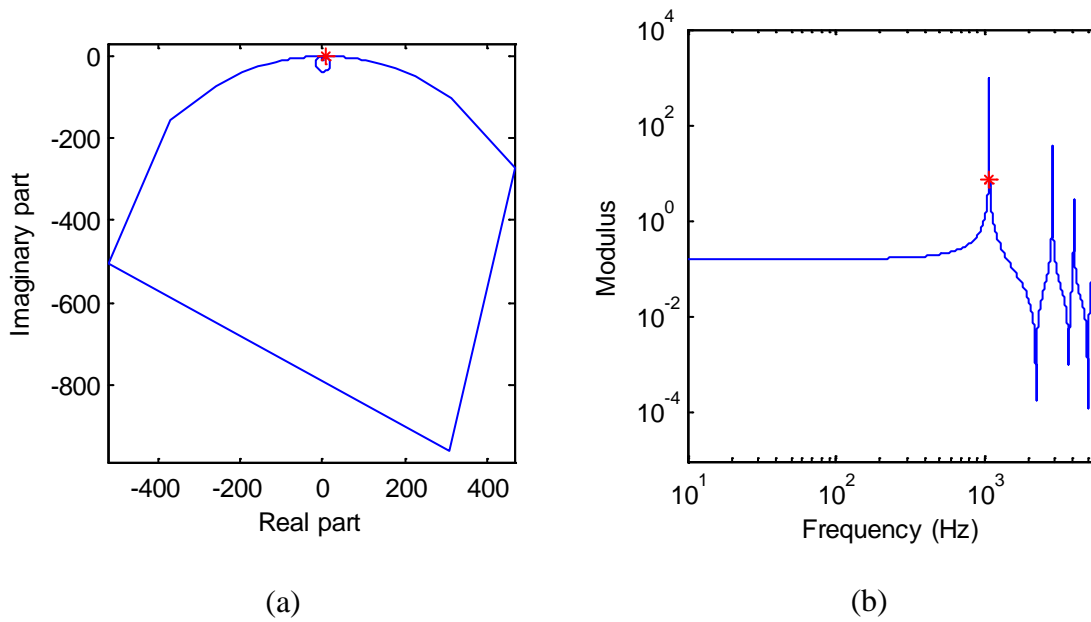
Figure 8-25. Stability analysis in frequency domain using friction curve A: (a) Nyquist locus; (b) modulus of the open loop transfer function. '*' unstable frequencies.
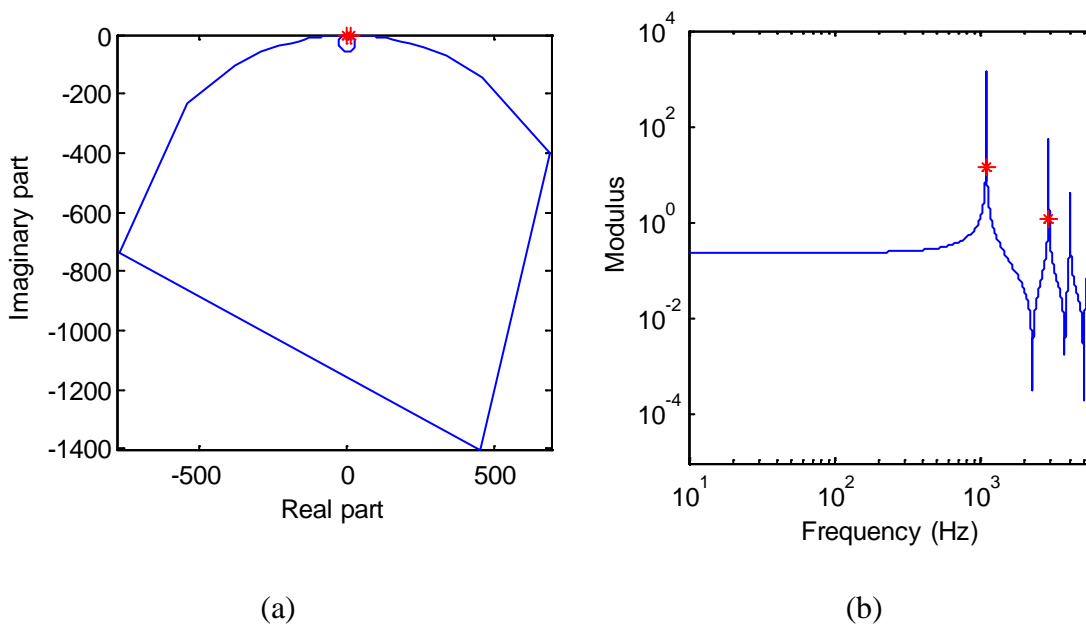
Figure 8-26. Stability analysis in frequency domain using friction curve B: (a) Nyquist locus; (b) modulus of the open loop transfer function. '*' unstable frequencies.

8.5 Summary

In this chapter, a simple laboratory measurement has been designed. Various tests have been performed including impact tests on a reduced scale wheel and vibration tests for the wheel on a rotating disc. From the impact test, it is found that the modes are well separated and the modes above 1 kHz only have a significant mode shape in one direction. The vibration test

shows that two squealing frequencies are found; in both cases the frequency shift and phase shift are close to zero. A mild falling trend is observed from the friction force measurement. For sliding velocities below 0.15 m/s the peak vibration velocity is found to be equal to the velocity of the rotating disc at the contact point. It can then be deduced that stick-slip or falling friction are at the origin of squeal for these measurements, while there is no evidence of mode coupling. Both squealing frequencies found in the measurement are also predicted by making use of the frequency domain curve squeal model presented in Chapter 4.

9 Conclusions and recommendations for further work

9.1 Conclusions

This thesis aims at giving a better understanding of the mechanism of curve squeal. First an existing curve squeal model is adopted and updated. By making use of this model, frequency domain and time domain results are obtained and different origins of curve squeal are found. Subsequently, different theoretical and experimental studies are carried out to give a detailed investigation of these different possible mechanisms of curve squeal.

The conclusions of this thesis can be summarised into four parts as below.

9.1.1 The utilization of an existing curve squeal model with an update of the track model

An existing curve squeal model has been improved by developing an equivalent modal model for the track dynamics. This equivalent track model is based on modal analysis of a multi-degree-of-freedom mass-spring system. This new track model is more physical and easier to apply in time domain calculations than the one used by Huang [27].

By making use of this curve squeal model, parametric studies are performed by varying the friction coefficient, presence of the track and friction characteristics at high creepage. The results show that there are different origins of the instability of the system. These can be described as falling friction, wheel mode coupling and wheel/rail coupling. Among these, falling friction can give instability in more situations and was accepted as the mechanism for curve squeal since 1970s, whereas mode coupling caught more attention in more recent years and is more widely adopted in other application areas. However, wheel/rail coupling has not been mentioned in previous studies.

The effect of wheel rotation, which will make the natural frequencies of the wheel split into pairs, is found to affect the curve squeal of different wheels in different ways. Conversely including the lateral contact spring has no influence. The time-domain calculations show that the dominant frequency is not necessarily the one with the largest loop gain in the frequency domain. Moreover, the dominant frequency in the time-domain results can change depending on whether the track dynamics are included.

9.1.2 The respective roles of falling friction and mode coupling

A two-mode model has been developed to illustrate the mode-coupling mechanism. Different pairs of modes have been considered, including modes from a regional train wheel, a freight train wheel and a resilient tram wheel.

By carrying out a parametric study using frequency-domain stability analysis, it is shown that the lateral position of the contact and the contact angle can both have a large effect on the squeal noise stability. The results suggest that both inner and outer wheels in a curve can result in squeal noise due to mode coupling or falling friction under appropriate conditions. Moreover, it is shown that the damping ratio of the wheel modes can play an important role. Increasing the damping of a single mode does not always have a beneficial effect on squeal noise and in some cases can actually make the system more prone to squeal. Increasing the damping ratios of both modes simultaneously has no effect until a certain limit is reached. For the wheels studied here this limit is found to be between 0.04% and 0.4%. The effects of the negative-slope and mode-coupling mechanisms are investigated together and it is shown that the negative slope of friction curve corresponds to a change in structural damping in the mode-coupling mechanism. As a consequence, when comparing with the stability of a single vibration mode, in some situations instability occurs for smaller values of friction slope but in other situations at higher values.

By analysing the system in the presence of a mode-coupling instability, it is demonstrated that a difference can exist between the squealing frequency and the natural frequency of the wheel modes. Moreover by studying the time-domain response, a phase difference between the vertical and lateral vibration is found to be a characteristic of mode coupling. If a negative friction slope is gradually included in the model this phase shift and frequency shift decreases and tends to vanish once the negative slope mechanism becomes dominant.

Finally, some qualitative comparisons haven been made with field measurements of wheel acceleration during curve squeal. The measurement data include two important characteristics of mode coupling: the squealing frequency lies between two adjacent modes or above one of the modes and there is a phase lag between the radial and axial directions. Both features have also been found in the results of the simplified model by including only two modes.

9.1.3 Effect of track dynamics

The role played by the track dynamics in the excitation of curve squeal has been investigated, with attention focused on the situation with a constant friction coefficient. The rail has been represented by various models of increasing complexity. Initially it is modelled as an infinite Timoshenko beam on a two-layer elastic foundation. It has been demonstrated that, even with this rail model, single wheel modes can couple with the rail and give squeal.

Subsequently, the influence of various rail resonances has been investigated. Various features in the track can introduce wave reflections and/or 'modes' in the rail: discrete supports, the presence of additional wheels on the track, the rail cross-section deformation and the introduction of a lateral offset on the rail. These have been included in the squeal model but the results were found not to be significantly modified: the unstable frequencies that were found were still largely the same as those predicted with an infinite supported Timoshenko beam.

Finally a reduced model is considered, in which the wheel and rail are each represented by single-degree-of-freedom systems. The rail vibration behaviour in the vertical direction is simplified to that of a mass, a spring, or a damper. For a mass or damper-like behaviour of the rail, the system was found to be unstable even with a very small friction coefficient. This indicates that it is not necessarily the introduction of 'modes' in the rail that causes the wheel modes to couple with the rail; instead the equivalent mass and especially damper behaviour of an infinite rail can be the origin of a wheel-rail coupling phenomenon.

9.1.4 Laboratory measurement.

A laboratory measurement is carried out and squeal noise is observed. First, the impact tests show that for the wheel adopted there are not two modes close to each other and the modes only have an important component of the mode shapes in one direction. This makes the wheel not prone to have mode coupling. Also the absence of frequency shift and phase difference also suggest that mode coupling is not present. In addition, the friction force shows a mild falling trend with increasing sliding velocity. These observations suggest that stick-slip and/or falling friction are at the origin for this squeal noise.

9.1.5 Summing up

This thesis explained three different mechanisms for curve squeal noise: falling friction, mode coupling, wheel/rail coupling. Among these, the third mechanism, i.e. wheel/rail

coupling, has never been mentioned before. The importance of the rail dynamics on the occurrence of curve squeal should be given more attention in the future. This may explain why the curve squeal noise is difficult to mitigate. Also, the characteristics of mode coupling are investigated. These are supported by both simulation and measurement results. This can give some indications for how to distinguish mode coupling and falling friction.

9.2 Recommendations for future work

Based on current work and previous studies, the suggestion for further work are given as below:

1) **Inclusion of longitudinal and spin creepages**. In the work presented in this thesis, the longitudinal and spin creepages are not included. However, in some previous studies [26] [50, 51] [53], it was shown that the creepages in these two directions could affect curve squeal. The longitudinal and spin creepage can affect the friction curve or, for some specific curving conditions, they can even induce curve squeal. It is recommended to introduce longitudinal and spin creepage in curve squeal models and/or in simplified models to discuss the possible mechanism for curve squeal in these situations.

2) **Two-point contact**. Except for the study in [31, 33], which considered the effect of two contact points, all other previous studies (including this thesis) only assumed a single contact point. Two contact points condition can occur during curving and can have an effect in exciting the radial direction. Both frequency domain and time domain models for two contact points can be developed.

3) **Effect of wheel wear.** In the railway field, the wear of the wheel is a common phenomenon after long-term operation of the train. The radius can be reduced with reprofiling by up to 50 mm. As the wheel wears the mode shapes and natural frequencies will change. It has been shown that the coupling between wheel modes can lead to curve squeal. The effect of the wheel wear on the mode coupling can be investigated. Different wheels at different degrees of wear can be considered to see how wheel wear affects the likelihood of curve squeal.

4) **Wheel rotation**. It is found in this thesis that the wheel rotation can affect the curve squeal results and the rolling velocity which can change the split frequencies also has an influence. Some further studies can be performed. A reduced model like the one in Chapter 6 can be developed for including wheel rotation, which then can be more convenient to carry out

parametric studies. For example, different pairs of modes from different wheels can be considered to see which ones are prone to squeal when wheel rotation is included.

5) **Laboratory measurement.** In the laboratory measurement designed in this thesis, the wheel is stationary. Also, mode coupling is not observed for this measurement with a specific wheel. It is suggested for future study that a rolling wheel is designed. Some more wheels can be tested to find a case with mode coupling and then try to identify the characteristics of mode coupling in a lab measurement. Moreover, the normal load should be measured, by using e.g. multi axial load cells or strain gauges on the wheel surface, to introduce the effect of the variation of the normal load, which will give a better measurement result for the friction force. The vibration velocity can be measured directly using laser vibrometers instead of obtaining it from integration of the acceleration data.

Appendix

Appendix A. Publications

Journal papers

1. **B. Ding**, Giacomo Squicciarini, David Thompson, Roberto Corradi. An assessment of mode-coupling and falling-friction mechanisms in railway curve squeal through a simplified approach. Journal of Sound and Vibration, 2018, 423: 126-140.
2. **B. Ding**, Giacomo Squicciarini, David Thompson. Effect of rail dynamics on curve squeal under constant friction conditions. Journal of Sound and Vibration, 2019, 442, 183-199.

Conference papers

1. **B. Ding**, G. Squicciarini, D. J. Thompson. Effects of rail dynamics and friction characteristics on curve squeal. Journal of Physics: Conference Series. Vol. 744. No. 1. IOP Publishing, In: XIII International Conference on Motion and Vibration Control and XII International Conference on Recent Advances in Structural Dynamics (MoViC/RASD), Southampton, UK, 2016.
2. D. J. Thompson, G. Squicciarini, **B. Ding** and L. Baeza. A state-of-the-art review of curve squeal noise: phenomena, mechanisms, modelling and mitigation. In: Anderson D. et al. (eds) Noise and Vibration Mitigation for Rail Transportation Systems. Notes on Numerical Fluid Mechanics and Multidisciplinary Design, vol 139. Springer, 2018.
3. **B. Ding**, G. Squicciarini, D. J. Thompson. Curve Squeal for a Tramway Wheel with both Falling and Constant Friction. In: First International Conference on Rail Transportation Chengdu, China, July, 2017.

Appendix B. Translation and rotation of wheel and track dynamics

This section provides the translation and rotation matrices to transform the wheel and track dynamics at the nominal contact to the local contact point.

The mode shape matrix of the wheel or the track can be defined as:

$$
\boldsymbol{\Phi} = \begin{bmatrix} \phi_{11} & \phi_{12} & \cdots & \phi_{1N} \\ \phi_{21} & \phi_{22} & \cdots & \phi_{2N} \\ \vdots & \vdots & \ddots & \vdots \\ \phi_{61} & \phi_{61} & \cdots & \phi_{6N} \end{bmatrix} \tag{B.1}
$$

where ϕ_{in} is the modeshape of mode n in the i direction.

Figure B.1 gives a schematic view of the transformation. The wheel tyre and rail head are both assumed not to deform. The original contact point is assumed to be at P_0; it moves to P_1 by a translation (l_1, l_2, l_3), then rotates by an angle θ.
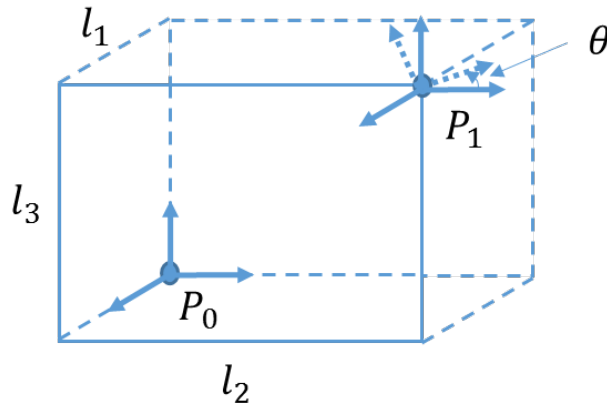
Figure B.1. Rigid transformation: translation from P_0 to P_1 and then rotatation about x-axis.

Hence the relationship between the mode shape matrix at P_0, $\boldsymbol{\Phi}_{P_0}$, and the mode shape matrix at P_1, $\boldsymbol{\Phi}_{P_1}$, is:

$$
\boldsymbol{\Phi}_{P_1} = \mathbf{T}_{\mathrm{rot}}\mathbf{T}_{\mathrm{off}}\boldsymbol{\Phi}_{P_0} \tag{B.2}
$$

where the translation matrix $\mathbf{T}_{\mathrm{off}}$ and rotation matrix $\mathbf{T}_{\mathrm{rot}}$ are [27]:

$$
\mathbf{T}_{\text{off}} = \left[\begin{array}{ccc|ccc}
1 & 0 & 0 & 0 & l_3 & -l_2 \\
0 & 1 & 0 & -l_3 & 0 & l_1 \\
0 & 0 & 1 & l_2 & -l_1 & 0 \\
\hline
0 & 0 & 0 & 1 & 0 & 0 \\
0 & 0 & 0 & 0 & 1 & 0 \\
0 & 0 & 0 & 0 & 0 & 1
\end{array}\right] \tag{B.3}
$$

$$
\mathbf{T}_{\text{rot}} = \left[\begin{array}{ccc|ccc}
1 & 0 & 0 & 0 & 0 & 0 \\
0 & \cos\theta & \sin\theta & 0 & 0 & 0 \\
0 & -\sin\theta & \cos\theta & 0 & 0 & 0 \\
\hline
0 & 0 & 0 & 1 & 0 & 0 \\
0 & 0 & 0 & 0 & \cos\theta & \sin\theta \\
0 & 0 & 0 & 0 & -\sin\theta & \cos\theta
\end{array}\right] \tag{B.4}
$$

Similarly, the transformation can be written in terms of mobility as:

$$
\begin{bmatrix}
Y_{11}^{P1} & Y_{12}^{P1} & \cdots & Y_{16}^{P1} \\
Y_{21}^{P1} & Y_{22}^{P1} & & Y_{26}^{P1} \\
\vdots & \vdots & \ddots & \vdots \\
Y_{61}^{P1} & Y_{62}^{P1} & \cdots & Y_{66}^{P1}
\end{bmatrix} = \mathbf{T}_{\text{tot}}
\begin{bmatrix}
Y_{11}^{P0} & Y_{12}^{P0} & \cdots & Y_{16}^{P0} \\
Y_{21}^{P0} & Y_{22}^{P0} & & Y_{26}^{P0} \\
\vdots & \vdots & \ddots & \vdots \\
Y_{61}^{P0} & Y_{62}^{P1} & \cdots & Y_{66}^{P0}
\end{bmatrix} \mathbf{T}_{\text{tot}}^{\text{T}} \tag{B.5}
$$

where Y_{ij} is the mobility in the i direction due to excitation at direction j and

$$
\mathbf{T}_{\text{tot}} = \mathbf{T}_{\text{rot}}\mathbf{T}_{\text{off}} \tag{B.6}
$$

Appendix C. The wheel mobility including effect of wheel rotation

When a wheel rolls along the track with velocity V, the force point moves around its circumference at an angular speed $\Omega = V/r_0$ as shown in Figure C.1. This will cause the natural frequencies to split into pairs when viewed from the forcing point. The theory of this effect will be given here based on [103].
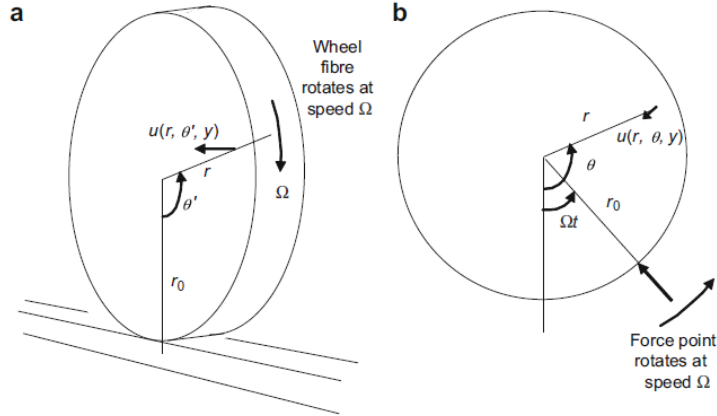
Figure C.1 (a) coordinates with reference point fixed at forcing point, (b) coordinates with reference point fixed in wheel (from [1])

According to the modal analysis, the vibration displacement (at the point x and time t) of the wheel can be approximated written as:

$$w(x,t) = \sum_{r=1}^{N} \psi_r(x) q_r(t) \tag{C.1}$$

where q_r are the generalized coordinates of r_{th} mode and ψ_r is the normal modes of the static wheel. q_r can be found from uncoupled modal equations:

$$m_r \ddot{q}_r(t) + c_r \dot{q}_r(t) + k_r q_r(t) = Q_r(t) \tag{C.2}$$

where m_r, c_r, k_r are the generalized mass, damping and stiffness. $Q_r(t)$ are generalized forces corresponding to the mode shapes ψ_r.

The generalized force depends on the time-varying boundary conditions: the force is a harmonic force with angular frequency ω and amplitude P acting at the moving point $(r, \theta, z) = (R, \Omega t, Z)$. The force is thus taken as:

$$P\delta(r,\theta,z|R,\Omega t,Z)e^{i\omega t} = P\frac{\delta(r-R)\delta(\theta-\Omega t)\delta(z-Z)}{r}e^{i\omega t} \tag{C.3}$$

The r_{th} wheel mode is now classified by its number of nodal diameters and nodal circles (n,m). These wheel modes are specified as having even (cosine) and odd (sine) angular distributions. The mode shape can be divided into two sets of coordinates: type *I*, the axial and radial displacements and the rotation about the circumferential direction, and type *II*, the circumferential displacement and the other two rotations. Then for 'even' modes the full mode shapes ψ_{mn}^e can be written as:

$$\psi_{mn}^e(r,\theta,y) = \psi_{mn}^I(r,\theta,y)\cos n\theta + \psi_{mn}^{II}(r,\theta,y)\sin n\theta \tag{C.4}$$

while for the odd modes:

$$\psi_{mn}^o(r,\theta,y) = \psi_{mn}^I(r,\theta,y)\sin n\theta - \psi_{mn}^{II}(r,\theta,y)\cos n\theta \tag{C.5}$$

where ψ_{mn}^I and ψ_{mn}^{II} consist of type *I* and type *II* coordinates, respectively.

Then for even modes Eq. (C.2) can be written as:

$$m_{mn}\ddot{q}_{mn}^e(t) + c_{mn}\dot{q}_{mn}^e(t) + k_{mn}q_{mn}^e(t) = Q_{mn}^e(t)$$

$$= \iiint_V [\mathbf{P}\delta(r,\theta,z|R,\Omega t,Z)e^{i\omega t}]\psi_{mn}^e(r,\theta,y)\mathrm{d}V \tag{C.6}$$

$$= \{\mathbf{P}^I\psi_{mn}^I(R,Z)\cos n\Omega t + \mathbf{P}^{II}\psi_{mn}^{II}(R,Z)\sin n\Omega t\}e^{i\omega t}$$

where the force vector $\mathbf{P}$ is also split into type *I* and type *II* components. Similarly, for odd modes:

$$m_{mn}\ddot{q}_{mn}^o(t) + c_{mn}\dot{q}_{mn}^o(t) + k_{mn}q_{mn}^o(t) = Q_{mn}^o(t)$$

$$= \{\mathbf{P}^I\psi_{mn}^I(R,Z)\sin n\Omega t - \mathbf{P}^{II}\psi_{mn}^{II}(R,Z)\cos n\Omega t\}e^{i\omega t} \tag{C.7}$$

By making use of

$$e^{i\omega t}\cos n\Omega t = (e^{i(\omega+n\Omega)t} + e^{i(\omega-n\Omega)t})/2 \tag{C.8}$$

$$e^{i\omega t}\sin n\Omega t = (e^{i(\omega+n\Omega)t} - e^{i(\omega-n\Omega)t})/2i \tag{C.9}$$

Eqs. (C.6) and (C.7) become:

$$q_{mn}^e = T_{mn}\frac{e^{i(\omega+n\Omega)t}}{2m_{mn}d_+(\omega)} + T_{mn}^*\frac{e^{i(\omega-n\Omega)t}}{2m_{mn}d_-(\omega)} \tag{C.10}$$

$$q_{mn}^o = -iT_{mn}\frac{e^{i(\omega+n\Omega)t}}{2m_{mn}d_+(\omega)} + iT_{mn}^*\frac{e^{i(\omega-n\Omega)t}}{2m_{mn}d_-(\omega)} \tag{C.11}$$

where $*$ denotes complex conjugate. T_{mn} and $d_\pm$ are given by:

$$T_{mn} = \mathbf{P}^I\psi_{mn}^I(R,Z) - i\mathbf{P}^{II}\psi_{mn}^{II}(R,Z) \tag{C.12}$$

$$d_\pm = \omega_{mn}^2 - (\omega \pm n\Omega)\char`\^2 + 2i\zeta_{mn}(\omega \pm n\Omega)\omega_{mn} \tag{C.13}$$

where $\omega_{mn} = \sqrt{k_{mn}/m_{mn}}$ and $\zeta_{mn} = c_{mn}/2\omega_{mn}m_{mn}$.

Substituting these into Eq. (C.1) gives:

$$w(r,\theta,y,t) = \sum_{m,n}\left(\Psi_{mn}(r,y)T_{mn}\frac{e^{i((\omega+n\Omega)t-n\theta)}}{2m_{mn}d_+(\omega)} + \Psi_{mn}^*(r,y)T_{mn}^*\frac{e^{i((\omega-n\Omega)t+n\theta)}}{2m_{mn}d_-(\omega)}\right) \tag{C.14}$$

where $\Psi_{mn} = \psi_{mn}^I + \psi_{mn}^{II}$. This consistes of two waves rotating in opposite directions with different frequencies, $\omega \pm n\Omega$.

Transforming the response into the reference frame in which the force point is stationary, the coordinates are (r,θ',y) with $\theta' = \theta - \Omega t$ and now Eq. (C.14) becomes:

$$\begin{aligned}
w(r,\theta',y,t) = e^{i\omega t}\sum_{m,n}\Bigg(&\mathbf{\Psi}_{mn}(r,y)T_{mn}\frac{e^{-in\theta'}}{2m_{mn}d_+(\omega)} \\
&+ \mathbf{\Psi}_{mn}^*(r,y)T_{mn}^*\frac{e^{in\theta'}}{2m_{mn}d_-(\omega)}\Bigg)
\end{aligned} \tag{C.15}$$

Eq. (C.15) allows the mobility of the wheel Y_{jk} to be determined, which is :

$$Y_{jk}(\omega) = i\omega\sum_{m,n}\left\{\frac{\psi_{mnj}(r,y)\psi_{mnj}(r_0,y_0)}{2m_{mn}}\left(\frac{\varepsilon_{jk}e^{-in\theta'}}{d_+(\omega)} + \frac{\varepsilon_{jk}^*e^{in\theta'}}{d_-(\omega)}\right)\right\} \tag{C.16}$$

where the force is at $\theta' = 0$ and the response at θ', and

$$\varepsilon_{jk} = \begin{cases} 1 & \text{If } j \text{ and } k \text{ are both of type } I \text{ or both of type II} \\ -i & \text{If } j \text{ is of type } I \text{ and k is of type } II \\ i & \text{If } j \text{ is of type } II \text{ and k is type } I \end{cases} \tag{C.17}$$

The denominators of Eq. (C.16) become zero when $d_\pm \to 0$. According to Eq. (C.13), this means

$$\omega = \omega_{mn} \mp n\Omega \qquad (C.18)$$

These are the natural frequencies of the rotating wheel as seen from the excitation point.

References

[1] D.J. Thompson, Railway noise and vibration: mechanisms, modelling and means of control, Elsevier, 2008.

[2] D.J. Thompson, C.J.C. Jones, Noise and vibration from railway vehicles, in: S. Iwnicki (Ed.) Handbook of railway vehicle dynamics, CRC Press, 2006.

[3] D.J. Thompson, C.J.C. Jones, A review of the modelling of wheel/rail noise generation, Journal of sound and vibration, 231 (2000) 519-536.

[4] D.J. Thompson, G. Squicciarini, B. Ding, L. Baeza, A state-of-the-art review of curve squeal noise: phenomena, mechanisms, modelling and mitigation, in: P.-E.G. David Anderson, Masanobu Iida, JamesT. Nelson, David J. Thompson, Thorsten Tielkes, David A. Towers, Paul de Vos, Jens C. O Nielsen (Ed.) Noise and Vibration Mitigation for Rail Transportation Systems: Proceedings for 12th International Workshop on Railway Noise, Springer, NNFM, volume 139, 2016.

[5] A. Wickens, Fundamentals of rail vehicle dynamics, CRC Press, 2005.

[6] J.J. Kalker, Three-dimensional elastic bodies in rolling contact, Springer Science & Business Media, 2013.

[7] R.C. Dorf, R.H. Bishop, Modern Control Systems, Pearson, New Jersey, USA, 2011.

[8] H. Von Stappenbeck, Streetcar curve noise, Zeitschriff Vereinschaft Deutscher Ingenieuren, 96 (1974) 171-175.

[9] M.J. Rudd, Wheel/rail noise—Part II: Wheel squeal, Journal of Sound and Vibration, 46 (1976) 381-394.

[10] C.J.M. van Ruiten, Mechanism of squeal noise generated by trams, Journal of Sound and Vibration, 120 (1988) 245-253.

[11] M. Nakai, Y. Chiba, M. Yokoi, Railway Wheel Squeal: 1st Report, On frequency of squeal, Bulletin of JSME, 25 (1982) 1127-1134.

[12] M. Nakai, Y. Chiba, M. Yokoi, Railway Wheel Squeal: 2nd report, Mechanism of specific squeal frequency, Bulletin of JSME, 27 (1984) 301-308.

[13] M. Nakai, M. Yokoi, Railway Wheel Squeal: 3rd Report, Squeal of a disk simulating a wheel in internal resonances, Bulletin of JSME, 28 (1985) 500-507.

[14] P. Remington, Wheel/rail squeal and impact noise: What do we know? What don't we know? Where do we go from here?, Journal of sound and vibration, 116 (1987) 339-353.

[15] E. Schneider, K. Popp, H. Irretier, Noise generation in railway wheels due to rail-wheel contact forces, Journal of sound and vibration, 120 (1988) 227-244.

[16] K. Kraft, Der Einfluß der Fahrgeschwindigkeit auf den Haftwert zwischen Rad und Schiene (The influence of the driving velocity on the friction coefficient between wheel and rail), Archiv für Eisenbahntechnik (Archive for railway technology), 22 (1967) 58-78.

[17] U. Fingberg, A model of wheel-rail squealing noise, Journal of Sound and Vibration, 143 (1990) 365-377.

[18] F. Périard, Wheel-Rail Noise Generation: Curve Squealing by Trams, PhD Thesis, Technische Universiteit Delft, 1998.

[19] M.A. Heckl, Curve squeal of train wheels, Part 2: which wheel modes are prone to squeal?, Journal of sound and vibration, 229 (2000) 695-707.

[20] M.A. Heckl, X. Huang, Curve squeal of train wheels, part 3: active control, Journal of Sound and Vibration, 229 (2000) 709-735.

[21] F. de Beer, M. Janssens, P. Kooijman, W. van Vliet, Curve squeal of railbound vehicles (part 1): frequency domain calculation model, Proceedings of Internoise, Nice, France, 3 (2000) 1560-1563.

[22] F.G. de Beer, M.H.A. Janssens, P.P. Kooijman, Squeal noise of rail-bound vehicles influenced by lateral contact position, Journal of Sound and Vibration, 267 (2003) 497-507.

[23] M. Janssens, W. van Vliet, P. Kooijman, F. De Beer, Curve squeal of railbound vehicles (part 3): measurement method and results, Proceedings of Internoise, Nice, France, 3 (2000) 1568-1571.

[24] P. Kooijman, W. van Vliet, M. Janssens, F. de Beer, Curve squeal of railbound vehicles (part 2): set-up for measurement of creepage dependent friction coefficient, Proceedings of Internoise, Nice, France, 3 (2000) 1564-1567.

[25] D. Thompson, B. Hemsworth, N. Vincent, Experimental validation of the TWINS prediction program for rolling noise, part 1: description of the model and method, Journal of Sound and Vibration, 193 (1996) 123-135.

[26] A. Monk-Steel, D.J. Thompson, Models for railway curve squeal noise, in: VIII International Conference on Recent Advances in Structural Dynamics, Southampton,UK, 2003.

[27] Z. Huang, Theoretical Modelling of Railway Curve Squeal, PhD Thesis, University of Southampton, UK, 2007.

[28] S.S. Hsu, Z. Huang, S.D. Iwnicki, D.J. Thompson, C.J.C. Jones, G. Xie, P.D. Allen, Experimental and theoretical investigation of railway wheel squeal, Proceedings of the Institution of Mechanical Engineers, Part F: Journal of Rail and Rapid Transit, 221 (2007) 59-73.

[29] D. Thompson, C. Jones, Sound radiation from a vibrating railway wheel, Journal of Sound and Vibration, 253 (2002) 401-419.

[30] J. Kalker, A fast algorithm for the simplified theory of rolling contact, Vehicle System Dynamics, 11 (1982) 1-13.

[31] G. Squicciarini, S. Usberti, D.J. Thompson, R. Corradi, A. Barbera, Curve squeal in the presence of two wheel/rail contact points, in: J. Nielsen, D. Anderson, P.-E. Gautier, M. Iida, J. Nelson, T. Tielkes, D. Thompson, D. Towers, P. de Vos (Eds.) Noise and Vibration Mitigation for Rail Transportation Systems: Proceedings of the 11th International Workshop on Railway Noise, Springer, NNFM, volume 126, 2015, pp. 603-610.

[32] J.R. Koch, N. Vincent, H. Chollet, O. Chiello, Curve squeal of urban rolling stock—Part 2: Parametric study on a 1/4 scale test rig, Journal of Sound and Vibration, 293 (2006) 701-709.

[33] I. Zenzerovic, Time-domain modelling of curve squeal: a fast model for one- and two-point wheel/rail contact, PhD, Chalmers University of Technology, Gothenburg, Sweden, 2017.

[34] G. Xie, P.D. Allen, S.D. Iwnicki, A. Alonso, D.J. Thompson, C.J.C. Jones, Z.Y. Huang, Introduction of falling friction coefficients into curving calculations for studying curve squeal noise, Vehicle System Dynamics, 44 (2006) 261-271.

[35] J.G. Giménez, A. Alonso, Gómez, Introduction of a friction coefficient dependent on the slip in the FastSim algorithm, Vehicle System Dynamics, 43 (2005) 233-244.

[36] X. Liu, P. Meehan, Wheel squeal noise: A simplified model to simulate the effect of rolling speed and angle of attack, Journal of Sound and Vibration, 338 (2015) 184-198.

[37] P.A. Meehan, X. Liu, Modelling and mitigation of wheel squeal noise amplitude, Journal of Sound and Vibration, 413 (2018) 144-158.

[38] N. Hoffmann, M. Fischer, R. Allgaier, L. Gaul, A minimal model for studying properties of the mode-coupling type instability in friction induced oscillations, Mechanics Research Communications, 29 (2002) 197-205.

[39] N. Hoffmann, L. Gaul, Effects of damping on mode-coupling instability in friction induced oscillations, ZAMM, 83 (2003) 524-534.

[40] H. Ouyang, W. Nack, Y. Yuan, F. Chen, Numerical analysis of automotive disc brake squeal: a review, International Journal of Vehicle Noise and Vibration, 1 (2005) 207-231.

[41] N.R. North, Disc brake squeal, in: Proceedings of IMechE, 1976, pp. 169-176.

[42] J.F. Brunel, P. Dufrénoy, M. Naït, J.L. Muñoz, F. Demilly, Transient models for curve squeal noise, Journal of Sound and Vibration, 293 (2006) 758-765.

[43] N. Kinkaid, O. O'reilly, P. Papadopoulos, Automotive disc brake squeal, Journal of Sound and Vibration, 267 (2003) 105-166.

[44] O. Chiello, J.B. Ayasse, N. Vincent, J.R. Koch, Curve squeal of urban rolling stock—Part 3: Theoretical model, Journal of Sound and Vibration, 293 (2006) 710-727.

[45] C. Collette, Importance of the wheel vertical dynamics in the squeal noise mechanism on a scaled test bench, Shock and Vibration, 19 (2012) 145-153.

[46] C. Glocker, E. Cataldi-Spinola, R.I. Leine, Curve squealing of trains: Measurement, modelling and simulation, Journal of Sound and Vibration, 324 (2009) 365-386.

[47] A. Pieringer, A numerical investigation of curve squeal in the case of constant wheel/rail friction, Journal of Sound and Vibration, 333 (2014) 4295-4313.

[48] J.J. Kalker, Three-dimensional elastic bodies in rolling contact, Springer Science & Business Media, 1990.

[49] A. Pieringer, L. Baeza, W. Kropp, Modelling of Railway Curve Squeal Including Effects of Wheel Rotation, in: J. Nielsen, D. Anderson, P.-E. Gautier, M. Iida, J. Nelson, D. Thompson, T. Tielkes, D. Towers, P. de Vos (Eds.) Noise and Vibration Mitigation for Rail Transportation Systems, Springer Berlin Heidelberg, 126, 2015, pp. 417-424.

[50] I. Zenzerovic, W. Kropp, A. Pieringer, An engineering time-domain model for curve squeal: Tangential point-contact model and Green′s functions approach, Journal of Sound and Vibration, 376 (2016) 149-165.

[51] I. Zenzerovic, W. Kropp, A. Pieringer, Influence of spin creepage and contact angle on curve squeal: A numerical approach, Journal of Sound and Vibration, 419 (2018) 268-280.

[52] G.X. Chen, J.B. Xiao, Q.Y. Liu, Z.Z. R., Complex eigenvalue analysis of railway curve squeal., in: B. Schulte-Werning, Thompson, D. J., Gautier, P.-E., Hanson, C., Hemsworth, B., Nelson, J., Maeda, T., de Vos, P. (Ed.) Noise and Vibration Mitigation for Rail Transportation Systems: Proceedings of the 9th International Workshop on Railway Noise, Springer, Heidelberg, NNFM, volume 99, 2008, pp. 433-439.

[53] D.J. Fourie, P.J. Gräbe, P.S. Heyns, R.D. Fröhling, Analysis of wheel squeal due to unsteady longitudinal creepage using the complex eigenvalue method, in: Noise and Vibration Mitigation for Rail Transportation Systems: Proceedings of 12th International Workshop on Railway Noise, Springer, NNFM, volume 139, 2016, pp. 57-69.

[54] D. Fourie, P. Gräbe, S. Heyns, R. Fröhling, Experimental characterisation of railway wheel squeal occurring in large-radius curves, Proceedings of the Institution of Mechanical Engineers, Part F: Journal of Rail and Rapid Transit, 230(6) (2016) 1561-1574.

[55] M. Janssens, W. van Vliet, P. Kooijman, F. de Beer, Curve squeal of rail bound vehicles, Part 3: measurement techniques for wheel/rail contact velocities and forces at squeal noise frequencies, in: Proceedings of the Internoise, 2000, pp. 27-30.

[56] A.D. Monk-Steel, D.J. Thompson, F.G. de Beer, M.H.A. Janssens, An investigation into the influence of longitudinal creepage on railway squeal noise due to lateral creepage, Journal of Sound and Vibration, 293 (2006) 766-776.

[57] E. Jie, J.Y. Kim, D.H. Hwang, J.H. Lee, K.J. Kim, J.C. Kim, An Experimental Study of Squeal Noise Characteristics for Railways using a Scale Model Test Rig, in: the Third International Conference on Railway Technology: Research, Development and Maintenance, Cagliari, Sardinia, Italy.

[58] I. Merideno, J. Nieto, N. Gil-Negrete, A. Landaberea, J. Iartza, Constrained layer damper modelling and performance evaluation for eliminating squeal noise in trams, Shock and Vibration, 2014 (2014).

[59] N. Vincent, J.R. Koch, H. Chollet, J.Y. Guerder, Curve squeal of urban rolling stock—Part 1: State of the art and field measurements, Journal of Sound and Vibration, 293 (2006) 691-700.

[60] R. Corradi, P. Crosio, S. Manzoni, G. Squicciarini, Experimental investigation on squeal noise in tramway sharp curves, in: Proceedings of the 8th International Conference on Structural Dynamics, EURODYN 2011, Leuven, 2011.

[61] D. Anderson, N. Wheatley, Mitigation of wheel squeal and flanging noise on the Australian rail network, in: Noise and Vibration Mitigation for Rail Transportation Systems, Springer, 2008, pp. 399-405.

[62] D. Anderson, N. Wheatley, B. Fogarty, J. Jiang, A. Howie, W. Potter, Mitigation of Curve Squeal Noise in Queensland, New South Wales and South Australia, CORE 2008: Rail; The Core of Integrated Transport, (2008) 625.

[63] D. Curley, D. Anderson, J. Jiang, D. Hanson, Field trials of Gauge face lubrication and top-of-rail friction modification for curve noise mitigation, in: Noise and Vibration Mitigation for Rail Transportation Systems, Springer, 2015, pp. 449-456.

[64] J. Jiang, R. Dwight, D. Anderson, Field Verification of Curving Noise Mechanisms, in: T. Maeda, P.-E. Gautier, C. Hanson, B. Hemsworth, J. Nelson, B. Schulte-Werning, D. Thompson, P. de Vos (Eds.) Noise and Vibration Mitigation for Rail Transportation Systems, Springer Japan, 118, 2012, pp. 349-356.

[65] J. Jiang, D.C. Anderson, R. Dwight, The Mechanisms of Curve Squeal, in: J. Nielsen, D. Anderson, P.-E. Gautier, M. Iida, J. Nelson, D. Thompson, T. Tielkes, D. Towers, P. de Vos (Eds.) Noise and Vibration Mitigation for Rail Transportation Systems, Springer Berlin Heidelberg, NNFM, volume 126, 2015, pp. 587-594.

[66] J. Jiang, D. Hanson, B. Dowell, Wheel Squeal: Insights from Wayside Condition Monitoring, in: P.-E.G. David Anderson, Masanobu Iida, JamesT. Nelson, David J. Thompson, Thorsten Tielkes, David A. Towers, Paul de Vos, Jens C. O Nielsen (Ed.) Noise and Vibration Mitigation for Rail Transportation Systems: Proceedings of the 12th International Workshop on Railway Noise, NNFM, volume 139, Australia, 2016, pp. 43-55.

[67] X. Liu, P. Meehan, Investigation of the effect of lateral adhesion and rolling speed on wheel squeal noise, Proceedings of the Institution of Mechanical Engineers, Part F: Journal of Rail and Rapid Transit, 227 (2013) 469-480.

[68] X. Liu, P. Meehan, Investigation of the effect of relative humidity on lateral force in rolling contact and curve squeal, Wear, 310 (2014) 12-19.

[69] X. Liu, P.A. Meehan, Investigation of squeal noise under positive friction characteristics condition provided by friction modifiers, Journal of Sound and Vibration, 371 (2016) 393-405.

[70] J.F. Brunel, P. Dufrénoy, J. Charley, F. Demilly, Analysis of the attenuation of railway squeal noise by preloaded rings inserted in wheels, The Journal of the Acoustical Society of America, 127 (2010) 1300-1306.

[71] S. Bühler, B. Thallemer, How to avoid squeal noise on railways state of the art and practical experience, in: Noise and Vibration Mitigation for Rail Transportation Systems, Springer, 2008, pp. 406-411.

[72] S.R. Marjani, D. Younesian, Suppression of Train Wheel Squeal Noise by Shunted Piezoelectric Elements, International Journal of Structural Stability and Dynamics, (2016) 1750027.

[73] D. Eadie, M. Santoro, J. Kalousek, Railway noise and the effect of top of rail liquid friction modifiers: changes in sound and vibration spectral distributions in curves, Wear, 258 (2005) 1148-1155.

[74] D.T. Eadie, M. Santoro, W. Powell, Local control of noise and vibration with KELTRACK™ friction modifier and Protector® trackside application: an integrated solution, Journal of Sound and Vibration, 267 (2003) 761-772.

[75] D. Eadie, M. Santoro, Top-of-rail friction control for curve noise mitigation and corrugation rate reduction, Journal of sound and vibration, 293 (2006) 747-757.

[76] D. Thompson, C. Jones, T. Waters, D. Farrington, A tuned damping device for reducing noise from railway track, Applied Acoustics, 68 (2007) 43-57.

[77] J. Jiang, I. Ying, D. Hanson, D. Anderson, An investigation of the influence of track dynamics on curve noise, in: Noise and Vibration Mitigation for Rail Transportation Systems, Springer, 2015, pp. 441-448.

[78] S. Bruni, R. Goodall, T. Mei, H. Tsunashima, Control and monitoring for railway vehicle dynamics, Vehicle System Dynamics, 45 (2007) 743-779.

[79] F. Elbers, E. Verheijen, Railway noise technical measures catalogue, in, UIC report UIC003-01-04fe, 2013.

[80] K.L. Johnson, Contact Mechanics, Cambridge University Press, 1987.

[81] J.L. Meriam, L.G. Kraige, Engineering mechanics: dynamics, John Wiley & Sons, 2012.

[82] S. Andersson, A. Söderberg, S. Björklund, Friction models for sliding dry, boundary and mixed lubricated contacts, Tribology International, 40 (2007) 580-587.

[83] R. Stribeck, Kugellager für beliebige Belastungen, Buchdruckerei AW Schade, Berlin N., 1901.

[84] X. Lu, M. Khonsari, E. Gelinck, The Stribeck curve: experimental results and theoretical prediction, Journal of tribology, 128 (2006) 789-794.

[85] H. Olsson, Control systems with friction, Lund University, 1996.

[86] R. Mindlin, Compliance of elastic bodies in contact, J. appl. Mech., 16 (1949) 259-268.

[87] A. Pieringer, Time-domain modelling of high-frequency wheel/rail interaction, PhD, Chalmers University of Technology, Sweden, 2011.

[88] P. Vermeulen, K. Johnson, Contact of nonspherical elastic bodies transmitting tangential forces, Journal of Applied Mechanics, 31 (1964) 338-340.

[89] J. Kalker, Review of wheel-rail rolling contact theories, The General Problem of Rolling Contact, 40 (1980) 77-91.

[90] J. Kalker, Survey of wheel—rail rolling contact theory, Vehicle System Dynamics, 8 (1979) 317-358.

[91] J. Kalker, Simplified theory of rolling contact, Delft Progress Rep., 1 (1973) 1-10.

[92] I.W. Kragelski, Reibung und Verschleiß., Berlin, Verlag Technik, Berlin, 1971.

[93] I.L. Singer, H. Pollock, Fundamentals of friction: macroscopic and microscopic processes, Springer Science & Business Media, 2012.

[94] J.J. Sinou, L. Jézéquel, Mode coupling instability in friction-induced vibrations and its dependency on system parameters including damping, European Journal of Mechanics - A/Solids, 26 (2007) 106-122.

[95] J.F. Barmanj, J. Katzenelson, A generalized Nyquist-type stability criterion for multivariable feedback systems, International Journal of Control, 20 (1974) 593-622.

[96] J.C. Butcher, Numerical methods for ordinary differential equations, Third ed., John Wiley & Sons, UK, 2016.

[97] D.J. Ewins, Modal testing: theory and practice, Research studies press Letchworth, 1984.

[98] S. Grassie, R. Gregory, D. Harrison, K. Johnson, The dynamic response of railway track to high frequency vertical excitation, Journal of Mechanical Engineering Science, 24 (1982) 77-90.

[99] T.X. Wu, D.J. Thompson, Analysis of lateral vibration behavior of railway track at high frequencies using a continuously supported multiple beam model, The Journal of the Acoustical Society of America, 106 (1999) 1369-1376.

[100] D.E.J. Lurcock, An investigation into the longitudinal vibration properties of railway track, University of Southampton, 2004.

[101] J. Yang, Time domain models of wheel/rail interaction taking account of surface defects, PhD thesis, University of Southampton, UK, 2012.

[102] T. Wu, D. Thompson, A hybrid model for the noise generation due to railway wheel flats, Journal of Sound and Vibration, 251 (2002) 115-139.

[103] D. Thompson, Wheel-rail noise generation, part V: inclusion of wheel rotation, Journal of Sound and Vibration, 161 (1993) 467-482.

[104] R.C. Dorf, R.H. Bishop, Modern Control Systems, 11th ed., Prentice Hall, Upper Saddle River, New Jersey, 2009.

[105] L. Charroyer, O. Chiello, J.-J. Sinou, Parametric study of the mode coupling instability for a simple system with planar or rectilinear friction, Journal of Sound and Vibration, 384 (2016) 94-112.

[106] D. Fourie, P. Gräbe, S. Heyns, R. Fröhling, Experimental characterisation of railway wheel squeal occurring in large-radius curves, Proceedings of the Institution of Mechanical Engineers, Part F: Journal of Rail and Rapid Transit, Published online (2015).

[107] T. Wu, D.J. Thompson, Vibration analysis of railway track with multiple wheels on the rail, Journal of Sound and Vibration, 239 (2001) 69-97.

[108] C.M. Nilsson, C.J.C. Jones, Theory manual for WANDS 2.1, in, ISVR Technical Memorandum No. 975, University of Southampton, 2007.

[109] C.M. Nilsson, C. Jones, D.J. Thompson, J. Ryue, A waveguide finite element and boundary element approach to calculating the sound radiated by railway and tram rails, Journal of Sound and Vibration, 321 (2009) 813-836.

[110] A. Metrikine, H. Dieterman, Instability of vibrations of a mass moving uniformly along an axially compressed beam on a viscoelastic foundation, Journal of Sound and Vibration, 201 (1997) 567-576.

[111] M. Ismail, T. Harvey, J. Wharton, R. Wood, A. Humphreys, Surface potential effects on friction and abrasion of sliding contacts lubricated by aqueous solutions, Wear, 267 (2009) 1978-1986.

[112] A. Blanchard, Measurement of railyway curve squeal noise on ISVR's 1/5 scale railway, Institute of Sound and Vibration research, University of Southampton, UK, 2005.